

**THE EFFECTS OF MEMBRANE DYNAMICS ON HIGH-RESOLUTION
NMR OF ORIENTED OR MAS TRANSMEMBRANE POLYPEPTIDES**

A Thesis

Presented to

The Faculty of Graduate Studies

of

The University of Guelph

by

CHRISTOPHE FARÈS

In partial fulfilment of requirements

for the degree of

Doctor of Philosophy

September, 2003

©Christophe Farès, 2003



National Library
of Canada

Bibliothèque nationale
du Canada

Acquisitions and
Bibliographic Services

Acquisitions et
services bibliographiques

395 Wellington Street
Ottawa ON K1A 0N4
Canada

395, rue Wellington
Ottawa ON K1A 0N4
Canada

Your file Votre référence

ISBN: 0-612-89253-0

Our file Notre référence

ISBN: 0-612-89253-0

The author has granted a non-exclusive licence allowing the National Library of Canada to reproduce, loan, distribute or sell copies of this thesis in microform, paper or electronic formats.

L'auteur a accordé une licence non exclusive permettant à la Bibliothèque nationale du Canada de reproduire, prêter, distribuer ou vendre des copies de cette thèse sous la forme de microfiche/film, de reproduction sur papier ou sur format électronique.

The author retains ownership of the copyright in this thesis. Neither the thesis nor substantial extracts from it may be printed or otherwise reproduced without the author's permission.

L'auteur conserve la propriété du droit d'auteur qui protège cette thèse. Ni la thèse ni des extraits substantiels de celle-ci ne doivent être imprimés ou autrement reproduits sans son autorisation.

In compliance with the Canadian Privacy Act some supporting forms may have been removed from this dissertation.

Conformément à la loi canadienne sur la protection de la vie privée, quelques formulaires secondaires ont été enlevés de ce manuscrit.

While these forms may be included in the document page count, their removal does not represent any loss of content from the dissertation.

Bien que ces formulaires aient inclus dans la pagination, il n'y aura aucun contenu manquant.

Canada

ABSTRACT

The effects of membrane dynamics on high-resolution NMR of oriented or MAS transmembrane polypeptides

Christophe Farès
University of Guelph, 2003

Advisor(s):
Professor J. H. Davis and
Professor F. J. Sharom

The present work provides new perspectives on the growing field of solid-state nuclear magnetic resonance (NMR) for the structural elucidation of membrane polypeptides and proteins. The effects of dynamics occurring on time scales spanning several orders of magnitude, and with widely differing geometries are emphasized. The various sections of this thesis describe the influence of motions on both well-established and novel heteronuclear multidimensional NMR experiments using both theoretical calculations and experimental measurements.

Through a series of simulations, natural irregularities and motional averaging in membrane proteins were shown to strongly affect the appearance of separated local field experiments (e.g. PISEMA) and to impose limitations on structure-based assignment strategies and on the interpretation of orientation constraints.

To demonstrate the influence of motions with medium-to-slow correlation times (ms to ns), a systematic study of the spin-lattice relaxation in the rotating frame was conducted for several nuclei (^1H , ^{13}C and ^{15}N) in small membrane polypeptides, either in oriented or magic angle spinning (MAS) samples. This study not only assessed the validity of some motional models, but also characterized the magnetization relaxation rates crucial for the design of coherence transfer experiments. It was found that relaxation time constant ($T_{1\rho}$) values on the order of $10^{-3} - 10^{-2}$ s for backbone nuclei and their dependence on sample orientation are consistent with the model of transmembrane polypeptides undergoing axial-diffusion ($\tau_c \sim 10^{-8} - 10^{-7}$ s) and small amplitude off-axis reorientation ($\tau_c \sim 10^{-6} - 10^{-5}$ s).

Important considerations are explored regarding the innovative use of ^1H MAS NMR to determine the structure of small membrane polypeptides undergoing sig-

nificant axial diffusion. A novel correlation experiment (2D-CROPSY) is proposed based on cross-polarization between ^1H and ^{15}N . This experiment was able to resolve a majority of backbone amide ^1H resonances in gramicidin A. This method was then extended to reveal structural information through ^1H - ^1H cross-relaxation exchange, or NOEs, in a combined experiment (2D-NOE-CROPSY). The significance of the NOE cross-peaks in transmembrane polypeptides was scrutinized through experimental measurements and simulations. Because of the anisotropic nature of motions in membranes, it was demonstrated that ^1H - ^1H cross-relaxation is highly efficient and adopts both distance and orientation dependence.

Finally, an unusual case of broadening of the amide ^1H resonances in ^1H MAS NMR was observed in membrane polypeptides. The scale of this effect suggests that the major mechanism of this broadening effect stems from the residual electric quadrupolar coupling of the covalently-bonded and dipolar-coupled ^{14}N .

À Mémé, An Oma...

Acknowledgements

After all those years, there is quite a list of people who contributed in some way to this thesis, and to whom I would like to express thanks.

I have been extremely fortunate to have been co-supervised by two of the finest scientists I know. To them go my deepest gratitude: *Jim*, my mentor, for his enormous faith in me, his sound advice, his good ideas and his comradeship. *Frances*, for her enthusiasm and inspiration, which was always there when I needed it. And also *Érick*, my supervisor in Bordeaux, who has also been abundantly helpful, and who has assisted me in numerous ways.

There have been many people who have opened their door along the way in moments of utter distress. They have all been teachers to me and I owe them unreserved appreciation: *Joseph*, *Dr. Tim Cross* and *Dr. Linda Nicholson* for their help with the biosynthesis of ^{15}N -labeled gramicidin A. *Carla*, *Fabien*, *Dr. John Silvius* and the members of *Dr. Adrian Schwan*'s group for their assistance with the organic synthesis of perdeuterated DMPC- d_{72} . *Valerie*, as a stand-in mother figure, for her guidance with my first steps in NMR and her unrelenting trust. *Filippo* and *Philip*, two very close friends, for initiating me to the pleasures of GNU/Linux, \LaTeX and the Free Software philosophy. *Case* and *Bill M.*, for lending a hand and a tool in the shop. *Yves*, whose glass-blowing skills outweighed my clumsiness. *Reggi*, *Carol*, *Brenda*, *Bonnie* and other staff members, the vertebrae of the department, without whom nothing less than chaos would reign.

Finally, there are student colleagues that I consider friends, and friends that I

consider family. They have all been there when quitting felt like a sensible option. *Scott*, my accomplice and shipmate during the last three years, for keeping hopes alive while our raft was adrift. And *Alexandre, Erin, Katarina, Sébastien, Jesse, Ben, Sarah, Denis, Samantha, Isabelle, Jin, Alexandra, Pierre, Amy, Jiro, Bryan, Dror* and *Vicky*, for enjoyable day-to-day life in the lab. *Chris*, my compadre, for the enormous amount of faith in me and lots of wise words. *Connie*, for all the pragmatic and helpful advice and all the breaths of fresh air. *Hank*, for useful discussions(!), useless conversations and midnight C++ codes. And all the other people who have made Guelph a very special place over all those years: *Stephanie, Nick, Marcela, Vern, Debbie, Jeff, Jessica, Christian G., Karim, Greg, Meirong, Karl, Jeremy, Éric, Al, Christian S., Chris, Bruno, Alexandre, Ilya, Tanya* and all the others who have passed through. Also, all the people in Bordeaux who have made my stay in France one of the most memorable of my life: *Maya, Damien, Frédéric, Céline E.-V., Céline F., Michael, Ivan, Nordine, Michel, Régis, Reiko, Éric P. and Gérard*. I will not forget *Guillaume, Patrick, Claudio* and *Mauricio*, my brothers, for instilling in me with the belief of invincibility. My close and extended families for their support and for teaching me the mysterious balance between working hard and enjoying life. And last but not least, *Corin*, for the very special person that she is. And for the incredible amount of patience she had with me in the difficult last six months. It's time to attack that list of things to do "after the thesis".



Table of contents

1	Introduction	1
1.1	Biological membranes	1
1.2	Membrane-associated proteins	2
1.3	Advances in solid-state NMR	5
1.4	Rationale	11
2	Theoretical Background	13
2.1	The classical description of spin angular momentum	13
2.2	Quantum description of NMR	16
2.3	The NMR interactions	23
2.4	Concluding Remarks	30
3	Materials and Methods	32
3.1	The biosynthesis of ^{15}N -gA	32
3.2	The synthesis of perdeuterated DMPC- d_{72}	38
3.3	Sample preparation	50
3.4	Technical aspects of NMR	52
4	Heteronuclear high-resolution NMR on gramicidin A in solution	65
4.1	Introduction	65
4.2	Sequential ^1H assignments of gA in TFE	66
4.3	Sequential ^{13}C assignments of gA in TFE	72

4.4	Sequential ^{15}N assignments of gA in three different solvents	75
4.5	$^1\text{H}_\text{N}$ - $^1\text{H}_\text{x}$ restraints from NOESY-HSQC experiments	78
4.6	Structure interpretation from ^1H - ^{15}N NOESY-HSQC experiments	79
4.7	Concluding remarks	87
4.8	Experimental conditions	89
5	The effects of structural variations on NMR spectra of membrane proteins in oriented bilayers	91
5.1	Introduction to separated local field spectroscopy	91
5.2	Methods	95
5.3	SLF spectroscopy of ideal polypeptide helices	95
5.4	Effect of helical irregularities	98
5.5	Effect of molecular reorientation	101
5.6	Conclusions	107
6	Rotating frame spin-lattice relaxation of small membrane polypeptides	110
6.1	Introduction	110
6.2	Theory	112
6.3	Materials and Methods	127
6.4	Results and Discussion	131
6.5	Conclusions	154
7	^1H, ^{15}N-Cross-polarization spectroscopy of gramicidin A	157
7.1	Introduction	157
7.2	^1H broadening in fluid membranes	158
7.3	Methods	164
7.4	Results	165
7.5	Conclusions	169
8	The nuclear Overhauser effect as a structural tool in ^1H MAS NMR of small membrane polypeptides	170
8.1	Introduction	170

8.2	Methods	172
8.3	Theoretical considerations	175
8.4	Anisotropic motions and NOE	179
8.5	The spin-diffusion limit	186
8.6	1D-NOE measurements	188
8.7	The 2D-NOESY and 2D-NOE-CROPSY experiments	191
8.8	Concluding remarks	198
9	The residual quadrupolar effect of ^{14}N on the resolution of ^1H	202
9.1	Introduction	202
9.2	Lability of H_N as a possible source of line broadening	203
9.3	The effect of the quadrupole moment of spin S on the dipolar-coupled spin I	205
9.4	Spectral simulation for the ^{14}N - ^1H coupled pairs in axially diffusing gA .	209
9.5	Conclusion	212
10	Summary and future considerations	214
10.1	Summary of the results	214
10.2	Prospective experiments	217
	References	220
A	Appendix: Simulations and computer programs	241
A.1	Xplor parameter, input and results files	241
A.2	Program code	242
A.3	Maple files	243
A.4	Bruker Pulse sequences	243
B	Appendix: Derivations	244
B.1	Chemical shift anisotropy in oriented membranes	244
B.2	The direct heteronuclear (IS) spin-spin dipolar interaction in oriented membranes.	246

B.3	The direct homonuclear (II) spin-spin dipolar interaction in oriented membranes.	248
B.4	The chemical shift anisotropy in MAS membrane samples	249
B.5	The direct heteronuclear (IS) spin-spin dipolar interaction in MAS membrane samples	250
B.6	The direct homonuclear (II') spin-spin dipolar interaction in MAS membrane samples	251

List of figures

1.1	Illustration of the membrane organization of a typical plant cell. . . .	2
1.2	Illustration of the molecular organization of a typical plasma membrane	4
1.3	Map of solid-state and high-resolution NMR approaches for membrane protein structure determination	6
2.1	Definition of Euler angles	20
2.2	Map of reference frames	22
3.1	Micrograph of <i>B. brevis</i>	36
3.2	Reversed phase HPLC of gramicidins	39
3.3	Circular dichroism spectrum of gA in SDS micelles	40
3.4	Mass spectrometry of gramicidins	41
3.5	The synthesis of G3P-d ₅	42
3.6	The synthesis of myristic anhydride-d ₅₄	44
3.7	The synthesis of L- α -DMPA-d ₅₉	46
3.8	The synthesis of L- α -DMPC-d ₇₂	48
3.9	The HR-MAS probehead and sample spinners	53
3.10	The Hahn echo	54
3.11	The INEPT pulse program	55
3.12	The CP experiment	56
3.13	The nuclear Overhauser effect experiments	57
3.14	The T _{1ρ} experiment	59

3.15	Basic multidimensional NMR techniques applied to proteins	61
4.1	The ^1H resonance spin systems for the 16 residues of gA in TFE (TOCSY and DQF-COSY).	67
4.2	H_N - H_α fingerprint region for gA in TFE	69
4.3	Example of ^{13}C assignment using ^1H - ^{13}C HSQC and HMBC of gA in TFE	73
4.4	^1H - ^{15}N HSQC of ^{15}N -gA in three different solvents	77
4.5	Box representation of a 3D ^1H - ^{15}N NOESY-HSQC of ^{15}N -gA in SDS micelles	80
4.6	Strip representation of a 3D ^1H - ^{15}N NOESY-HSQC of ^{15}N -gA in SDS micelles	81
4.7	NOE connectivities in ^{15}N -gA in SDS micelles	82
4.8	Final acceptable structures of gA in SDS micelles based on $^1\text{H}_\text{N}$ - $^1\text{H}_\text{x}$ restraints	88
5.1	Pulse sequence for PISEMA	93
5.2	Molecular model of an α -helical Ala with two adjacent peptide planes	94
5.3	Configuration of an ideal 22-residue polyalanine and corresponding HN/N spectrum	97
5.4	Configuration of an ideal antiparallel β -strand pair	99
5.5	The effect of natural helical irregularities on HN/N spectra	102
5.6	HN/N spectrum of Neu transmembrane domain	105
5.7	HN/N SLF spectra of the Neu protein transmembrane domain submit- ted to MD	108
6.1	Variations of correlation coefficients $\mathcal{A}_{ m }$ and $\mathcal{B}_{ m }$	123
6.2	Dipolar second moment maps	128
6.3	^1H MAS NMR 1D spectra of gA/DMPC- d_{67}	132
6.4	$\text{T}_{1\rho}$ exponential decay fit	133
6.5	^1H $\text{T}_{1\rho}$ data for gA under MAS vs temperature	135

6.6	^1H $T_{1\rho}$ data for gA under MAS vs ω_{rf}	136
6.7	^1H NMR of ALGA polypeptide	138
6.8	^1H $T_{1\rho}$ results of ALGA polypeptide vs ω_1	139
6.9	^1H NMR of the Neu polypeptide	140
6.10	^{15}N MAS spectrum of $^{15}\text{N}_{20}$ -labelled gA dispersed DMPC- d_{67}	141
6.11	Results of $T_{1\rho}$ obtained by ^{15}N NMR	144
6.12	^{13}C MAS spectrum of L16 dispersed in a membrane bilayer	147
6.13	Results of $1/T_{1\rho}$ of polypeptide L16 carbonyl ^{13}C with ν_R	148
6.14	Changes in $1/T_{1\rho}$ of polypeptide L16 carbonyl ^{13}C with offset frequency	149
6.15	Predicted rotating-frame spin-lattice relaxation rates of $^{13}\text{C}'$ in an ideal α -helix	151
6.16	^{13}C static NMR spectra of oriented $^{13}\text{C}'_{16}$ -L16/DMPC	152
6.17	^{13}C $1/T_{1\rho}$ results of oriented L16 vs sample orientation	153
6.18	^{13}C $1/T_{1\rho}$ results of oriented L16 vs rf field	155
7.1	Pulse profile of CROPSY	165
7.2	2D-CROPSY of ^{15}N -gA/DMPC	166
8.1	2D-NOE-CROPSY pulse sequence	174
8.2	Quantum energy state diagram for a homonuclear coupled spin system	176
8.3	The effect of motional models on cross-correlation rates.	182
8.4	The spectral density functions of two different ^1H spin pairs	184
8.5	Ratio of indirect and direct NOE cross-peak intensity	188
8.6	1D NMR spectrum of multilamellar gA/CsL- d_{25} with MAS	189
8.7	1D NOE build-up curves for multilamellar gA/CsL- d_{25} with MAS ($\nu_R =$ 9 kHz)	190
8.8	2D-NOESY strip plot of gA	193
8.9	2D-NOE-CROPSY of ^{15}N gA in DMPC- d_{67}	196
9.1	^1H NMR spectrum of SM/DMPC mixtures at different pH conditions	204

9.2	Theoretical MAS powder spectra for a single ^1H with and without coupling to ^{14}N	210
9.3	Amide region of the ^1H MAS NMR of unlabelled and ^{15}N -labelled gA in DMPC- d_{67}	211

List of tables

2.1	List of relevant γ and ω_0	14
3.1	The constituents of MMSM	33
3.2	The constituents of AGM	34
3.3	C ₁₈ RP-HPLC solvent composition for gA separation	37
4.1	¹ H assignments for gA in TFE	71
4.2	¹³ C assignments for gA in TFE	74
4.3	¹⁵ N assignments for gA in three different solvents	76
4.4	Experimental conditions for all high-resolution NMR experiments of gA in solution.	90
6.1	¹ H T _{1ρ} for MAS gA in DMPC-d ₆₇	134
7.1	¹⁵ N and ¹ H assignments for gA in different soluble form	167
7.2	The rms difference of CROPSY peak frequencies	168
7.3	CROPSY assignment for gA/DMPC	168
8.1	Tentative assignments of the 2D-NOE-CROPSY spectrum	199

Abbreviations

A

AGM	asparagine-glycerol medium
Ala	alanine (A)
Arg	arginine (R)
Asn	asparagine (N)
Asp	aspartic acid (D)
ATCC	American Type Culture Collection
ATP/ADP	adenosine 5'-triphosphate / adenosine 5'-diphosphate

B

<i>B. brevis</i>	<i>Bacillus brevis</i>
bR	bacteriorhodopsin

C

CHCl ₃	chloroform
CROPSY	CROss-Polarization SpectroscopY
CP	cross-polarization
CS	chemical shift
CSA	chemical shift anisotropy
Cys	cysteine (C)

D

DCC	N,N-dicyclohexylcarbodiimide
DCU	N,N-dicyclohexylurea
DEPT	Distortionless Enhancement Polarization Transfer
DMPA	dimyristoyl-glycerophosphate
DMPC	dimyristoyl-glycerophosphatidyl choline
DPC	dodecanoyl-phosphatidyl choline
DQF-COSY	Double Quantum Filtered COReLation SpectroscopY
DRTF	double rotating tilted frame

E

<i>E. coli</i>	<i>Escherichia coli</i>
EAM	ethanolamine (e)

F

FID	free induction decay
-----	----------------------

G

G3P	L- α -glycerophosphate
gA	gramicidin A
gB	gramicidin B
gC	gramicidin C
Gln	glutamine (Q)
Glu	glutamic acid (E)
Gly	glycine (G)

H

His	histidine (H)
HMBC	Heteronuclear Multiple-Bond Correlation spectroscopy
HPLC	high-performance liquid chromatography
HSQC	Heteronuclear Single-Quantum Correlation spectroscopy

J

Ile	isoleucine (I)
INEPT	Insensitive Nuclei Enhanced by Polarisation Transfer

L

L16	polyleucine peptide
Leu	leucine (L)
Lys	lysine (K)

M

MAS	Magic Angle Spinning
MeOH	methanol
Met	methionine (M)
MMSM	minimal mineral salts medium

N

NMR	Nuclear Magnetic Resonance
NOE	Nuclear Overhauser Effect
NOESY	Nuclear Overhauser Effect Spectroscopy

O

OD	optical density
Orn	ornithine

P

PAS	principal axis system
PDB	Protein Data Bank
Phe	phenylalanine (F)
PISEMA	Polarization Inversion Sensitivity Enhancement at the Magic Angle
Pro	proline (P)

R

R ²	Rotational Resonance
REDOR	Rotational Echo DOuble Resonance
rf	radio frequency
RFDR	Radio Frequency-Driven Recoupling
rms	root mean square
ROESY	Rotating-frame nuclear Overhauser Effect Spectroscopy

S

SDS	sodium dodecylsulfate
Ser	serine (S)
SL	spin-lock
SLF	Separated Local Field
SM	sphingomyelin

T

TFE	2,2,2-trifluoroethanol
Thr	threonine (T)
TLC	thin layer chromatography
TMD	transmembrane domain
TOCSY	TOtal Correlation Spectroscopy
TPB	tetraphenylborate
TPS	triisopropylbenzene sulfonyl chloride
Trp	tryptophan (W)
Tyr	tyrosine (Y)

V

Val	valine (V)
-----	------------



Symbols

NUMBERS

$\vec{1}$ unit second rank tensor.

Alphabetical symbols

A

$\mathcal{A}_0, \mathcal{A}_1, \mathcal{A}_2$ symmetric fluctuating components

B

\vec{B} local magnetic field
 $\mathcal{B}_0, \mathcal{B}_1, \mathcal{B}_2$ asymmetric fluctuating components

C

\mathcal{C}_{jk}^i spin commutation terms

D

D diffusion constant
 $\mathcal{D}^{(1)}$ Wigner rotation matrix of the 1st order
 $\mathcal{D}^{(2)}$ Wigner rotation matrix of the 2nd order
 \vec{D}_{IS} dipole-dipole interaction between spins I and S

E

E_{m_s} energy eigenstates

F

$\vec{\mathbf{F}}$	2^{nd} rank tensor representation of the spatial-dependent component of an interaction
$\mathcal{F}_{k,m}$	spherical tensor term of $\vec{\mathbf{F}}$

G

$G_m(\tau)$	autocorrelation function
$g_{m'm}(\tau)$	normalized autocorrelation function

H

\hbar	Planck's constant/ 2π
\vec{H}_0	static magnetic field
\vec{H}_1	applied magnetic field
\vec{H}_e	effective magnetic field
\mathcal{H}	Hamiltonian
$\bar{\mathcal{H}}$	average Hamiltonian
\mathcal{H}_{CS}	chemical shift anisotropy Hamiltonian
\mathcal{H}_D	dipole-dipole interaction Hamiltonian
\mathcal{H}_J	J-coupling Hamiltonian
\mathcal{H}_Q	quadrupolar interaction Hamiltonian
\mathcal{H}_{rf}	Zeeman Hamiltonian with the applied field
\mathcal{H}_Z	Zeeman Hamiltonian with the static field

I

I	a spin label
\vec{I}	angular momentum
I_z	angular momentum operator

J

$J_{mm'}(\omega)$	spectral density function
$j_{mm'}(\omega)$	Lorentzien part of the spectral density function
J_{IS}	J-coupling constant between spins I and S
$\vec{\mathbf{J}}_{IS}$	J-coupling 2^{nd} rank tensor representation

K

k	Boltzmann's constant
k	a constant

M

m_s	spin number
M_2	second moment
ΔM_2	fluctuating second moment
M'_2	residual second moment
N	
\vec{N}	torque
R	
\vec{r}_{IS}	internuclear distance between spins I and S
\vec{R}	relaxation matrix
S	
S	a spin label
S	order parameter
T	
\vec{T}	2^{nd} rank tensor representation of the spin-dependent component of an interaction
$T_{k,m}$	spherical tensor term of \vec{T}
T_1	spin-lattice relaxation time constant or Longitudinal relaxation time constant.
$T_{1\rho}$	spin-lattice relaxation time constant in the rotating frame.
T_2	spin-spin relaxation time constant or Transverse relaxation time constant.
t_p	pulse duration
Z	
\vec{Z}	Zeeman interaction 2^{nd} rank tensor($= -\gamma\vec{1}$)

Greek symbols

A	
α	1^{st} Euler angle ("azimuthal") (see Figure 2.1)
B	

β_m	magic angle (= 54.7°)
β	2 nd Euler angle ("tilt") (see Figure 2.1)
Γ	
γ_I, γ_S	gyromagnetic ratio
γ	3 rd Euler angle ("azimuthal") (see Figure 2.1)
Δ	
δ_0	isotropic chemical shift value
δ	chemical shift anisotropy
Z	
$\zeta^{i,j}$	periodically varying geometrical function
ζ	dipolar coupling proportionality constant
H	
η	asymmetry parameter of the chemical shift
η_Q	asymmetry parameter of the electric field gradient (quadrupolar interaction)
Θ	
$\theta_{max}, \theta_{min}$	helix tilt optima
$\langle \theta \rangle$	average helix tilt angle
$\Delta\theta$	amplitude of the helix tilt fluctuation
M	
$\vec{\mu}$	magnetic moment
μ_0	permissivity of vacuum (= $4\pi \times 10^{-7}$ N/A ²)
N	
ν_R	MAS rate (in Hz)
P	
ρ	autorelaxation rate
Σ	

$\vec{\sigma}$	chemical shift anisotropy 2^{nd} rank tensor
$\vec{\sigma}_0$	isotropic part of $\vec{\sigma}$
$\vec{\sigma}_A$	asymmetric part of $\vec{\sigma}$
$\vec{\sigma}_S$	symmetric part of $\vec{\sigma}$
$\sigma_{11}, \sigma_{22}, \sigma_{33}$	chemical shift anisotropy principal components
σ^ρ	density operator
σ_{nm}	cross-relaxation rate
T	
τ_c	correlation time
τ_{mix}	mixing time
τ_R	MAS rotation period
τ_{SL}	pin-lock duration
Φ	
Φ	backbone dihedral angle formed by atoms $C^i-N^{i+1}-C_\alpha^{i+1}-C^{i+1}$
X	
χ	sidechain dihedral angle
Ψ	
Ψ	backbone dihedral angle formed by atoms $N^i-C_\alpha^i-C^i-N^{i+1}$
Ω	
$\vec{\Omega}$	angular velocity of the rotating frame ($= \gamma \vec{H}_0$)
Ω	Euler angle set (α, β, γ)
ω_0	Larmor frequency in the static frame (in rad/s)
ω_1	Larmor frequency in the applied rf field (in rad/s)
ω_e	effective frequency (in rad/s)
ω_{off}	offset frequency (in rad/s)
ω_R	MAS rate (in rad/s)
ω_{rf}	frequency of applied rf pulse (in rad/s)
ω	backbone dihedral angle formed by atoms $C_\alpha^i-C^i-N^{i+1}-C_\alpha^{i+1}$



1

Introduction

1.1 Biological membranes

All living cells are delimited and compartmentalized by biological membranes. Figure 1.1 illustrates the complex membranous structures of the surface and many organelles in a plant cell. One could argue that all cellular processes must at one point or another involve the active participation of a membrane. Given the complexity and diversity of cellular activities, it is not surprising that the membranous components of a cell are highly specialized and exhibit an amazing variety of functions [1]. It is for instance within the membranous structure of the mitochondrion (A) and the chloroplast (B) that the essential eukaryotic energy conversion processes of oxidative phosphorylation and photosynthesis take place. The membranes of the rough endoplasmic reticulum (C) are the site of manufacture of proteins targeted to the membranes or the extracellular matrix. These immature proteins are then relayed to the Golgi apparatus (D), a membranous complex important for their post-translational modification and trafficking. The plasma membrane (E) not only forms the cell envelope, it must simultaneously carry out numerous other functions, such as adhesion, protection, bidirectional communication, secretion, nutrient uptake and toxin efflux. The study of biological membranes is an extremely rich area of research of great importance for many disciplines, particularly microbiology, pathology, immunology and medicine. Indeed, this is emphasized by the fact that they are the initial target for all biological and chemical pathogens, they often house the triggering mechanism of

malignant cells [2] and they are responsible for the failure of some cancer treatment. Similarly, it is estimated that about 50% to 60% of all pharmaceutical drugs today, including β -blockers and anti-histamines, are targeted specifically to the large family of membrane-associated G protein-coupled receptor proteins [3].

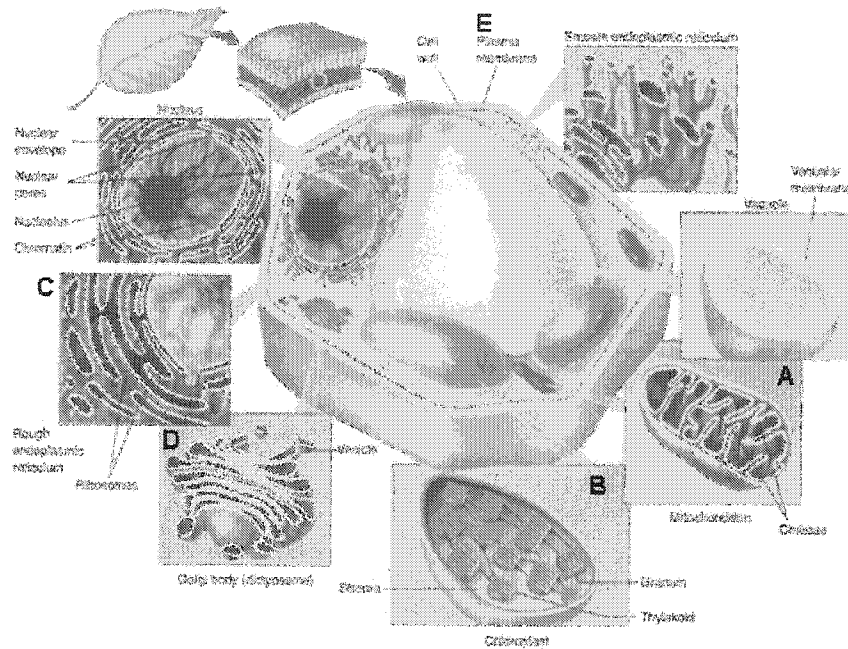


Figure 1.1: Illustration of the interior organization of a typical plant cell. The emphasis is placed on a number of the membrane-rich organelles. From *Introductory Botany: Plants, People and the Environment* 1st edition by L. R. Berg. 1997 [4, p. 39]. Reprinted with permission of Brooks/Cole, a division of Thomson Learning: www.thomsonrights.com, Fax 800-730-2215.

1.2 Membrane-associated proteins

Associated with biological membranes, either peripherally or integrally, are membrane proteins. They are in large part endowed with the enzymatic or transport properties that control membrane function. Among these active players are gated ion channels, transporters of ions and small molecules, signalling receptors, and many other enzymes. To truly understand membrane function, it is necessary to gain knowledge of

the structural and dynamic properties of these molecules. While the structure will yield information on their topology, subunit and domain organization or location of the catalytic sites, the dynamic properties may reveal their folding mechanism, conformational changes or catalytic rate constants. Unfortunately, there is an extraordinary void in our understanding of membrane protein structures. This is emphasized by the following contrast: genomic statistics indicate that about one third of all open reading frames encode membrane-associated proteins [5], yet less than 1% of all known protein structures are membrane-associated, according to the Protein Data Bank (PDB) [6], an up-to-date world-wide scientific repository for high-resolution protein structures.

The difficulty in obtaining high-quality structures of membrane proteins resides in the physical properties of membranes. Biological membranes are lyotropic liquid crystals, which exhibit both positional disorder and orientational order. Because of this, the amphiphilic molecules found in membranes are in a partially orientationally ordered state. Figure 1.2 presents a simplified view of the asymmetric composition and organization of a plasma membrane in a typical cell. The amphiphilic lipids, primarily phospholipids, tend to organize into bilayer sheets, with their hydrophobic acyl chains directed towards the membrane interior, thus exposing only the hydrophilic headgroup to the aqueous media on either side. This bilayer serves as a matrix for specially-designed protein molecules which expose only hydrophobic residues to the lipid acyl chains inside the membrane. Other structural components are displayed in Figure 1.2. The peripheral cytoskeleton and other fibers play essentially structural and protective roles, the sterols control the fluidity of the membrane, and the carbohydrate chains are extracellular membrane signatures. This “fluid mosaic model” proposed 30 years ago by Singer and Nicolson [7] illustrates the simultaneous lateral fluidity and orientational order of membranes. Despite its value, this picture is viewed today as too simplistic. The large diversity of lipids and sterols in membranes seem to play more complex roles, such as in the lateral organization of bilayers, and as regulators of membrane function [8].

Because they are part of a lyotropic liquid crystalline phase, the proteins of membranes are not ideally suited for either of the two common experimental techniques

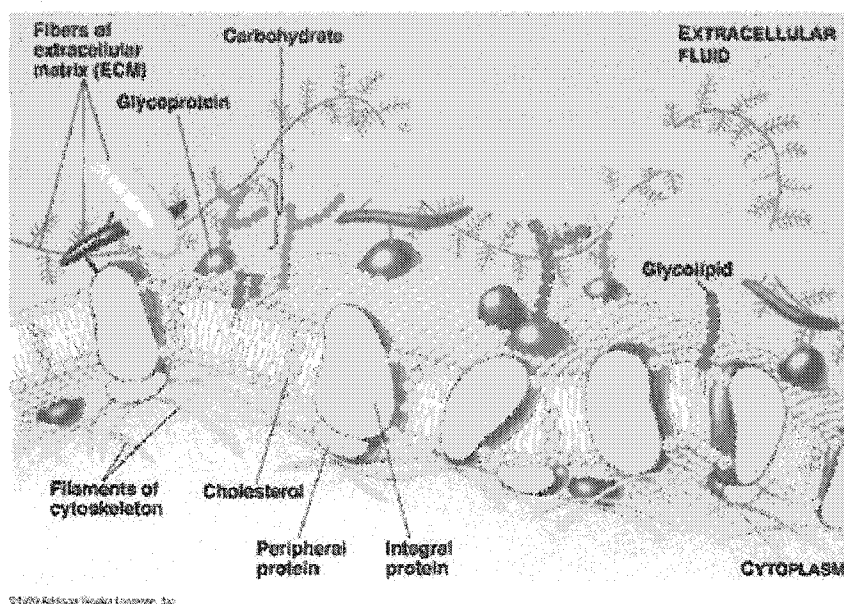


Figure 1.2: Illustration of the molecular organization of a typical plasma membrane. From Biology (6th Edition) by N. A. Campbell and J. B. Reece. ©2002 [9, p.142]. Reprinted by permission from Pearson Education, Inc.: www.pearsoneducation.com, Fax: 201-236-3290.

for protein structure determination. Indeed, amphiphilic membrane proteins are generally not easily amenable to forming good quality crystalline samples for use in diffraction by crystallographic techniques; nevertheless, important advances are being made in this field, especially with very large protein complexes. At the time of writing this thesis, a total of 62 structures of membrane-associated proteins (among them 42 unrelated ones) had been solved by diffraction techniques and deposited in the PDB. The latest additions include photosystem II from the cyanobacterium *T. vulcanus* (PDB:1izl) [10], the fatty acid amide hydrolase from rat (PDB:1mt5) [11], the multidrug efflux transporter AcrB from *E. coli* (PDB:1iwg) [12], the sensory rhodopsin II-transducer complex from *N. pharaonis* (PDB:1h2s) [13], and the Ca^{2+} -ATPase from rabbit muscle (PDB:1iwo) [14].

Solution NMR has been used to determine the detailed structure of many soluble proteins, however, this technique demands rapid and isotropic reorientation to attain

high-resolution signals. Membrane protein molecules cannot meet this condition either individually, due to their motional restriction within a bilayer, or collectively, since even the smallest membrane vesicle does not reorient fast enough. However, some success has been attained in this field for small membrane proteins dispersed in membrane-mimetic media, such as organic solvent mixtures and detergent micelles (e.g. the dimeric transmembrane domain of human glycophorin A (PDB:1afo) [15], Fd major coat protein (PDB:1fdm) [16], and the bacterial outer membrane protein OmpX (PDB:1orm) [17]).

1.3 Advances in solid-state NMR

Despite its limitations, NMR is still a viable technique even for incompletely reorienting proteins. The solid-state branch of NMR has long been used to study the intimate effect of anisotropic motions on the orientational-dependent second rank tensor interactions of the nuclear spins with each other and with their electronic environment. NMR is, in fact, exquisitely suited to reveal both spatial and dynamic information on a molecular scale. The application of this technique to membrane proteins is a rapidly growing field. However, before this technique can become routine, many difficulties must be overcome, principally those involving sensitivity and resolution. At ambient temperatures, NMR is a rather insensitive technique, typically requiring milligram amounts of proteins, as well as their costly isotopic enrichment, usually with ^{13}C and ^{15}N . In addition, because of the partial order of the membrane, orientation-dependent interactions persist and a wide distribution of frequencies is observed for each spin. These are so important that large overlaps and degeneracies of resonances are common for two or more spin labels. Considering that proteins are composed of hundreds to thousands of residues, resolution is the most important limitation. Another difficulty resides in the interpretation of the NMR measurements: analysis of structural data often rely on a clear motional model and, vice versa, reliable elucidation of dynamic properties require a known structure. It will be important to exercise caution and avoid erroneous assumptions.

Nevertheless, much improvement has been realized in recent years in this field.

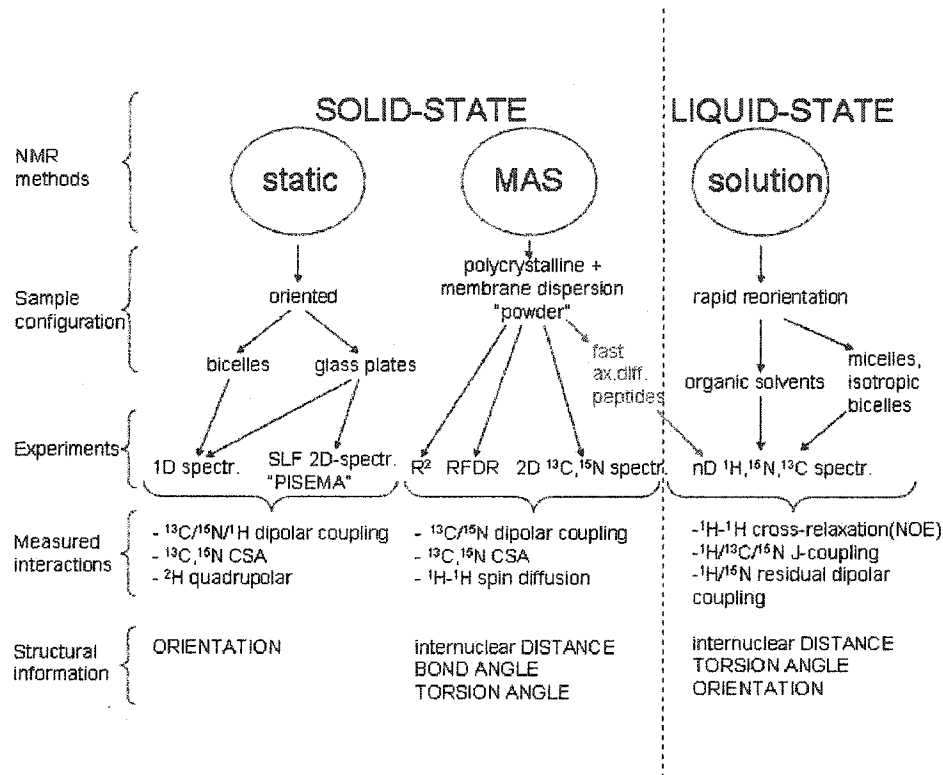


Figure 1.3: Overview of some of the solid-state and solution NMR approaches used to study membrane protein structures.

Two distinct solid-state NMR approaches have been predominant and a short review of some applications to membrane proteins is presented in the following sections. A brief overview of these applications is also presented in Figure 1.3.

1.3.1 Static samples

The first approach aims at measuring orientational constraints from the residual anisotropies of orientation-dependent interactions. Three interactions lend themselves most readily to this approach: the chemical shift anisotropy (CSA), the dipole-dipole interaction and the quadrupolar interaction. Based on the principal values of the residual CSA tensor, its direction in the magnetic field for individual spins, say ¹⁵N and ¹³C, can be measured from the spectral shift and an orientational constraint can be retrieved for that part of the molecule based on the orientation of the tensor

within the molecular group containing the nucleus. Similarly, for nuclei with an electric field gradient, such as ^2H in proteins, an orientation constraint can be identified from a spectral splitting based on the residual quadrupolar tensor and its orientation within the molecular fixed frame. Finally, using any combination of two nuclear labels, namely ^1H , ^{13}C and/or ^{15}N , one can introduce defined interacting spin pairs at specific locations. The spectral measurement of the residual dipolar coupling between the members of such pairs also provides a local orientational constraint for the internuclear vector. All these constraints are most readily measured in bilayer samples with a uniform uniaxial orientation, a configuration to which membranes can adjust easily. When the membrane normal is parallel to the field, the tensor orientation distribution is reduced to a minimum and the constraint is computed directly from the narrow distribution of spectral shift or splitting. Most commonly, the samples are uniformly supported and layered between thin glass plates, but magnetically-aligned bilayer phases, called “bicelles”, have also been used [18–20].

The potential, but also the challenge, of this approach is exemplified by the only high-resolution structure of a membrane protein deposited in the PDB based solely on solid-state NMR orientation constraints. This pioneering work, led by T.A. Cross ([21], [22], [23] and [24]) over a period of 7 years was applied to gramicidin A (gA), a short 16 amino acid residue polypeptide chain which has the property of forming an ionic pore in membranes. Cross’ group chose to systematically measure the orientation of the principal axis system of three specific interactions, namely, ^{15}N CSA, ^{15}N - ^{13}C dipolar interaction and ^{15}N - ^1H dipolar interaction, within the polypeptide chain. For this, a number of samples were prepared, introducing the required isotopic label(s) within each of the sixteen backbone peptide bonds. Assuming that the peptide group forms a rigid plane, their strategy was to use three vector orientation constraints within this plane to define its orientation. The relative orientation of two consecutive planes can help resolve the Φ and Ψ torsion angles which define the local backbone structure. This protocol was repeated for each of the 15 sets of torsion angles. Despite the attainment of a final structure, this method is not straightforward. Indeed, each interaction can yield up to four orientation solutions and so even

the three interactions are insufficient to pinpoint a single plane orientation. It was with additional empirical peptide geometric constraints and molecular dynamics that the PDB:1mag configuration could finally be proposed. It should be noted as well that the experiments in question were conducted on gA dispersed in dynamic membrane bilayers, yet the interpretation assumed that motions were not important. This assumption is questionable.

A promising development with oriented samples uses advanced decoupling schemes and the simultaneous measurement of CSA and dipolar coupling in a 2D spectrum to resolve a number of orientation constraints within the peptide backbone in a single experiment. In this family of separated local field (SLF) experiments, of which PISEMA (Polarity Inversion Sensitivity Enhancement at the Magic Angle) is the most well-known, one can in principle decipher the tilt angle of the transmembrane α -helical portion of a membrane protein, and given a “triggering” assignment in a regular helical polypeptide, one can assign and capture the orientation of every other peptide plane. However, this method depends heavily not only on the ideality of the α -helix, but also on the perfect rigidity of the protein.

1.3.2 MAS samples

The second approach requires no special membrane configuration, although the entire sample must be rotated at the magic angle ($\theta = 54.7^\circ$) to eliminate the orientation dependent interactions, which all scale as $(3 \cos^2 \theta - 1)$, where θ is the angle between the magnetic field and the principal axis of the tensor involved. This approach provides significantly higher resolution for the ^{13}C and ^{15}N nuclei of proteins than the static approach described above. However, since the orientation-dependent shifts and splittings have been removed by MAS, only the isotropic part of the chemical shift defines the frequency domain for each resonance peak. Thus, the isotropic range is much narrower compared to the static case; for example, the amide ^{15}N resonance spread is reduced from over 170 ppm to only 15 ppm upon the application of MAS. Also, since the orientation information is lost, other methods must be devised to obtain structural information. A number of recoupling techniques for selectively reintro-

ducing orientation-dependent interactions such as the hetero- or homonuclear dipolar coupling between spin pairs (any combination of ^{15}N , ^{13}C or ^1H) or the anisotropic chemical shift of a specific type of nucleus, have been developed. Recoupling strategies are possible because the averaging out of the interaction is coherent with the revolution speed of the sample undergoing MAS. The reintroduction of the interaction allows the measurement of internuclear distances, relative bond and torsion angles.

A common homonuclear recoupling technique called rotational resonance (R^2) requires the MAS speed ν_R to match the chemical shift difference, $\Delta\nu$ of the two interacting spins. More generally, this experiment is possible when $\Delta\nu = n\nu_R$, where $n = 1, 2, 3, \dots$. Another more general method is called rf-driven recoupling (RFDR) whereby the MAS period is fixed to match the duration of a series of 180° inversion pulses. By inverting the magnetization once per period, this average no longer vanishes. The most popular method to measure *heteronuclear* distances is called rotational echo double resonance (REDOR). For all recoupling techniques, the internuclear distance is obtained from the rate of exchange of the longitudinal magnetization.

R^2 and RFDR are the most commonly used MAS techniques for structural elucidation. They were used to study the isomerization process of the retinal cofactor in bacteriorhodopsin (bR) [25, 26], a membrane-associated light-driven proton pump which undergoes structural changes, specifically at the retinal site, upon exposure to light. Specifically, R^2 allowed determination of the structural configuration of the Schiff base group (C=N bond linking the retinal molecule to the Lys protein side chain) based on distance measurements between $^{13}\text{C}_{14}$ of retinal and ^{13}C - ϵ -Lys of bR. Experiments have shown that bR₅₅₅ (conformation obtained upon exposing the molecule to 555 nm photons) has an internuclear distance of $3.0 \pm 0.2 \text{ \AA}$, and hence the C=N bond was concluded to be in the *syn* configuration. In contrast, bR₅₆₈ showed a distance of $4.1 \pm 0.3 \text{ \AA}$ and thus, the *anti* configuration was deduced. Similar experiments have been used to further characterize the configuration of several photocycle intermediates [27].

Some details of the structure and mechanism of dimerization of membrane α -helices can also be obtained through distance constraint measurements. This was first

applied to the hydrophobic region of glycoporphin A, an integral membrane protein known to dimerize within the bilayer in red blood cells [28]. The approach used R² on synthesized glycoporphin A transmembrane polypeptide with several combinations of ¹³C labels on side chain methyl groups with ¹³C on carbonyl groups of the backbone. The small ¹³C_{methyl}/¹³C' distances between Gly-79 and Val-80 as well as Gly-83 and Val-84 demonstrated that these pairs of residues are interacting through van der Waals forces at the contact interface of the dimer.

As in the case of static experiments, MAS recoupling techniques can only answer specific local structural questions in the vicinity of the isotope label site. To be able to retrieve a high-resolution structure from distance and angle constraints would demand unrealistic labor and time resources. Advances have been made, however, with uniformly ¹³C- and ¹⁵N-labelled derivatives of at least two proteins in polycrystalline form undergoing MAS; the basic pancreatic trypsin inhibitor [29]; and the SH3 domain of the membrane-associated α -spectrin protein [30]. These groups were able to develop multidimensional experiments and resolve a majority of the expected resonance peaks. Strategies are being devised to allow peak assignment and structural elucidation based on dipolar coupling [31] and proton-driven spin-diffusion [32] in a set of experiments on a single uniformly-labelled sample.

Another MAS approach based on ¹H resonance has shown some potential. This novel approach, which will only apply to a restricted class of small membrane-associated molecules, relies on the rapid axially symmetric reorientation characteristic of a fluid membrane bilayer phase. If the molecular axial diffusion about the local bilayer normal is fast enough, the orientation-dependent interactions are projected onto the diffusion axis. This has the subtle but important effect of transforming the otherwise homogeneous, like-nucleus, dipolar broadening among the abundant ¹H nuclei into an inhomogeneous broadening which can be effectively narrowed by MAS [33]. In cases where this approach will work, the resolution obtainable for ¹H (the most abundant and sensitive nucleus in biological systems) can approach that obtainable in solution. Systems of this type can be studied by developing experiments analogous to those used for structure determination of proteins in solution. As for solution

NMR, the principal problems to be solved are the sequence-specific assignment of the resonances and the measurement of structural restraints. In addition to distance restraints obtained through nuclear Overhauser effect spectroscopy, it should also be possible to obtain orientational restraints by selective reintroduction of dipolar interactions between ^1H and ^{13}C or ^{15}N labelled positions within the molecule. The necessity for rapid axial diffusion will almost certainly restrict the application of this approach to small molecules or fragments of molecules.

For recent reviews of these and other methods, the reader is referred to recent reviews [29, 34–39].

1.4 Rationale

The work presented in this thesis brings new perspectives to the growing field of solid-state NMR for structural elucidation of membrane proteins. A very large emphasis is placed on the effects of motions occurring on time scales spanning several orders of magnitude, and with widely differing geometries. The work attempts to present a meticulous and unbiased description of the impact of motions on several aspects of NMR experimentation using both theoretical calculations and experimental measurements. Specifically, Chapter 5 (p. 91) uses theoretical calculations to explore the effect of natural irregularities and motional averaging on the appearance of SLF experiments. In Chapter 6 (p. 110), a systematic spin-lattice relaxation study in the rotating frame is conducted for three nuclei in membrane polypeptides, either in a static oriented sample or a sample undergoing MAS. This indispensable study not only assesses the validity of some motional models, but also characterizes the magnetization relaxation rates crucial for the design of coherence transfer experiments. The next four chapters deal with important considerations regarding the innovative use of ^1H MAS NMR of small membrane polypeptides to determine their structure. Using gA as a model transmembrane polypeptide, Chapter 4 (p. 65) presents a non-exhaustive liquid-state high-resolution NMR study of the ^{13}C and ^{15}N chemical shift assignments, ^1H NOE correlations and structural determination to be used as guidelines for the solid-state work on the same molecule under MAS. Chapter 7

(p. 157) puts forward a novel correlation experiment based on cross-polarization (CP) which resolves a majority of backbone amide ^1H resonances in gA, and an indirect assignment strategy based on similarity with solution NMR assignment of the same molecule. In the following Chapter 8 (p. 170), an in-depth theoretical characterization of the cross-relaxation exchange rates in a membrane bilayer is presented in relation to the anisotropic motions. The significance of ^1H - ^1H NOE cross-peaks in membrane proteins is scrutinized through experimental measurements and simulations. Finally, in Chapter 9 (p. 202), the unusual case of the residual quadrupolar effect of ^{14}N spin on the neighboring amide ^1H is described. It is the author's hope that the conclusions reached through this body of work will serve as guidelines and warnings for the design and interpretation of solid-state NMR techniques applied to membrane proteins.



*- Le peu que je sais, c'est à mon
ignorance que je le dois!*

- Sacha Guitry

2

Theoretical Background

The most important technique used in the present study is NMR spectroscopy. This chapter is restricted to a general overview, relevant to this project, of several important phenomenological aspects of NMR, as well as the mathematical and geometrical tools needed to describe them. The next chapter will deal with experimental considerations when applying NMR to membrane systems. For a more exhaustive treatment of NMR, the reader is invited to consult the well-established texts [40–43].

2.1 The classical description of spin angular momentum

Although NMR is concerned with angular momentum at the atomic scale, where quantum mechanics dominate, the nuclear spins behave in many respects just like a macroscopic magnet. For this reason, one may find it more intuitive to treat magnetic resonance classically. The classical picture is briefly presented here, followed by the quantum description in the next section.

Any atomic nucleus with a spin angular momentum \vec{I} larger than zero (all except those with even mass and even charge) will have magnetic properties described by its magnetic dipolar moment:

$$\vec{\mu} = \gamma \vec{I}, \quad (2.1)$$

where the proportionality constant, γ , is called the gyromagnetic ratio of the nucleus. A list of relevant γ for this work (in units of $\text{rad s}^{-1} \text{T}^{-1}$) is presented in Table 2.1.

Table 2.1: Spin number, gyromagnetic value and Larmor frequency at 11.7 T of relevant biochemical nuclei [44, Chapter 1].

nucleus	spin I	gyromagnetic ratio γ (10^7 rad s $^{-1}$ T $^{-1}$)	Larmor frequency at 11.7 T $\omega_0/2\pi$ (MHz)
^1H	1/2	26.751	500.0
^{13}C	1/2	6.726	125.7
^{15}N	1/2	-2.710	50.7
^{14}N	1	1.933	36.1
^2H	1	4.106	76.8

The most fundamental interaction of a magnetic dipolar moment is that with a magnetic field. In the presence of a static magnetic field, \vec{H}_0 , it will be subjected to a torque \vec{N} as described by:

$$\vec{N} = \vec{\mu} \times \vec{H}_0. \quad (2.2)$$

According to Newton's second law, this torque is also equivalent to the time rate of change of angular momentum, \vec{I} :

$$\vec{N} = \frac{d\vec{I}}{dt} = \vec{\mu} \times \vec{H}_0, \quad (2.3)$$

and with the statement of Equation 2.1, the following expression for the evolution of the dipolar moment can be written:

$$\frac{d\vec{\mu}}{dt} = \vec{\mu} \times \gamma \vec{H}_0. \quad (2.4)$$

This equation states that, at any given time, a change in the dipole $\vec{\mu}$ occurs perpendicularly to the static magnetic field, and the dipole itself. Consequently, if the dipole is aligned at an angle with respect to the static magnetic field, its orientation will describe a cone of precession around the static field. By convention and for the rest of this manuscript, the static field will define the positive z direction ($\vec{H}_0 \cdot \hat{k} = 0$).

The rate of precession $\omega_0 = \gamma H_0$ is also known as the Larmor frequency and is unique for any given nucleus in a given field. This frequency defines the resonant condition of NMR. For a superconducting magnet of 11.7 Tesla, one will have the Larmor frequencies listed in the third column of Table 2.1 for the common biochemical

nuclei. These are low-energy frequencies, in the range of typical radio-frequency (RF) waves.

The effect of an rf excitation pulse is best described by first moving into a rotating reference frame. It is defined by the three axes (x', y', z') to differentiate it from the laboratory static frame with axes (x, y, z). It is noted that z and z' are parallel ($z \parallel z'$). When following the evolution of magnetic moments in this frame, one writes:

$$\frac{d\vec{\mu}}{dt} = \vec{\mu} \times \gamma \vec{H}_0 - \vec{\Omega} \times \vec{\mu} = \vec{\mu} \times (\gamma \vec{H}_0 - \vec{\Omega}), \quad (2.5)$$

where $\vec{\Omega} = \Omega \hat{z}$ is the angular velocity of the rotating frame. A special condition is met when this angular velocity equals the Larmor frequency ($\vec{\Omega} = \vec{\omega}_0 = \gamma \vec{H}_0$). The magnetic moment will then appear to be static ($\frac{d\vec{\mu}}{dt} = 0$).

An alternating current at frequency Ω is applied in a coil wrapped around the spins of interest, in such a way as to produce an alternating magnetic field along the x -axis:

$$H_x(t) = 2H_1 \cos(\Omega t) \quad (2.6)$$

This varying field can be broken up into two rotating components, each of amplitude H_1 , one rotating clockwise (static in the rotating frame, i.e. on resonance) and the other counterclockwise (rotating with angular frequency -2Ω in the rotating frame). The latter can be neglected since it is far off resonance.

In the presence of this field, the magnetic dipole will behave as described by the following equations, first stated generally and then for the case when $\Omega = \gamma H_0$:

$$\frac{d\vec{\mu}}{dt} = \vec{\mu} \times [(\gamma H_0 - \Omega)\hat{k} + \gamma H_1 \hat{i}] \quad (2.7)$$

$$= \vec{\mu} \times \gamma \vec{H}_e \quad (2.8)$$

$$\text{where } \gamma \vec{H}_e = (\gamma H_0 - \Omega)\hat{k} + \gamma H_1 \hat{i} \quad (2.9)$$

and if $\Omega = -\gamma H_0$ then:

$$\frac{d\vec{\mu}}{dt} = \vec{\mu} \times H_1 \hat{i} \quad (2.10)$$

These equations depict vectorially how the system is perturbed in NMR spectroscopy. Furthermore, they show how NMR can be used to manipulate spins in a phase-

sensitive way. Typically, an NMR experiment will begin with a pulse of oscillating magnetic field (Equation 2.6), say in the “rotating” x-direction (referred to as the x'-direction), of amplitude H_1 and at a frequency matching the Larmor frequency of the spins of interest for a duration τ where $\tau = \frac{\pi}{2\omega_1}$ such that the magnetic moment describes a quarter of a revolution (90° flip angle) around the x' axis from the z axis into the -y' axis. Once the magnetization is transferred into the x'-y' plane, its induction of current in the coil can be measured. Usually, the magnetization is allowed to relax back to its equilibrium state before this experiment is repeated. The mechanisms of relaxation will be covered in a later section.

Many variations of this simple experiment can be attempted. (1) The excitation pulse duration or its amplitude H_1 allows careful adjustment of the magnetization tilt angle; (2) the orientation of the applied field allows a change in the direction around which the moments precess; (3) the rf frequency allows determination of the type of nuclei excited; (4) the amplitude of the pulse also allows determination of the range of frequencies affected by this excitation. A very large number of experiments exist where these pulses are joined in different combinations to reveal almost any kind of interaction involving the observed spins. Some of these experiments are summarized in Chapter 3 (p. 53).

2.2 Quantum description of NMR

Whereas the classical picture sheds light on the vectorial and phase-sensitive properties of NMR, quantum mechanics provides a thorough description of all of its aspects.

2.2.1 NMR eigenstates

The quantum mechanical energy of the interaction between a nuclear dipole and the static magnetic field (along the z-direction) begins with \mathcal{H}_Z , the Zeeman Hamiltonian. It is defined (in units of joules) by :

$$\mathcal{H}_Z = -\gamma\hbar H_0 I_z \quad (2.11)$$

where I_z is the dimensionless spin angular momentum operator with eigenvalues m_s , which can take values of:

$$m_s = -I, -I + 1 \cdots I - 1, I \quad (2.12)$$

where I is the spin number, an integer multiple of $1/2$. Examples of the spin number for common nuclei are given in Table 2.1. The Zeeman Hamiltonian operator can thus be applied to the angular momentum eigenstates to yield the allowed eigenvalues of the energy levels of the system, given by:

$$E_{m_s} = -\gamma\hbar H_0 m_s. \quad (2.13)$$

One can then elicit quantum transitions between states by involving photons of angular frequency:

$$\omega = \frac{\Delta E_{m_s}}{\hbar} = \frac{1}{2}\gamma H_0 - \left(-\frac{1}{2}\gamma H_0\right) = \gamma H_0 = \omega_0 \quad (2.14)$$

which was defined earlier as the Larmor frequency. By irradiating the system with photons of energy $\hbar\omega_0$, one can induce a change in the energy level populations and observe energy absorption by the system. The magnitude of the signal is proportional to the equilibrium population difference between levels, which according to the fundamental Boltzmann law, is affected by the temperature of the system. At equilibrium, the population of each energy state is proportional to $\exp(-E_{m_s}/kT)$. Since $E_{m_s} \ll kT$ near ambient temperatures, the Taylor series, to first order approximation, shows direct proportionality of the magnetization with the magnitude of the static magnetic field.

Nuclear magnetic spins not only interact with the static field, but also with the local fields of their molecular context. In a majority of cases, these interactions can be treated quantum mechanically as perturbation of the Zeeman Hamiltonian. These local fields can provide valuable information on the structure and dynamics of its molecular context. This section presents some general mathematical concepts to describe these NMR interactions. In the following section, the most important interactions are reviewed individually.

2.2.2 Formalism

In general, one can assume that the spin interactions require no more than a second rank tensor to describe them, since the higher rank tensors are small. All spin interaction Hamiltonians, in units of energy, have the general form:

$$\mathcal{H} = \vec{I} \cdot \vec{\vec{A}}_\lambda \cdot \vec{B}_\lambda \quad (2.15)$$

where $\vec{\vec{A}}_\lambda$ is a second-rank tensor describing the spatial aspects of the spin interaction λ , where \vec{I} is the vectorial representation of the spin angular momentum, and where \vec{B}_λ is a local field originating either from the static or applied (RF) magnetic fields (Zeeman effect), from the electronic shielding (chemical shift anisotropy (CSA)) or from another neighboring magnetic moment (dipolar coupling, J-coupling). The treatment for the electronic quadrupolar coupling is different and should follow the notation suggested by Mehring [41].

Ultimately, once each interaction is defined, the total Hamiltonian will resemble:

$$\mathcal{H} = \mathcal{H}_Z + \mathcal{H}_{RF} + \mathcal{H}_D + \mathcal{H}_{CS} + \mathcal{H}_J + \mathcal{H}_Q. \quad (2.16)$$

The following list defines each Hamiltonian (the spin-rotation interaction is neglected here) along with a range of typical maximum interaction amplitudes encountered with modern instrumentation on biological samples:

- \mathcal{H}_Z = the Zeeman interaction with the static field, ($10^6 - 10^9$ Hz)
- \mathcal{H}_{rf} = the Zeeman interaction with the applied rf field, ($10^3 - 10^4$ Hz)
- \mathcal{H}_D = the direct dipole-dipole coupling between like and unlike nuclei, ($0 - 10^6$ Hz)
- \mathcal{H}_{CS} = the chemical shift, ($10^3 - 10^4$ Hz)
- \mathcal{H}_J = the J-coupling or indirect dipole-dipole coupling, ($10 - 10^3$ Hz)
- \mathcal{H}_Q = the quadrupolar interaction, ($10^3 - 10^7$ Hz, for $I \geq 1$)

A detailed description of these interactions are presented in the following section. For studies of molecular structures and their spatial fluctuations by NMR, the most commonly-used formalism uses a notation where the spatial (or structural) component is kept separate from the spin component, for any interaction, λ :

$$\mathcal{H}_\lambda = \vec{\vec{F}}_\lambda \cdot \vec{\vec{T}}_\lambda \quad (2.17)$$

where $\vec{\mathbf{F}}$ is the spatial second rank tensor (corresponding to $\vec{\mathbf{A}}$ in Equation 2.15) and $\vec{\mathbf{T}}$ is the spin second rank tensor corresponding to the dyadic product of the vectors \vec{I} and \vec{B} from Eq. 2.15. In addition, since each interaction is defined within different reference frames, it is necessary to ultimately unify all the interactions into the same reference frame. For this reason, the spherical tensor notation (rather than the cumbersome 3 by 3 Cartesian matrices) will be used upon which the Wigner rotation matrices can be applied to allow transformations between reference systems. In this spherical tensor form, the general expression of the Hamiltonian will be:

$$\mathcal{H}_\lambda = \sum_{k=0}^2 \sum_{m=-k}^{+k} (-1)^m \mathcal{F}_{km,\lambda}^L T_{k-m,\lambda}^L, \quad (2.18)$$

where L represents the laboratory frame defined by the static magnetic field.

2.2.3 Wigner rotation matrices

Generally, the spatial operators, \mathcal{F}_{km}^L , in the laboratory frame (index L) are derived from their simplest expression in the interaction or “principal axis system” (PAS) frame (index P) using a second-rank Wigner transformation, $\vec{\mathbf{D}}^{(2)}(\Omega)$. Each component of this tensor is given in terms of the set of Euler angles $\Omega = (\alpha, \beta, \gamma)$ by:

$$\mathcal{D}_{pq}^{(2)}(\Omega) = e^{i\alpha} d_{pq}^{(2)}(\beta) e^{-i\gamma} \quad (2.19)$$

so that the simplest expression of the spatial tensor is written as:

$$\mathcal{F}_{2m}^L = \sum_{m'} \mathcal{F}_{2m'}^P \mathcal{D}_{m'm}^{(2)}(\Omega_{PL}), \quad (2.20)$$

where Ω_{PL} refers to the three Euler angles $(\alpha_{PL}, \beta_{PL}, \gamma_{PL})$, defined simply in Figure 2.1 and in more detail in [45]. The index PL indicate the direction of the transformation.

For partially ordered systems such as proteins embedded in biological membranes, it is justifiable to factor this transformation into several sequential Wigner rotations, as represented on the map of Figure 2.2 and summarized in the following equation:

$$\mathcal{F}_{2m}^L = \sum_{m''''', m'''', m'', m'} \mathcal{F}_{2m'''''}^P \mathcal{D}_{m''''', m''''}^{(2)}(\Omega_{Pp}(t)) \mathcal{D}_{m''''', m''}^{(2)}(\Omega_{pM}) \mathcal{D}_{m''', m'}^{(2)}(\Omega_{MN}(t)) \mathcal{D}_{m', m}^{(2)}(\Omega_{NL}). \quad (2.21)$$

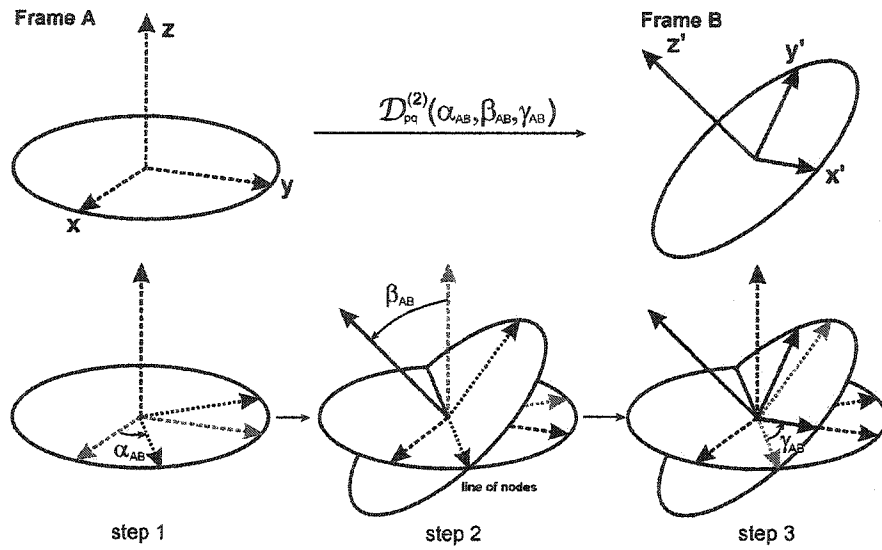


Figure 2.1: The 3-step transformation from xyz frame A to the $x'y'z'$ frame B: the angle α defines the rotation around the z axis bringing the x axis onto the “line of nodes” (defined as the intersecting axis of the two planes defined by xy and $x'y'$). The angle β defines the rotation around the line-of-nodes to establish the coincidence of z with z' . Finally, the angle γ is the rotation around z' bringing the line of nodes onto x' .

The first transformation $\mathcal{D}_{pq}^{(2)}(\Omega_{Pp})$ links the PAS frame (P) to a frame fixed within the unitary protein structural element, namely the peptide plane (index p) defined by the atoms C_α^i , C^i , O^i , N^{i+1} , H_N^{i+1} and C_α^{i+1} (see Figure 5.2 on p. 94 for the identification of the atoms in the plane). In this frame, the x-axis is normal to the plane and the z-axis along the N-H_N bond. Then, the transformation $\mathcal{D}_{pq}^{(2)}(\Omega_{pM})$ links the peptide element to the protein molecular-fixed frame (index M). The z-axis of the latter is defined by the principal axis of the moment of inertia tensor ($\sum_{i=atoms} m_i \times \vec{r}_i^2$) of the protein, with the origin at its centre of mass. For single-spanning transmembrane helices, the z-axis of this frame usually lies along the helix axis. In Chapter 5 (p. 91), the variabilities of some molecular bond lengths, bond angles and torsional angles both intra- and inter-peptide plane which inflict variations onto the transformations $\mathcal{D}_{pq}^{(2)}(\Omega_{Pp})$ and $\mathcal{D}_{pq}^{(2)}(\Omega_{pM})$ are explored. In further chapters, these first two transformations are collected into a single one, $\mathcal{D}_{pq}^{(2)}(\Omega_{PM})$, whereby the PAS is directly related to the helix-axis and, for simplicity, the internal rapid motions are assumed to be of too small amplitude to affect the Euler angles defining this transformation unless mentioned otherwise. The third transformation is represented by $\mathcal{D}_{pq}^{(2)}(\Omega_{MN}(t))$ and connects the molecular-fixed frame to the axially-symmetric membrane normal frame (N). Any whole-body molecular reorientation can be interpreted as fluctuations in the angles α_{MN} , β_{MN} and/or γ_{MN} , as will be seen in the section on motional models (Section 6.2.4, p. 121) for axial diffusion and off-axis molecular reorientation, caused by wobble motions, global undulations, etc. Finally, the fourth Wigner matrix $\mathcal{D}_{pq}^{(2)}(\Omega_{NL})$ relates the membrane normal frame to the laboratory frame (L). Because of axial symmetry of these two frames, a single Euler angle (β_{NL}) suffices to fully describe the sample configuration in both oriented samples or powder distributions.

For magic angle spinning (MAS) samples, the last transformation in Equation 2.21 can be further factored into:

$$\mathcal{D}_{m'm}^{(2)}(\Omega_{NL}) = \sum_r \mathcal{D}_{m'r}^{(2)}(\Omega_{NR}) \mathcal{D}_{rm}^{(2)}(\Omega_{RL}(t)). \quad (2.22)$$

for which the first term relates the local membrane normal (N) to the rotor frame (R) whose z-axis lies along the rotor axis of rotation. The second term brings the rotor

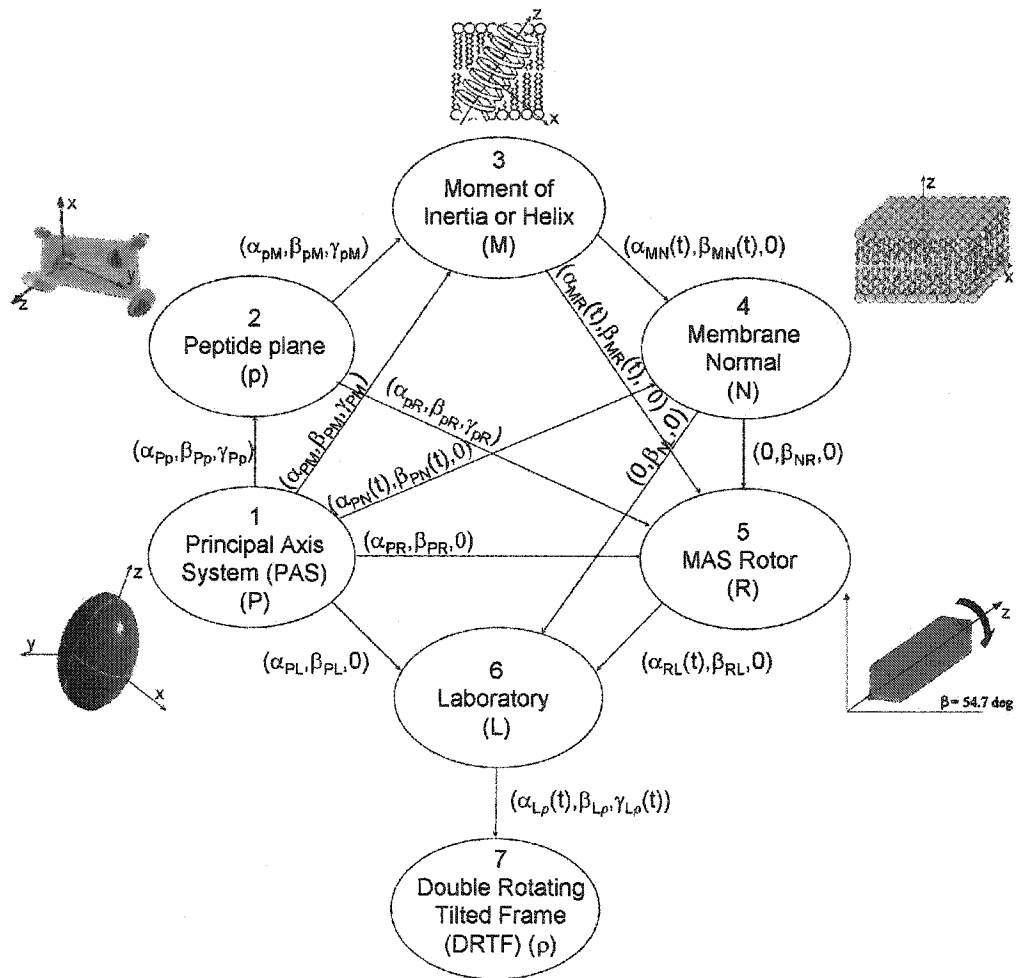


Figure 2.2: Orientation map summarizing the reference frames and transformation Euler angles used in this manuscript.

frame to the laboratory frame. The time dependence in $\Omega_{RL}(t)$, for which $\alpha_{RL} = \omega_R t$ and $\beta_{RL} = \arctan(\sqrt{2})$, will be important in the treatment of the relaxation mechanisms and the average Hamiltonian theory seen later in Sections 6.2.1 (p. 112) and 7.2.1 (p. 159).

A final transformation is shown at the bottom of Figure 2.2 involving $\Omega_{L\rho}$ and describes the passage from the laboratory frame (L) to the double rotating tilted frame (ρ). This transformation is unique as it applies to the spin-dependent portion of the Hamiltonian and is described in more details in Section 6.2.2 (p. 113).

2.3 The NMR interactions

2.3.1 The Zeeman interactions: \mathcal{H}_Z and \mathcal{H}_{rf}

A rigorous description of the total Hamiltonian of a magnetic nucleus must include the Zeeman terms, mentioned previously and which involves the simple interaction of the spin angular momentum with the external static magnetic field. The Zeeman Hamiltonian for the static field \vec{H}_0 given by:

$$\mathcal{H}_Z = \vec{I} \cdot \vec{Z} \cdot \vec{H}_0, \quad (2.23)$$

where $\vec{Z} = -\gamma_I \vec{1}$ with $\vec{1}$ being the unit matrix. The energy eigenstates for this Hamiltonian have already been described in Equation 2.13.

This interaction is also used, with similar notation, to describe the interaction of spins with an applied rf field in a rotating frame defined by the direction of the effective field \vec{H}_e :

$$\mathcal{H}_{rf} = \vec{I} \cdot \vec{Z} \cdot \vec{H}_e, \quad (2.24)$$

The effective field \vec{H}_e was defined in Equation 2.9.

Energetically, the Zeeman effect with the static field is generally so large that all other interactions can be considered only small perturbations. Also, it affects all spins with the same γ with the same magnitude. For these reasons, as was mentioned previously, this interaction can be generally ignored simply by moving to a reference frame rotating at the Larmor frequency. This is generally true, except for the case

of the large quadrupolar interaction \mathcal{H}_Q existing for certain nuclei with very large electric field gradient. A striking example of this involves the ^{14}N spin as described in Chapter 9 (p. 202).

All external spin manipulations by rf pulses can be treated with \mathcal{H}_{rf} . Usually hard pulses are short enough (a few μs) so that all other interactions are usually ignored. In the $T_{1\rho}$ experiments (Chapter 6, p. 110), however, where the rf pulse is applied for longer times, it is useful to move to the double-rotating tilted frame (DRTF), which conveniently allows the description of the spin evolution under the influence of other interaction while ignoring the Zeeman interactions (\mathcal{H}_Z and \mathcal{H}_{rf}).

2.3.2 The dipole-dipole interaction: \mathcal{H}_D

A magnetic moment produces a local field, \vec{B}_{loc} at a distance r of:

$$\vec{B}_{loc} = \frac{\vec{\mu}}{|\vec{r}|^3} - \frac{3(\vec{\mu} \cdot \vec{r})}{|\vec{r}|^5} \vec{r}. \quad (2.25)$$

Hence, any two non-zero spins in the vicinity of one another will be mutually perturbed by their local fields. Classically, the energy associated with the proximity of two magnetic dipoles is expressed as:

$$E = \frac{\vec{\mu}_1 \cdot \vec{\mu}_2}{|\vec{r}_{12}|^3} - \frac{3(\vec{\mu}_1 \cdot \vec{r}_{12})(\vec{\mu}_2 \cdot \vec{r}_{12})}{|\vec{r}_{12}|^5}. \quad (2.26)$$

This is the basis of the direct dipole-dipole interaction in NMR. For the ^1H spins, the largest nuclear magnetic moments, in close proximity (*ca.* 1 Å), this interaction can reach magnitudes of 10^6 Hz. In the general form (Equation 2.15), the Hamiltonian of the dipolar interaction of the field produced by spin \vec{S} on spin \vec{I} (or vice versa) will be described as:

$$\mathcal{H}_D = \vec{I} \cdot \vec{\mathbf{D}}_{IS} \cdot \vec{S}. \quad (2.27)$$

One can show from Equation 2.26 that $\vec{\mathbf{D}}_{IS}$ is both traceless and symmetric, so that in spherical notation, the zeroth and first rank terms are zero. The spin-space separated form (Eq. 2.15) therefore reduces to:

$$\mathcal{H}_D = \sum_{m=-2}^{+2} (-1)^m \mathcal{T}_{2,m} \mathcal{F}_{2,-m}^L \quad (2.28)$$

where the $\mathcal{T}_{2,m}$ are the spin terms:

$$\begin{aligned}\mathcal{T}_{2,0} &= \frac{1}{\sqrt{6}}[3I_z S_z - \vec{I} \cdot \vec{S}], \\ \mathcal{T}_{2,\pm 1} &= \mp \frac{1}{2}[I^\pm S_z + I_z S^\pm], \\ \mathcal{T}_{2,\pm 2} &= \frac{1}{2}I^\pm S^\pm\end{aligned}\tag{2.29}$$

for which the raising/lowering spin operator I^\pm is defined as $I_x \pm I_y$. The spatial dependence is described by the tensor elements $\mathcal{F}_{2,m}$, first described in the principal axes system P (where \vec{r}_{IS} is aligned along the \hat{k}):

$$\begin{aligned}\mathcal{F}_{2,0}^P &= \frac{-\sqrt{6}\gamma_I\gamma_S\hbar^2}{r_{IS}^3}, \\ \mathcal{F}_{2,\pm 1}^P &= 0 \\ \mathcal{F}_{2,\pm 2}^P &= 0\end{aligned}\tag{2.30}$$

and then, in the laboratory frame L (where \vec{B}_0 is aligned along the \hat{k}), after the application of the Wigner rotation matrix, $\mathcal{D}^{(2)}(\alpha_{PL}\beta_{PL}\gamma_{PL})$ as prescribed in 2.20:

$$\mathcal{F}_{2,0}^L = -\frac{\sqrt{6}}{2} \frac{\gamma_I\gamma_S\hbar^2}{r_{IS}^3} (3\cos^2\beta_{PL} - 1),\tag{2.31}$$

or

$$\mathcal{F}_{2,0}^L = -\frac{\sqrt{6}}{4} \frac{\gamma_I\gamma_S\hbar^2}{r_{IS}^3} (3\cos^2\beta_{PN} - 1)(3\cos^2\beta_{NL} - 1).\tag{2.32}$$

The two-transformation Equation 2.32 assumes a motional axis of symmetry in the membrane bilayer, and hence the azimuthal angles α and γ are dropped.

To first order approximation and in the absence of all other interactions, the dipolar interaction between two unlike spins results in a symmetrical spectral splitting equivalent to $2 \times |\Delta\nu_D|$ (in units of Hz) about a central frequency determined by the Zeeman interaction (Section 2.3.1):

$$\Delta\nu_D = \pm \frac{1}{4} \frac{\mu_0}{4\pi} \frac{\gamma_I\gamma_S\hbar^2}{r_{IS}^3} (3\cos^2\beta_{PN} - 1)(3\cos^2\beta_{NL} - 1)\tag{2.33}$$

It is noted that the two variables β_{PL} and r_{IS} are potentially useful for answering specific structural questions. For instance, if the internuclear distance is known, say if it involves two covalently bonded nuclei, such as the labelled ^{13}C and ^{15}N in a peptide

bond, one could infer the possible orientations of this bond relative to the magnetic field. A particularly interesting case is when the sample is oriented; in such a system, one might expect a single value for the splitting rather than a distribution. It is important to note here that a given splitting $\Delta\nu_D$ does not give a unique solution. If the splitting is between 0.5 and 1 times the $\Delta\nu_{D,max}$, there are 2 angular solutions between 0 and 180° (the solutions being supplementary angle pairs). If the splitting is between 0 and 0.5 time $\Delta\nu_{D,max}$, there will be a total of four solutions. In principle, the ambiguity can be lifted with additional orientation constraint measurements, say from the CSA of the same nuclei.

The case of homonuclear dipolar coupling is more complicated, especially when the magnitude of the splitting and the difference in chemical shift between the two nuclei are of the same order. In general, in this “strong coupling” situation, the intensities of the resonances and their splittings can change dramatically. This situation will not be addressed in this work. However, further complication exists in the case of MAS NMR since, when using the average Hamiltonian theory to describe the NMR of a rotating sample, the Hamiltonian, for homogeneously dipolar broadened lines, does not generally commute with itself at all times. The effect of axial diffusion on this situation will be considered in Section 7.2.2 (p. 160).

2.3.3 The chemical shift anisotropy: \mathcal{H}_{CS}

The electronic context around a given nuclear spin is responsible for the CSA interaction. This interaction involves a nuclear spin and the small field produced by the electronic spins around it. Since this (de)shielding effect is directly proportional to the external field, it is often interpreted as a chemical shielding fraction σ . Also, since the distribution of electrons is anisotropic around the nucleus, the chemical shift is orientation-dependent. In fact, the chemical shift anisotropy is usually represented by a 3×3 shielding second-order tensor, $\vec{\sigma}$. In the general notation for the spin-field interaction, \mathcal{H}_{CS} is depicted as:

$$\mathcal{H}_{CS} = -\vec{I} \cdot \gamma_I \vec{\sigma} \cdot \vec{B}_0 \quad (2.34)$$

As before, the spherical tensor notation is preferred to easily perform real space rotations. The spin- and space-dependent terms of Equation 2.18 are developed here for consistency with the other interactions. However, when transformations need be applied in spin space, such into a rotating frame, the static field should not be part of the spin-dependent terms. A special treatment for this situation is described later in this section. The 9-component notation for the spin-dependent part of the spherical tensor is:

$$\mathcal{T}_{0,0} = -\frac{1}{\sqrt{3}}\vec{I}_z \cdot \vec{B}_0 \quad (2.35)$$

$$\mathcal{T}_{1,0} = 0$$

$$\mathcal{T}_{1,\pm 1} = -\frac{1}{2}\vec{I}^\pm \cdot \vec{B}_0$$

$$\mathcal{T}_{2,0} = \sqrt{\frac{2}{3}}\vec{I}_z \cdot \vec{B}_0$$

$$\mathcal{T}_{2,\pm 1} = \mp \frac{1}{2}\vec{I}^\pm \cdot \vec{B}_0$$

$$\mathcal{T}_{2,\pm 2} = 0, \quad (2.36)$$

and for the spatial-dependent part:

$$\mathcal{F}_{00} = -\frac{1}{\sqrt{3}}\gamma \text{Tr}[\vec{\sigma}] = -\sqrt{3}\gamma\delta_0$$

$$\mathcal{F}_{10} = i\sqrt{2}\gamma\sigma_{12}$$

$$\mathcal{F}_{1\pm 1} = \gamma(\sigma_{13} \pm \sigma_{23})$$

$$\mathcal{F}_{20} = \sqrt{\frac{3}{2}}\gamma(\sigma_{33} - (1/3)\text{Tr}[\sigma]) = \sqrt{\frac{3}{2}}\gamma\delta$$

$$\mathcal{F}_{2\pm 1} = 0$$

$$\mathcal{F}_{2\pm 2} = \frac{1}{2}\gamma(\sigma_{11} - \sigma_{22}) = \frac{1}{2}\gamma\eta\delta. \quad (2.37)$$

The asymmetric σ components of the \mathcal{F}_{1m} are generally small enough that, to first order, they do not contribute to this interaction and so these terms are often neglected. The scalar part (\mathcal{F}_{00}) is independent of orientation and is sometimes set to zero to define the origin of the spectrum in some simulations. There exists a reference frame where the symmetric tensor components of \mathcal{F}_{2m} form a diagonal matrix, and it can be considered to be fixed within the molecular structure. The diagonal elements,

or principal components, are referred to as σ_{11} , σ_{22} , and σ_{33} and are assigned in this work, according to the convention ($|\sigma_{33} - \delta_0| \geq |\sigma_{11} - \delta_0| \geq |\sigma_{22} - \delta_0|$, where $\delta_0 = 1/3\text{Tr}[\vec{\sigma}]$). These value can be read directly in frequency units from the powder pattern spectrum of a polycrystalline sample. Furthermore, two more parameters are defined here, namely, the chemical shift anisotropy, δ , and the asymmetry parameter, η :

$$\delta = \sigma_{33} - \delta_0 \quad (2.38)$$

$$\eta = \frac{|\sigma_{22} - \sigma_{11}|}{\delta}. \quad (2.39)$$

These simplify the expression of the frequency chemical shift, ν_{CS} (again, in units of Hz), obtained as a function of the tilt and azimuthal Euler angles for the direct $P \rightarrow L$ or for the two-step $P \rightarrow N \rightarrow L$ transformations. The third angle γ is omitted due to the axial symmetry of the membrane and laboratory frames:

$$\nu_{CS} = \frac{1}{2\pi} \left[\gamma B_0(1 - \delta_0) + \frac{1}{2}[(3 \cos^2 \beta_{PL} - 1) + \eta \sin^2 \beta_{PL} \cos(2\alpha_{PL})] \gamma \delta B_0 \right]. \quad (2.40)$$

$$\begin{aligned} \nu_{CS} = \frac{1}{2\pi} \left[\gamma B_0(1 - \delta_0) + \frac{1}{4}(3 \cos^2 \beta_{NL} - 1) \times \right. \\ \left. [(3 \cos^2 \beta_{PN} - 1) + \eta \sin^2 \beta_{PN} \cos(2\alpha_{PN})] \gamma \delta B_0 \right]. \end{aligned} \quad (2.41)$$

As for the dipolar interaction, orientation information can be extracted from an ordered system as long as the principal components (σ_{11} , σ_{22} , σ_{33}) are known as well as their relative orientation angles to a molecular fixed frame (e.g. the Euler angle set α_{Pp} , β_{Pp} and γ_{Pp}). These can be measured from single crystal NMR or predicted *ab initio* by quantum calculations with some accuracy.

When applying rotations to the spin-part of the CSA interaction, as is the case in Section 6.2.2.1 of Chapter 6 (p. 6.2.2.1), it is useful to rewrite the expression of the Hamiltonian as suggested in [41, Appendix A]. By evaluating the effective field, B_σ , simply as the the product of $\vec{\sigma}$ with \vec{B}_0 , the Hamiltonian is expressed in the form of a first rank tensor (with only three components).

$$\mathcal{H}_{CS} = -\gamma_I \vec{I} \cdot \vec{B}_\sigma, \quad (2.42)$$

where $\vec{B}_\sigma = \vec{\sigma} \vec{B}_0$. Expressed in spherical tensor notation, but keeping the static field out of the spin-dependent part, the following new definition of the the CSA Hamiltonian is obtained:

$$\mathcal{H}_{CS} = \sum_{m=-1}^1 (-1)^m \mathcal{F}_{1,m} \mathcal{T}_{1,-m}, \quad (2.43)$$

with the spin-dependent part components:

$$\begin{aligned} \mathcal{T}_{1,0} &= I_z \\ \mathcal{T}_{1,\pm 1} &= \mp \frac{1}{\sqrt{2}} I^\pm \end{aligned} \quad (2.44)$$

and the spatial-dependent part components:

$$\begin{aligned} \mathcal{F}_{1,0} &= -\gamma_I B_{\sigma z} \\ \mathcal{F}_{1,\pm 1} &= \pm \frac{1}{\sqrt{2}} \gamma_I B_\sigma^\pm \end{aligned} \quad (2.45)$$

2.3.4 The electric quadrupole interaction: \mathcal{H}_Q

The interaction between the electric field gradient of all charges around a nucleus of spin ≥ 1 and its electric quadrupolar moment is called the electric quadrupole interaction. It dominates the spectrum of ^2H , broadening its lines up to a few 100 kHz in a polycrystalline sample. The present study does not make use of this interaction but it suffices to say this interaction can also deliver useful orientation information. As for the CSA, 3 principal components are necessary in a particular molecular-fixed frame to describe this interaction. Effectively, the quadrupolar interaction on a spin=1 is expressed as a splitting with a peak separation following a similar orientation dependence as the CSA. Its expression is given as:

$$\Delta\nu_Q = \frac{3e^2qQ}{4h} [(3 \cos^2 \beta_{PL} - 1) + \eta \sin^2 \beta_{PL} \cos(2\alpha_{PL})] \quad (2.46)$$

where the term $3e^2qQ/4h$ usually equal to 167 kHz in the case of a C- ^2H bond. As before, η is the asymmetry term and β and α are two Euler angles part of the Wigner rotation matrix connecting the principal axis system to the laboratory frame.

2.3.5 The indirect dipole-dipole coupling (J-coupling): \mathcal{H}_J

The last interaction is the indirect spin-spin or dipole-dipole coupling a.k.a. the J-coupling. It is called “indirect” because it requires the assistance of the bonding electrons in the coupling mechanism. Briefly, the presence of the nuclear spin lifts the degeneracy between the “up-down” and “down-up” states of the paired bonding electrons which is observed spectrally through small splittings. It is thus a weak interaction between two spins within the same molecular structure connected by only a few covalent bonds. Its Hamiltonian is expressed as follows:

$$\mathcal{H}_J = 2\pi\hbar\vec{I} \cdot \vec{J} \cdot \vec{S} \quad (2.47)$$

Although, like the previous interactions, it has an orientation dependence, it is usually supplanted in solids by the direct dipole-dipole coupling between the same two spins. It is however in isotropic liquids that it is mainly used and has become an invaluable tool to relay magnetization between spins in a chemically-relevant way so that the chemically-shifted spin resonance can be unambiguously assigned. Indeed, since the direct dipole-dipole coupling has no trace, it vanishes in liquids yielding the non-zero isotropic part of the J-coupling (sometimes called the scalar coupling), given by

$$J_{IS} = \frac{1}{3}(J_{11}^{IS} + J_{22}^{IS} + J_{33}^{IS}), \quad (2.48)$$

reminiscent of the isotropic chemical shift, δ_0 . The ensuing splitting, both for like or unlike spins, is given simply as:

$$\Delta\nu_J = J_{IS}. \quad (2.49)$$

The scalar coupling provides the basic coherence transfer mechanism in some of the experiments, such as INEPT and TOCSY, used and discussed in Chapter 4. It is also alluded to in the search for a high-resolution transfer mechanism for ^1H in Chapter 7.

2.4 Concluding Remarks

This chapter presented only some general theory of NMR, particularly in relation to the specific interactions present in membrane proteins and to the geometry and

dynamics of bilayer membranes. More in-depth theory is needed to understand some of the results presented in this thesis. The author preferred to develop these specific derivations within their corresponding chapters.



- *C'est encore peu de vaincre il faut
savoir séduire.*

- Voltaire

Materials and Methods

In this chapter, a general description is provided for the synthesis and purification of the sample constituents (polypeptide and lipids), the preparation protocols for the samples and the NMR experimental procedures used to study them.

3.1 The biosynthesis of ^{15}N -gA

^{15}N -labelled gA (^{15}N -gA) was biosynthesized, as previously described [46, 47], following a two-step bacterial culture growth protocol: autoclaved cell paste from *Escherichia coli* (*E. coli*) grown on $^{15}\text{NH}_4\text{Cl}$ -enriched (CDN Isotopes, Pierrefonds, Canada) minimal medium was used as the sole nitrogen source for the growth of *Bacillus brevis* (*B. brevis*) (American Type Culture Collection (ATCC) 8185 or 10068). ^{15}N -gA was purified by reversed phase high-performance liquid chromatography (RP-HPLC) on a C_{18} column (8 x 100 mm, 300 Å, Waters, Mississauga, Canada). In the following, I describe the detailed protocol used in our laboratory. The reader is invited to also consult a new protocol published recently [48].

3.1.1 Successive growth of *E. coli*

A single colony of a common strain of *E. coli* (in this case, the K12 strain), grown on a sterile 2% nutrient agar plate, was used to inoculate 10 mL of ^{15}N -labelled minimal mineral salts medium (^{15}N -MMSM) (see Table 3.1) in a 50 mL flask. The medium was agitated at 180 rpm in a 37 °C incubator for 18 h. The 10-mL culture was then used to further inoculate 40 mL of ^{15}N -MMSM which was incubated under the

Table 3.1: The constituents of 1 L of minimal mineral salts medium (MMSM).

¹⁵ N-MMSM	
Amount	chemical
7.0 g	Na ₂ HPO ₄
3.0 g	KH ₂ PO ₄
0.5 g	NaCl
1.0 g	¹⁵ NH ₄ Cl
15.0 g	glucose
0.12 g	MgSO ₄ -7H ₂ O ^a
0.015 g	CaCl ₂ -2H ₂ O ^a
1.0 mg	FeSO ₄ -7H ₂ O
1 L	H ₂ O

^a dissolved separately

same conditions for 6 h. Finally, the 50-mL culture was transferred into a 4-L flask containing 1 L of ¹⁵N-MMSM for the final inoculation and grown under the same conditions, maintaining the pH at 7.2 with 4 M KOH, until the optical density (OD) at 600 nm reached 1.3-1.4. This step generally took around 6 h.

3.1.2 Harvesting *E. coli* cultures

The cells were harvested by sedimentation at 16,000 × g for 10 min. The sedimented paste was weighed (the yield was typically 4 g for 1 L of culture) and suspended in a modified asparagine-glycerol medium (AGM, see Table 3.2) to a concentration of 1.0 g of cell paste per 5.0 mL. The suspension was then autoclaved for 1 h to break down all *E. coli* cells, thus sterilizing the paste. The autoclaved mixture was streaked onto a 2% nutrient agar plate to test the non-viability of the cells.

3.1.3 Long-term storage of *B. brevis* stock culture

Lyophilized cells of *B. brevis* (ATCC, 8185 or 10068, Manassas, VA, USA) were used to inoculate 10 mL of AGM in a 50-mL flask. The culture was agitated vigorously at 250 rpm in a 37 °C shaker bath until sporulation was verified by malachite green staining (see Section 3.1.5). When a good level of sporulation was obtained, 10 mL of culture were first mixed with 10 mL of sterile glycerol, heated to 80 °C for 10 min,

Table 3.2: The constituents of 1 L of asparagine-glycerol Medium (AGM).

AGM	
Amount	chemical
655 mg	K ₂ HPO ₄ ·3H ₂ O
500 mg	KH ₂ PO ₄
100 mg	MgSO ₄ ·7H ₂ O ^a
10 mg	NaCl
7.6 mg	MnSO ₄ ·H ₂ O ^a
10 mg	FeSO ₄ ·7H ₂ O ^a
150 mg	CaCl ₂ ·2H ₂ O ^a
4.0 mL	glycerol
2.5 g	L-asparagine ^b
in 1 L	H ₂ O

^a dissolved separately

^b replace by 4 g of autoclaved *E. coli* cell paste for modified AGM

and cooled. The heat activated spores were aliquoted into 20 × 1 mL samples in 1.5-mL cryovials and stored in a -80 °C freezer.

3.1.4 Successive growth of *B. brevis*

A frozen stab of heat-activated *B. brevis* culture (ATCC, 8185 or 10068) was thawed and used to streak the surface of a 2% nutrient agar plate. The plate was incubated at 37 °C for 24 h. A single colony with rough edges was chosen to inoculate 10 mL of AGM lacking L-asparagine but supplemented with uniformly ¹⁵N-labelled *E. coli* cell paste in a 50-mL flask; “rough” colonies are shown to have a higher propensity towards spore-formation as opposed to “smooth” ones. It was necessary to monitor this growth microscopically to determine when the cells had advanced from the vegetative stage to the sporulation process. The onset of sporulation usually took place after 10 h of growth at 37 °C and under vigorous agitation (250 rpm). It has been demonstrated that a good level of oxygenation is indispensable for good sporulation (formation of foam on the medium was a good indication of sufficient aeration).

For the second step, 1 L of modified AGM in a 4-L flask was inoculated with the 10-mL culture once sporulation was attained. The flask was agitated at 250 rpm for 18-26 h at 37 °C. The growth was monitored periodically every 2-4 h both

spectrophotometrically (turbidity at 600 nm reached 3-5) and microscopically by malachite green staining. Growth was terminated just after the onset of sporulation was observed on the microscope slides.

3.1.5 Malachite green staining procedure for assessment of sporulation

A drop of culture was deposited on a microscope slide, and allowed to air-dry. The smear was heat-fixed over a flame. A few drops of malachite green solution (5% (w/v) in water) were deposited over the cell smear. The slide was heated over a flame for 1 min adding more malachite green solution as needed. The slide was cooled and rinsed under a light stream of water. Once the slide was dried, 1-2 drops of safranin red solution (0.25% (w/v) in 20% ethanol) was placed over the smear for 15 seconds and then rinsed off. The dry sample was covered with a drop of permount and a cover slip. The slide was examined under a light microscope (1000X magnification): spores were distinguished as small green ellipses whereas vegetative bacilli showed up as red rods (Figure 3.1).

3.1.6 Isolation of ¹⁵N-tyrothricin

The name tyrothricin was proposed [49] to refer to the family of apolar (alcohol-soluble and water-insoluble) peptides produced non-translationally by *B. brevis*. This atypical class of peptides, composed of L- and D- amino acids, have bactericidal activity against Gram-positive microorganism such as *pneumococci* (hence the origin of the name gramicidin). These polypeptides include a group of gramicidins (A, A', B, B', C, C') differing by one or two residues, and the cyclic peptide tyrocidine. They were isolated by solvent extraction from the cell lysate once the cell growth reached the sporulation stage. The sequences for the linear pentadecapeptides are [50]:

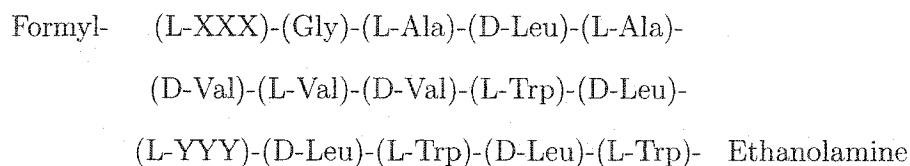
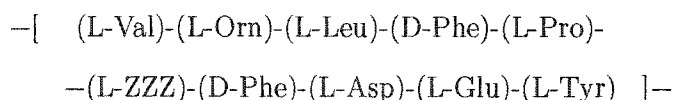




Figure 3.1: Micrograph showing *B. brevis* (ATCC 8185) culture smear as growth entered the sporulation phase. Bacilli were stained red (safranin red) and spores were stained green (malachite green).

where XXX denotes Val or Ile in proportions of 85% and 15% for unprimed and primed gramicidins, respectively, while YYY denotes Trp, Phe or Tyr in proportions of 80%, 15% and 5% for gA, B and C, respectively. The sequence of the cyclic decapeptide tyrocidine is [51]:



for which ZZZ is either Phe or Tyr.

A volume of 125 mL of 4 M KOH was added to 1 L of *B. brevis* culture to lyse the cells and the mixture was stirred for 10 min. The lysate were transferred into base-resistant centrifuge tubes (polypropylene for example) and centrifuged (10,000 rpm) for 20 min at 4 °C. The sedimented pellet was washed by suspending it in 300 mL of chilled 1% NaCl solution and centrifuged once more for 10 min at 4 °C. This step was repeated a second time with 200 mL of 1% cold NaCl. The tyrothricin was then

Table 3.3: RP-HPLC solvent composition profile for gA separation on C₁₈-column.

time (min:sec)	H ₂ O/MeOH ratio (vol/vol)
0	20/80
8:30	14.3/86.7
18:00	14.3/86.7
19:00	0/100
28:30	0/100
30:00	20/80

extracted from the pellet by suspending it in 40 mL of ethanol/0.2 M HCl (9:1 v/v) and allowing it to stir for 2 h at 4 °C. The mixture was centrifuged again (10,000 rpm for 20 min at 4 °C). The pellet was re-extracted overnight with 40 mL of 100% ethanol at 4 °C followed by a final centrifugation step (10,000 rpm for 20 min at 4 °C).

The combined ethanol supernatants were subjected to solvent evaporation *in vacuo*. The residue was dissolved in 20 mL methanol (MeOH) and treated through heating to a gentle boil with 100 mg of activated charcoal for 30 min. The charcoal was separated through vacuum filtration and the resulting filtrate was concentrated under reduced pressure down to a few milliliters.

3.1.7 Reversed phase HPLC purification of ¹⁵N-gA

Tyrothricin, as mentioned above, is a mixture of highly hydrophobic peptides. These can be separated from one another quite well using RP-HPLC, despite the fact that gramicidins may differ by as little as a single hydroxyl group on one of the 16 residues. About 250 µg of peptide in 100 µL of MeOH were loaded on an semi-preparative size (8 mm x 100 mm, Delta-pak, Waters) C₁₈ column [52]. A solvent mixture of H₂O/MeOH in varying concentration according to Table 3.1.7 was run through the column at a flow rate of 3 mL/min. For better resolution, and since gA was thermostable, the column was heated to 55 °C during elution.

The eluent was analysed spectrophotometrically at a wavelength of 220 nm. The largest peak, observed between 8.6 and 9.6 min (see Figure 3.2) corresponded to gA,

which was collected as a separate fraction. The folded structure of the gA was assessed by circular dichroism spectroscopy (Jobin-Yvon CD6-SPEX Circular Dichroism Spectrometer), where it displayed a unique optical rotation profile with maxima near 215 and 230 nm (Figure 3.3) when dispersed in sodium dodecyl sulfate (SDS) aqueous solution (1/100 mol/mol) [53]. Finally, mass spectra were obtained for unlabelled and ^{15}N -labelled tyrothricin samples on a VG Quattro II (Fisons, UK) triple quadrupole mass spectrometer equipped with an atmospheric pressure ion source using an electrospray interface. A 300 $\mu\text{g/mL}$ sample solution was prepared in 50% acetonitrile and 50% water containing 5% acetic acid. The mass spectra averaged over 4 scans are shown in Fig 3.4(A) and (B), for unlabelled gramicidins and ^{15}N -gramicidins, respectively. The major peak in both samples, corresponding to the doubly positively charged species of gA, are different by 10 m/z units, exactly the mass difference expected between the two samples (there are 20 nitrogen atoms in gA).

3.2 The synthesis of perdeuterated DMPC- d_{72}

Deuteron-enriched phospholipids have been used mostly in the study of dynamics and structure by ^2H -NMR. Their popularity in the seventies and eighties triggered the development of chemical methodologies to synthesize and purify phospholipids labelled specifically on the backbone, headgroup or acyl chains [54–64]. Today, many of these lipids are available commercially.

The scope of the present study deals with ^1H -NMR on protein samples which constitute less than 20% of the sample mass. The remainder is composed of phospholipids and water. Whereas the water proton signal may be irradiated and eliminated using pulse strategies, the only way to eliminate proton signals from the lipids is to substitute all protons by deuterons. To date, such fully perdeuterated lipids are not available commercially. However, two papers have presented complete protocols for the synthesis of diacylglycerophospholipids [60, 64]. A simplified protocol is proposed here consisting of four reactions, and starting from three affordable commercially available deuterated starting reagents, namely glycerol- d_5 , myristic acid- d_{27} and choline-bromide- d_{13} (all from CDN isotopes, Pierrefonds, Canada).

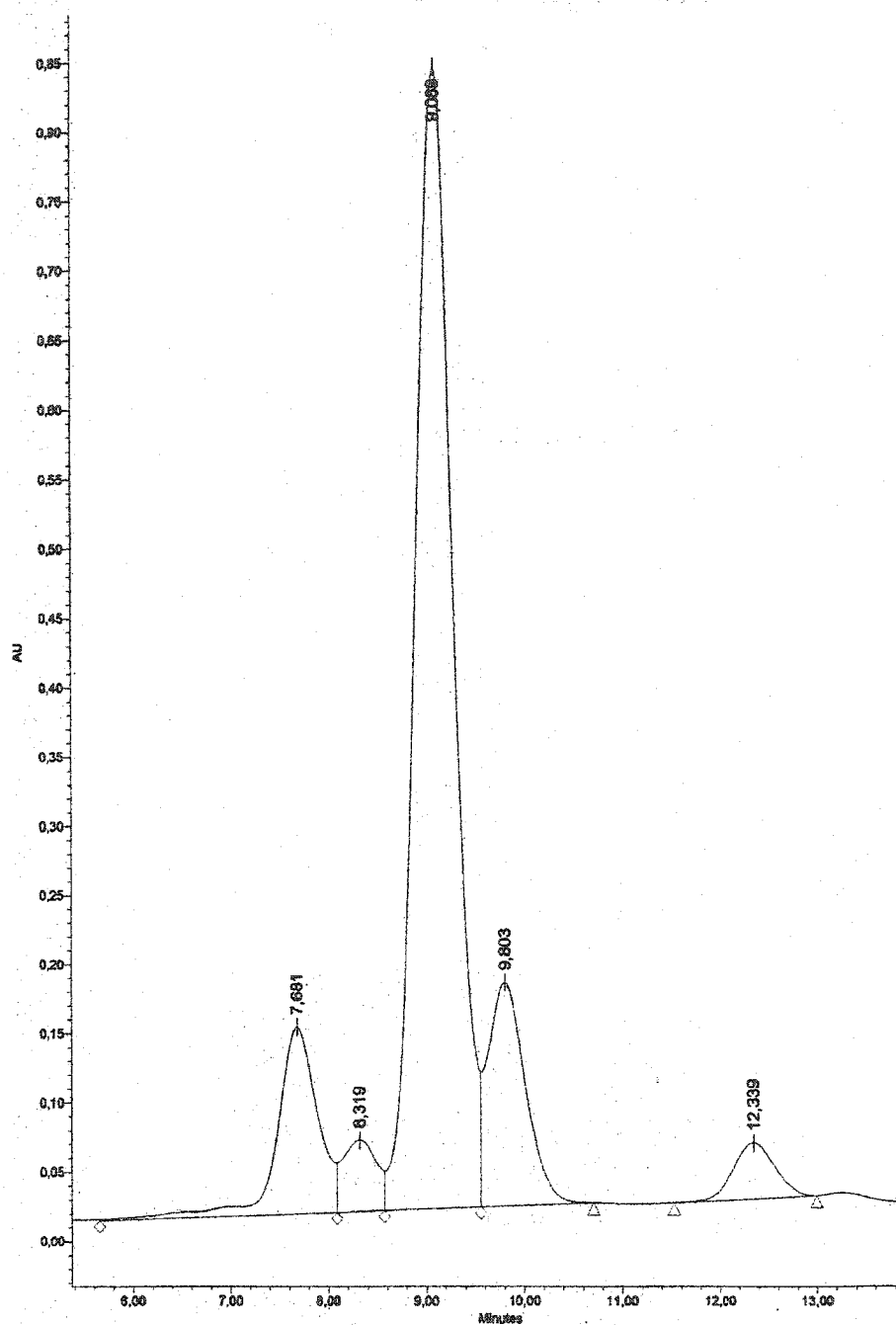


Figure 3.2: Elution profile of gramicidins by RP-HPLC as monitored spectrophotometrically at 220 nm. Six peak maxima eluted at 7.7 min (gB), 8.3 min (gB'), 9.1 min (gA), 9.8 min (gA'), 12.3 min (gC), 13.2 min (gC'). The fractions collected between 8.6 and 9.6 min were pooled and contained 95% gA. The elution of tyrocidine occurred around 3 min (not shown).

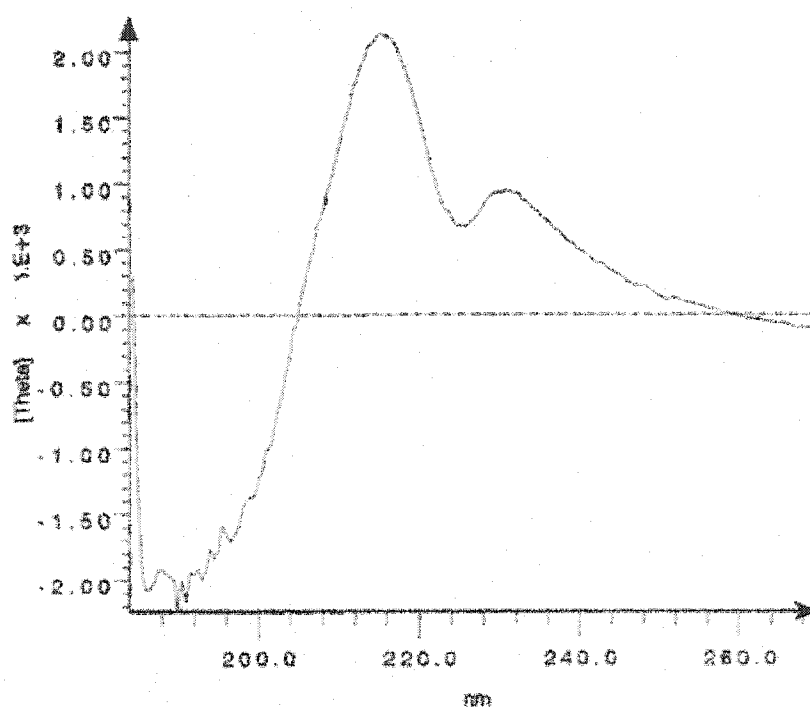


Figure 3.3: Circular dichroism spectrum of gA in SDS micelles.

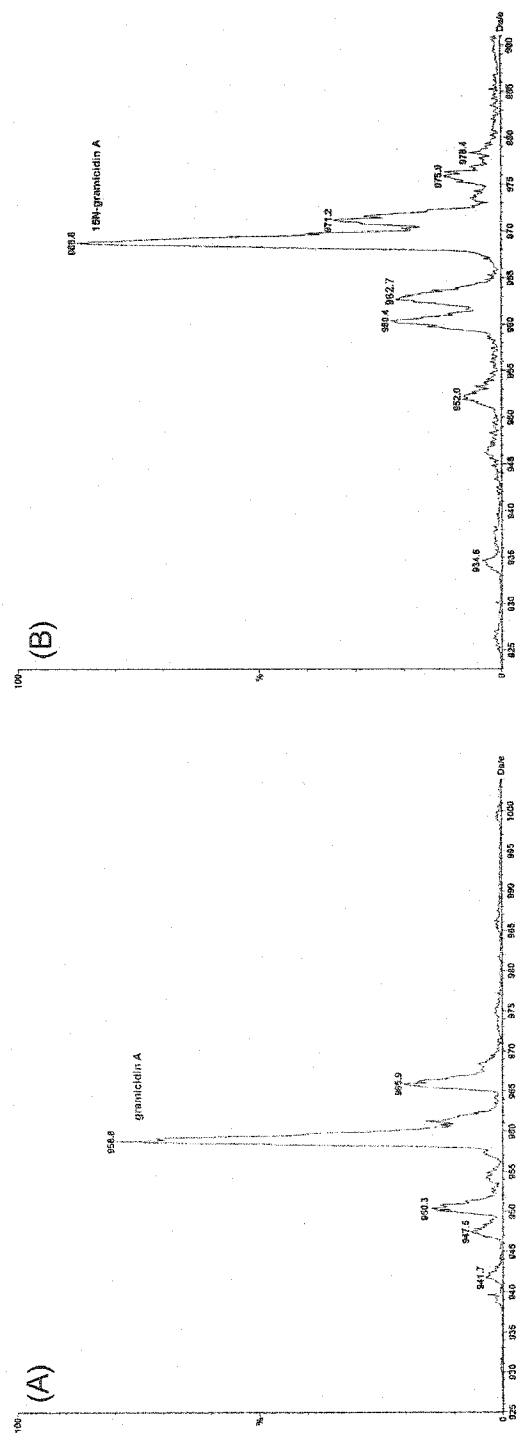


Figure 3.4: Mass spectrometry of purified (A) unlabelled and (B) ^{15}N -labelled gramicidins.

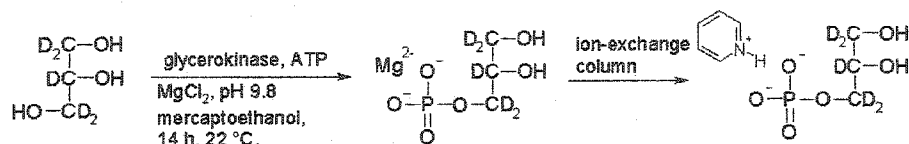


Figure 3.5: The synthesis of G3P-d₅

3.2.1 The phosphorylation of glycerol-d₅ (synthesis of G3P-d₅)

The L-stereoisomer of α -glycerophosphate (G3P, L-glycero-3-phosphate or 3-phospho-L-glycerol) deuterated at every non-labile position was prepared by transferring the γ -phosphate group from adenosine 5' triphosphate (ATP) to glycerol-d₅ in the presence of glycerokinase from *E. coli*. The enzymatic reaction was necessary to preserve the naturally occurring chirality at the β position of the glycerol backbone of all phospholipids as illustrated in Figure 3.5 [60, 64, 65].

The reaction mixture consisted of 5 mmol (460 mg) of glycerol-d₅, 6 mmol (3.3 g) of ATP(sodium salt, grade 1, Sigma), 3 mmol (609 mg) of MgCl₂·H₂O and 2 mL of 1 mM mercaptoethanol dissolved in 60 mL of deionized water. The pH was adjusted to 9.8 using about 10 mL of NaOH (1 M) for optimal enzymatic activity. About 100 units of the glycerokinase (Sigma) were first dissolved in 5 μ L of sodium phosphate buffer (pH 7.0, 0.02 M) with 1 mM of mercaptoethanol and then transferred to the reaction vessel to initiate the reaction. The mixture was allowed to stir at room temperature. The pH was monitored and readjusted to within 9.8-10.0 with the addition of small aliquots (10's of μ L) of NaOH. This was done continuously for the first two hours and less frequently as the reaction rate slowed down. The reaction was completed after 14 h.

The progress of the reaction was monitored by thin layer chromatography (TLC) using a solvent system consisting of 2-propanol:H₂O (70:30, v/v). The separated components are revealed upon KMnO₄ treatment (spray and heat, solution: 3 g KMnO₄, 100 mL acetic acid 5%, 300 mL H₂O, 20 g K₂CO₃). The R_f values were 0.8 (glycerol), 0.5 (G3P), 0 (ATP/ADP).

Once the reaction was completed, 24 g of activated charcoal were added directly

to the vessel to absorb the enzyme and the mixture was allowed to stir for 30 min. The charcoal was removed and washed by filtration on GF/C Whatman paper in a Büchner funnel. The mixture was filtered a second time over Celite. The filtrates were then pooled to give a final volume of about 115 mL, and the pH was adjusted to 8.2 with acetic acid. The barium salt of GP was created by adding 7.5 mL of 1 M barium acetate. The mixture was chilled in an ice bath for 2 h and then centrifuged for 10 min at 6000 rpm at 4 °C. The addition of 4 volumes of ethanol (95 %) to the combined supernatants caused the barium salt of GP to precipitate. The mixture was chilled at 4 °C overnight and centrifuged as before to retrieve the precipitated GP. The counterion was exchanged back to sodium by dissolving the pellet in 100 mL of water and adding 4.0 mmol of sodium carbonate. The precipitated barium carbonate was filtered off and washed with water. The filtrate volume was reduced to 10-20 mL and passed through a cation-exchange column in the pyridinium form (Dowex 50W-x8, Dow, Midland, MI, USA; 100 mL bed volume, 0.5 mL/min flow rate, 500 mL eluent), to exchange the counterion to pyridinium, which will allow the product to be easily solubilized in the next reaction. The solvent was removed under reduced pressure and by lyophilization.

The purity and the yield was assayed by ^{31}P and ^{13}C NMR. The yield was usually greater than 90 %.

3.2.2 The diacylation of glycerophosphate- d_5 (synthesis of L- α -DMPA- d_{59})

The synthesis of dimyristoyl-glycerophosphatidic acid- d_{59} (DMPA- d_{59}) was performed in two steps. First, the acyl chains were activated by preparing myristic anhydride from the free deuterated fatty acid according to the reaction reported by Selinger and Lapidot [66] (Figure 3.6). Then, the acyl chains were coupled to the G3P via ester links at position 1 and 2 following the reaction described by Gupta *et al.* [59] (Figure 3.7).

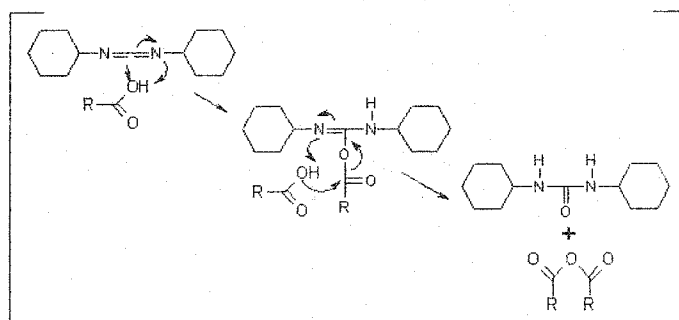
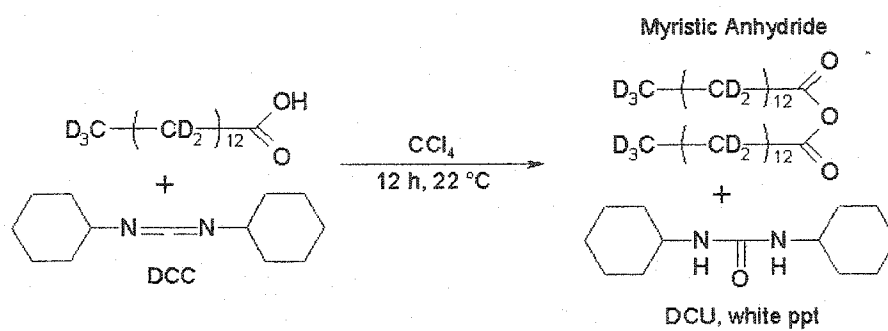


Figure 3.6: The synthesis of myristic anhydride- d_{54}

3.2.2.1 The synthesis of myristic anhydride-d₅₄

About 16 mmoles of fatty acid, in this case myristic acid-d₂₇ (4 g), was vacuum dried overnight and dissolved in 132 mL of freshly distilled carbon tetrachloride (CCl₄). Then, 8 mmoles of dicyclohexylcarbodiimide (DCC, Sigma-Aldrich, Canada, 1.98 g) were added as a separate suspension in 25 mL of CCl₄ to increase its solubility. Within the first minute of the reaction a white precipitate was observed due to the formation of insoluble N,N-dicyclohexylurea (DCU) according to the reaction shown in Figure 3.6. The mixture was left to stir sealed from atmospheric air at room temperature for 5 h. After completion, the DCU was filtered off and washed thoroughly with anhydrous CCl₄. The filtrate was vacuum evaporated and the white residue was recrystallized from acetone. A typical yield was 80 %. The reaction was followed by TLC using petroleum ether/diethyl ether (80:20 v/v) as the solvent system and charring with aqueous sulfuric acid 1:1 (v/v) as an indicator. The R_f values of interest were 0.5 (myristic anhydride), 0.4 (DCU, DCC), 0.2 (myristic acid) and 0.1 (dicyclohexylacetylurea).

3.2.2.2 Coupling reaction

The synthesis of DMPA requires high quality starting reagents and the lowest degree of water content possible. Prior to the reaction, the solvent, pyridine, was allowed to reflux for 5-7 days over calcium hydride. Twenty-four hours prior to the reaction, 0.5 mmol of pyridinium G3P-d₅ was transferred to a 250-mL flask and dried by repeated additions and evaporations of anhydrous pyridine. The pyridinium G3P-d₅ was then left to dry under vacuum overnight. Also, both myristic anhydride-d₅₄ and 9-pyrrolidinopyridine were freshly recrystallized from acetone and n-pentane, respectively. 2 mmol of myristic anhydride and 2.5 mmol of 9-pyrrolidinopyridine were allowed to dry separately on a lyophilizer overnight.

Under an argon atmosphere, the anhydride and the catalyst as well as 100 mL of freshly distilled pyridine were transferred to the flask containing the syrupy pyridinium G3P-d₅. The pyridinium G3P-d₅ was slow to detach from the walls of the flask and may require the assistance of a stir bar to lift it off. The reaction was left

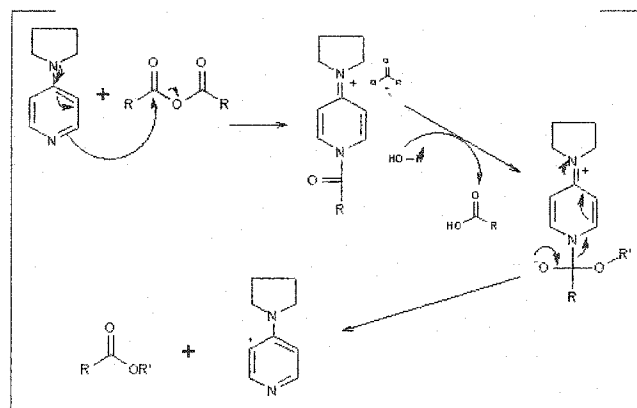
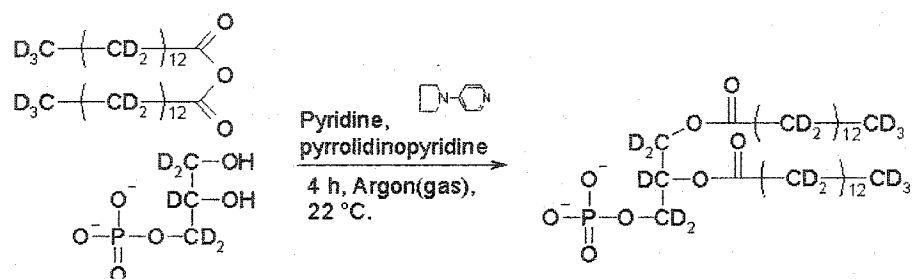


Figure 3.7: The diacylation of glycerophosphate- d_5

to proceed sealed from ambient humidity under a steady stream of argon gas. The reaction required at least 4 h to complete but was usually left until all the pyridinium G3P had completely detached from the flask walls. The reaction was monitored by TLC using a fresh mixture of dichloromethane/ethanol/water 80:20:2.5 (v/v/v) as the mobile phase and iodine vapors as the revealing agent (R_f : myristic acid (0.8), mixed anhydride (0.6), DMPA (0.3) and monomyristoylphosphate (0.1)).

After completion, 10 mL of H_2O were added and the mixture was left stirring overnight; this allowed the breakdown of any mixed anhydride co-formed. The solvents were then removed under reduced pressure. All pyridinium species were extracted by running the mixture through an cation-exchange column (AG 50W-x8, Bio-rad Laboratories, Mississauga, Canada; hydrogen form, 60 mL bed volume). About 3 bed volumes were used to elute the protonated mixture at a flow rate of 1 drop/s. The eluate was dried under reduced pressure, and the resulting white solid was dissolved in 10-20 mL of chloroform ($CHCl_3$) and applied to a carboxymethyl-cellulose column (CM54, Fisher Scientific, Nepean, Canada; 200 mL bed volume) for separation of the lipid species as described by Comfurius *et al.* [58]. The free fatty acid eluted first with pure $CHCl_3$ and was recycled for another round of reaction. DMPA- d_{59} eluted with $CHCl_3/CH_3OH$ (75/25, 3 bed volumes) and finally monomyristoylphosphate- d_{32} eluted with $CHCl_3/CH_3OH$ (50/50, 3 bed volumes). The column was regenerated with 10 bed volumes of MeOH and reequilibrated with 5 bed volumes of $CHCl_3$. The elution of product was monitored by the same TLC test described above. The best yields were 70%.

3.2.3 The phosphodiester coupling of choline to DMPA (synthesis of L- α -DMPC- d_{72})

The final step of this synthesis must be carried out under optimal conditions. Both starting materials, DMPA- d_{59} and choline- d_{13} tetraphenylborate (TPB), must be associated with their proper counterion for solubility in pyridine, recrystallized and thoroughly dried. Furthermore, the catalyst, triisopropylbenzene sulfonyl chloride (TPS) must be freshly recrystallized.

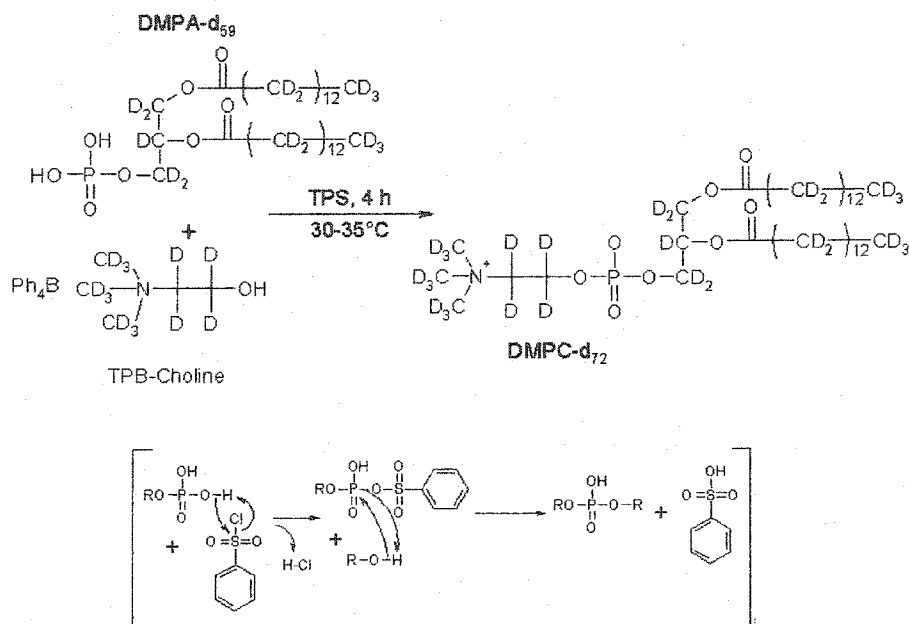


Figure 3.8: synthesis of L- α -DMPC-d₇₂

The diammonium salt of DMPA-d₅₉ was recrystallized according to the procedure described in Kates, 1972 [67]. The bromide counterion of commercial choline-d₁₃ was exchanged for TPB as described in [64]. NaTPB (3.08 g, 9 mmol) and choline-d₁₃ bromide (1.178 g, 6.4 mmol) were dissolved separately in 45 mL and 25 mL of H₂O, respectively. Instantaneously, a gelatinous white precipitate formed, which was filtered through a sintered glass filter and rinsed thoroughly with 400 mL of H₂O. The newly-formed salt was dried azeotropically with toluene/ethanol (20/75 v/v) 2 or 3 times, resulting in a white crystalline residue. The TPB salt of choline-d₁₃ was further recrystallized from acetonitrile (20 mL). This step yields quantitative large hexagonal crystalline prisms, which were stored dry below 0 °C.

The TPS was purified just prior to its use, as it was highly sensitive to light. Approximately 8.5 g of TPS were weighed to which was added 0.5 mL of freshly distilled thionylchloride and 50 mL of n-pentane. The mixture was quickly heated until the TPS was completely dissolved. Upon gradual cooling of the solution to 0 °C, new crystals formed which were collected by vacuum filtration, dried under vacuum

and stored at low temperature in an opaque vial.

As in the previous reaction, pyridine was distilled under very dry conditions by refluxing over CaH_2 for a week. This pyridine is used to azeotropically dry DMPA (146 mg, 0.225 mmol) and choline (206 mg, and 0.5 mmol) first separately, then combined in the same flask. The mixture and TPS were dried under vacuum until used. It is important that all reactants be kept under an argon atmosphere and all transfers be performed through rubber septa, to avoid any contact of the reactants with the humidity of ambient air. The TPS was combined with the two starting reagents, along with 100 mL of dry pyridine. The mixture usually turned yellow and all starting materials went into solution. The mixture was stirred for 4 h at 30-35 °C. After the reaction was complete, 1.5 mL of H_2O was added to the reaction mixture to decompose TPS. After 10 min, the solvents were removed under reduced pressure, and the residue was further dried azeotropically with 50 mL of toluene. The product was suspended in 50 mL of trichloroethylene (TCE) and the insoluble material was filtered away. This step was repeated for the filtrate, after evaporation of the solvent, with another 30 mL of TCE. The second filtrate was dried and dissolved in 40 mL of TCE/MeOH (1/1 v/v) and transferred to a 150-mL glass centrifuge tube. Several solvents were sequentially added, mixing vigorously between additions: 10 mL of H_2O , 20 mL of TCE and 10 mL of aqueous NaCl (0.9% w/v). The mixture was centrifuged for 15 min at $1500 \times g$ to separate the solvent layers. The upper aqueous phase was removed and discarded. The lower organic phase was washed three times with 15 mL portions of a mixture containing TCE/MeOH/aqueous NaCl(0.9% w/v) in volumetric ratio 3/48/47. Each time the upper phase was removed after centrifugation. The lower organic phase solvent was then evaporated and the product dissolved in a minimal amount of CHCl_3 /MeOH 1:1 (v/v). This solution was applied to a carboxymethyl-cellulose column (CM54, Fisher Scientific, Nepean, Canada; 200 mL bed volume) for a separation similar to the previous reaction. Before eluting DMPC, 3 bed volumes of CHCl_3 then 3 bed volumes of CHCl_3 /MeOH 98:2 (v/v) were applied to the column first. DMPC- d_{72} eluted with several hundreds of mL of CHCl_3 /MeOH 96:4 (v/v). DMPA- d_{59} eluted as before with CHCl_3 /MeOH 75:25

(v/v). The chromatographic eluent was monitored by TLC. The mobile phase was composed of CHCl_3 /acetone/MeOH/acetic acid/water 10:4:4:2:1 (v/v/v/v/v) and the migration of products were revealed with iodine vapors (R_f : DMPA (0.8) and DMPC (0.25)). The DMPC fractions were pooled, evaporated and the product submitted to a final acetone precipitation protocol [67, Chapter 5]. The best yields were 70% relative to DMPA.

3.3 Sample preparation

A number of solution samples were used in the present work. Solubilization of hydrophobic polypeptides in the membrane mimetic solvent system is straightforward, and is described in the figure legends in later chapters.

Micellar dispersions of hydrophobic polypeptides were made in the standard way described by Arseniev *et al.* [53] for gA. To make a 500- μL sample, about 0.200 g of SDS- d_{25} (MW = 297 Da) was first recrystallized from 95% ethanol. Then 74.3 mg of recrystallized SDS- d_{25} was dissolved in 450 μL of 0.5 mM potassium phosphate buffer solution adjusted to pH = 6.5. Meanwhile, 4.8 mg of gA (MW = 1899 Da) was dissolved in 50 μL of 2,2,2-trifluoroethanol- d_3 (TFE- d_3 , Cambridge isotopes, Andover, MA, USA). The TFE- d_3 solution was then slowly added, 10 μL at a time, to the aqueous solution with gentle vortexing (to avoid foam formation), ensuring complete dissolution of the gA after each small addition. The final sample consisted of approximately 500 mM SDS- d_{25} , 50 mM phosphate buffer and 5 mM gA.

For multilamellar dispersions of gA and other peptides, the samples were optimized to maintain the fluid lamellar phase of the membranes while maximizing the amount of material and signal-to-noise ratio. Based on past experience, the best conditions was obtained when the mixture was composed of about 10-20 molecules of lipids for every transmembrane species (gA dimer or α -helical monomer). A volume of aqueous buffer equivalent to no more than three quarters of the dry sample mass was necessary to hydrate the lamellar phase (or equivalent to 43% v/w); any excess was extracted out of the sample by the large centripetal forces caused by the rapid sample spinning. The 4-mm MAS rotors may contain a volume up to 66 μL , equivalent to 30 mg of

sample (the sample compresses upon MAS but any addition of more sample reduces the stability of the spinning).

A typical sample of gA/DMPC (1/10 mol/mol or 20 lipids for one gA dimer) was prepared by separately weighing 19.5 mg of DMPC (MW = 678 Da) and 5.5 mg of gA (MW = 1899 Da), combining them in a small, clean round bottom flask (RBF) and dissolving them in a small volume of 100% MeOH¹. The mixture was subjected to reduced pressure on a rotary evaporator to rid the solution of the majority of the solvent. The solid material formed a thin film on the walls of the flask. Using a stainless-steel spatula, the film was separated from the walls and broken down before the flask was placed under vacuum for about 12 h to remove any excess solvent or moisture left behind. The dry solid peptide/lipid mixture was then carefully transferred to a clean 0.5- μ L Eppendorf tube and weighed. The sample was rehydrated using a volume equivalent to three quarters of the dry sample weight of 50 mM potassium phosphate buffer solution, pH 6.5. The viscous sample paste was then meticulously mixed mechanically using a small narrow stainless-steel rod with a sharpened tip to reach the bottom of the tube. To assure complete homogeneity, the sample was blended this way for 15 min in a dust-free area, with intermittent centrifugation cycles to bring the paste back to the bottom of the tube. The sample was then transferred to a pre-weighed, clean 4-mm MAS rotor by slow centrifugation using a truncated pipette tip as an improvised funnel. The open lip of the rotor was carefully decontaminated of any viscous sample material to ensure a tight fit when the turbine cap was snapped on and to prevent the caps from sliding off during high-speed MAS. The final sample mass was recorded after collection of the NMR data to monitor potential water evaporation at the end of the experiment. Under ideal conditions, a 30-mg sample was obtained. The rotor was typically rotated under MAS conditions at temperatures between 50-60 °C. It should be noted that the sample needed at least 24 h under experimental MAS conditions to anneal to a stable state.

¹ Although the gA sample was allowed to stabilize under experimental conditions for several days, it is recommended by Killian *et al.* [68] to pre-dissolve gA in TFE to prevent the formation of intertwined intermediates.

3.4 Technical aspects of NMR

Nuclear magnetic resonance was the principal experimental technique used in the present work. It is a well established spectroscopic technique for obtaining exquisite structural and dynamical details of biological systems with molecular resolution. To obtain the results in this thesis, I made use of several modern solution- and solid-state methodologies. In this section, an overview of the major experimental components and approaches used is sketched.

3.4.1 The spectrometer

The majority of NMR experiments described in this thesis were carried out using one of two commercial spectrometers assembled by Bruker BioSpin GmbH (Karlsruhe, Germany). The first is based on a 14.1 T magnet (54-mm bore) and is designed for high-resolution solution-state experimentation with up to 4-channel capabilities (a 150-W amplifier at 500-600 MHz, two 300-W amplifiers at 6-243 MHz, and a low-power lock channel for ^2H). It was also implemented to permit some low-power solid-state experiments, using a XC4 Doty HR-MAS probe (see below). The second spectrometer is equipped with a 11.7 T magnet with a 89-mm wide bore and with high-power capabilities for static and MAS-type solid-state NMR experimentations through 3-channels including two 1-kW amplifier for ^1H (500 MHz) and for X (6-243 MHz) as well as a 300-W amplifier for low-frequency work (6-243 MHz).

3.4.2 High-resolution MAS probe

For studies under MAS conditions, a triple-tuned $^1\text{H}/\text{X}/\text{Y}$, XC4 narrow bore probe (Doty Scientific, Columbia, USA) capable of spinning at speeds up to 25 kHz (see Figure 3.9) was used. This probe allows high-resolution studies of liquids and solids and can withstand substantially high-power ^1H decoupling (specifications: 140 kHz). The samples, with volumes between 66 μL and 124 μL , were loaded into 4-mm (outer radius) silicon nitride (Si_3N_4) rotors with aurum front and back end machined caps with turbines. The rotor spinning rates were monitored via fiber optic cables and

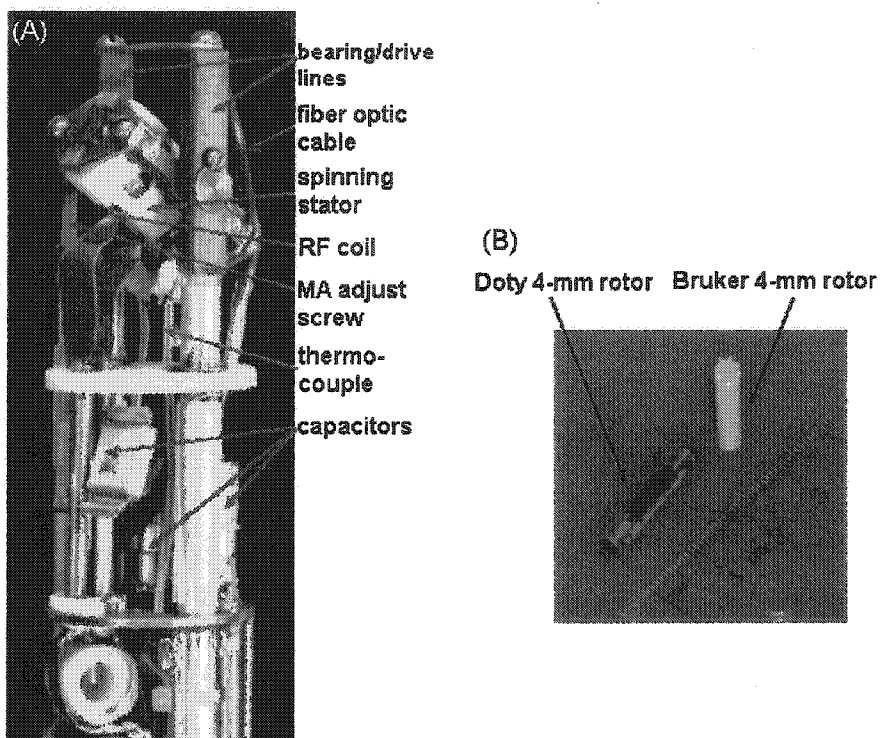


Figure 3.9: (a) Doty Scientific XC4 HR MAS probehead. (b) MAS rotors (or sample spinners) designs by Doty Scientific (SiNO_3 body and aurum turbine front and back end caps) and by Bruker Biospin GmbH (zirconia body and Kel-F turbine end cap).

controlled by the Bruker MAS Unit using compressed air for bearing and drive. The spinning speeds were stable within ± 2 Hz even for extended periods of time (several days). The temperature was controlled by the Bruker temperature unit by heating the bearing air. Spinning speed-dependent temperature corrections, due to air friction, were taken into account when setting the sample temperature, based on calibration with ethylene glycol. The stator angle was carefully adjusted to 54.7° (the magic angle) by maximizing the bromine signal from solid KBr [69].

3.4.3 The experiments

FT-NMR is an extremely versatile technique, as illustrated by the hundreds of pulse sequences, each with different acronyms, described in the literature today. The pulse

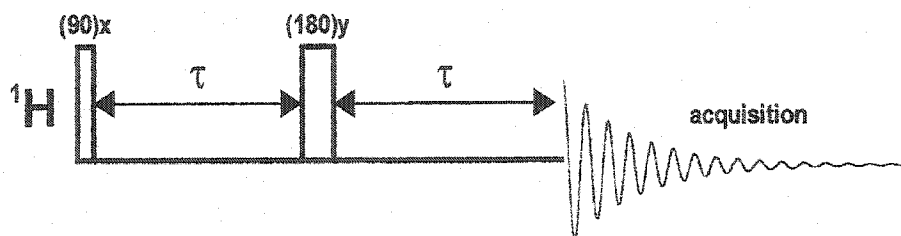


Figure 3.10: Pulse program profile for a simple Hahn echo

sequences are usually composed of blocks for preparation, transfer, manipulation, evolution and finally acquisition of magnetic coherences. In this thesis, numerous sequences were utilized; however, this section describes only four simple experiments with individual purposes. Often, these are combined for more complex experiments which are described in later chapters. In the following, I distinguish the channels involving a strongly magnetic (high sensitivity or high γ) nuclear spin (^1H) and a weakly magnetic (low sensitivity or low γ) spin, referred to as X, which can represent either ^{13}C and ^{15}N in this work.

3.4.3.1 The Hahn echo

The Hahn echo is the simplest of pulse sequences. It consists of the combination of a 90° pulse and a 180° pulse (90° out of phase from one another) on the same channel (see Figure 3.10). With this sequence, transverse magnetization is created by the first pulse, which dephases during the τ delay. The dephasing is reversed by the second pulse and a symmetric rephasing occurs during the second delay thus creating an echo at the end of a second delay τ . In Figure 3.10, the acquisition is initiated at that point. The Hahn echo can be added in any experiment, replacing a single 90° pulse with no delays. It has the advantage of displacing the signal maximum from the end of the pulse, allowing acquisition to begin precisely at the top of the echo. The only difference in terms of signal intensity comes from transverse relaxation (T_2) occurring during the delays; in fact, the Hahn echo is the basic experiment used to measure T_2 relaxation constants. In practice, the Hahn echo also permits the operator to insert commands, such as power-switching, during the τ delays in more complex

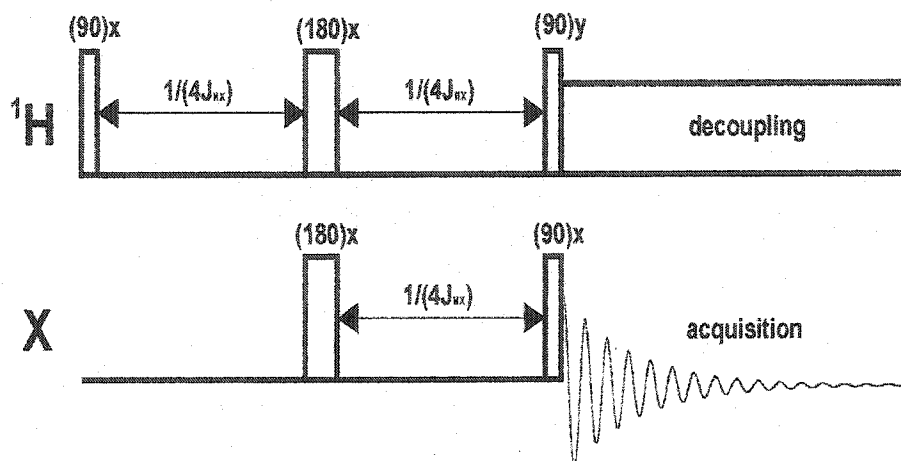


Figure 3.11: The pulse program for the INEPT experiment used in soluble samples for magnetization transfer to the weak nuclei.

pulse programs. For MAS, it was found that spinning side-bands were better when τ matches the rotor period, $(1/\nu_R)$.

3.4.3.2 The INEPT experiment

As its name implies, the “Insensitive Nuclei Enhanced by Polarization Transfer”, or INEPT, pulse sequence allows enhancement of the signal-to-noise ratio of a low-sensitivity nuclear spin such as ^{15}N and ^{13}C through a transfer based on their J-coupling interaction with ^1H . Besides the enhanced signal advantage (of up to $|\gamma(^1\text{H})/\gamma(\text{X})|$), it also allows repetition of the experiment at a faster rate, since high- γ spins tend to have shorter spin-lattice relaxation times. The mechanism of INEPT can be described by following the evolution of the magnetic coherences through product operator formalism [70]. As shown in Figure 3.11, the signal transfer is maximized with delays equivalent to $1/4J_{\text{HX}}$, where J_{IS} is the J-coupling constant between spins I and S. The juxtaposition of an INEPT element with a reversed INEPT element separated by an indirect evolution period constitutes the sequence of the commonly used 2D Heteronuclear Single Quantum Coherence (or HSQC), whereby any directly-bonded HX pairs are correlated according to their chemical shifts in a two-dimensional spectrum [71]. In turn the HSQC experiment is an important component of many 3D-

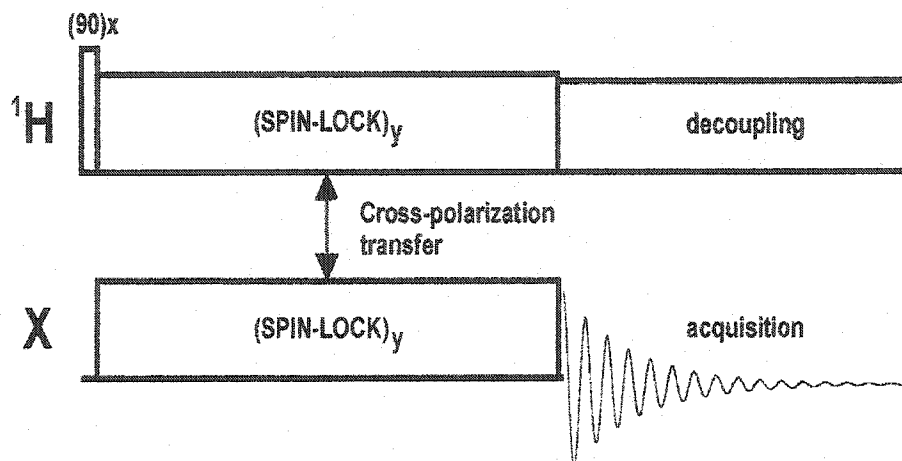


Figure 3.12: The pulse program for the CP experiment which transfers magnetization to weak nuclei in solid samples.

or 4D-experiments. In this thesis, the HSQC was employed within a number of high-resolution experiments on gA in solution to obtain the chemical shift information for ^{15}N and ^{13}C .

3.4.3.3 Cross-polarization transfer

In solid or highly viscous samples, residual orientation-dependent interactions cause the magnetization to experience fast transverse relaxation (short T_2). In the limit where $T_2 \ll 1/J_{HX}$, the INEPT experiment will be useless, since the short-lived magnetization will have irreversibly dephased by the end of the two delays. Fortunately, the disappearance of the indirect spin-spin coupling (J-coupling) is accompanied by the persistence of the direct spin-spin coupling (or dipolar coupling). The same advantages (signal-to-noise, shorter T_1) of the INEPT experiment can thus be implemented for solid samples using the cross-polarization transfer [72, 73] shown in Figure 3.12. Here, the experiment begins with a 90° rf pulse of phase i on the ^1H channel to create transverse magnetization. This is followed immediately by a prolonged pulse of phase $i \pm 90^\circ$. An rf pulse of matching power is applied simultaneously on the X channel. This condition, called the “Hartmann-Hahn” condition [74], enables the exchange of magnetization from the usually large population of hydrogen to the weak

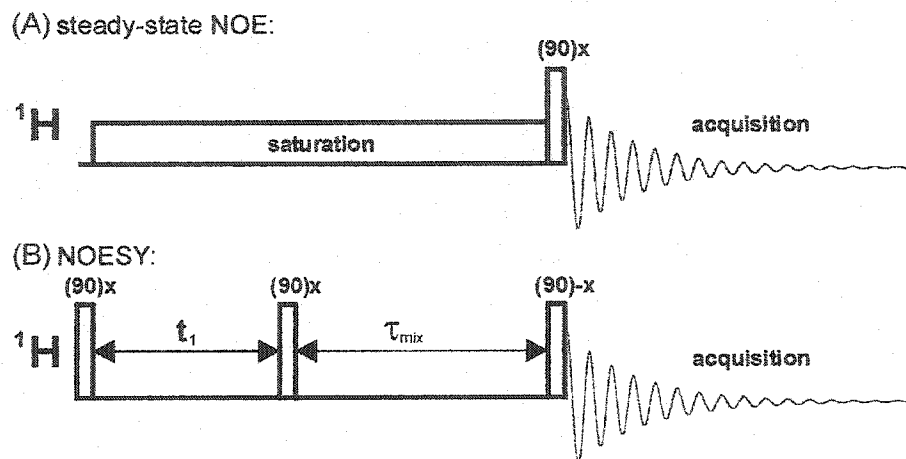


Figure 3.13: Two experiments to measure the nuclear Overhauser effect between dipolar coupled like spins.

spins through their mutual dipolar coupling. Here the advantages are even more pronounced, as the X nuclei typically have a T_1 relaxation constant of tens of seconds compared to only a few seconds for hydrogens. Furthermore, whereas INEPT requires a directly bonded hydrogen, CP only necessitates hydrogens in close proximity, typically within 5 Å. Thus, the magnetization of carbonyl and quaternary carbons or nitric nitrogens are often observed in solids using this approach. In the present work, cross-polarization is the basis of the 2D-CROPSY experiment discussed in Chapter 7.

3.4.3.4 NOE

The wide use of NMR in the structural study of molecules in solution would not be possible without the nuclear Overhauser effect (NOE). The Solomon equations predict that spins (nuclear or electron) in close proximity can undergo cross-relaxation through their mutual dipole-dipole coupling. The efficiency of this cross-relaxation can be related at least qualitatively to internuclear distances, since the spin-spin dipolar interaction is inversely proportional to the third power of the internuclear distance. This effect can be measured in at least two different ways. The first case is the original experiment which measures the steady-state NOE: a single resonance line is selectively irradiated for an extended period of time (typically up to hundreds

of ms), with the effect of equalizing the spin population across its energy transition. Through double- or zero-quantum coherence exchange, either a reduction or an enhancement, respectively, is observed for the population difference of neighboring spins. To observe the transient NOE transfers, one compares the spectra obtained after a simple 90° pulse with and without a trailing selective irradiation on the resonance line of interest (see Figure 3.13(A)). The rate of exchange, measured through peak intensity growth or decline, is inversely related to the average internuclear distance to the sixth power [75].

The 1D steady-state NOE experiment only provides an approximate measure of the distances between the irradiated spin and those in its vicinity. The NOESY experiment, on the other hand, combines the resolution of multidimensional experiments with the cross-relaxation exchange of NOEs. In the homonuclear NOESY experiment (Figure 3.13(B)), transverse magnetization is created and allowed to evolve during the incremental t_1 delay, thus labelling the spin signal with its chemical shift frequency. It is then returned to the longitudinal axis for a duration τ_{mix} to allow cross-relaxation to take place simultaneously between any neighboring pairs of spins after which it is returned to the transverse plane by a third 90° pulse for detection. The appearance of the 2D-NOESY experiment for protein NMR is described in Section 3.4.3.7.

In liquids, the exponential NOE buildup is initially linear for mixing times of the order of 0-300 ms. At longer mixing times, the exchange plateaus and is complicated by spin-diffusion, whereby magnetization is relayed from one spin to another via mutual neighbors. In solids, where homonuclear dipole-dipole interactions are very important, the spin-diffusion limit is attained at much shorter mixing times. In this work, some NOE exchange rates are measured for ^1H in small membrane proteins where the dipolar coupling is considerably diminished through molecular axial diffusion and MAS.

3.4.3.5 $T_{1\rho}$

A number of relaxation time constants (T_1 , T_2 and $T_{1\rho}$) are discussed in this thesis. Whereas the first two are measured with standard inversion-recovery [76] and Hahn

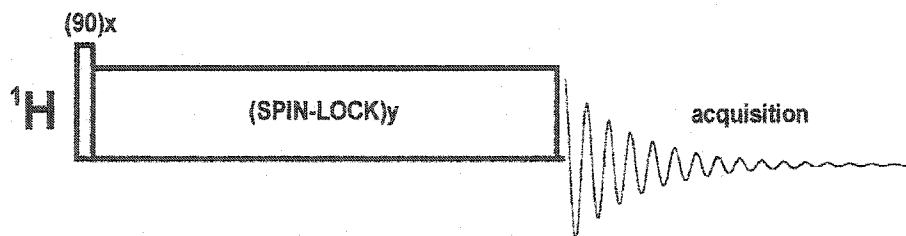


Figure 3.14: The pulse program for $T_{1\rho}$ measurements.

echo experiments, respectively, the time constant $T_{1\rho}$, referred to as the longitudinal or spin-lattice relaxation in the rotating frame, is measured using a prolonged spin-lock (SL) rf pulse. The pulse program shown in Figure 3.14 was used to measure the $T_{1\rho}$ constants for ${}^1\text{H}$ spins. The transverse magnetization is prepared with a 90° pulse and is immediately submitted to a transverse field rotating at or near the Larmor frequency (the SL pulse) for a period of time τ_{SL} . The magnetization is released and immediately observed. The signal exponential decay as a function of time t leads to the direct measurement of $T_{1\rho}$. In Chapter 6, $T_{1\rho}$ time constants are explored for several nuclei in small membrane proteins (${}^1\text{H}$, ${}^{13}\text{C}$ and ${}^{15}\text{N}$), for several field intensities (ω_1) and for several offsets from the Larmor frequency (ω_{off}).

3.4.3.6 Heteronuclear decoupling

${}^{13}\text{C}$ or ${}^{15}\text{N}$ spectra can be complicated by the indirect (liquids) and direct (solids) dipolar coupling, respectively, of the observed nuclei with the ${}^1\text{H}$ in close proximity. Many techniques have been reported in the literature to optimize the “decoupling” of these spectra by the application of spin manipulations on the ${}^1\text{H}$ channel during the acquisition period, as seen during the FID in the pulse sequences of Figure 3.11 and Figure 3.12. These looped sequences, usually composed of trains of pulses with the same intensity but with alternating phases and flip angles, are aimed at coherently averaging away the heteronuclear dipolar coupling for the duration of the acquisition. In solution samples, the WALTZ-16 [77], MLEV-17 [78] or DIPSI-2 [79] sequences were used to eliminate the J-coupling. In static-oriented samples, the simplest method used was continuous wave (CW) decoupling which strongly irradiates the ${}^1\text{H}$ spin

population. The TPPM method [80] which employs (x,-x) phase-alternating pulses with flip-angles near 180° , was used initially in MAS samples, but better results were obtained using the recently proposed decoupling sequence, XiX [81], whereby a similarly (x,-x)-phase-alternating pulse train is chosen with the condition that the pulse duration, t_p , avoids any multiple or simple fraction of the rotor period τ_R . Good decoupling results were obtained with $t_p/\tau_R = 1.85$.

3.4.3.7 High-resolution multidimensional NMR of proteins

The high resolution signal accessible by solution NMR has provided an avenue to study the structure of proteins in precise detail. Depending on the characteristics of the sample, the techniques used today can require complex pulse sequences, correlating signal in 2, 3, or 4 dimensions and involve up to three resonance channels for ^1H , ^{13}C and ^{15}N . However, the overall strategy to study any protein structure can be summarized in three steps, namely (1) the identification of coupled spin-system resonance patterns corresponding to a unique type of amino acid residue, (2) the unambiguous assignment of each resonance pattern to a **specific** residue in the protein and (3) the measurement of a large number of structural restraints involving the assigned spins. Each of these tasks is accomplished by a multidimensional experiment (or a combination thereof) which must provide sufficient resonance dispersion to resolve a majority of the resonance peaks. This section describes the mechanism and the appearance of the spectrum for five basic 2D experiments used in this thesis. These are: the double-quantum filtered correlation spectroscopy (DQF-COSY), the total correlated spectroscopy (TOCSY), the nuclear Overhauser effect spectroscopy (NOESY), the heteronuclear single-quantum correlation spectroscopy (HSQC) and the heteronuclear multiple bond correlation spectroscopy (HMBC). Detailed description of these pulse sequences can be found elsewhere [44, 75].

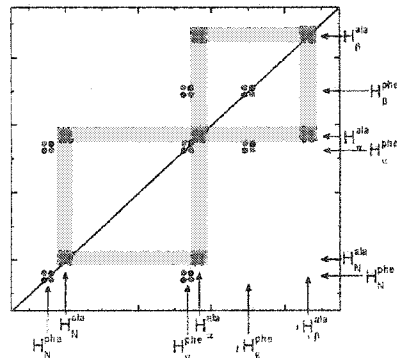
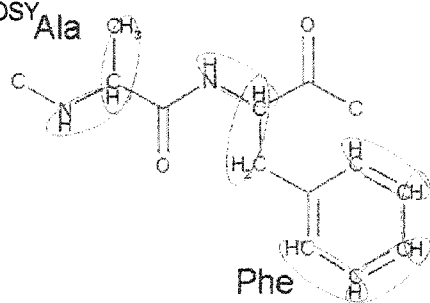
The basic DQF-COSY relates in a 2D spectrum the resonances of ^1H 's which are chemically connected by no more than three bonds. These interact through a weak scalar J-coupling on the order of Hz. For any pair of J-coupled $^1\text{H}_A$ and $^1\text{H}_B$, the spectrum will display positive cross-peaks at the frequency coordinates

Figure 3.15: (Next page) Theoretical spectra for five basic high-resolution 2D NMR experiments applied to the 2-residue peptide Ala-Phe. (A) the 2D-DQF-COSY correlates directly J-coupled ^1H shown by ellipses in the left-hand figure of the peptide. Cross-peaks appear as anti-phase absorptive groups according to the magnitude of the J coupling and centered at the frequency of the interacting spins. For simplicity, higher multiplicity of cross-peaks are not shown. (B) The 2D-TOCSY correlates all spins part of a common J-coupled spin-system. Spin-systems are encircled on the left-hand figure. Any combination of spin pairs within a system results in a corresponding cross-peak on the 2D spectrum. (C) The 2D-NOESY correlates ^1H in close proximity ($<6\text{\AA}$). A vertical strip centered at the frequency of $^1\text{H}_N^{\text{phe}}$ shows the correlation of this spin with all its spatial ^1H neighbors in the Ala-Phe dipeptide. Of importance to the assignment strategies are the cross-peaks between $^1\text{H}_N^{\text{phe}}$ and $^1\text{H}_\alpha^{\text{ala}}$ or $^1\text{H}_N^{\text{ala}}$. (D) The 2D-HSQC and 2D-HMBC experiments correlate covalently-bonded heteronuclear spin pairs. The HSQC and HMBC spectra on the right show the 1- and 2-bond correlation cross-peaks for ^{15}N - ^1H spin pairs. In the spectra of (A), (B) and (D), the correlations specific to the Ala residues are highlighted. For simplicity, the correlations involving the aromatic side chain spin-system were not included in any of the spectra.

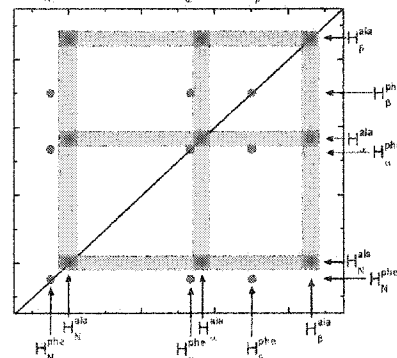
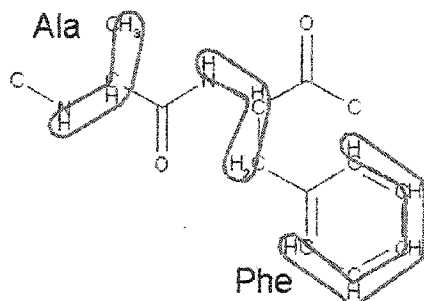
$(\Omega_A \pm \frac{1}{2}J_{AB}, \Omega_B \pm \frac{1}{2}J_{AB})$ and $(\Omega_B \pm \frac{1}{2}J_{AB}, \Omega_A \pm \frac{1}{2}J_{AB})$ and negative ones at coordinates $(\Omega_A \pm \frac{1}{2}J_{AB}, \Omega_B \mp \frac{1}{2}J_{AB})$ and $(\Omega_B \pm \frac{1}{2}J_{AB}, \Omega_A \mp \frac{1}{2}J_{AB})$. Figure 3.15(A) displays the theoretical 2D-DQF-COSY spectrum for a 2-residue peptide Ala-Phe. The correlated path from $^1\text{H}_N$ to $^1\text{H}_\alpha$ and $^1\text{H}_\alpha$ to $^1\text{H}_\beta$ for the Ala residue is highlighted. A similar pattern is obtained for the $^1\text{H}_N$ - $^1\text{H}_\alpha$ - $^1\text{H}_\beta$ system of the Phe residue but with slightly different chemical shifts. The combined information from the number of cross-peaks, the chemical shift and the multiplicity of the cross-peak pattern is often sufficient to identifying the spin-system as belonging to one of the 20 natural amino acid residues. For regions in the spectrum with degenerate or near-degenerate cross-peaks, the spectrum is complicated by the overlap of positive and negative signal. For this reason, this experiment is often complemented with the TOCSY experiment.

The TOCSY experiment employs isotropic mixing which allows magnetization exchange not only between J-coupled spins (as in the DQF-COSY) but also between spin-pairs with one or more J-coupled intermediate partners. For example, a spin-

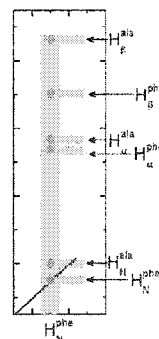
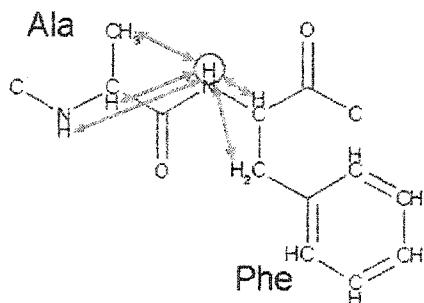
(A) DQF-COSY



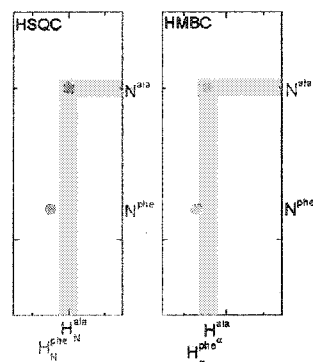
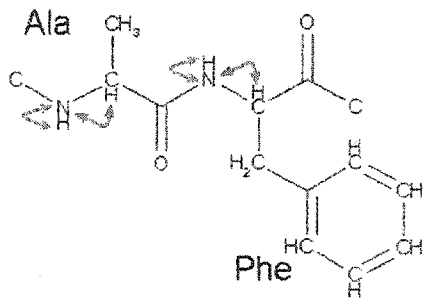
(B) TOCSY



(C) NOESY



(D) HSQC+
HMBC



system with $^1\text{H}_A$ coupled to $^1\text{H}_B$ and with $^1\text{H}_B$ coupled to $^1\text{H}_C$ (but in which $^1\text{H}_A$ and $^1\text{H}_C$ are not necessarily coupled) will yield cross-peaks at 6 positions: (Ω_A, Ω_B) , (Ω_A, Ω_C) , (Ω_B, Ω_A) , (Ω_B, Ω_C) , (Ω_C, Ω_B) , and (Ω_C, Ω_A) . The spectrum for the Ala-Phe dipeptide is simulated in Figure 3.15(B) where two sets of nine aligned peaks (including diagonal peaks) are visible and for which the Ala cross-peak pattern is highlighted. Again, the characteristics of the pattern permit the identification of the spin-system to a specific type of residue. This experiment is often accompanied with a DQF-COSY experiments since difficulties may arise because (a) the spectrum is more heavily crowded, (b) total correlation does not permit to differentiate directly and indirectly J-coupled pairs and (c) peak intensities have a strong dependence on the isotropic mixing time, occasionally leading to cross-peaks with undetectable intensity. The TOCSY and DQF-COSY experiments constitute the basic first step of multidimensional NMR spectroscopy of proteins of identifying all the spin-system (step (1) from above).

As discussed in Section 3.4.3.4, the 2D-NOESY experiments correlates the resonances of spins which undergo cross-relaxation through their dipolar coupling. In the case of spins $^1\text{H}_A$ and $^1\text{H}_B$ in close proximity, the 2D frequency spectrum will show diagonal peaks at the frequency coordinates (Ω_A, Ω_A) and (Ω_B, Ω_B) for non-exchanged magnetization and cross-peaks at (Ω_A, Ω_B) and (Ω_B, Ω_A) for mutually exchanged magnetization. A vertical strip from the theoretical 2D-NOESY experiment for the Ala-Phe peptide is shown in Figure 3.15(C) where a positive cross-peak is observed at the horizontal frequency of $^1\text{H}_N^{\text{Phe}}$ and at the vertical frequency of each of its close neighbors. The intensity of each of these cross-peaks represents a measure of the internuclear distance between the two correlated spins. This experiment is crucial to complete the the spin assignment and the structural elucidation of the protein (step (2) and (3) from above). First, it allows the easy assignment of spin-systems to specific residues in the polypeptide chain according to cross-peaks relating neighboring residues along the protein primary sequence. Cross-peaks found in the “fingerprint” region between the $^1\text{H}_\alpha^i$ and $^1\text{H}_N^{i+1}$ or between $^1\text{H}_N^i$ and $^1\text{H}_N^{i+1}$ (where i represents a residue position) are most commonly used. Second, every cross-peak represents a

distance restraint which is used towards obtaining and refining the overall protein structure. The NOESY spectrum can easily yield hundreds of these restraints in a single experiment.

Heteronuclear multidimensional experiments such as the HSQC and HMBC allow the direct correlation of covalently bonded heteronuclear spin pairs, most commonly ^1H - ^{13}C or ^1H - ^{15}N . The magnetization is exchanged through the one- or two-bond scalar coupling, on the order of tens of Hz. The simple ^1H - ^{15}N HSQC and ^1H - ^{15}N HMBC spectra of the Ala-Phe peptide are displayed in Figure 3.15(D), where each residue is represented by a single cross-peak at the horizontal frequency of the ^1H and the vertical frequency of ^{15}N . The cross-peak for the Ala H-N pairs are highlighted. Given the correct assignments of the ^1H according to the homonuclear experiments already described, these experiments facilitate the assignment of the coupled ^{13}C and ^{15}N resonances. Heteronuclear experiments are most useful in combination with the experiments described above by creating additional peak dispersion through an extra frequency dimension.

These 2D experiments were sufficient to carry out the solution work applied to a small polypeptide, gA, described in Chapter 4. It should be noted however that modern high-resolution NMR uses much more complex experiments, most of which are beyond the scope of this thesis, to solve structures of proteins up to several hundreds of kDa [82].



- *Tout acte de création est d'abord
un acte de destruction.*

- Pablo Picasso

Heteronuclear high-resolution NMR on gramicidin A in solution

4.1 Introduction

One of the early observations about the structure of gA was that it is sensitive to its environment. Results from molecular modeling, CD and IR spectroscopy and later high-resolution NMR and X-ray crystallography have shown that there exist two major folding patterns for gA, namely the two-strand double-helix form and the single-strand end-to-end helix form. These structures can be subdivided into stable helical conformations with different handedness, stagger and N-to-C direction (see reviews [39, 83, 84]). Although it is still not clear whether all forms have active channel functions, studies have shown that structural flexibility is necessary for gA to conformationally interconvert rapidly between environments to carry out its proposed bactericidal and signaling functions. An interesting artefact from this property is the structural “memory” of gA, whereby the membrane active channel form can fold more naturally from its extended form in TFE or dioxane than from its intertwined form in alcohols [68].

In the effort to characterize the individual structures of gA, NMR has been an indispensable tool. The NMR literature has reported numerous assignments and structural studies for this molecule in membrane mimetic organic solvents such as dioxane [85], ethanol [86, 87], MeOH/CHCl₃ (with CsCl salt) [53], TFE [88], ethanol/benzene [89], MeOH (with CaCl₂ salt) [90], as well as in detergent micelles formed by SDS [91]

and DPC [92]. Because of the simplicity and small size of gA, sufficient dispersion can generally be obtained from ^1H NMR alone and all proposed solution-state high-resolution NMR structures have relied solely on ^1H - ^1H through-bond or through-space correlations.

From the standpoint of solid-state NMR, although gA represents one of the simplest membrane proteins, it poses a complex structural problem. A complete refined structure, suggesting the helical dimer form proposed by Urry [93], was obtained for the first time solely based on orientation constraints from NMR measurements on individually introduced isotopic labels [24]. This ground-breaking but tedious endeavor took the better part of a decade to accomplish. While novel approaches are being developed to study poorly soluble biological systems by solid-state NMR, at least two important considerations have become clear from these developments: (1) These methods will rely heavily on isotopic labeling (^{13}C , ^{15}N and perhaps ^2H) to enhance signal dispersion in multidimensional experiments and increase the number of available interaction constraints, and (2) assignment, structural constraint refinement, and modeling strategies will at least at first be inspired by the established methods of high-resolution solution NMR. This type of endorsement from solution NMR for solid-state NMR results has already been applied elsewhere [29, 30, 94]. This chapter presents a number of heteronuclear high-resolution NMR experiments on ^1H , ^{13}C and ^{15}N of gA, in different stable forms. These will be used in later chapters to guide the interpretation of the solid-state NMR results.

4.2 Sequential ^1H assignments of gA in TFE

A complete set of ^1H assignments were obtained from a combination of high-resolution multidimensional experiments [70, 75] for gA solubilized in TFE- d_2 at a concentration of 10 mg/ml at 40 °C. To assign unambiguously all ^1H chemical shifts, one must 1) identify a complete list of ^1H chemical shifts, 2) correlate these chemical shifts into spin-systems according to 3-bond J-coupling networks, and 3) relate the spin-systems using close range through-space interactions according to the known primary sequence.

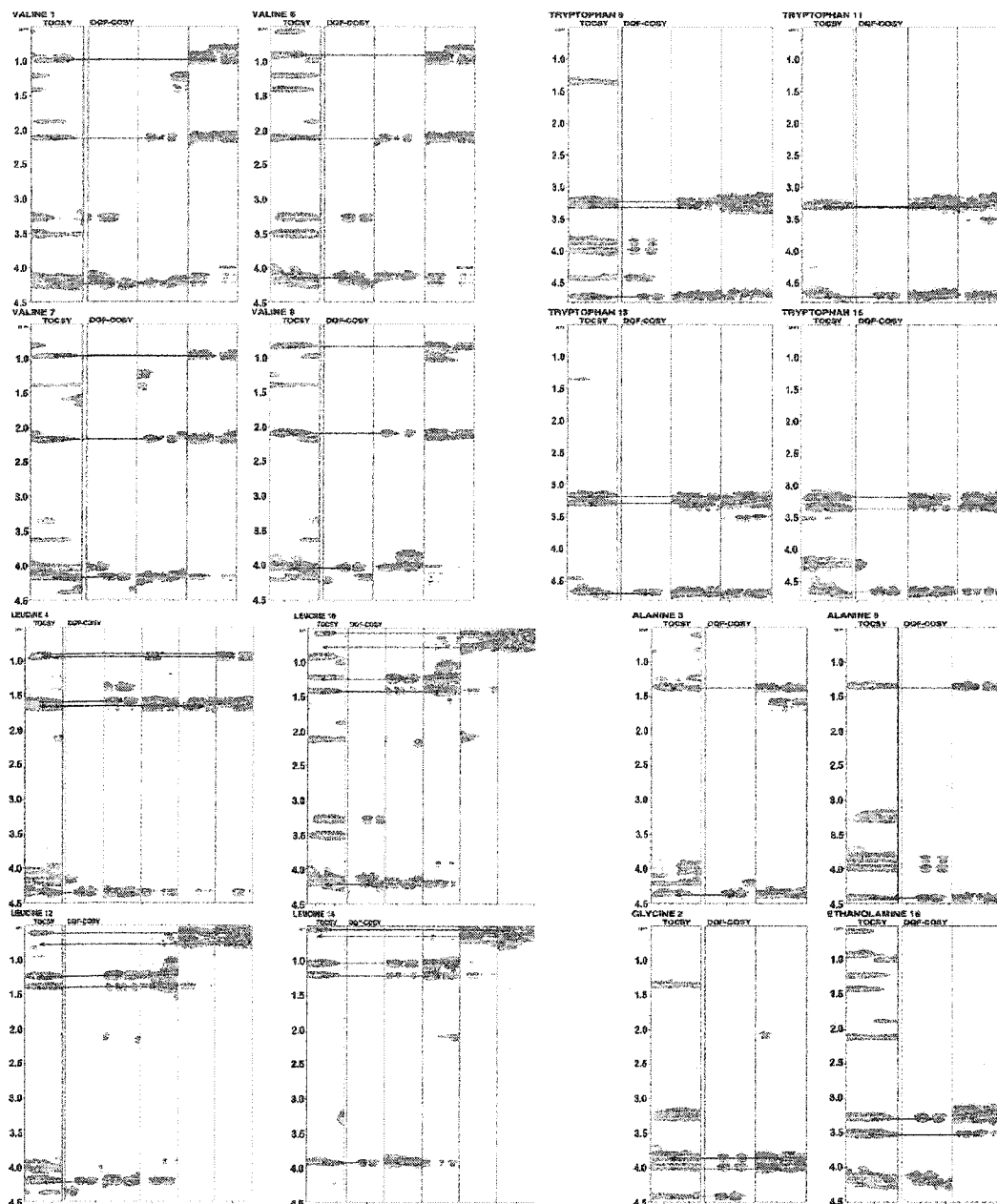


Figure 4.1: Aligned 2D vertical strip plots for the TOCSY (MLEV-17) experiment (taken at the H_N frequency) and for the DQF-COSY experiment (taken at the H_N , H_α and/or H_β and/or H_γ frequencies) showing the shifts for the 16 ^1H resonance spin systems of gA in TFE at 40 $^\circ\text{C}$. The peak correspondence for both experiments are shown with the double-headed arrows. The sequential identification of these spin systems were obtained later with the primary sequence connectivities from the ROESY experiment (see Figure 4.2). The shifts assignments are summarized in Table 4.1. The experimental setup parameters are listed in Section 4.8.

The chemical shifts for the 24 spin systems of gA, corresponding to the backbone- and sidechain networks of the 16 amino acid residues and to the 8 aromatic spin systems belonging to the four Trp indole rings, were identified using a 2D-DQF-COSY [95, 96] and a 2D-TOCSY [78, 97] with a MLEV-17 coherence mixing times of 100 ms. No further mixing time for the latter experiment were necessary to identify any missing or ambiguous assignments. Figure 4.1 displays the peak positions and correspondence (arrows) in both experiments for four Val, four Trp, four Leu, two Ala, one EAM and one Gly. Among these peaks, the total correlation experiment at the amide frequencies is missing only the four Leu H_γ cross-peaks due to the chosen mixing time; the chemical shift for these nuclei are however identified elsewhere on the TOCSY spectrum and confirmed by the DQF-COSY. The setup parameters for these experiments are listed in Section 4.8.

The unique sequential assignment of these spin systems was obtained by identifying the NOE interaction between neighboring H_α^i and H_N^{i+1} for consecutive amino acid residues along the known primary sequence. Likewise, the Trp aromatic spin systems were associated with its corresponding backbone spin system using the NOE between the Trp H_α or H_β with any one of the aromatic hydrogens ($H_{N\epsilon1}$ - $H_{\delta1}$ and $H_{\epsilon3}$ - $H_{\zeta3}$ - $H_{\eta2}$ - $H_{\zeta2}$). Because of unfavorable correlation times for this 2 kDa molecule in solution, the conventional NOESY experiment [98, 99], which relies on the cross-relaxation of magnetization, showed poorly detectable cross-peaks [100]. To alleviate this problem, the equivalent rotating-frame cross-relaxation experiment, called CAMELSPIN or ROESY [101, 102], was employed because of its sensitivity to different time scales. The assignment sequence is demonstrated in Figure 4.2 in which strips cut out from the 2D plots at the same H_N frequency region for both the ROESY (R) and the TOCSY (T) experiments are juxtaposed to show the correspondence of an H_α^i cross-peak with an H_N^i in the TOCSY spectrum and with an H_N^{i+1} in the ROESY spectrum. The results of these assignment strategies are summarized in Table 4.1, referenced to the position of the TFE methylene peak at 3.88 ppm.

For gA in TFE, no substantial long-range NOE cross-peaks were identified. Also, the spectra displayed only a narrow distribution of the H_N (7.02–7.61 ppm) and

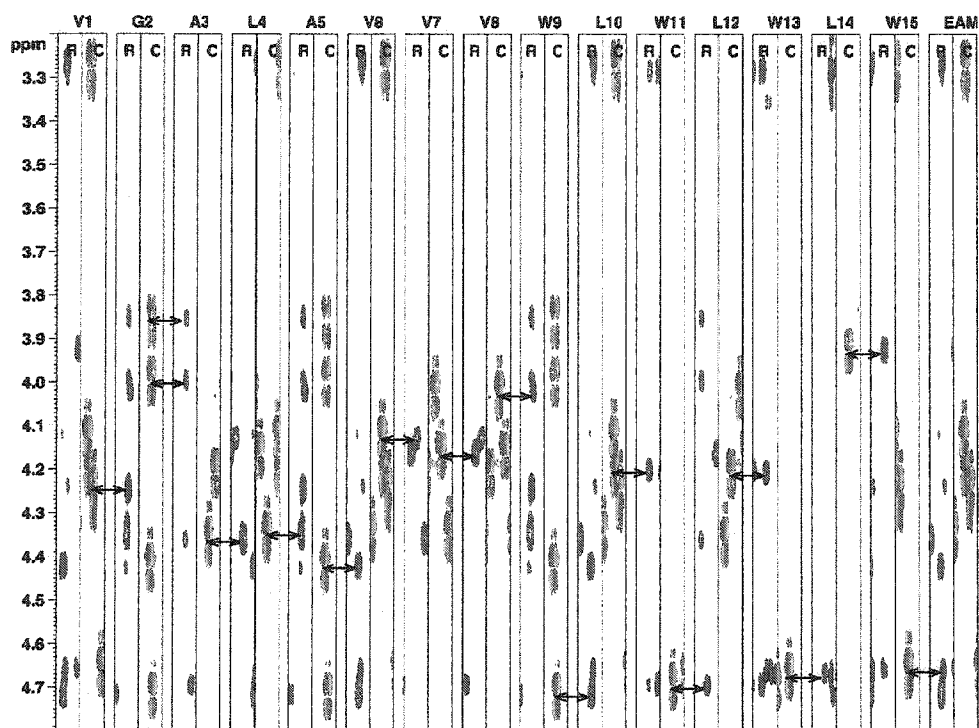


Figure 4.2: Aligned 2D vertical strip plots of the H_N - H_α fingerprint region of the DQF-COSY (C) and ROESY (R) experiments on gA in TFE at 40 °C. The order of the juxtaposed plots follows the primary sequence of the polypeptide to highlight the correspondence of the DQF-COSY H_α^i - H_N^i cross-peaks with the ROESY H_α^i - H_N^{i+1} cross-peaks in adjacent residues (arrows). The experimental setup is summarized in Section 4.8.

H_α (3.83–4.68 ppm) chemical shifts. These observations suggest that the gA chain adopts an extended form with a low level of secondary structure [103]. It is not clear from these results whether gA adopts a preferred extended configuration or if it rapidly isomerizes through a number of structures. Even the information on the ϕ torsional dihedral angle measurable through the scalar 3-bond J-coupling between H_N^i and H_α^i according to the Karplus calibration curves [104, 105] does not settle this question. Scalar couplings were measured between 3–8 Hz for 12 of the 16 residues in the fingerprint region of the DQF-COSY spectrum. These fall in the range of ϕ angles between -150° and 150° , expected for an extended conformation, but may also be interpreted as reflecting the average splitting conferred by motional averaging through multiple conformations.

It is important to compare these results with the assignment and interpretation suggested by Abdul-Manan and Hinton [88], for which gA was also solubilized in TFE. Only a small subset of the 1H assignments do not agree within 0.1 ppm of their assignments (5/16 of the H_N , 0/18 of the H_α , 5/24 of the H_β). The relative distribution of the cross-peaks in the key regions showed good correspondence in both DQF-COSY spectra, with the highest shifts occurring for residues with largest flexibility such as the four Leu and the first two N-terminal residues. Another important difference is seen in the NOESY/ROESY spectra. Contrary to the results of Abdul-Manan, the NOESY spectrum (300 ms) displayed no usable cross-peaks, and the ROESY spectrum did not show any major cross-relaxing peaks other than the aforementioned H_N^{i+1} cross-peaks with H_α^i and H_α^{i+1} . However, these differences can be attributed to differences in the sample conditions. Their sample was more concentrated (100 mg/mL) and was maintained at a lower temperature (room temperature); both these conditions will favor slower correlation times and oligomerization. Overall, however, the paucity of cross-relaxing peaks and the small chemical shift distribution of 1H spins strongly suggests that gA assumes a poorly folded configuration in TFE. The isomerization of this extended/random form into a helical folded form is energetically favourable and supports the solvent history properties of gA mentioned above.

Table 4.1: ^1H assignments for gA in TFE (10 mg/ml) at 40 °C based on the 2D-TOCSY, DQF-COSY and ROESY experiments (referenced to the TFE methylene hydrogen resonance at 3.88 ppm).

	Res.	H_N	H_α	H_β	H_γ	H_δ	Others		
0	For						H_{form} 8.080		
1	Val	7.175	4.211	2.083	0.963				
					0.963				
2	Gly	7.441	3.825						
			3.967						
3	Ala	7.364	4.328	1.354					
4	Leu	7.244	4.316	1.566	0.857	0.882			
				1.645		0.919			
5	Ala	7.445	4.389	1.334					
6	Val	7.199	4.094	2.081	0.884				
					0.911				
7	Val	7.276	4.133	2.138	0.931				
					0.931				
8	Val	7.301	3.993	2.049	0.779				
					0.801				
9	Trp	7.431	4.684	3.171			$\text{H}_{\epsilon 1}$ 8.90	$\text{H}_{\epsilon 3}$ 7.49	$\text{H}_{\eta 2}$ 7.17
				3.262			$\text{H}_{\delta 1}$ 7.00	$\text{H}_{\zeta 3}$ 7.07	$\text{H}_{\zeta 2}$ 7.36
10	Leu	7.194	4.170	1.192	0.748	0.554			
				1.395		0.554			
11	Trp	7.608	4.661	3.250			$\text{H}_{\epsilon 1}$ 8.90	$\text{H}_{\epsilon 3}$ 7.56	$\text{H}_{\eta 2}$ 7.18
				3.266			$\text{H}_{\delta 1}$ 7.00	$\text{H}_{\zeta 3}$ 7.10	$\text{H}_{\zeta 2}$ 7.37
12	Leu	7.339	4.174	1.217	0.713	0.586			
				1.354		0.586			
13	Trp	7.556	4.637	3.127			$\text{H}_{\epsilon 1}$ 8.87	$\text{H}_{\epsilon 3}$ 7.53	$\text{H}_{\eta 2}$ 7.17
				3.249			$\text{H}_{\delta 1}$ 6.98	$\text{H}_{\zeta 3}$ 7.07	$\text{H}_{\zeta 2}$ 7.36
14	Leu	7.022	3.894	1.012	0.640	0.528			
				1.185		0.528			
15	Trp	7.139	4.627	3.156			$\text{H}_{\epsilon 1}$ 8.90	$\text{H}_{\epsilon 3}$ 7.55	$\text{H}_{\eta 2}$ 7.18
				3.326			$\text{H}_{\delta 1}$ 7.00	$\text{H}_{\zeta 3}$ 7.10	$\text{H}_{\zeta 2}$ 7.37
16	EAM	7.189	3.244	3.487					
			3.244	3.487					

4.3 Sequential ^{13}C assignments of gA in TFE

To obtain the complete set of ^{13}C assignments of gA in TFE (10 mg/ml) at 40 °C, a combination of three high-resolution heteronuclear experiments based on the scalar J-coupling between ^1H and ^{13}C was carried out. The one-dimensional DEPT (Distortionless Enhancement by Polarisation Transfer) experiment [106] yields a sensitivity-enhanced ^{13}C spectrum based on the transfer of coherence from ^1H to ^{13}C through their 1-bond J-coupling. To assist in peak assignments, delays can be adjusted to reveal the hydrogen multiplicity such that tertiary (CH) and primary (CH_3) carbon resonances are identified as positive peaks, whereas secondary (CH_2) carbon peaks are negative [106]. The HSQC experiment [71] is a 2D experiment which uses two INEPT transfers [107] (see Chapter 3) to correlate the frequency of a ^{13}C spin with its covalently-bonded ^1H spin. The majority of the ^{13}C assignments can be obtained from the combination of DEPT and HSQC, however quaternary and carbonyl carbons usually elude these spectra because they have no directly-bonded ^1H spins. The 2D experiment HMBC (heteronuclear multiple bond correlation spectroscopy) [108] makes use of longer range 2- or 3-bond J-couplings to reveal these carbons and was employed to assign all carbonyl carbons as well as the $\text{C}_{\gamma 1}$, $\text{C}_{\delta 2}$ and $\text{C}_{\epsilon 2}$ of the four tryptophan residues. This experiment also helped to confirm the assignments from the crowded regions of the HSQC.

As examples, Figure 4.3 illustrates the use of these three experiments, along with the pre-assigned ^1H TOCSY spectrum, to make the ^{13}C assignments for the four Val and four Leu residues of gA. The upper three regions show the side-chain spin system (H_α - H_β - H_γ -etc) frequency alignment at the H_N frequency (horizontal line) of the TOCSY spectrum. By matching the ^1H frequencies (vertical lines) on the HSQC and HMBC spectra, the covalently-bonded and neighboring ^{13}C cross-peaks are identified. The projected 1D-DEPT experiment helps confirm the nature of the carbon. Table 4.2 lists the complete assignments for gA based on the analysis of these experiments and referenced to the methylene carbon resonance of TFE at 126.3 ppm. The parameters used for these experiments are summarized in Section 4.8.

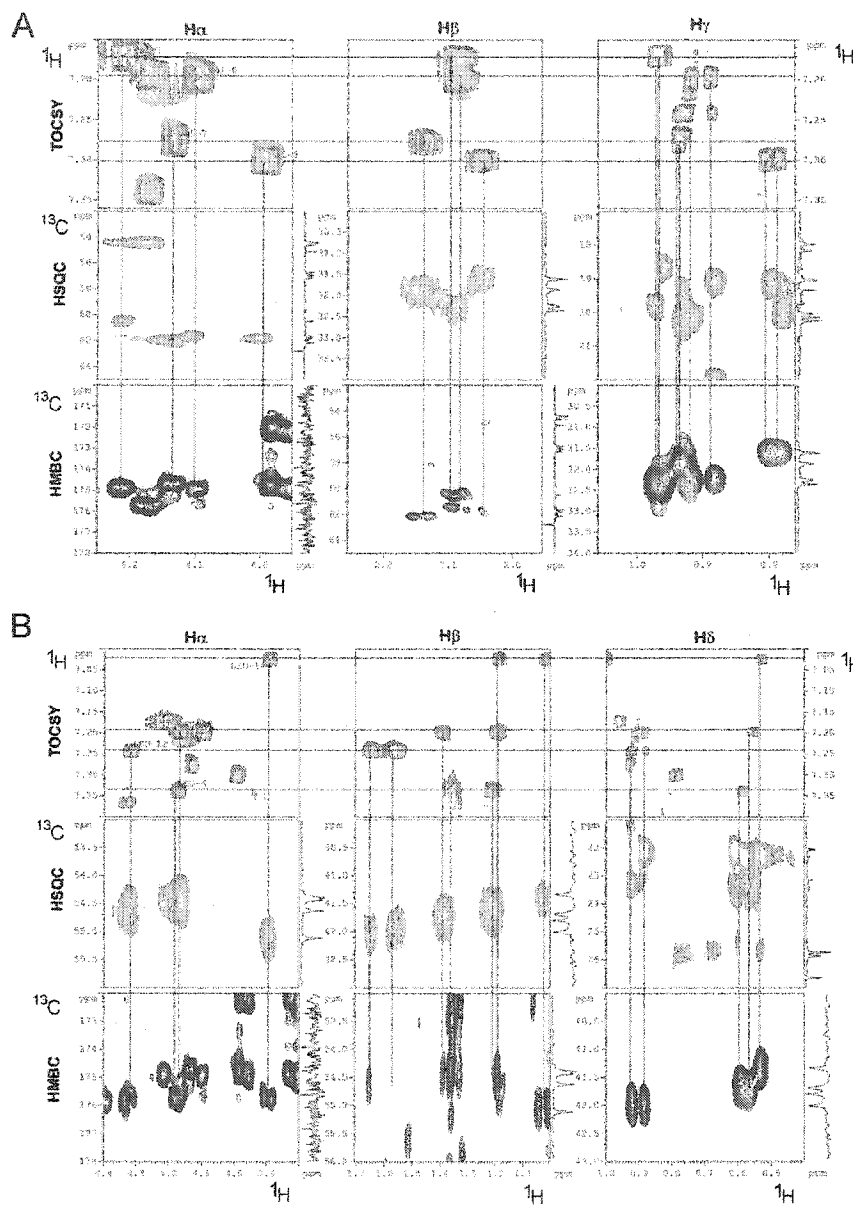


Figure 4.3: Example of ^{13}C assignment strategy for the four Val (A) and four Leu (B) residues using ^1H - ^{13}C HSQC and HMBC of gA in TFE. Horizontal lines in the three aligned TOCSY regions are positioned at the $^1\text{H}_N$ frequency of the four Val (A) and Leu (B) and intersect cross-peaks for the $^1\text{H}_\alpha$ (left), the $^1\text{H}_\beta$ (middle) and the $^1\text{H}_\gamma$ / $^1\text{H}_\delta$ (right) of the same spin system. Vertical lines intersect the cross-peaks in the HSQC and the HMBC spectra corresponding to the correlated ^{13}C resonances. These are assigned based on consistency with all 2D experiments and with the 1D-DEPT experiment shown as projections to the right of each of the ^{13}C regions. Complete ^{13}C assignments are summarized in Table 4.2. For experimental parameters, see Section 4.8.

Table 4.2: ^{13}C assignments for gA in TFE (10 mg/ml) at 40 °C based on the 1D-DEPT, 2D-HSQC and 2D-HMBC experiments (referenced to TFE methylene at 126.3 ppm).

	Res.	C'	C $_{\alpha}$	C $_{\beta}$	C $_{\gamma}$	C $_{\delta}$	Others
0	For	165.50					
1	Val	174.90	60.48	32.22	18.64 19.80		
2	Gly	175.04 172.05?	44.34				
3	Ala	175.83	51.69	17.97			
4	Leu		54.63	41.97	26.64	22.16 23.34	
5	Ala	179.89	51.57	18.14			
6	Val	174.95	61.64	32.22	19.06 20.13		
7	Val	174.72	61.92	31.84	19.42 20.31		
8	Val	174.88 172.07?	61.83	31.59	19.08 20.04		
9	Trp	175.02	56.75	28.89			C $_{\gamma 1}$ 111.44 C $_{\delta 2}$ 129.19 C $_{\zeta 2}$ 113.50 C $_{\epsilon 3}$ 120.14 C $_{\delta 1}$ 125.36 C $_{\epsilon 2}$ 138.65 C $_{\eta 2}$ 124.06 C $_{\zeta 3}$ 121.46
10	Leu	175.77	54.52	41.66	25.87	22.39 23.52	
11	Trp	175.04	57.01	28.89			C $_{\gamma 1}$ 111.44 C $_{\delta 2}$ 129.19 C $_{\zeta 2}$ 113.50 C $_{\epsilon 3}$ 120.14 C $_{\delta 1}$ 125.36 C $_{\epsilon 2}$ 138.65 C $_{\eta 2}$ 124.06 C $_{\zeta 3}$ 121.46
12	Leu	175.77	54.48	41.77	25.73	22.09 23.50	
13	Trp	175.50	56.88	29.19			C $_{\gamma 1}$ 111.44 C $_{\delta 2}$ 129.19 C $_{\zeta 2}$ 113.50 C $_{\epsilon 3}$ 120.14 C $_{\delta 1}$ 125.36 C $_{\epsilon 2}$ 138.65 C $_{\eta 2}$ 124.06 C $_{\zeta 3}$ 121.46
14	Leu	175.77	55.12	41.31	25.73	22.31 23.38	
15	Trp	175.34	56.75	28.75			C $_{\gamma 1}$ 111.44 C $_{\delta 2}$ 129.19 C $_{\zeta 2}$ 113.50 C $_{\epsilon 3}$ 120.14 C $_{\delta 1}$ 125.36 C $_{\epsilon 2}$ 138.65 C $_{\eta 2}$ 124.06 C $_{\zeta 3}$ 121.46
16	EAM		44.10	62.79			

4.4 Sequential ^{15}N assignments of gA in three different solvents

Heteronuclear assignments for the ^{15}N spins of gA under three different solvation conditions are presented in this section. The assignment strategy is more straightforward for this nucleus. First, there are only 20 nitrogen spins in gA, sixteen of which are part of the backbone amide chain, with a relatively small chance of overlap. Also, these nitrogen nuclei are covalently bound to a single hydrogen, making their chemical shifts easy to identify, based on their direct correlation with the already-assigned $^1\text{H}_\text{N}$, in a single HSQC experiment. Finally, although this nucleus is naturally poorly abundant, 100% ^{15}N -labelled gA (see Chapter 3, p. 32) was prepared, allowing for very rapid experimentation with abundant NMR signal.

Figure 4.4(A) shows the ^1H - ^{15}N HSQC spectrum for ^{15}N -gA in the extended monomer form dissolved in the membrane mimetic solvent TFE- d_2 at a concentration of 2 mg/mL with the sample temperature maintained at 27 °C. In Figure 4.4(B), gA is dissolved in 1:1 (v/v) of MeOH- CHCl_3 at a concentration of 57 mg/mL. An equal concentration of CsCl is also added to the solution to elicit the formation of the antiparallel right-handed double-helical dimer (7.2 residues/turn) proposed by Arseniev *et al.* [53]. The sample temperature was maintained at 27 °C. Finally, the HSQC spectrum for ^{15}N -gA under the same conditions as described by Arseniev *et al.* [53] is presented in Figure 4.4. For this sample, a gA suspension in TFE was diluted ten fold to a final concentration of 5 mM (*ca.* 10 mg/mL) in a pH 6.5 potassium phosphate buffer (50 mM) containing 500 mM SDS- d_25 . The final protein/detergent molar ratio was 1/100 and the sample temperature was set at 55 °C. Under these conditions, gA folds into the active channel conformation proposed by Urry [93], described as single right-handed helical N-to-N dimer with a pitch of 6.3 residues/turn pitch. Since the ^1H chemical shifts were reported previously in the literature, the ^{15}N assignments are straightforward for all three forms of gA. The experimental conditions for the three spectra shown in Figure 4.4 are shown in Table 4.4 of Section 4.8. The chemical shift assignments for all 20 nitrogen spins of gA are given in Table 4.3 and are simply

Table 4.3: ^{15}N assignments for gA in TFE, in a MeOH- CHCl_3 mixture with CsCl and a SDS micellar dispersion. The assignments are based on the results of ^1H - ^{15}N HSQC experiments as shown in Figure 4.4. For comparison, all spectra were referenced with respect to the glycine chemical shift at 114.2 ppm.

		SDS (1/100)	TFE	MeOH/ CHCl_3 (+CsCl)
	Res			
1	Val	130.1	129.8	120.9
2	Gly	114.2	114.2	114.2
3	Ala	129.9	126.8	128.5
4	Leu	126.7	124.3	123.3
5	Ala	129.1	128.7	130.7
6	Val	124.2	128.9	132.1
7	Val	126.7	125.2	122.8
8	Val	126.4	125.5	125.2
9	Trp	131.8	127.5	132.0
10	Leu	132.0	120.7	128.4
11	Trp	128.6	126.7	129.5
12	Leu	127.5	129.1	127.9
13	Trp	126.3	126.1	131.4
14	Leu	126.2	129.6	130.8
15	Trp	127.8	125.7	132.4
16	EAM	116.9	118.6	123.3
	indole 1	130.3 (9)	129.4	132.6
	indole 2	129.9 (11)	129.4	133.5
	indole 3	130.0 (13)	129.4	132.7
	indole 4	130.5 (15)	129.4	131.9

referenced to one another with the glycine peak at 114.2 ppm set for the gA/SDS sample against external ^{15}N -formamide.

It is interesting to notice that the structural variability of gA under different conditions is apparent from the chemical shift dispersion of the ^1H spins [103], but not from the ^{15}N chemical shift range, which was spread over 15 ppm in every case. These spectra will be used in Chapter 7 (p. 165) to search for a matching chemical shift distribution pattern with the proposed CROPSY experiment [94] of ^{15}N -gA in DMPC under MAS conditions. A close match will permit a tentative assignment of the resonances in the membrane sample without relying on the identification of the ^1H spin systems.

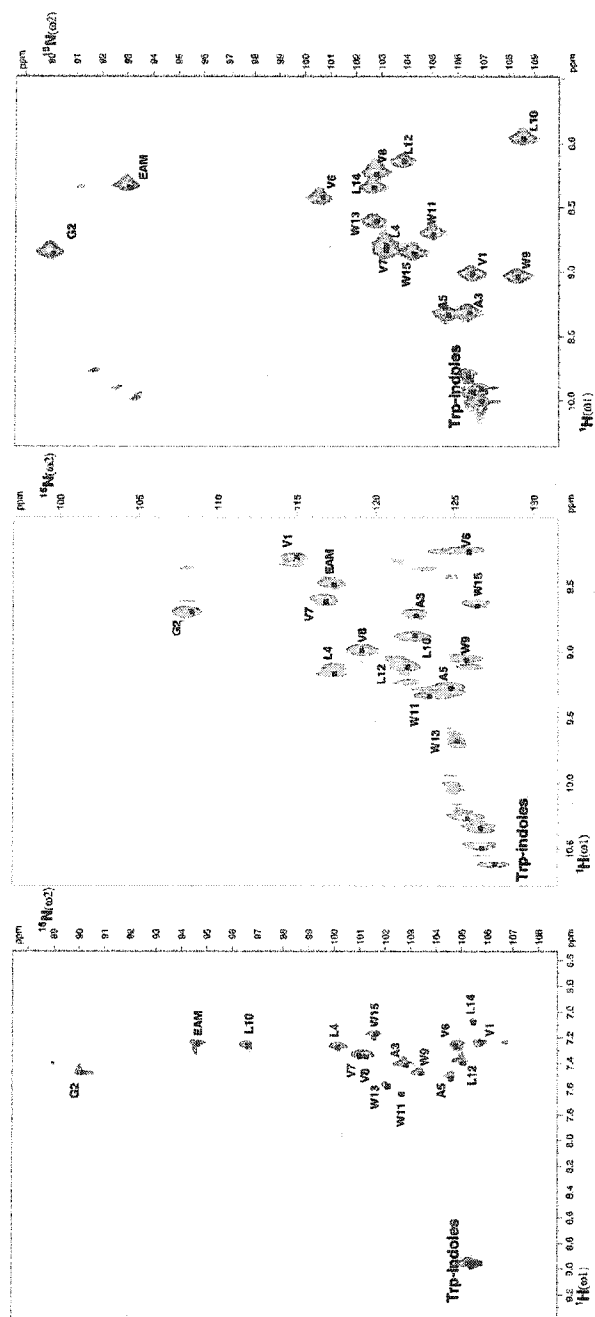


Figure 4.4: ^1H - ^{15}N HSQC of ^{15}N -gA: (A) 2 mg/ml in TFE-d₂ at 27 °C, (B) 57 mg/mL (0.03 M) in MeOH/ CHCl_3 (1:1 v/v) with an equimolar concentration of CsCl salt at 27 °C and (C) 10 mg/mL in a 100 mM SDS solution in a potassium phosphate buffer (pH 6.5, 50 mM) at 55 °C. Experimental acquisition and processing parameters are given in Section 4.8.

4.5 $^1\text{H}_N$ - $^1\text{H}_x$ restraints from NOESY-HSQC experiments

In Chapter 8, a novel experiment is described whereby the $^1\text{H}_N$ resonances, which are resolved through their dipolar correlation with the covalently-bonded ^{15}N , are transferred via their NOE interaction to neighboring ^1H . This is done in the hope of establishing a method of identifying internuclear distance restraints for small membrane polypeptides embedded in a fluid membrane bilayer. This experiment is closely related to the high-resolution 3D-NOESY-HSQC solution experiment [109], which relies first on the NOE transfer (through-space) from $^1\text{H}_x \rightarrow ^1\text{H}_N$ for internuclear distance restraint measurements and, secondly, on the scalar 1-bond J-coupling transfer of magnetization from $^1\text{H}_N \rightarrow ^{15}\text{N}$ for resolution enhancement.

In contrast to a 2D-NOESY, the 3D-NOESY-HSQC experiment provides a third correlation dimension for improving resolution, but with the drawback of fewer restraints since they must strictly involve at least one $^1\text{H}_N$. Using only these restraints will necessarily lead to a final structure of lesser quality; however, since the majority of restraints involve nuclei directly attached to the backbone, it is expected that the overall fold of the polypeptide will still be discerned. In preparation for the CROPSY-NOESY experiment in membranes, the $^1\text{H}_N \rightarrow ^1\text{H}_x$ restraints obtained for a soluble sample of gA/SDS (in the active channel form) are used to calculate its structure.

Figure 4.5 shows the results of a 3D ^1H - ^{15}N -NOESY-HSQC on gA/SDS with a cross-relaxation mixing time of 75 ms during the NOESY segment. Peak positions are defined in three frequency dimensions with coordinates $(\omega_1^H, \omega_2^N, \omega_3^{H_N})$. The intensity of the cross-peaks, displayed by colour-coded contour volumes, represents the magnitude of the cross-relaxation and is related to the internuclear distance between the two hydrogen nuclei defined by the frequencies ω_1^H and $\omega_3^{H_N}$. To identify cross-peaks, Figure 4.6 shows 16 one-dimensional strips extracted from the 3D-spectrum at the coordinates $(\omega_1^N, \omega_2^{H_N})$ for each residue. The boxed cross-peak in each strip represents the expected $\text{H}_\alpha^i \leftrightarrow \text{H}_N^{i+1}$ connectivities. This 40-hour experiment was only performed once at a mixing time of 75 ms. Since the extra resolution was not absolutely nec-

essary for gA in solution, the conventional 2D-NOESY experiment was performed at four different mixing times, 100 ms, 150 ms, 200 ms and 300 ms, without the third ^{15}N dimension.

A total of 90 well-resolved NOEs were identified involving at least one H_N . Those were categorized into three qualitative strengths: 22 “strong” cross-peaks, 42 “medium” cross-peaks, and 26 “weak” cross-peaks. These distance restraint ranges were calibrated according to the NOE growth curve assigned for the two geminal α -hydrogens of the glycine (1.8 Å). The cross-peaks were also classified according to the structural information that they provided. There were 32 intra-residue cross-peaks (i to i), 32 inter-residue cross-peaks (i to i+1), 23 inter-loop cross-peaks (i to i+5, i+6 or i+7) and finally 3 inter-monomer cross-peaks. These results are summarized in Figure 4.7, where the four classes of structural connectivities are shown by the length of the bar between the spatially neighboring residues and the maximum intensity is shown as the width of each bar.

4.6 Structure interpretation from ^1H - ^{15}N NOESY-HSQC experiments

The determination of protein structure based on high-resolution NMR data composed mainly of distance restraints is a complex problem [110]. The challenge resides in arriving at correct sets of atom coordinates which satisfy simultaneously all NMR restraints without resorting to unfavorable deviations from typical bonded and non-bonded interaction geometries. To this end, two approaches have been put forward to assist in the convergence towards coherent structures: distance geometry and simulated annealing [111, 112]. In the former, a set of crude structures for an n -atom molecule is obtained by translating an $n \times n$ matrix of internuclear distances in which all elements are simultaneously set to respect the upper- and lower-bounds dictated by all geometrical restraints; this procedure, termed “embedding”, is often applied only to a subset of atoms from within the protein principal chains and is used as a starting point for the dynamic simulated annealing [111]. In this latter method,

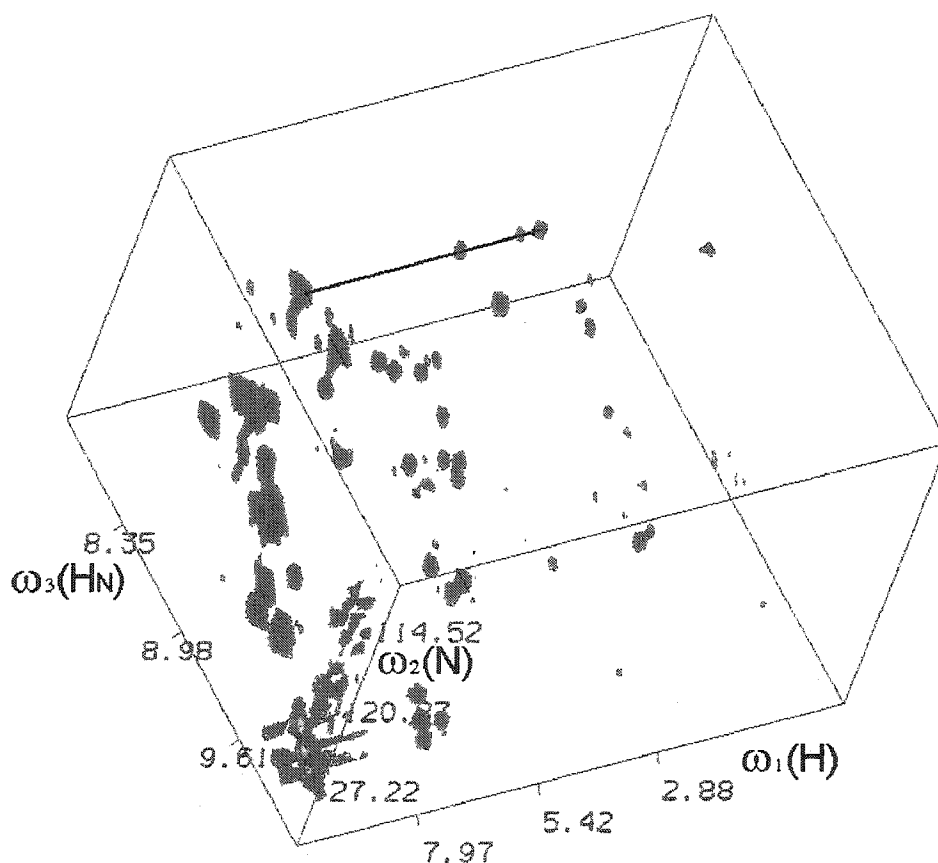


Figure 4.5: Box representation of a 3D ^1H - ^{15}N NOESY-HSQC of ^{15}N -gA in SDS micelles, demonstrating the resolution potential of this experiment in three dimensions. For instance, the arrow connects all the cross-peaks occurring on the axis defined by the frequencies $(\omega_3^{H_N}, \omega_2^N)$ representing cross-relaxing connectivities with the H_N spin of the C-terminal ethanolamine residue (this axis is also displayed in the right-most strip plot of Figure 4.6)

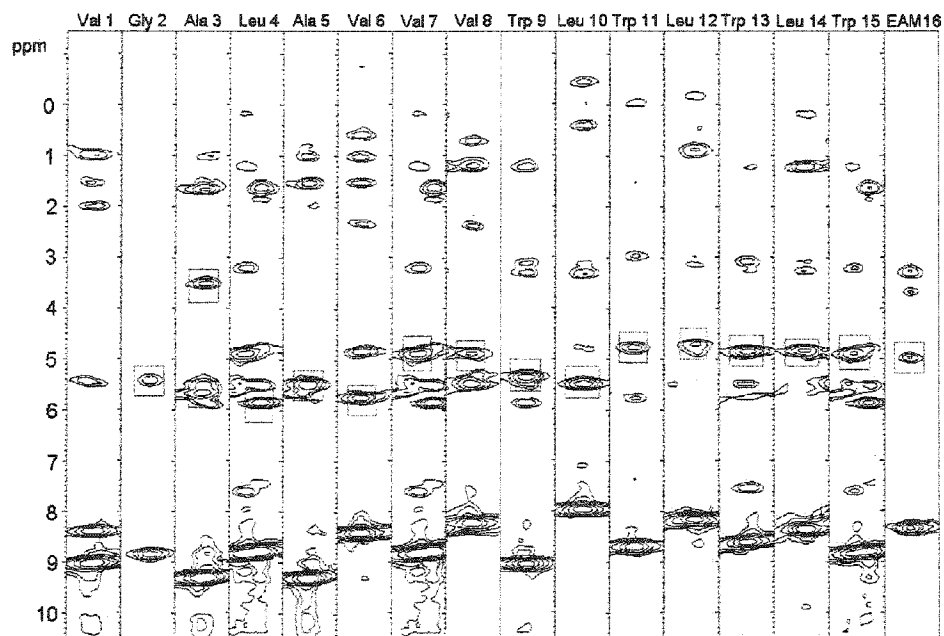


Figure 4.6: Strip representation of a 3D ^1H - ^{15}N NOESY-HSQC of ^{15}N -gA in SDS micelles ordered according to the primary sequence of gA. The strips were extracted at the ω_2^N frequency of each residue and centered at the ω_3^{HN} frequency. The sequence-specific $\text{H}_\alpha^i \rightarrow \text{H}_N^{i+1}$ cross-peaks are boxed for each residue. A total of 90 cross-peaks were identified in this experiment.

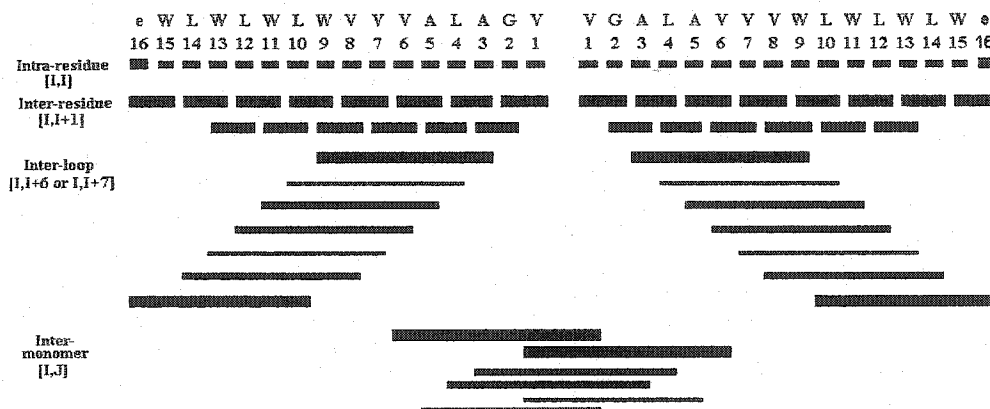


Figure 4.7: Diagram summarizing the $^1\text{H}_N$ - H_x connectivities measured in the 3D-NOESY-HSQC spectrum and used in the distance geometry/simulated annealing protocol described in Section 4.6. The length and position of the bars under the primary sequence of gA illustrates the residues correlated by the NOE interactions measured. The length of the bars represents either intra-residue connectivities ($i \rightarrow i$), inter-residue ($i \rightarrow i+1$), inter-loop ($i \rightarrow i+5, i+6, i+7$) or inter-monomer (i, j) connectivities. The widths of the bar relate to the maximum strength of the measured cross-relaxing interactions. The wide bars correspond to strong NOEs (1.8–3.0 Å), the medium widths to medium strength NOEs (2.4–3.6 Å) and the narrow bars to weak NOEs (3.0–5.0 Å).

molecular dynamics calculations are combined with distance constraints and are applied to a random or to a (sub-)embedded initial structure. The protein molecule is raised to high temperature (several 1000's of K) to permit the search of a large conformation space, and then the temperature of the system is slowly lowered back to an ambient state. During the simulation, Newtonian mechanics are applied to the set of atoms for which the position, velocity, friction and force are computed at the end of each time-step (*ca.* 5 fs). The instantaneous interatomic force is computed as the negative of the spatial gradient of the total potential function. This function is predicted as the sum of all energy functions for all bonded and non-bonded interactions. These include Lennard-Jones potentials for van der Waals-type interactions, as well as bond lengths and angles, dihedral angles defining 3-bond torsions, 3-bond planarities or tetrahedral chiralities, etc. A number of macromolecular computational programmes, such as XPLOR, DYANA, CNS, etc. have been developed to accomplish these tasks and to output the most plausible and energetically favorable structures. In the present work, version 2.0.6 of XPLOR-NIH [113] based on A. Brünger's X-Plor 3.851 [114] was used (<http://atb.csb.yale.edu/xplor/>). Input files with specific XPLOR commands were generated by editing tutorial input files with similar NMR structural purposes. The input files and the associated modified topology, parameter and restraint files can be found in the appendix of this thesis.

The strategy used to determine the structure of the gA dimer consisted of two steps, one to generate the structure of each of the symmetric monomers and a second to dock the monomers into the dimeric form of gA. The combination of distance geometry and simulated annealing was employed to reach this end. These tasks were applied in the presence of energy functions dictating penalties for deviating from a preferred geometry. Soft functions were applied for the experimental restraints. The ^1H - ^1H NOE distance restraints followed a square-well potential function [114, Chapter 18] delimited by quadratic function walls beyond the range of 1.8-3.0 Å for strong couplings, 2.4-3.6 Å for medium strength couplings and 3.0-5.0 Å for weak couplings. For comparison, one run of distance geometry and simulated annealing step also included non-experimental hydrogen-bond square-well potential energy functions

between $O^{m/n} \leftrightarrow H_N^{m+6/n-6}$ and $O^{m/n} \leftrightarrow N^{m+6/n-6}$ (m is even, n is odd) for intramonomeric bonding and between $O^i \leftrightarrow H^j$ and $O^i \leftrightarrow N^j$ for (i,j) residue pairs corresponding to (1,5), (3,3), (5,1) (see files: "ga-hbondsA.noe", "ga-hbondsB.noe" and "ga-hbonds-inter.noe"). These were based on the PDB:1mag structure of gA [24]. Torsion angles functions were also employed in this comparative set of structures based on measured J-couplings [115] for the backbone (file: "ga-dihang-bb.tbl"). No other external geometric energy functions such as those based on symmetry, 1-bond J-coupling, proton chemical shift, diffusion or susceptibility anisotropies were used. Standard bonded and non-bonded geometrical energy functions were chosen to describe the empirical chemical interactions. These included standard harmonic functions for the bonded interactions composed of bond lengths, bond angles, planarity, impropers (chirality) and torsion angles. For the non-bonded interaction, a quartic energy function was applied to impose the repulsive van der Waals interaction. The energies and average geometry for all these interaction can be found in the parameter file (protein-allhdg.param, see Appendix, p. 241) which was implemented with the energy and geometry terms for the uncommon terminal formyl and ethanolamine groups of gA. Since gA carries no charge, no electrostatic term was used during the computations.

4.6.1 Calculation of the monomeric structure

All the input files described in the following section can be found in the appendix of this thesis (p. 241). The XPLOR simulations required the creation of a complete definition of the topology ("gasdsA.psf") and an extended structure ("gasdsA.pdb") for a single strand of gA using the standard command files ("1-make-psf-ga.inp" and "2-gen-templ-gasdsA.inp"). These are necessary for defining the initial conditions for the distance geometry and simulated annealing stages. The monomeric structure of gA was obtained from the unambiguous restraints of the 2D- and 3D-NOESY experiments, which were classified either as intra-residue, inter-residue or inter-loop according to the definitions in Section 4.5. The inter-monomer restraints were left out during this stage. Ambiguities were introduced only for methyl hydrogens within

the same residue. These ambiguities were applied by satisfying the restraint with the central average position for the three methyl hydrogens. Using these restraints, the standard distance geometry protocol (file: "3-xplor-dgse.inp") was used for sub-embedding the key structural backbone atoms (C_α , H_α , N , H_N , C' , C_β , C_γ) in a configuration favorable for simulated annealing. Next, again relying only on the 87 internal NOE distance restraints, the standard distance geometry/simulated annealing protocol (file: "4-xplor-dgsa.inp") was applied to the complete set of atoms using the sub-embedded structures as an initial structural configuration. The resulting structures were then refined using a short cooling gradient simulated annealing (file: "5-xplor-refine.inp") and screened for valid structures (file: "6-xplor-accept.inp"). This protocol yielded about 60 % acceptable low-energy structure with no geometrical or NOE violations. Out of a 100 structures, the 63 acceptable structures had an overall energy of between 9 and 149 kcal/mol.

4.6.2 Calculation of the dimeric structure

A non-standard protocol was used to dock two monomeric structures into a valid dimeric pair of gA molecules with the goal of satisfying the 3 inter-monomer distance restraints. To reach this goal, the best 50 structures (with lowest overall energy) were taken from the monomeric simulated annealing stage and paired up randomly into a single structure input file, and the two segments were differentiated with labels "A" and "B". The two centres of mass were separated by 40 Å to avoid any initial steric interaction. The input command file used for this stage was inspired by the protocol used for glycophorin A dimer docking [15, 116, 117]. The simulated annealing (file "7-xplor-growinter.inp") was performed in three stages, starting with the gradual introduction of the 3 inter-monomer distance restraints (applied twice: from $A \rightarrow B$ and from $B \rightarrow A$) at high temperature (2000 K) over 8000 annealing steps, followed by a high-temperature dynamic run of 8000 steps and, finally, by the application of a cooling gradient over 8000 steps. The 87 intra-monomeric distance restraints were still present throughout this protocol. It was important to gradually increase the scaling factor for the energy function of the inter-monomer distance restraints by adjusting

their scale over 40 geometrical steps from 0.01 to 10, for a smooth and successful docking of the two monomers. A more abrupt onset of these restraints between the 40-Å-separated monomers created a large energetic instability that resulted in important distortions of the initial monomeric structures. The resulting docked monomers were finally submitted to a refinement protocol (file "8-xplor-refine.inp") similar to that applied to the annealed monomeric structures.

4.6.3 Final distance geometry/simulated annealing computed structures

These XPLOR computations generated families of 25 dimer structures. Of those, 22 showed no NOE violations with overall acceptable geometries. The energies of the final structures ranged between 573-704 kcal/mol. The dihedral angle terms were systematically the major contributors for these energies. Figure 4.8(A) shows the best-fit alignment of the backbone traces for all acceptable structures and Figure 4.8(D) and (G) show the average structure from a side and top perspective, respectively. The average structure traces out a helical dimer of 6.3 residues/turn and with the dimerization interface occurring at the N-terminal end of the helix. The channel pore has a cross-section diameter of about 7.5 Å throughout its entire length. This model crudely matches that proposed by Urry [93] and elucidated by Arseniev [91, 115] and later by Ketchum [24]. The goodness of fit between the 22 acceptable structures is clearly imperfect and can be evaluated by the total root mean square (rms) deviation over all backbone atoms. A value of 0.898 Å was obtained. In an attempt to refine the quality of the backbone structure, the entire protocol was repeated in the presence of artificial restraining interactions corresponding to the hydrogen-bonding pairs and dihedral angles described above. The addition of these restraints only produced 11 acceptable structures shown in a best-fit alignment in Figure 4.8(B), with the average structure displayed in Figure 4.8(E) (side view) and (H) (top view). Although the fit still shows a substantial spread, the rms deviation was reduced to 0.478 Å. For comparison, the same protocol applied to an ideal set of 121 $^1\text{H}_\text{N}$ and 79 $^1\text{H}_\alpha$ NOEs and 31 inter-monomer ^1H NOEs (back-calculated from the PDB:1mag structure) yielded

a family of 16 acceptable structures (Figure 4.8(C) best-fit alignment, (F) and (I) average structure) with an rms deviation of 0.365 Å.

This exercise, whereby a unique overall polypeptide fold is sought from experimental H_N-H_x restraints alone, seems to indicate that these restraints will yield a moderately resolved structure. From the comparative study, the quality of the structure strongly depends on the number of restraints used and can be substantially refined with additional restraints such as those from the predicted hydrogen bonding network. It is predicted, however, that with the resolution available from experiments in solid-state, only a small fraction of restraints will be identifiable and even a low-quality structure will not be accessible unless the simulated annealing protocol can be complemented by other types of restraints such as H_C-H_x restraints (*i.e.* from a 1H - ^{13}C CROPSY-NOESY experiment), J-coupling-related torsion angles and perhaps even orientational constraints such as those measured by Ketchum *et al.* [24].

4.7 Concluding remarks

In the search for novel solid-state NMR approaches to study the structure of membrane proteins, important advances have been made on simple polypeptide structures such as gA. These small molecules are ideally suited for NMR development because of their ability to associate with membrane bilayers, as well as dissolve without major loss of structure in the so-called membrane mimetic solvent systems (TFE, $CHCl_3$ /MeOH, detergent micelles, bicelles). This opens the way to complementary experimentation based on both the well-established solution-state NMR techniques and novel solid-state NMR approaches. NMR spectroscopists may also use the results from the high-resolution experimentation to interpret results from solid-state NMR, which is often limited by low resolution.

In this chapter, a number of results are gathered from liquid-state NMR of gA which may become invaluable in the application of multinuclear NMR approaches to gA in membrane bilayers. For the first time, a complete ^{13}C and ^{15}N isotropic chemical shift assignment list is compiled for this molecule in several different relevant forms and solvents. These may prove to be useful in the interpretation or confirmation of the

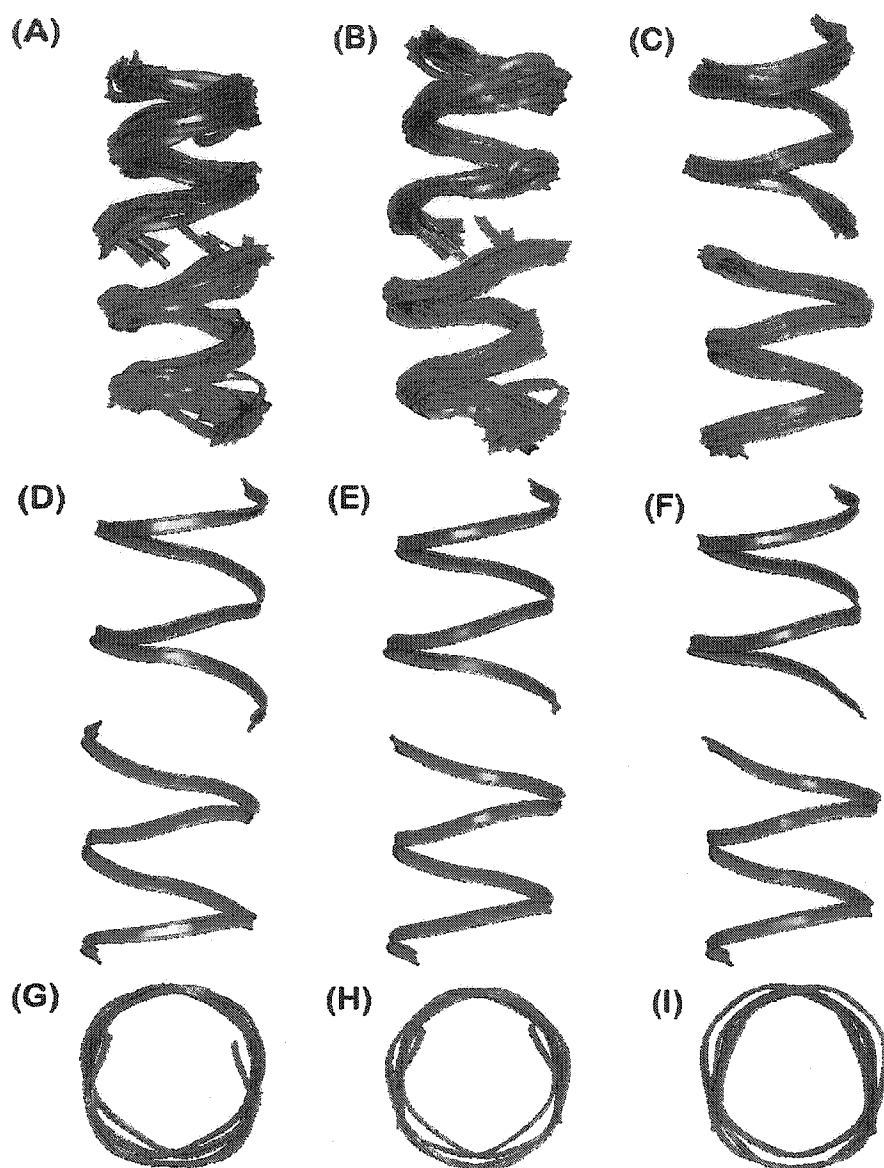


Figure 4.8: Ribbon trace of the gA backbone structures calculated from $^1\text{H}_N \rightarrow ^1\text{H}_\alpha$ NOE connectivities. Results are presented for the calculations using: (A), (D), (G) the 90 experimental restraints alone (22 structures); (B), (E), (H) the 90 experimental restraints plus hydrogen-bond distance and ϕ and ψ dihedral angle restraints (11 structures); and (C), (F), (I) an ideal set of 231 NOE restraints involving at least one $^1\text{H}_N$ or $^1\text{H}_\alpha$ based on distance back-calculations from the PDB structure 1mag [24] (16 structures). Structures in (A), (B), (C) display the best-fit alignment of the backbone atoms showing the consistency of fit and the quality of the proposed structure. Structures in (D), (E), (F) show a side view and (G), (H), (I) show a top view of the average backbone structure.

^{13}C and ^{15}N assignments of gA undergoing MAS which also reveals isotropic chemical shifts. Direct use of the liquid-state ^{15}N chemical shift assignment is presented in the Chapter 7. A full backbone structure elucidation of gA in SDS only from $^1\text{H}_\text{N}$ - $^1\text{H}_\text{x}$ NOE cross-relaxing correlations was carried out to evaluate the potential quality of the structure. Again, this will be helpful in the design of solid-state NMR experimentation based on the same restraints (Chapter 8).

4.8 Experimental conditions

The following presents in table form the most important parameters used in the high-resolution experiments referred to in this chapter.

Table 4.4: Experimental conditions for all high-resolution NMR experiments of gA in solution.

	TOCSY	DQF-COSY	ROESY	^1H - ^{13}C HSQC	^1H - ^{13}C HMB
sample	gA/TFE	gA/TFE	gA/TFE	gA/TFE	gA/TFE
# scans	32	96	96	32	32
repetition delay	1.5 s	1.5 s	2 s	1.2 s	1.5 s
bruker ppg	mlevphpr2	cosydfphpr	roesyphpr2	invietgpsi	inv4gplprdqf
spectr. freq. 1	600.13 MHz	600.13 MHz	600.13 MHz	150.916 MHz	150.916 MHz
spectr. freq. 2	600.13 MHz	600.13 MHz	600.13 MHz	600.13 MHz	600.13 MHz
sweep width 1	10 ppm	12 ppm	10 ppm	190 ppm	190 ppm
sweep width 2	10 ppm	10 ppm	10 ppm	10 ppm	10 ppm
# points	4096	4096	4096	4096	2048
# increments	256	320	256	256	256
mixing time	100 ms		200 ms		
processing 1	phased	phased	phased	phased	magnitude
window func. 1	Gaussian (0.2)	qsine (90)	Gaussian (0.15)	sine (90)	sine (90)
processing 2	phased	phased	phased	phased	phased
window func. 2	qsine (90)	qsine (90)	qsine (90)	qsine (90)	qsine (0)

	DEPT	^1H - ^{15}N HSQC	^1H - ^{15}N HSQC	^1H - ^{15}N HSQC	3D-NOESY-HSQC
sample	ga/TFE	ga/TFE	ga/(Meth/Chlor) (CsCl)	ga/SDS	ga/SDS
# scans	20000	4	1024	32	8
repetition delay	1.5 s	1.5 s	1 s	1 s	1 s
bruker ppg	dept135	invietfpf3gpsi	invietfpf3gpsi	invietgpsi	noesy14pr3d
spectr. freq. 1	60.818 MHz	60.818 MHz	60.818 MHz	40.544 MHz	400.13 MHz
spectr. freq. 2		600.13 MHz	600.13 MHz	400.13 MHz	40.544 MHz
spectr. freq. 3					400.13 MHz
sweep width 1	190 ppm	35 ppm	70 ppm	30 ppm	12 ppm
sweep width 2		10 ppm	10 ppm	12 ppm	30 ppm
sweep width 3					12 ppm
# points	16384	4096	1024	1024	1024
# increments 1		64	108	256	96
# increments 2					192
mixing time					75 ms
processing 1	phased	phased	phased	phased	
window func. 1	exp (2 Hz)	exp (3 Hz)	exp (0.5 Hz)	sine (90)	
processing 2		phased	phased	phased	
window func. 2		qsine (90)	qsine (90)	qsine (90)	
processing 3					
window func. 3					



- It is curious that physical courage should be so common in the world and moral courage so rare.

- Mark Twain

5

The effects of structural variations on NMR spectra of membrane proteins in oriented bilayers

5.1 Introduction to separated local field spectroscopy

One of the most direct ways to obtain structural constraints by solid-state NMR is by measuring the residual magnitudes of the second rank tensor interactions directly from the spectrum of a static, oriented sample. As mentioned in Chapter 1, the challenge of this approach is to resolve and measure sufficient structural constraints to uniquely solve the structure of interest. A more promising avenue to alleviate both problems lies in multi-dimensional experiments, referred to as Separated Local Field (SLF) experiments. These are designed to allow the spin system to evolve under \mathcal{H}_1 during t_1 , under \mathcal{H}_2 during t_2 , etc. In static samples, the range of anisotropic chemical shifts, dipolar couplings and quadrupolar splittings can be quite large, which can overcome to some degree the relatively low resolution typical of solids due to their inherently broad lines (even for well oriented samples). In some cases, significant resolution enhancement is achievable using homonuclear ^1H decoupling techniques such as the frequency shifted Lee-Goldberg sequence [118].

The problem of peak assignment may limit the application of SLF experiments for large uniformly labelled protein systems. Some assignment strategies based on the repeating pattern of protein substructures (α -helices, β -strands) have been proposed

but require a level of rigidity and regularity unusual for proteins. However, the flexibility of this general approach through the number of available interactions should ultimately lead to a series of sequence specific experiments (such as those commonly used for soluble proteins) to enable the complete assignment of uniformly labelled proteins. It is likely that experiments measuring the anisotropic interactions of nuclei along or near the protein backbone will prove to be the most useful. In a recent article, Vosegaard *et al.* [119] review the broad range of possible SLF experiments and discuss their potential utility. The discussion here will be focused on only one of these experiments which is considered to be both feasible and useful. This experiment, which is referred to as HN/N in this chapter, measures ^{15}N chemical shift and ^1H - ^{15}N dipolar coupling from the same peptide plane as illustrated in Figure 5.2.

Figure 5.1 shows the 3-step pulse scheme for a specific case of the HN/N experiment. Cross-polarization is used to transfer coherence from the abundant ^1H spin population to ^{15}N . Then the ^{15}N magnetization is allowed to evolve under its dipolar coupling with the directly bonded ^1H during t_1 . The chemical shift interaction can be eliminated with an inversion pulse or by letting ^{15}N evolve under a rf spin lock. The use of Lee-Goldburg schemes [120] during the t_1 interval, to suppress the ^1H - ^1H homonuclear coupling, has a dramatic effect (up to 4-fold improvement) on the resolution in the ω_1 dimension [118]. The homonuclear decoupling is achieved by first applying a 35.3° pulse to the ^1H to bring their magnetization along the magic angle and then by setting the rf field offset such that the ^1H effective field remains at the magic angle in the rotating frame. In this specific form, the HN/N experiment is also known as PISEMA [118]. Finally, after t_1 , the free induction decay is recorded on the ^{15}N channel while decoupling ^1H to leave only the ^{15}N chemical shift during t_2 . So far this has been the most common of the SLF spectroscopy experiments applied to polypeptides in oriented membrane samples.

Besides the resolution improvement in ω_1 , this experiment potentially has very good peak dispersion because of the strong ^1H - ^{15}N dipolar coupling (up to 23 kHz) and the large range of ^{15}N chemical shifts (170 ppm). However, it should be noted that although the potential range of dispersion for both interactions is large, they are

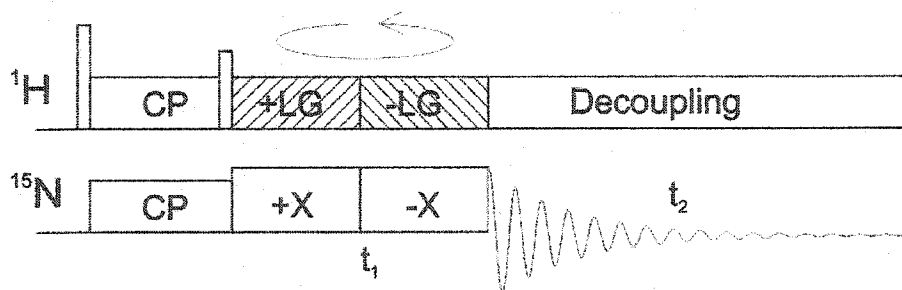


Figure 5.1: Pulse sequences for the HN/N two-dimensional SLF spectroscopy experiment PISEMA [118].

not independent. Indeed, because directions corresponding to σ_{33} and the NH dipolar coupling are almost colinear, as seen in Figure 5.2, the allowed peak position domain covers only a small fraction of the total spectral area in the 2D plane. As discussed below, this results also in a general clustering of the peaks in a restricted region of the spectral plane in proteins with secondary structures with repeating patterns.

Another advantage of this experiment is its relatively good signal-to-noise because the pulse sequence does not require any long transfer delays which are prone to suffer from relaxation effects or any transfer mechanisms with orientation-dependent efficiency. Furthermore, this experiment only requires the uniform introduction of the isotopic nuclear spin label ^{15}N . This can be achieved biosynthetically on ^{15}N minimal media, with the result of some overlap with side chain signal contributions in the spectrum (for Trp, Gln, Asn, His and Arg). Finally, this experiment is technically relatively simple, since it requires only two channels whereas most potential SLF experiments employ at least three [119].

In this chapter, theoretical calculations are used to predict the appearance of SLF experiments based on orientational restraints from membrane proteins in oriented bilayer samples. The simulation work will investigate the impact on the peak dispersion in SLF experiments due to membrane protein natural irregularities allowed in helical domains or motional variations existing in membrane bilayers. These variations potentially have large implications for the interpretation of these spectra.

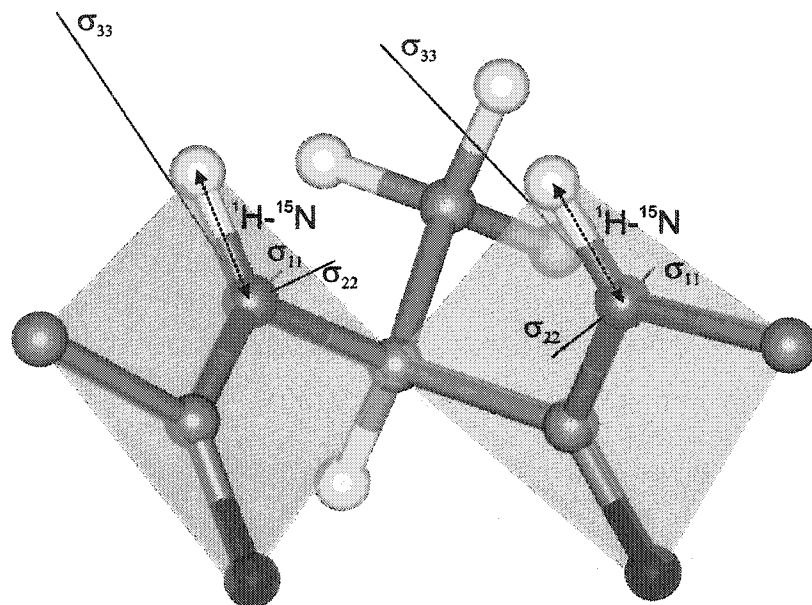


Figure 5.2: Molecular model of an α -helical Ala residue with its two adjacent planar peptide bonds. To support the discussion, the dipole-dipole interaction is displayed between directly-bonded ^1H - ^{15}N (dashed arrows) and the relative size and direction of the chemical shift anisotropy principal values σ_{11}, σ_{22} and σ_{33} are indicated for ^{15}N (straight lines). For ^{15}N , $(\sigma_{11}, \sigma_{22}, \sigma_{33}) = (40, 68, 202)$ ppm and $(\alpha_{Pp}, \beta_{Pp}, \gamma_{Pp}) = (90^\circ, 104^\circ, 0^\circ)$ [121].

5.2 Methods

All simulations were obtained by calculating the expected chemical shift and dipolar splittings from a number of key nuclear sites along the backbone of model structures. The structures were either ideal helical structures built using the modeling program QUANTA, published structures from the PDB, or snap-shot structures obtained from molecular dynamics simulation trajectories. The shifts and splittings were obtained from the expression of the interaction Hamiltonian derived in Chapter 2 (p. 23), specifically using Equations 2.33 and 2.41. All chemical shift simulations were calculated for a field of 14.1 T and principal axis system elements and orientations in the molecular frame available from the literature based on single crystal measurements. These are compiled in the review by Davis and Auger [121]. Typical values are given and illustrated in Figure 5.2. Gyromagnetic ratios are available from Table 2.1 (p. 14).

The calculations were conducted using of a Fortran-77 program, "PDBMIf" (author: J. H. Davis). In summary, this program (1) reads the coordinate files (PDB format) of a protein structure, (2) predicts its moment of inertia principal axis, and, optionally, applies axial diffusion averaging around the principal axis, (3) calculates the shifts and splittings for a set of five interactions within each peptide unit for a given set of tilt and rotation angles of the moment of inertia principal axis relative to the external static field. The spectral features calculated were the ^{15}N chemical shift, the ^{15}N - ^1H dipolar coupling, the $^{13}\text{C}'$ chemical shift, the $^{13}\text{C}'$ - $^{13}\text{C}_\alpha$ dipolar coupling and the $^2\text{H}_\alpha$ quadrupolar splitting. Only the first two were used in this work, however all five could potentially be used in other SLF experiment simulations. The complete annotated code is available in the appendix of this thesis.

5.3 SLF spectroscopy of ideal polypeptide helices

The transmembrane domains of membrane proteins are often formed from α -helices, either single transmembrane helices (Neu, glycophorin A) or transmembrane helix bundles (bacteriorhodopsin, photosynthetic reaction centre, K^+ -ion channel). Alternatively, they may form a β -barrel channel configuration (bacterial outer membrane

porins). These secondary structures are defined by their repeating peptide backbone dihedral angles, namely ϕ_i ($\text{CO}^{i-1}\text{-N}^i\text{-C}_\alpha^i\text{-CO}^i$), ψ_i ($\text{N}^i\text{-C}_\alpha^i\text{-CO}^i\text{-N}^{i+1}$) and ω ($\text{C}_\alpha^i\text{-CO}^i\text{-N}^{i+1}\text{-C}_\alpha^{i+1}$). In the α -helix, the first two angles have typical values of -65° and -40° , respectively, whereas in β -strands, these angles are typically -139° and 130° . Because of the resonant nature of the peptide bond, ω is generally very close to 180° . In order to span a typical membrane, the protein backbone will form these regular structures over a significant stretch of amino acid residues. Such extended secondary structural domains have characteristic signatures in SLF spectroscopy.

Following the description above, using the principal axis frame of the moment of inertia tensor as an intermediate reference frame for an ideal polyalanine α -helix (with all $(\phi, \psi, \omega) = (-65^\circ, -40^\circ, 180^\circ)$), the corresponding SLF spectra can be predicted for any orientation of the helix long axis with respect to the membrane normal/magnetic field (tilt angle τ)¹ and for any rotation about the helix long axis (rotation angle ρ)¹. For a helix with no irregularities, all the resonance peaks will lie on a smooth closed curve as is shown in Figure 5.3 (C) for 7 different values of τ . These figures, called “PISA wheels” (Polarity Index Slant Angle [122, 123]) in the case of PISEMA spectra, possess two interesting characteristics. Firstly, as is evident from Figure 5.3 (C), the overall position along the diagonal and the shape of these figures are indicative of the helical tilt angle. Indeed, for the HN/N spectrum, a helix parallel to the magnetic field ($\tau = 0^\circ$), shows both a large chemical shift (σ_{33}) and a large dipolar coupling, resulting in a pattern of peaks near the upper left corner of the figure. However, when such a helix is tilted perpendicular to the field ($\tau = 90^\circ$), the chemical shift is much smaller and the dipolar coupling is negative.

A second property of SLF spectra of regular helices is related to the rotation or polar angle ρ . Although changing the polar orientation of the polypeptide about a given azimuthal axis direction does not alter the shape or position of the smooth curves (PISA wheel patterns), it does shift the relative position of any individual peak along the closed outline of each curve. Consequently, once one peak in a pattern has

¹ The angles τ and ρ follow the naming conventions set by Marassi *et al.* [122] and correspond to the angles β_{ML} and α_{ML} defined in Figure 2.2 of Chapter 2

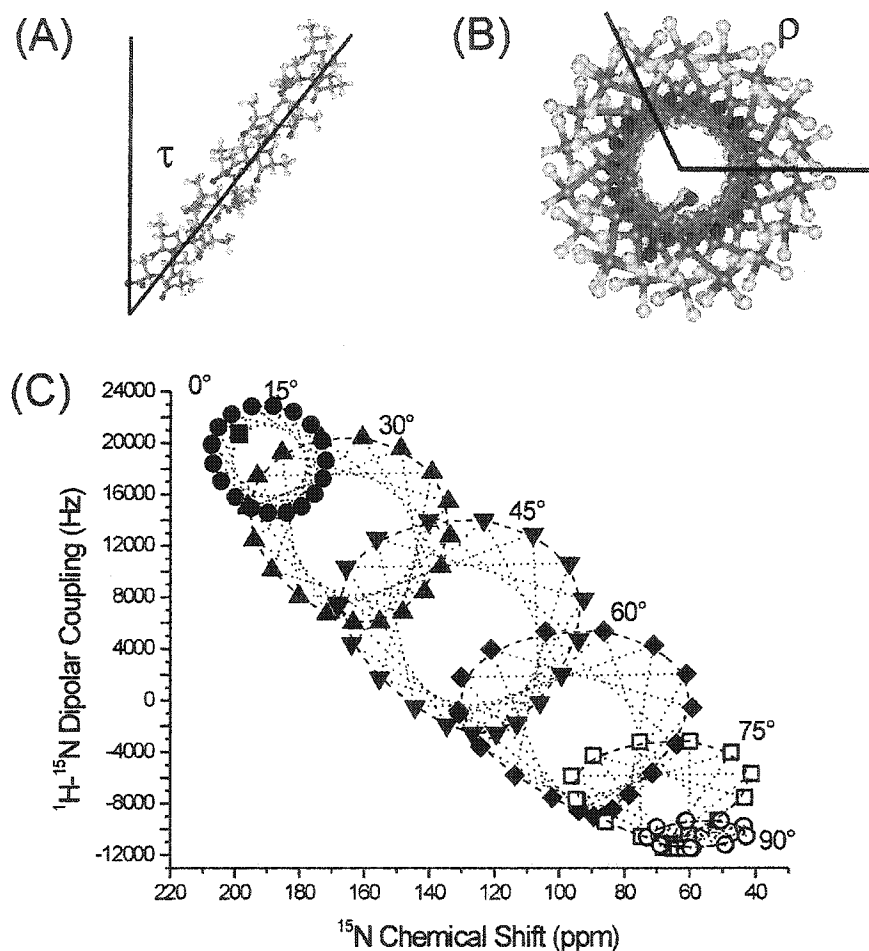


Figure 5.3: (A) and (B) Configuration of an ideal 22-residue polyalanine α -helix and the definition of the tilt (τ) and rotation (ρ) angles. (C) Typical patterns expected for an ideal alpha-helix (-65,-40) in the HN/N spectra. In (C), the dotted lines joins the signal peaks of adjacent residues along the polypeptide primary sequence, and the dashed curves give the expected locus of peak positions (as ρ varies) for the tilt angles given in the figure.

been assigned, one could in principle trace out the amino acid sequence and assign all the peaks of an ideal, regular α -helix since two adjacent residues are separated by $\Delta\rho = 100^\circ$.

The results of similar simulations on an ideal, regular β -strand with dihedral angles $(-139^\circ, 130^\circ, 180^\circ)$ are shown in Figure 5.4. Since β -strands are very elongated and have only a small degree of helicity (Figure 5.4 (A,B)), the orientations of consecutive peptide planes will alternate by close to 180° relative to the long axis. The predicted spectrum in Figure 5.4 (C) shows how this peptide geometry translates into a binary pattern in SLF spectroscopy. Here the simulations are restricted to a stretch of 14 residues (it takes a minimum of 7 to span a typical membrane bilayer) keeping the tilt direction approximately parallel to the peptide planes as is observed in all members of the bacterial outer membrane porin family. For tilt angles near 0° , the NH bonds are nearly perpendicular to the field so that the chemical shifts are near their minimum value and the dipolar couplings are negative in the HN/N spectrum; for a tilt τ near 90° , the opposite effect is observed, with chemical shifts near their maximum value and large positive dipolar couplings. It is also observed that, for intermediate tilt angles, the alternation in peak position arising from consecutive residues is observed to vary mostly in chemical shift in an HN/N spectrum; this effect is due to the alternation in the orientation of the chemical shift tensor with respect to the moment of inertia tensor principal axis (the long axis of the helix).

It is important to stress here that these ideal patterns are simply a spectroscopic signature of a protein's most common secondary structural elements. As seen in the next section, there are many structural variations and fluctuations which will greatly affect the appearance of these spectra in real systems.

5.4 Effect of helical irregularities

The diversity of folds found in proteins leads to significant structural variability even within the secondary structural elements. For example, there are large ranges in the dihedral angles ϕ (with a typical rms standard deviations of $\sigma = 10^\circ$) and ψ (with $\sigma = 10^\circ$) and in other internal angles [124] which still permit the typical hydrogen bonding

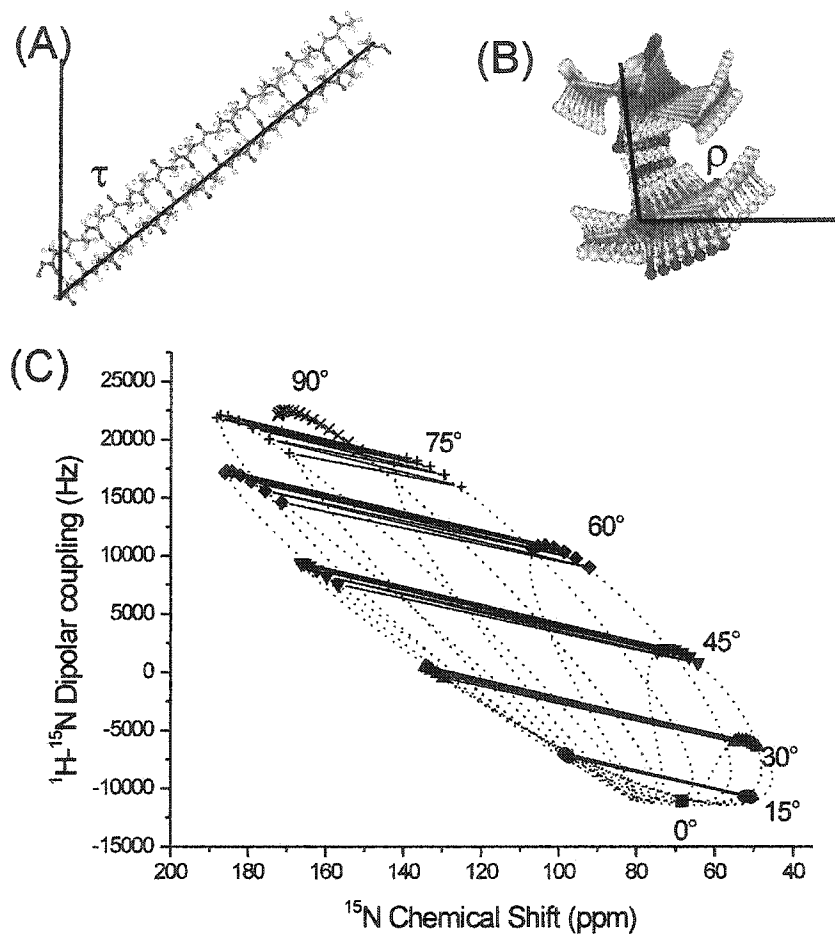


Figure 5.4: (A) and (B) Configuration of an ideal hydrogen-bonded antiparallel β -strand pair and the definition of the tilt (τ) and rotation (ρ) angles. (C) Typical patterns expected for a 14-residue β -strand (-139, 130), when it is tilted as shown, in the HN/N spectrum. Dotted lines show the locus of peak positions (as ρ varies) expected for the given tilt angles.

patterns found in α -helices (NH^i to CO^{i+3}) or in β -strands. Statistical analysis of known structures shows that the peptide “plane” may also deviate from planarity with the ω torsion angles having standard deviations of up to about 7° [125]. At least as significant as these structural variations, the chemical shift tensor principal values and their orientation within the molecule may vary significantly with residue type and local structure (variations in principal values of several tens of parts per million is typical). How do these common structural irregularities in complex proteins influence the appearance of these solid-state SLF NMR spectra? Using computer simulations on known membrane protein structures, for example, from the PDB coordinate files [6], the expected SLF spectra can be obtained for any combination of second rank tensor interactions.

The model structure employed is that of the light-driven proton pump bacteriorhodopsin (PDB:1c3w [126]), a typical helical membrane protein having 7 transmembrane α -helical segments. The structure was obtained by X-ray crystallography in a matrix forming a cubic lipid phase and is one of the the highest resolution structures available to date for a membrane protein (1.55 \AA). Figure 5.5 shows the expected position of the peaks from the 7 transmembrane helices in the HN/N (Figure 5.5 (A)) spectra of this molecule oriented with the crystal unit cell z-axis aligned parallel to the magnetic field direction. Unlike the ideal helix case, the peak positions for any one of the 7 helices do not follow any simple closed curve but rather are clustered throughout the accessible region of the spectral plane. The obvious departure of the peak positions from the ideal curves can be attributed to large variations in a number of structural elements. Statistics on the structure show that there is a broad distribution of dihedral angles even within the 7 helical transmembrane domains. For different residues within these helices, ϕ varies from -120° to -50° and ψ varies from -52° to $+5^\circ$. These distributions have standard deviations of 10.3° and 10.2° , respectively. The planarity of the peptide linkages shows a distribution with a standard deviation of 4.8° in ω , but this narrow range may result to some degree from the refinement procedures used in deducing the structure. Variations also arise from residue specific differences in the anisotropic chemical shift tensor principal values and orientations

[121]. An important effect not included here is the sensitivity of the chemical shift tensor elements to the details of local structure. The tensor's principal values and its orientation within the molecular subunit can vary dramatically with the peptide dihedral angles.

To see even more clearly the effect of structural imperfections, the 8 Leu residues (position 87, 92, 93, 94, 95, 97, 99 and 100) of bacteriorhodopsin's transmembrane helix 3 are compared, since all of these Leu residues have different positions (different values of ρ) along the tilted helix. The dependence of the predicted peak positions, for each of these Leu residues, on the angle ρ at a constant tilt angle, $\tau = 8.8^\circ$, corresponding to the orientation of this helix relative to the crystallographic z-axis, is shown in Figure 5.5 (B) for HN/N. In these figures, the points give the positions of the peaks that would arise from a given Leu as ρ is varied from 0 to 2π . For an ideal helix, all 8 of these sets of points (one set corresponding to each Leu) would have traced out exactly the same smooth curve. Again the static structural irregularities in helix 3 have a large effect on the shape of these patterns although their positions still roughly indicate the overall helical tilt orientation.

Of course, it is uncertain how accurately the crystal structure represents the structure of bacteriorhodopsin in its native membrane environment. There is some concern that extensive structure refinement may bias the experimental measurements towards ideal bond lengths and angles. Perhaps "on average" bacteriorhodopsin does adopt this structure, but the solid-state NMR measurements are not only strongly influenced by structural variability such as that discussed above but are equally sensitive to dynamical fluctuations in orientation of the particular molecular group being examined. In the next section, the impact of motion on the observable solid state NMR spectra is discussed.

5.5 Effect of molecular reorientation

In addition to its effect on NMR relaxation, any fast molecular motion that causes the second rank tensor of either the chemical shift or the dipolar coupling to reorient in the magnetic field will effectively reduce the strength of these interactions and

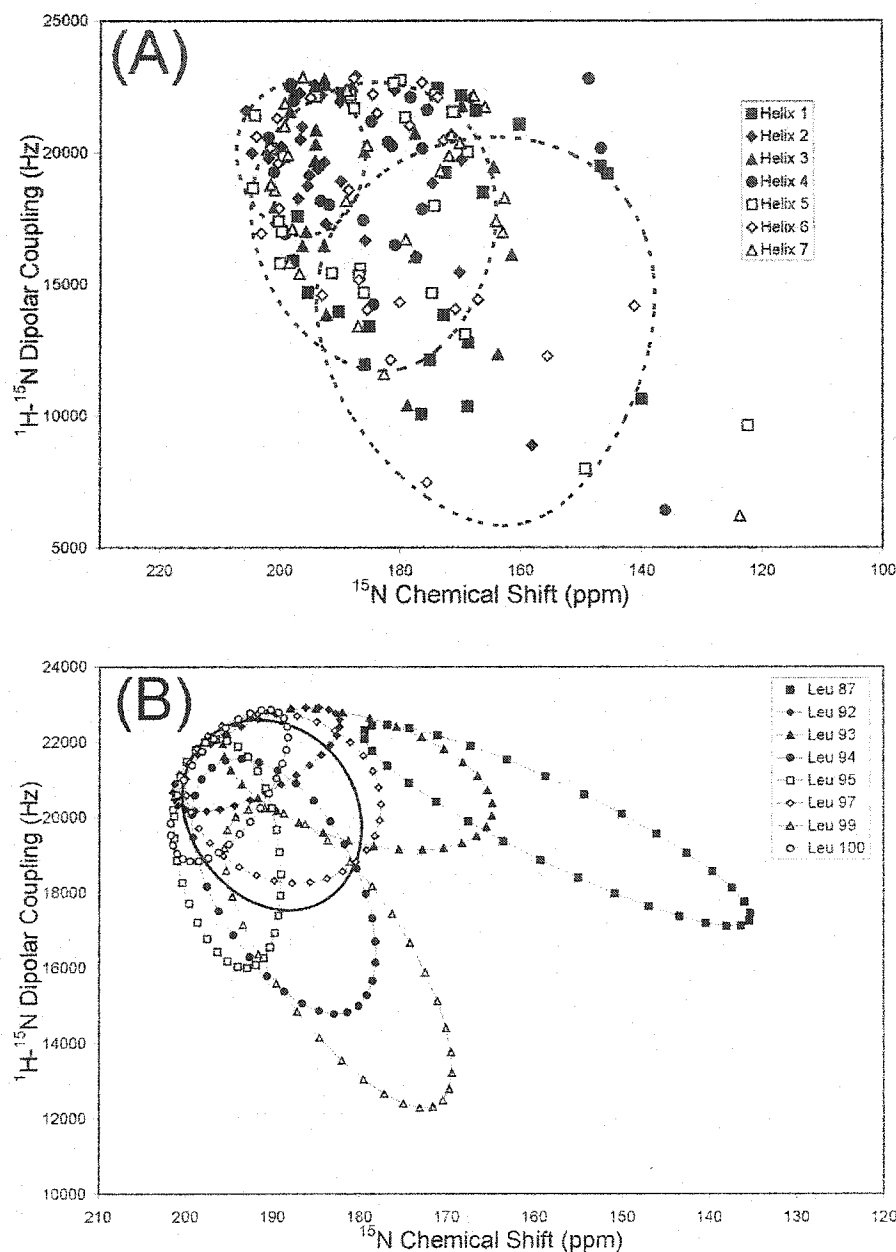


Figure 5.5: The effect of natural helical irregularities on HN/N spectra. (A) The expected spectra from the 7 static helices of bacteriorhodopsin based on the structure reported by X-ray crystallography (PDB:1c3w [126]) The dotted curves give the locus of peak positions (as ρ varies) for several tilt angles. (B) Individual peak patterns for each of the 8 Leu residues from helix 3, tilted at 8.8° . These curves are traced out as ρ is varied. For an ideal helix, all 8 Leu residues would trace out the same curve.

will have to be considered in the interpretation of the residual couplings in terms of orientational restraints. Molecular structures obtained by X-ray crystallography are presented as static since motions only affect resolution. Even at very low temperature, it is wrong to assume that NMR can be interpreted the same way and can provide the same type of static structure. Rather, solid-state NMR measurements provide an average tensor strength, where that averaging process is simultaneously an ensemble average over the distribution of orientations present within the sample and a time average over the orientational fluctuations. Assuming the motions are in the “fast limit” regime, the influence of some simple types of molecular motion can easily be examined on the predicted NMR spectra. For the simulation of SLF spectra, the static structures available from the PDB are incomplete and it is required to introduce molecular reorientation into the process. NMR relaxation studies can be used to characterize the form, the amplitude and time scale of some of these motions and provide a valuable starting point for our consideration of the effects of motion on the spectra [127–130]).

In this section several types of motion are considered and their effects on the SLF spectra are evaluated. The modeled motions include first, the whole molecule axial diffusion about the moment of inertia tensor principal axis, then the fluctuations in the orientation of this axis (“wobble”), and finally the internal “librational” motion of the individual peptide planes. Finally, the results of full atom molecular dynamics simulations are used to model the types of motions which occur during the NMR averaging time scale and to see their effects on the SLF spectra.

As for membrane lipids, axial diffusion can be quite appreciable for small transmembrane proteins. gA, a 2 kDa polypeptide which forms a transmembrane head-to-head dimer channel for monovalent cations, has been reported to rapidly diffuse about its long axis with a correlation time of $\approx 7 \times 10^{-9}$ s [130]. Neglecting all other motions, molecules with their axis of reorientation parallel to the magnetic field, will appear invariant under this motion. As a result, for this orientation, this kind of motion does not reduce the magnitude of the tensor interactions and the NMR spectra are unchanged by the motion. In order to calculate the effect of axial diffusion about

an axis inclined at an angle τ relative to the magnetic field, one needs to introduce an intermediate reference frame, as described in Chapter 2 (p. 22). For a long α -helix, where the moment of inertia principal axis can be considered to be the diffusion axis, one simply need to average the angle γ_{PM} (the rotation angle ρ) from 0 to 2π .

The test molecule used is the 36-residue transmembrane domain (TMD) of the rat growth factor receptor Neu, a receptor tyrosine kinase. The TMD primary sequence is QRASPVTFIIATV-V⁶⁶⁴-GVLLFLILVV-VVGILIKRRRQK-amide. What makes this polypeptide so interesting is that a single point mutation (V⁶⁶⁴:E) results in constitutive activation of the protein and cell transformation. The structure of the TMD was obtained by standard solution-state NMR methods based on nuclear Overhauser effect distance restraints. In tri-fluoroethanol, the TMD forms an α -helix [131] with some unravelling of the helix at each end. Due to its length and hydrophobic sequence, it is likely that it would form a transmembrane helix in lipid bilayers. Because the hydrophobic segment is somewhat longer than the typical fluid phase phospholipid bilayer thickness, the TMD is expected to tilt in the membrane. In fact, molecular dynamics simulations of this protein in a phospholipid bilayer demonstrated that at the end of a 10 ns simulation trajectory, the helix tilts at an angle of 20° relative to the membrane normal [132].

A series of calculated HN/N spectra of the transmembrane domain of this polypeptide axially diffusing about its predicted moment of inertia principal axis and tilted at increasing angles is shown in Figure 5.6 (A) along with the traces of the rotation patterns (vs ρ) of an ideal helix with similar tilt angles. Whereas the locus of peak positions for an ideal axially diffusing helix would lie along a straight diagonal line (at the centres of each of the static rotation patterns), the peak positions for this imperfect helix are spread out over a significant area. As the tilt angle approaches the magic angle, the spread in peak positions becomes smaller and smaller. In the presence of axial diffusion, the peak dispersion is limited and renders resolution of the signals difficult. SLF spectroscopy is clearly better suited for non-reorienting proteins. However, rapid axial diffusion becomes an advantage when using MAS ^1H NMR as it reduces the effect of homogeneous ^1H - ^1H dipolar broadening [33] (see below).

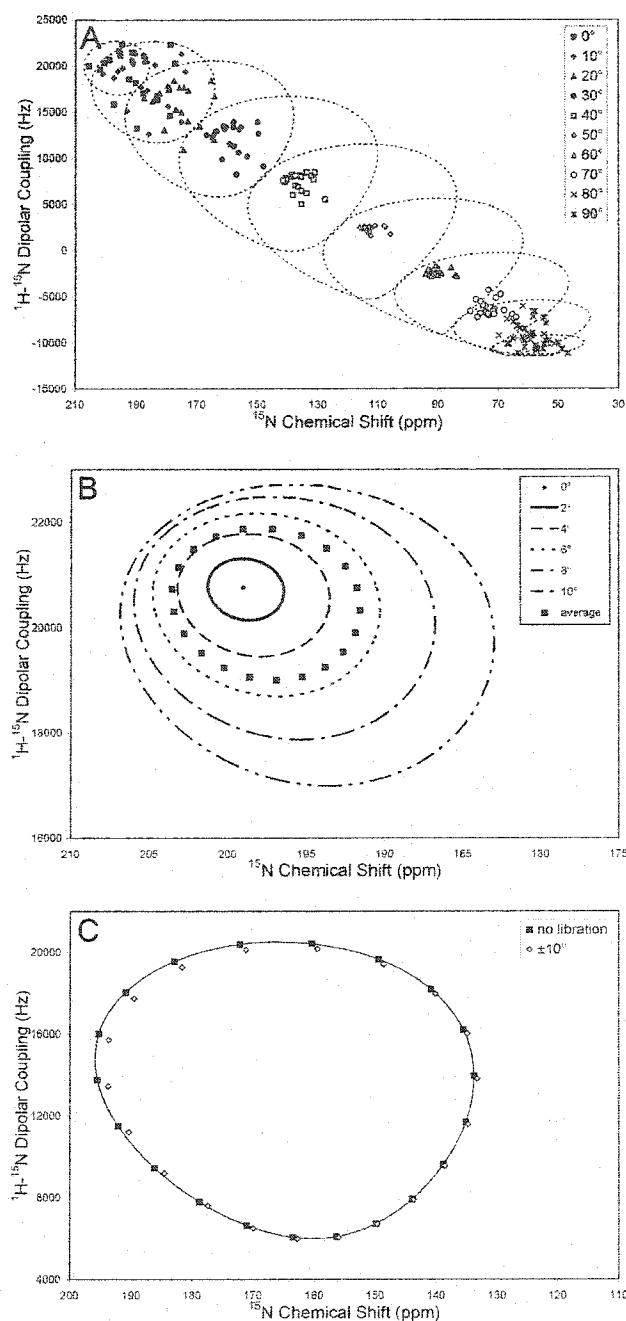


Figure 5.6: (A) The effect of axial diffusion on HN/N spectrum of Neu trans-membrane domain based on the structure reported by Houliston *et al.* [131]. (B) Effect of ± 10 degree wobble of an ideal helix with no tilt on the HN/N spectrum (C) Effect on the HN/N spectra, of a librational fluctuation in the orientation of the $(j-1, j)$ peptide plane about the $\text{C}_\alpha^{j-1}-\text{C}_\alpha^j$ direction for an ideal helix tilted at 30° . In all spectra, the closed curves give the expected locus of peak positions (as ρ varies) for a given tilt angle.

Another important whole-molecule motion is the wobbling motion whereby the orientation of the director axis fluctuates with time. This can be due either to the reorientation of the tilt axis of the molecule within the membrane or to local fluctuations of the membrane normal (sometimes referred to as “undulations”). These motions are therefore not necessarily restricted to smaller polypeptides. As an example of this type of motion, relaxation measurements on gA in oriented lipid bilayers have indicated that the polypeptide’s long axis reorients with a correlation time of the order of 6×10^{-6} s and an rms amplitude of about 16° relative to the normal to the glass plates (which were fixed parallel to the magnetic field) [130].

In order to simulate the dynamic effect on SLF spectra, the values of the interactions were averaged over an evenly distributed population of orientations within a cone centered at the average tilt angle. An ideal helix with no average tilt, but with a wobble range of $\pm 10^\circ$ will have an SLF pattern resembling that of a static helix tilted at about 5° , as shown in Figure 5.6 (B) for the HN/N spectrum. It is obviously crucial to be aware of the effects of this type of motion even when only estimating the tilt angle based on the pattern of peaks observed in SLF spectroscopy [122].

A third type of motion is the peptide plane librations which occur locally within the protein and, thus, may have different rates, amplitudes and average orientations depending on the position of the residue within the molecule. To model this type of motion, the j -th peptide plane is allowed to rock about the C_α^{j-1} - C_α^j direction by varying amounts around an average orientation. Within a range of $\pm 10^\circ$ around the average position, this motion has a relatively small effect on the HN/N spectrum (Figure 5.6 (C)). However, it does result in different shifts in peak position depending on the position of the peptide plane within the molecule. At an average tilt angle of 30° , the larger ^{15}N chemical shifts or ^1H - ^{15}N dipolar couplings are reduced more than the smaller ones. In any case, the shifts in this spectrum are of the order of 10 ppm, for chemical shift, and 500 Hz, for dipolar coupling.

As a final illustration of the effect of molecular motion on SLF spectra, “snapshots” taken from a molecular dynamics simulation of the Neu TMD in a fully hydrated dimyristoyl-*sn*-glycero-3-phosphocholine (DMPC) bilayer [132] are employed.

The internal and whole body motions which occur during the course of this 10 ns simulation trajectory lead to fluctuations in the orientations of the chemical shift and dipolar tensors relative to the bilayer normal (presumed parallel to the magnetic field) and, therefore, to fluctuations in the magnitudes of the couplings. At each instant of time (represented by a “snap-shot” in the trajectory file) an HN/N SLF spectrum can be calculated. The spectrum that would be observed experimentally would be an average over these rapid motions.

The simulated spectra shown in Figure 5.7 (A-C) are for instants of time during the 10 ns trajectory. The differences between these three spectra illustrate the sorts of variations being averaged over during an actual NMR experiment. Figure 5.7 (D) shows the evolution of two individual peaks in the HN/N SLF spectrum over the course of the trajectory. The simulation covers only 10 ns, and the NMR averaging time scale is much longer than this (several milliseconds) so that the motional averaging which occurs during the experiment is undoubtedly even more severe than what can be illustrated by such a simulation.

It has been seen through this brief summary that different types of rapid fluctuations influence the appearance of SLF spectra to various degrees and in different manners. Whole body motions tend to reduce the spread of peaks in the spectrum in a generalized manner, whereas internal motions may result in effects ranging from essentially no effect to quite substantial shifts in peak position simply based on the location of the residue involved.

5.6 Conclusions

The high-resolution molecular structures obtainable by diffraction methods are based on experimental data which precisely define atomic positions through the electron density. To supplement the experimental data, refinement procedures use, to varying degrees, the well characterized bond length and bond and torsion angle distributions found in high precision structures of small molecules. Some refinement protocols also introduce interatomic potential functions defined for bond lengths, bond angles, dihedral angles, etc. Protein structure determination by solution-state high-resolution

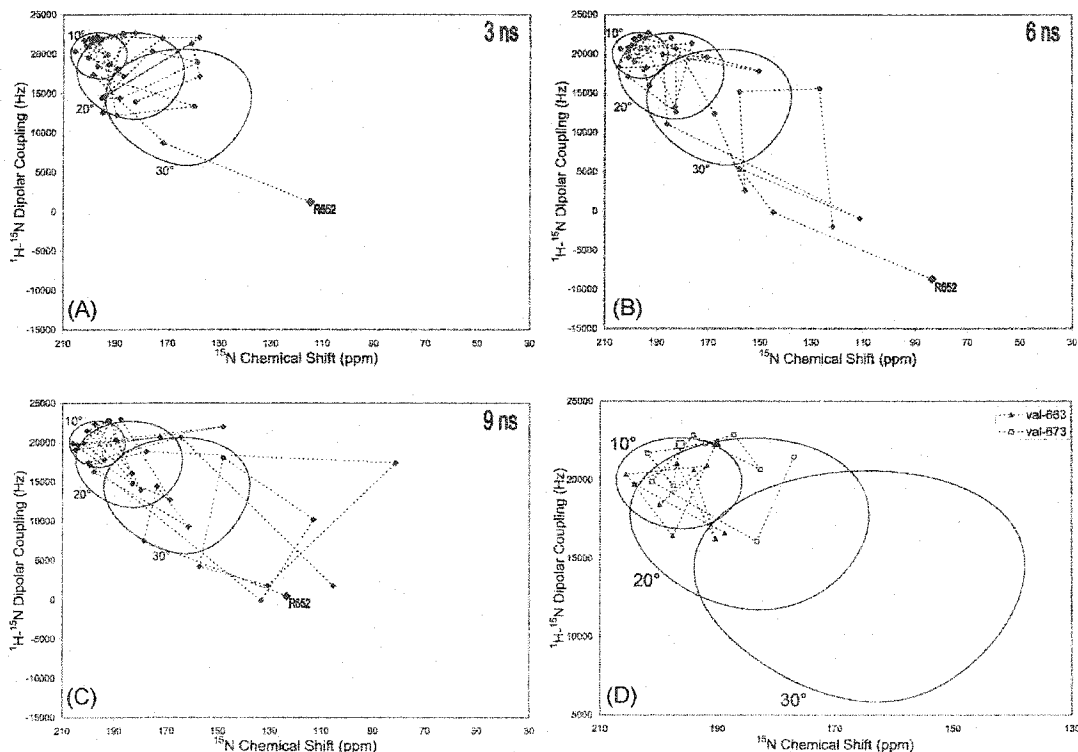


Figure 5.7: Simulated HN/N SLF spectra of the Neu protein transmembrane domain (TMD) using coordinates extracted from the trajectory file of a 10 ns molecular dynamics simulation of the Neu TMD in a fully hydrated phospholipid bilayer [132]. Snap-shots taken: (A) 3 ns into the simulation; (B) 6 ns into the simulation; (C) 9 ns into the simulation. (D) The peaks corresponding to two of the residues located well within the stable α -helical core of the TMD. The solid symbols are for Val-663 while the open symbols are for Val-673. In (A), (B) and (C) the dotted lines connect consecutive points according to the primary sequence starting at Arg-652. In (D), the dotted lines connects the positions of the peaks chronologically based on the 10 snapshots from 1 ns (large symbol) to 10 ns. The solid curves in all figures show the expected locus of points as ρ is varied, for an ideal helix tilted at the angles given.

NMR is based on measurements of internuclear J-couplings, internuclear nuclear Overhauser effect distance restraints, and most recently, small residual internuclear dipolar couplings. Refinement protocols again introduce known bond length and angle distributions and interatomic molecular potential functions. Although there is a qualitative difference in the type of information obtained from the two types of experiments, diffraction vs solution NMR, both can be effectively used to generate "high resolution" molecular structures. The principal difference between the structures obtained is that the NMR structures show the influence of molecular motion more readily. For this reason, a family of structures consistent with the NMR restraints is usually generated.

The situation with solid-state NMR is fundamentally different. Here one can measure orientational restraints as well as distance restraints. In order to convert orientational restraints to atomic positions it is necessary to use standard peptide geometry. In so doing, it will be important to include bond angle variability just as is done in diffraction and solution state NMR structure refinement. Since the experiments measure average or residual second rank tensor couplings, the effect of molecular motion is inherently contained in the raw data. This too must be included when modelling the molecular structure.

This chapter illustrates how structural variability and dynamic effects can influence the measured tensor couplings through the use of simulations of SLF NMR spectra. From these sorts of examples, the nature of the problems presented in using solid-state NMR to study protein molecular structure becomes clear. The more difficult problem is learning how to include these effects and ultimately arrive at a high resolution protein structure.



*- Wissenschaft und Kunst gehören
der Welt. Vor ihnen verschwinden
die Schranken der Nationalität.*

- Johann Wolfgang von Goethe

Rotating frame spin-lattice relaxation of small membrane polypeptides

6.1 Introduction

Important advances in high-resolution transmembrane protein structure studied by NMR have taken place over the last decade through the use of liquid-state techniques for detergent-protein micellar complexes [133] and of several solid-state approaches for lipid-dispersed or other types of “static” samples [35, 38, 121]. Still, the complexity of the problem of solving membrane-associated protein structures has limited the application of NMR techniques mostly to relatively small proteins, usually spanning the membrane only once and generally on the order of 3-10 kDa in size. For comparison, most G protein-coupled receptors, ion channels or multidrug-resistance protein pumps are large protein units, which are constituted from up to dozens of topological transmembrane segments, and usually with molecular masses on the order of several hundred kDa. Nevertheless, small membrane polypeptides or protein segments represent an interesting class of relevant biological structures serving important functions. These include antibacterial cytotoxins, growth factor receptors and surface antigens of cells and viruses. Furthermore, they are indispensable models systems for developing novel NMR techniques as well as for understanding transmembrane folding intermediates for larger membrane-associated proteins. For example, among the small membrane polypeptides most studied by NMR are the 4-kDa gA dimer [24, 91, 115], the 3-kDa transmembrane region of the M2 coat protein of the

influenza A virus [134, 135], the 4-kDa Neu/Erb-B2 membrane spanning segment [131, 136], the 10-kDa glycophorin A transmembrane dimer [15], the 6-kDa Fd major coat protein [16, 137], and other antibiotic/hemolytic polypeptides such as the 3-kDa magainin [138], zervamicin [139], alamethicin [140], etc. On the other hand, these proteins have been mostly inaccessible to X-ray crystallography and other diffraction techniques.

The study of the structure of these molecules by NMR techniques is complicated by the unusual molecular dynamics existing in liquid crystals such as membrane bilayers. Unlike species in solution, components of these phases are unable to reorient isotropically. This important characteristic allows for the persistence of orientation-dependent NMR interactions, namely the chemical shift anisotropy, the dipole-dipole interaction and the quadrupolar interaction for $\text{spin} \geq 1$, which usually affect the NMR spectra of such systems by severely broadening the resonance lines. However, these mutually restrained molecules are very dynamic, albeit in an anisotropic way, and their characteristic motional rates cover several orders of magnitude. Like all biomolecules at physiological temperatures, they undergo rapid small-amplitude internal conformational changes involving vibrational modes and isomerizations in the ps to ns time-range. In fluid membrane phases, they are also known to undergo intermediate scale (ns to ms) whole-body motions, such as lateral translation and axial diffusion. They are further subjected to slower scale off-axis reorientational motions on the order of μs to ms due to single molecule “wobble” or collective membrane undulation.

These dynamic variations of the molecule have important implications for the feasibility and interpretation of most NMR experiments. For instance, all motions with correlation times faster than the NMR spectroscopic time scale and which effectively causes a variation of the strength of the interaction have the effect of averaging the expression of this interaction on the resulting NMR spectrum. In Chapter 5, the simulations show how rapid motions such as whole-body axial diffusion and off-axis reorientation or peptide-plane libration influence HN/N (PISEMA) experiments (Figure 5.6).

Another consequence of motions occurs when a modulation of the residual amplitude of an interaction takes place at a rate close to that of the key spin transition frequencies. If this is the case, the motions provide a relaxation mechanism for the spin system back to equilibrium. Thus, the presence or absence of these motions can impose important limitations on the application of routine techniques. Indeed, fast transverse relaxation (T_2) results in poor spectral resolution and slow longitudinal relaxation (T_1) imposes a longer repetition delay. The relevant relaxation mechanism studied in this chapter is that of the spin coherence along an applied rf field of effective frequency, ω_e . It is referred to as the spin-lattice relaxation in the rotating frame and characterized by the time constant $T_{1\rho}$. The rate of this relaxation has important implications on the performance of key pulse sequence elements such as SL pulses, CP and isotropic mixing sequences.

Because of the large impact of motions on the spectra, NMR spectroscopy is an indispensable tool to study dynamics. In one case, the extent of the spectral averaging can be related to the geometry of the fast motions. In the second case, the measurement of the relaxation rates can provide invaluable information about the amplitude and rate of motions.

In this chapter, a series of $T_{1\rho}$ measurements is compiled for gA and other α -helical polypeptides with a hydrophobic stretch long enough to span a membrane bilayer. The relative contributions of the residual chemical shift anisotropy and dipole-dipole interaction to the rotating-frame relaxation process are reported for backbone and side-chain ^1H , as well as backbone ^{13}C and ^{15}N , under MAS. Finally, through simple models, the characterization of the mechanism of this relaxation process is proposed based on measurements in oriented samples.

6.2 Theory

6.2.1 Spin-lattice relaxation in the rotating frame

This chapter presents a series of relaxation experiments for different nuclear spin species present in short polypeptide chains dispersed in phospholipid bilayers in the

fluid phase. More specifically, this is a study of the effect of motions within these bilayers on the spin-lattice relaxation in the rotating frame, defined by the relaxation time $T_{1\rho}$. As will be seen, this relaxation depends both on the motional correlation times, τ_c , and on the size of the fluctuations in the mean squared strength (or second moment), ΔM_2 . The motions that specifically contribute to this type of relaxation have correlation times within about two orders of magnitude of the inverse magnitude of the applied rf, referred to below as ω_1 . Throughout this chapter, the use of the somewhat loose terms “low-frequency” or “slow” is restricted to motions that fall within this time-scale interval, usually of the order of 10^{-6} to 10^{-2} seconds. By contrast, “fast” motions are simply comparatively faster. Because of the co-existence of these fast and slow anisotropic motions, it is necessary to clarify that the term “reduced second moment” refers to the remaining effective mean squared interaction strength, already reduced by fast fluctuations, yet modulated by the slower ones.

To interpret the data, it is necessary to develop a theory of the evolution of magnetization in the presence of a rotating rf field for a partially ordered system like membranes. This theory has been developed by Peng *et al.* [141] specifically for the chemical shift anisotropy (CSA) of ^{19}F -labels in a ^{19}F -NMR study of fluorinated phospholipids in oriented lipid bilayers. With few modifications and corrections, their description is extended to the following interactions existing in membrane polypeptides: (1) the chemical shift anisotropy (dominant in $^{13}\text{C}'$, ^{15}N), (2) the homonuclear ^1H - ^1H dipolar coupling, and (3) heteronuclear dipolar couplings of $^{13}\text{C}'$, ^{15}N with surrounding ^1H . Also, a more general approach is taken in order to include samples with bilayers either oriented between glass-plates or randomly dispersed in a MAS rotor.

6.2.2 The spin-lattice relaxation in the rotating frame ($T_{1\rho}$) for oriented systems

Before describing the dependence of the rotating-frame relaxation on individual interactions and sample configurations, a slight modification of the general expression for the interaction Hamiltonian (Equation 2.18) is needed to consider the spin evo-

lution under an applied rf field. Here, the notation of the Hamiltonian for an interaction λ still involves the product of irreducible spherical operators, namely the spin-independent spatial operators, \mathcal{F} , and the spatially-independent spin operators, \mathcal{T} :

$$\mathcal{H}_\lambda^\rho = \sum_k \sum_{m=-k}^k (-1)^m \mathcal{T}_{km,\lambda}^\rho \mathcal{F}_{k-m,\lambda}^L. \quad (6.1)$$

The difference lies in the choice of unifying reference frames. Whereas the space-dependent operator is still defined relative to the static magnetic field (L frame), the spin angular momentum in the operator $\mathcal{T}_{2m,\lambda}^\rho$ is now evolving in the double-rotating tilted frame (DRTF) with index ρ , defined by the effective field. Following Blicharski [142], a second type of transformation is introduced for the spin operator, \mathcal{T} , also shown in Figure 2.2 (p. 22). This is described by the following expression:

$$\mathcal{T}_{km}^\rho = \sum_{n=-k}^k \mathcal{T}_{kn}^L \mathcal{D}_{nm}^{(k)}(\Omega_{L\rho}(t)), \quad (6.2)$$

where:

$$\Omega_{L\rho}(t) = (\alpha_{L\rho}(t), \beta_{L\rho}, \gamma_{L\rho}(t)). \quad (6.3)$$

The angular Euler components of Equation 6.3 depend on three distinct frequencies: the Larmor frequency of the observed nuclear spin (ω_0), the applied rf field intensity (ω_1) and its frequency (ω_{rf}). Also defined therein are the offset frequency (ω_{off}) and the effective field frequency (ω_e):

$$\alpha_{L\rho}(t) = \omega_0 t, \quad (6.4)$$

$$\beta_{L\rho} = \arctan\left(\frac{\omega_1}{\omega_0 - \omega_{rf}}\right) = \arctan\left(\frac{\omega_1}{\omega_{off}}\right), \text{ and} \quad (6.5)$$

$$\gamma_{L\rho}(t) = \left(\sqrt{(\omega_{off})^2 + (\omega_1)^2}\right) t = \omega_e t. \quad (6.6)$$

Often, the rf field is applied on resonance ($\omega_{off} = 0$), so that $\beta_{L\rho} = 90^\circ$ and $\omega_e = \omega_1$.

In second order perturbation theory [40], the evolution of the ensemble average of a spin operator will only depend on its commutation with the fluctuating part of the Hamiltonian. For anisotropic motions, the fluctuating part of the Hamiltonian, $\Delta\mathcal{H}$, is given by the difference between the full Hamiltonian and its time-independent

part, or more succinctly:

$$\Delta\mathcal{H}_\lambda^\rho = \mathcal{H}_\lambda^\rho - \langle\mathcal{H}_\lambda^\rho\rangle_t. \quad (6.7)$$

where $\langle\rangle_t$ represents the average over the motions in question.

$T_{1\rho}$ is the exponential decay time constant for the relaxation of longitudinal magnetization in the rotating frame ($d\langle I_z^\rho\rangle/dt = -(1/T_{1\rho})\langle I_z^\rho\rangle$). It follows that it can be calculated starting from the time-derivative of a spin operator I_z^ρ , as described in Abragam [40, Chapter 8], but applied to the Hamiltonian in the DRTF (ρ):

$$\begin{aligned} \frac{d\langle I_z^\rho\rangle}{dt} &= \int_0^\infty \langle [\Delta\mathcal{H}_P^\rho(t), [\Delta\mathcal{H}_\lambda^{\rho*}(t+\tau), I_z^\rho]] \rangle d\tau, \\ &= \sum_{m=-k}^k \sum_{n=-k}^k [T_{kn}^L, [T_{kn}^{L*}, I_z^\rho]] (d_{nm}^{(k)}(\beta_{L\rho}))^2 \int_0^\infty G_m(\tau) \cdot e^{-i(m\omega_0+n\omega_e)\tau} d\tau. \end{aligned} \quad (6.8)$$

For simplicity, the spin operator superscript ρ is dropped from here on. The parameter $G_m(\tau)$ corresponds to the autocorrelation function of the m^{th} spatial term \mathcal{F}_{2m}^L in the laboratory frame:

$$\begin{aligned} G_m(\tau) &= \langle \mathcal{F}_{2m}^L(t) \mathcal{F}_{2m}^{L*}(t+\tau) - |\langle \mathcal{F}_{2m}^L \rangle_t|^2 \rangle \\ &= \sum_{m'} |\mathcal{F}_{2m'}^P|^2 g_{m'm}^{PL}(\tau), \end{aligned} \quad (6.9)$$

for which

$$g_{m'm}^{PL}(\tau) = \mathcal{D}_{m'm}^{(2)}(\Omega_{PL}(t)) \mathcal{D}_{m'm}^{(2)*}(\Omega_{PL}(t+\tau)) - |\langle \mathcal{D}_{m'm}^{(2)}(\Omega_{PL}) \rangle|^2 \quad (6.10)$$

$$= \left(|\langle \mathcal{D}_{m'm}^{(2)*}(\Omega_{PL})|^2 \rangle - |\langle \mathcal{D}_{m'm}^{(2)*}(\Omega_{PL}) \rangle|^2 \right) e^{-\tau/\tau_c}. \quad (6.11)$$

The definitions in Equation 6.9 to 6.11 are based on the assumption that all the interaction fluctuations are orientational in nature (rather than related to internuclear distances, chemical exchanges, torsion angles, for example) and thus, the autocorrelation functions, $g_{m'm}$, depend only on the time variations of the Euler angles as shown in Equation 6.10. The passage from Equation 6.10 to Equation 6.11 is possible if one assumes a simple exponential form of the autocorrelation function. The associated spectral density function $J_{m'm}^{PL}(\omega)$ is given as the Fourier transform of the

autocorrelation function:

$$J_{m'm}^{PL}(\omega) = 2 \int_0^\infty g_{m'm}^{PL}(\tau) e^{-i\omega\tau} d\tau. \quad (6.12)$$

In the simple exponential form, the autocorrelation function yields a spectral density in the form of a Lorentzian function with the correlation time (τ_c) and represented hereafter by $j(\omega)$ ¹:

$$J_{m'm}^{PL}(\omega) = 2\langle\Delta\mathcal{D}_{m'm}^{PL2}\rangle \frac{\tau_c}{1 + \omega^2\tau_c^2} = 2\langle\Delta\mathcal{D}_{m'm}^{PL2}\rangle j(\omega), \quad (6.13)$$

where the short form $\langle\Delta\mathcal{D}_{m'm}^{XY2}\rangle$ is defined by the general equation:

$$\langle\Delta\mathcal{D}_{m'm}^{XY2}\rangle = \langle|\mathcal{D}_{m'm}^{(2)}(\Omega_{XY})|^2\rangle - |\langle\mathcal{D}_{m'm}^{(2)}(\Omega_{XY})\rangle|^2, \quad (6.14)$$

which relates to the fluctuation of the Hamiltonian, introduced in Equation 6.7.

When $\omega_0 \gg \omega_e$, and assuming that only slow motions ($1/\tau_c \simeq \omega_e$) contribute significantly to the spin-lattice relaxation in the rotating frame, all terms except those with $m = 0$ in Equation 6.8 can be neglected, leading to a final expression of the relaxation rate in the rotating frame:

$$\frac{1}{T_{1\rho}} = \frac{1}{\langle I_z \rangle} \sum_{n=-2}^2 \sum_{m'=-2}^2 [T_{2n}^L, [T_{2n}^{L*}, I_z]] (d_{n0}^{(2)}(\beta_{L\rho}))^2 |\mathcal{F}_{2m'}^P|^2 \langle\Delta\mathcal{D}_{m'0}^{PL2}\rangle j(n\omega_e). \quad (6.15)$$

The following four subsections present the results of the derivation of the expression of the spin-lattice relaxation rate specifically due to fluctuating CSA and dipole-dipole interactions in oriented and MAS samples. A full derivation for each of these cases can be found in the Appendix B (p. 244).

6.2.2.1 Chemical shift anisotropy in oriented membranes

The first interaction developed is that of the CSA. Because of the transformation in spin space applied to the \mathcal{T}_{km} defined in Equation 6.2, the first rank tensor representation of \mathcal{H}_{CS} [41], already defined at the end of Section 2.3.3 (Equation 2.42 on p. 28), must be used. Furthermore, only a first rank Wigner rotation matrix, $\mathcal{D}_{m'm}^{(1)}(\Omega)$ [45],

¹ The definitions presented in Equations 6.9 through 6.13 for $g(\tau)$ and $G(\tau)$ and for $j(\omega)$ and $J(\omega)$ are slightly different from the strict definitions given by Abragam in Chapter 8 [40]

is used giving the expression of the spin-part of the CSA interaction in the rotating frame:

$$\mathcal{T}_{1m}^\rho = \sum_{m'=-1}^1 \mathcal{T}_{1m'}^L \mathcal{D}_{m'm}^{(1)}(\Omega_{L\rho}(t)), \quad (6.16)$$

As mentioned previously, the terms varying as $\omega_0 t$ or $(\omega_0 \pm \omega_e)t$ in the full expression of the chemical shift Hamiltonian, \mathcal{H}_{CS} , do not significantly contribute to $\mathcal{T}_{1\rho}$. Then, the general expression for this Hamiltonian reduces to:

$$\begin{aligned} \mathcal{H}_{CS}^\rho = & \frac{1}{24} \gamma B_0 \delta \times \\ & \left(\sin(\beta_{L\rho}) [I_+ e^{-i\omega_e t} + I_- e^{i\omega_e t}] \times \right. \\ & \quad \left(6\sqrt{3} \mathcal{D}_{00}^{(2)}(\Omega_{PL}(t)) - 3\sqrt{2} \eta \left(\mathcal{D}_{20}^{(2)}(\Omega_{PL}(t)) + \mathcal{D}_{-20}^{(2)}(\Omega_{PL}(t)) \right) \right) \\ & + \cos(\beta_{L\rho}) I_z \times \\ & \quad \left. \left(24 \mathcal{D}_{00}^{(2)}(\Omega_{PL}(t)) - 4\sqrt{6} \eta \left(\mathcal{D}_{20}^{(2)}(\Omega_{PL}(t)) + \mathcal{D}_{-20}^{(2)}(\Omega_{PL}(t)) \right) \right) \right). \end{aligned} \quad (6.17)$$

The expression for the inverse of the spin-lattice relaxation time constant ($1/T_{1\rho}^{CS}$) can be obtained from Equation 6.8 for a partially ordered system with a fixed sample orientation, Ω_{NL} [40]:

$$\begin{aligned} \frac{1}{T_{1\rho}^{CS}} = & \frac{1}{16} \gamma^2 B_0^2 \delta^2 \sin^2(\beta_{L\rho}) \times \\ & \int_0^\infty \cos \omega_e \tau d\tau \sum_{m=-2}^2 \left| \mathcal{D}_{m0}^{(2)}(\Omega_{NL}) \right|^2 (12g_{0m}^{PN}(\tau) + 2\eta^2 (g_{2m}^{PN} + g_{-2m}^{PN})) \end{aligned} \quad (6.18)$$

where the correlation functions, g_{pq}^{PN} , is defined as in Equation 6.10 but for the P→N transformation.

Introducing here two sets of three generic coefficients ($\mathcal{A}_0, \mathcal{A}_1, \mathcal{A}_2$ and $\mathcal{B}_0, \mathcal{B}_1, \mathcal{B}_2$) which depend on the fluctuating Wigner operators described by $\langle \Delta \mathcal{D}_{0m}^{PN2} \rangle$ and $\langle \Delta \mathcal{D}_{\pm 2m}^{PN2} \rangle$, a complete expression of $1/T_{1\rho}^{CS}$ useful for the interpretation of CSA fluctuations in oriented membrane samples is obtained:

$$\begin{aligned} \frac{1}{T_{1\rho}^{CS}} \Big|_{oriented} = & \frac{1}{32} \gamma^2 B_0^2 \delta^2 \sin^2(\beta_{L\rho}) j(\omega_e) \left[\begin{aligned} & (6\mathcal{A}_0 + \eta^2 \mathcal{B}_0) \quad (3 \cos^2 \beta_{NL} - 1)^2 \\ & + (6\mathcal{A}_1 + \eta^2 \mathcal{B}_1) \quad 3 \sin^2 2\beta_{NL} \\ & + (6\mathcal{A}_2 + \eta^2 \mathcal{B}_2) \quad 3 \sin^4 \beta_{NL} \end{aligned} \right], \end{aligned} \quad (6.19)$$

where

$$\begin{aligned}
\mathcal{A}_0 &= \langle \Delta \mathcal{D}_{00}^{PN^2} \rangle \\
\mathcal{A}_1 &= \langle \Delta \mathcal{D}_{01}^{PN^2} \rangle = \langle \Delta \mathcal{D}_{0-1}^{PN^2} \rangle \\
\mathcal{A}_2 &= \langle \Delta \mathcal{D}_{02}^{PN^2} \rangle = \langle \Delta \mathcal{D}_{0-2}^{PN^2} \rangle \\
\mathcal{B}_0 &= \langle \Delta \mathcal{D}_{20}^{PN^2} \rangle = \langle \Delta \mathcal{D}_{-20}^{PN^2} \rangle \\
\mathcal{B}_1 &= \langle \Delta \mathcal{D}_{21}^{PN^2} \rangle + \langle \Delta \mathcal{D}_{-21}^{PN^2} \rangle = \langle \Delta \mathcal{D}_{2-1}^{PN^2} \rangle + \langle \Delta \mathcal{D}_{-2-1}^{PN^2} \rangle \\
\mathcal{B}_2 &= \langle \Delta \mathcal{D}_{22}^{PN^2} \rangle + \langle \Delta \mathcal{D}_{-22}^{PN^2} \rangle = \langle \Delta \mathcal{D}_{22}^{PN^2} \rangle + \langle \Delta \mathcal{D}_{-22}^{PN^2} \rangle.
\end{aligned} \tag{6.20}$$

It is important to note that Equation 6.19 features three terms with differing dependence on β_{NL} . Later a description of the relevance of the $\mathcal{A}_{|m|}$ and $\mathcal{B}_{|m|}$ coefficients is presented for different types of motional models.

6.2.2.2 The direct spin-spin dipolar interaction in oriented membranes.

The other dominant interaction involving spin-1/2 nuclei is the axially symmetric dipole-dipole interaction between spins I and S (either like or unlike) and characterized in Section 2.3.2. A focus on the heteronuclear case ($I \neq S$) is presented here while the homonuclear situation is generalized later.

Following the same procedure as for the CSA, the application of the operators in Equation 2.29 and 2.30 to Equation 6.1 results in the following expression for the dipole-dipole interaction Hamiltonian (after converting to units of s^{-1}):

$$\begin{aligned}
\mathcal{H}_{IS} = \frac{3}{4} \frac{\mu_0}{4\pi} \frac{\gamma_I \gamma_S \hbar}{r_{IS}^3} \mathcal{D}_{00}^{(2)}(\Omega_{PL}(t)) \times \\
\left[\sin^2 \beta_{L\rho} (I_- S_- e^{-2i\omega_e t} - I_+ S_+ e^{2i\omega_e t}) \right. \\
+ \sin 2\beta_{L\rho} ([I_z S_+ + I_+ S_z] e^{-i\omega_e t} + [I_z S_- + I_- S_z] e^{+i\omega_e t}) \\
\left. - (3 \cos^2 \beta_{L\rho} - 1) 2I_z S_z \right]
\end{aligned} \tag{6.21}$$

As before, only the terms with no dependence on ω_0 were preserved.

Since the interaction is axially symmetric, only the $\mathcal{D}_{00}^{(2)}(\Omega_{PL}(t))$ component of the P→L transformation is needed. Furthermore, unlike the CSA, this internuclear interaction requires second rank Wigner rotations for the spin terms, and thus the Hamiltonian is also sensitive to terms in $2\omega_e$.

After applying Equation 6.8 to this interaction and factoring the Wigner transformations to show the dependence on the fixed β_{NL} orientation of the glass-oriented membranes, the expression for $T_{1\rho}^{IS}$ (oriented sample) is obtained:

$$\left. \frac{1}{T_{1\rho}^{IS}} \right|_{\text{oriented}} = \frac{3}{8} \left(\frac{\mu_0}{4\pi} \right)^2 \frac{\gamma_I^2 \gamma_S^2 \hbar^2}{r_{IS}^6} S(S+1) \sin^4(\beta_{L\rho}) j(2\omega_e) \left[\begin{aligned} &\mathcal{A}_0 (3 \cos^2 \beta_{NL} - 1)^2 \\ &+ 3\mathcal{A}_1 \sin^2 2\beta_{NL} \\ &+ 3\mathcal{A}_2 \sin^4 \beta_{NL} \end{aligned} \right]. \quad (6.22)$$

for which \mathcal{A}_0 , \mathcal{A}_1 and \mathcal{A}_2 maintain the definitions stated in Equation 6.20. These coefficients modulate three terms with the same geometrical functions of β_{NL} as in Equation 6.19). It should also be noted that for off-resonance experiments, the relaxation rate varies as a function of $\sin^4(\beta_{L\rho})$, rather than the $\sin^2(\beta_{L\rho})$ form in the equivalent expression for the CSA. Finally, this expression can be extended to the like spin case ($T_{1\rho}^{II'}$), by multiplying this expression by a factor of 2 [40].

6.2.3 The spin-lattice relaxation in the rotating frame ($T_{1\rho}$) for magic angle spinning systems

For samples rapidly rotating at the magic angle, the rotating-frame spin-lattice relaxation will also be sensitive to the coherent motion of the rotor, especially when the spinning rate is of the same order as the effective frequency ($\omega_R \simeq \omega_e$). To obtain a theoretical expression for $T_{1\rho}$ under these conditions, the Wigner rotation $\mathcal{D}_{pq}^{(2)}(\Omega_{PL})$ in the general Equations 6.17 and 6.21 for CSA and dipole-dipole interaction, is first factored into the sub-transformations given in 2.21 and 2.22 (see Figure 2.2, p. 22). The Euler elements of $\Omega_{RL}(t)$ are known as:

$$\alpha_{RL}(t) = \omega_R t, \quad \beta_{RL} = \arctan(\sqrt{2}), \quad \text{and} \quad \gamma_{RL} = 0. \quad (6.23)$$

6.2.3.1 The chemical shift anisotropy in MAS membrane samples

Keeping once again only the terms that modulate the interaction at frequencies near ω_e , the effective Hamiltonian describing the chemical shift interaction in the rotating

frame with MAS can be expressed as:

$$\begin{aligned}
\mathcal{H}_{CS}^{\rho} = & \frac{\sqrt{3}}{48} \gamma \delta B_0 \sin(\beta_{L\rho}) \\
& \times \sum_{m=-2}^2 \left(2\sqrt{3} \mathcal{D}_{0m}^{(2)}(\Omega_{PN}(t)) - \sqrt{2} \eta \left(\mathcal{D}_{2m}^{(2)}(\Omega_{PN}(t)) + \mathcal{D}_{-2m}^{(2)}(\Omega_{PN}(t)) \right) \right) \\
& \times \left(\sqrt{2} \mathcal{D}_{m-2}^{(2)}(\Omega_{NR}) [I_+ e^{-it(\omega_e - 2\omega_R)} + I_- e^{it(\omega_e + 2\omega_R)}] \right. \\
& - 2 \mathcal{D}_{m-1}^{(2)}(\Omega_{NR}) [I_+ e^{-it(\omega_e - \omega_R)} + I_- e^{it(\omega_e + \omega_R)}] \\
& + 2 \mathcal{D}_{m+1}^{(2)}(\Omega_{NR}) [I_+ e^{-it(\omega_e + \omega_R)} + I_- e^{it(\omega_e - \omega_R)}] \\
& \left. + \sqrt{2} \mathcal{D}_{m+2}^{(2)}(\Omega_{NR}) [I_+ e^{-it(\omega_e + 2\omega_R)} + I_- e^{it(\omega_e - 2\omega_R)}] \right). \tag{6.24}
\end{aligned}$$

For further simplicity, the terms that commute with I_z were also omitted since they do not contribute to $T_{1\rho}$.

For a non-oriented sample with a random distribution, the observed magnetization relaxation function in the rotating frame will assume a powder-sum of exponential decays for each orientation of the polypeptide throughout the volume of the sample. The assumption that the polypeptide does not diffuse rapidly between sites with differently-oriented local membrane normal is maintained. It is known however that the *initial* relaxation time constant correspond to the solid-angle integration over Ω_{NR} [143]. Thus, the expression for $T_{1\rho}^{CS}|_{mas}$ due to slow-motion modulation of the anisotropic chemical shift in membrane proteins in a powder average is given by:

$$\begin{aligned}
\left\langle \frac{1}{T_{1\rho}^{CS}} \right\rangle_{powder}^{MAS} = & \frac{1}{240} \gamma^2 \delta^2 B_0^2 \sin^2(\beta_{L\rho}) \times \\
& (j(\omega_e + 2\omega_R) + j(\omega_e - 2\omega_R) + 2j(\omega_e + \omega_R) + 2j(\omega_e - \omega_R)) \times \\
& \sum_{m=-2}^2 (6\mathcal{A}_{|m|} + \eta^2 \mathcal{B}_{|m|}). \tag{6.25}
\end{aligned}$$

In this expression for the relaxation, there are four spectral density functions with combinations of ω_e with $\pm\omega_R$ or $\pm 2\omega_R$. “Resonant features” are expected for the conditions when $\omega_e = 2\omega_R$ and $\omega_e = \omega_R$, at which the relaxation time constant reaches a local minimum.

6.2.3.2 The direct spin-spin dipolar interaction in MAS membrane samples

Equivalently, in an identical sample configuration with a predominant IS dipolar interaction and with fluctuation rates near the applied effective field frequency, the Hamiltonian in the rotating-frame is described by (again keeping only the rotating frame relaxation-relevant terms):

$$\begin{aligned} \mathcal{H}_{IS}^{\rho} = & \frac{\sqrt{3}}{8} \frac{\mu_0}{4\pi} \frac{\gamma_I \gamma_S \hbar}{r_{IS}^3} \sin^2(\beta_{L\rho}) \sum_{m=-2}^2 \mathcal{D}_{0m}^{(2)}(\Omega_{PN}(t)) \times \\ & \left(\sqrt{2} \mathcal{D}_{m-2}^{(2)}(\Omega_{NR}) [I_+ S_+ e^{2it(\omega_e + \omega_R)} - I_- S_- e^{-2it(\omega_e - \omega_R)}] \right. \\ & - 2 \mathcal{D}_{m-1}^{(2)}(\Omega_{NR}) [I_+ S_+ e^{it(2\omega_e + \omega_R)} - I_- S_- e^{-it(2\omega_e - \omega_R)}] \\ & + 2 \mathcal{D}_{m+1}^{(2)}(\Omega_{NR}) [I_+ S_+ e^{it(2\omega_e - \omega_R)} - I_- S_- e^{-it(2\omega_e + \omega_R)}] \\ & \left. + \sqrt{2} \mathcal{D}_{m+2}^{(2)}(\Omega_{NR}) [I_+ S_+ e^{2it(\omega_e - \omega_R)} - I_- S_- e^{-2it(\omega_e + \omega_R)}] \right). \end{aligned} \quad (6.26)$$

The fluctuating part of this Hamiltonian gives rise to the following expression for the time constant, $T_{1\rho}^{IS}$, in a powder distribution under MAS:

$$\begin{aligned} \left\langle \frac{1}{T_{1\rho}^{IS}} \right\rangle_{\text{powder}}^{MAS} = & \frac{1}{20} \left(\frac{\mu_0}{4\pi} \right)^2 \frac{\gamma_I^2 \gamma_S^2 \hbar^2}{r_{IS}^6} S(S+1) \sin^4(\beta_{L\rho}) \times \\ & (j(2\omega_e + 2\omega_R) + j(2\omega_e - 2\omega_R) + 2j(2\omega_e + \omega_R) + 2j(2\omega_e - \omega_R)) \times \\ & \sum_{m=-2}^2 \mathcal{A}_{|m|}. \end{aligned} \quad (6.27)$$

Once again, due to the symmetric nature of the interaction, this expression simplifies to only four spectral density terms with slightly different resonant conditions of $\omega_e = \omega_R$ and $\omega_e = \frac{1}{2}\omega_R$. Also, as for the oriented case, the equivalent homonuclear II' dipolar interaction expression is larger by a factor of 2.

6.2.4 Motional models for intermediate and slow scale dynamics

Motions of phospholipids within biological membranes have been characterized by correlation times spanning over 10 orders of magnitude. Small membrane proteins with molecular weights about 3-4 times that of phospholipids, will necessarily undergo similar types of motions, although they have not been thoroughly studied. It is

speculated that whole-body motions such as translation, axial diffusion and off-axis reorientation dominate the ms to μ s time scale. The effect of translation over a curved surface will only be noticeable when the vesicular radius of curvature approaches $\sqrt{D/4\pi\omega_e}$, where D is the two-dimensional diffusion constant; this effect will be neglected here. Using simple models, the differences in the modes of influence of each specific type of motion on the $T_{1\rho}$ profiles can be highlighted in both oriented and in magic angle spinning samples.

6.2.4.1 Simple axial diffusion model

The $T_{1\rho}$ relaxation due to axial diffusion of the molecule about its moment of inertia principal axis can be calculated by allowing only the angle α_{MN} in the expression of the term $\langle \Delta \mathcal{D}_{pq}^{MN2} \rangle$ to fluctuate with time. These terms can be easily calculated by evaluating:

$$\langle \Delta \mathcal{D}_{pq}^{MN2} \rangle = \frac{1}{2\pi} \int_0^{2\pi} |\mathcal{D}_{pq}^{(2)}(\Omega_{MN})|^2 d\alpha_{MN} - \frac{1}{2\pi} \left| \int_0^{2\pi} \mathcal{D}_{pq}^{(2)}(\Omega_{MN}) d\alpha_{MN} \right|^2 \quad (6.28)$$

which directly yields the correlation coefficients $\mathcal{A}_{|m|}$ and $\mathcal{B}_{|m|}$ according to Equation 6.20. The dependences of these coefficients on the angles β_{PM} and α_{PM} are compared in Figure 6.1(A) and (B) for the case where the helix long axis is parallel to the membrane normal ($\beta_{MN} = 0^\circ$). Whereas \mathcal{A}_0 and \mathcal{B}_0 do not contribute to $T_{1\rho}$, \mathcal{B}_2 dictates its behavior for β_{PM} near 0° , while \mathcal{A}_2 and \mathcal{B}_1 are dominant near a 90° . The effect of \mathcal{A}_1 reaches a maximum near $\beta_{PM} = 45^\circ$.

6.2.4.2 "Diffusion-in-a-cone" model

It is likely that axial diffusion takes place at rates of the order of $10^6 - 10^8 \text{ s}^{-1}$ [130] and thus, it may contribute to $T_{1\rho}$ in a limited way, in as much as the applied field is of the order of a few kHz. However, it may considerably reduce the effective residual interaction for the typically slower off-axis reorientations. These slower motions can be mimicked using a number of models, a common one being the application of an orienting potential about a preferred equilibrium orientation. This has been described by Prosser and Davis [130] and Wittebort and Szabo [144]. Perhaps the simplest, yet

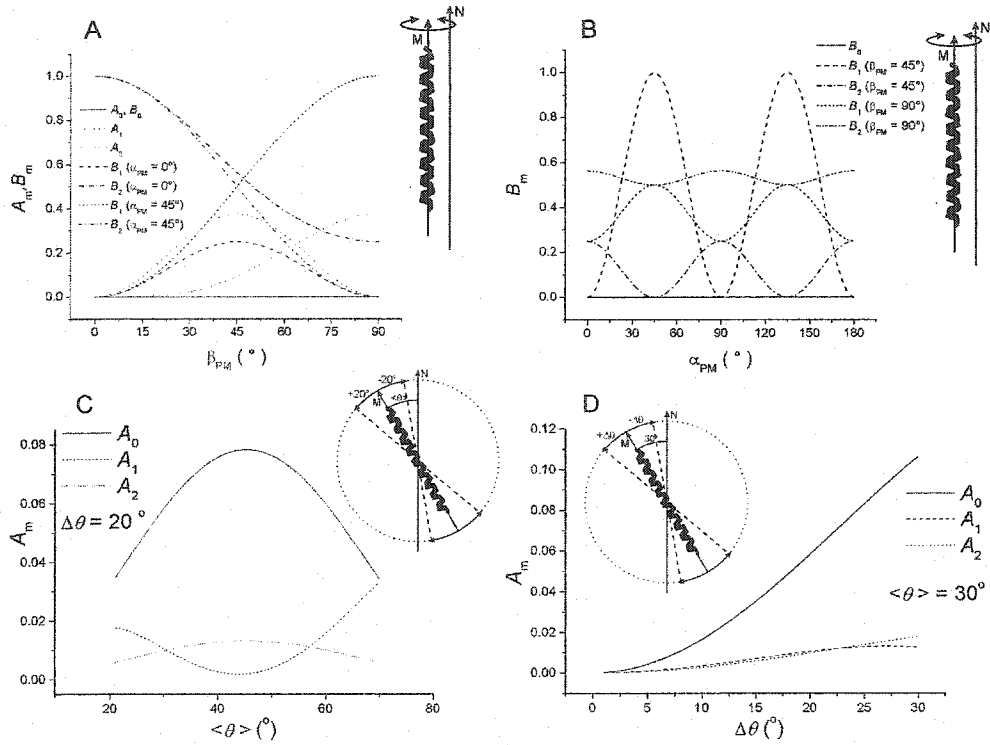


Figure 6.1: Variation of the “correlation” coefficients $A_{|m|}$ and $B_{|m|}$ (Equation 6.20)) on key geometrical angles for the motional models described in the theoretical section. (A) and (B) Variation of $A_{|m|}$ and $B_{|m|}$ on the angles between the interaction PAS and the helix axis, β_{PM} and α_{PM} , for a freely axially diffusing elongated helix with the diffusion axis oriented parallel to the membrane normal according to Equation 6.28. Since only B_1 and B_2 depend on the azimuthal angle α_{PM} , these are plotted for two different sets of angles. Plots (C) and (D) examine the influence of two geometrical parameters in the “diffusion-in-a-cone” model of Equation 6.29. (C) Variation of the three $A_{|m|}$ coefficients as the tilted helix freely diffuses within $\pm 20^\circ$ of the average tilt angle $\langle \theta \rangle$. (D) Variation of the three $A_{|m|}$ coefficients as the tilted helix freely diffuses within $\pm \Delta\theta$ of a fixed average tilt angle of 30° . The inset figures illustrate the range of reorientation (within dashed angles) permitted for each case. They fail, however, to show the full 2π precession allowed around the normal to trace the “cone” volumes.

still useful, model is one where the helix axis is distributed uniformly over some range of angles about an average tilt angle. This “diffusion-in-a-cone” model has also been described by Lipari and Szabo [145], where a single semi-angle $\Delta\theta$ describes the distribution. To allow more flexibility, the model proposed here permits the helix to diffuse between any two tilt angles $\theta_{min} = \langle\theta\rangle - \Delta\theta$ and $\theta_{max} = \langle\theta\rangle + \Delta\theta$ relative to the membrane normal. In other words, the polypeptide molecule director can be tilted at an average angle $\langle\theta\rangle$ and still be allowed to fluctuate about this angle by $\pm\Delta\theta$. In this way, the energetically favorable tilted conformation, often observed when the helix length and the membrane thickness are mismatched, can be mimicked. The expression for the correlation terms $\langle\Delta\mathcal{D}_{pq}^{MN2}\rangle$, thus becomes:

$$\langle\Delta\mathcal{D}_{pq}^{MN2}\rangle = (4\pi \sin\beta_{MN} \sin\Delta\theta)^{-1} \quad (6.29)$$

$$\left[\int_0^{2\pi} \int_{\theta_{min}}^{\theta_{max}} |\mathcal{D}_{pq}^{(2)}(\Omega_{MN})|^2 \sin\beta_{MN} d\beta_{MN} d\gamma_{MN} - \left| \int_0^{2\pi} \int_{\theta_{min}}^{\theta_{max}} \mathcal{D}_{pq}^{(2)}(\Omega_{MN}) \sin\beta_{MN} d\beta_{MN} d\gamma_{MN} \right|^2 \right] \quad (6.30)$$

The evaluation of the coefficients can be simplified when a few simple assumptions are made. Since this motion is typically slower than axial diffusion, at least for small membrane proteins, it is assumed that any residual interaction will be axially symmetric ($\eta=0$) and thus the relaxation will only involve the coefficients \mathcal{A}_0 , \mathcal{A}_1 and \mathcal{A}_2 , even for the CSA. In addition, this axial symmetry simplifies the expression of the first Wigner transformation (Ω_{PM}), since the principal components of this averaged tensor are now coincident with those of the molecular moment of inertia. Figure 6.1(C) and (D) show the dependence of the three coefficients $\mathcal{A}_{|m|}$ on two cone parameters, namely the average tilt angle, $\langle\theta\rangle$, and the amplitude of the angular fluctuation, $\Delta\theta$. These graphs show that the coefficients are small (> 0.05) for a typical transmembrane peptide geometry with the long axis nearly parallel to the membrane normal and fluctuations of $\pm 20^\circ$.

From the relative importance of these coefficients, an intuitive approach to identifying and characterizing some of the principal motional sources of relaxation for small membrane proteins in both oriented and MAS samples is available. However,

this picture is limited to whole-body motions and does not attempt to describe the complex details of local site-specific dynamics in real systems.

6.2.5 Second Moment

The spectral second moment, M_2 , can be calculated for a given spectrum, $f(\omega)$, using:

$$M_2 = \frac{\int_{-\infty}^{\infty} \omega^2 f(\omega) d\omega}{\int_{-\infty}^{\infty} f(\omega) d\omega}. \quad (6.31)$$

In the limit of a perfectly static sample, the second moment takes on a maximum value, M_2^{stat} and for rapidly and completely reorienting sample, the resulting narrow spectrum results in a residual second moment approaching zero. Anisotropic motions have the intermediate effect of partially reducing the spectral second moment, as represented by this simple expression:

$$M_2 = M'_2 + \Delta M_2. \quad (6.32)$$

M_2 is the size of the second moment without the motion and M'_2 is the residual portion after the motional averaging.

The residual second moment represents the mean squared strength of all the interactions (e.g. dipole-dipole, CSA, quadrupolar) averaged by fast spatial fluctuations relative to the NMR time scale. If this total effective M_2 is modulated by anisotropic motions with correlation times near a transition frequency, relaxation occurs across this transition at a rate proportional to the ΔM_2 portion of the above equation [40, Chapter 10]. This term is related to the interaction-specific constant coefficients in front of the spectral density Lorentzian terms $j(\omega)$ in the formulae for the relaxation rates (Equations 6.19, 6.22, 6.25, and 6.27). For the purposes here, two types of motions will be investigated, namely the axial diffusion (*AD*) and the off-axis reorientation (*DC*). Since axial diffusion is more rapid, the two fluctuating portions will be defined in the following order:

$$\Delta M_2|_{AD} = M_2^{stat} - M'_2|_{AD}, \quad (6.33)$$

$$\Delta M_2|_{DC} = M'_2|_{AD} - M'_2|_{DC}. \quad (6.34)$$

For CSA or dipolar interaction between two spins, the fluctuating part of the second moment ΔM_2 can be evaluated in a straightforward way, by subtracting the mean squared strength of the interaction, over all possible geometries sampled by the fast motion from the full second moment without the motion. It can be shown that Equations 6.25, and 6.27 can be rewritten either in terms of the fluctuating portion of the second moment:

$$\left\langle \frac{1}{T_{1\rho}^{CS}} \right\rangle_{\text{powder}}^{MAS} = \frac{1}{8} \Delta M_2 (j(\omega_e + 2\omega_R) \cdots), \quad (6.35)$$

$$= \frac{3}{4} M_2 \left(\sum_{m=-2}^2 6\mathcal{A}_{|m|} + \eta^2 \mathcal{B}_{|m|} \right) (j(\omega_e + 2\omega_R) \cdots), \quad (6.36)$$

$$\left\langle \frac{1}{T_{1\rho}^{IS}} \right\rangle_{\text{powder}}^{MAS} = \frac{3}{16} \Delta M_2 (j(2\omega_e + 2\omega_R) \cdots), \quad (6.37)$$

$$= \frac{3}{16} M_2 \sum_{m=-2}^2 \mathcal{A}_{|m|} (j(2\omega_e + 2\omega_R) \cdots). \quad (6.38)$$

For the complex case where a spin I ($1/2$) interacts with n spins S ($1/2$) simultaneously, the total dipolar second moment is evaluated by summing the orientation-dependent contribution of each dipolar-coupled spin S . This can be done in the static case and in the situation where the polypeptide helix is undergoing rapid axial diffusion around its long axis:

$$M_2^{stat} = \frac{1}{3} \left(\frac{\mu_0}{4\pi} \right)^2 \gamma_I^2 \gamma_S^2 \hbar^2 S(S+1) \frac{1}{n} \sum_{k=1}^n \frac{(3 \cos^2 \beta_{PL,k} - 1)^2}{r_k^6} \quad (6.39)$$

$$M_2'_{AD} = \frac{1}{12} \left(\frac{\mu_0}{4\pi} \right)^2 \gamma_I^2 \gamma_S^2 \hbar^2 S(S+1) \frac{1}{n} (3 \cos^2 \beta_{ML} - 1)^2 \times \sum_{k=1}^n \frac{(3 \cos^2 \beta_{PM,k} - 1)^2}{r_k^6} \quad (6.40)$$

Equation 6.39 was first suggested by Van Vleck [146] for the purposes of measuring the second moment in a CaF_2 crystal, where $\beta_{PL,k}$ is the angle between the PAS of the k^{th} spin-pair and the magnetic field. This equation was extended to an axially reorienting molecule in Equation 6.40, where $\beta_{PM,k}$ is the angle between the PAS of the k^{th} spin-pair and the axis of reorientation and β_{ML} is the angle between the reorienting helix and the magnetic field. Using PDB coordinates of the model transmembrane peptide

gA in the right-handed single helix N-to-N dimer conformation (PDB:1mag) and for an ideal 16-mer polyleucine α -helix (with $\Psi = -65^\circ$ and $\Phi = -40^\circ$), the dipolar interaction second moment was evaluated for a representative backbone amide ^{15}N (Val-8 of gA) and the carbonyl ^{13}C (Leu-8 of L16). The contour maps in Figure 6.2 show the values of the second moment of each of these interactions, for all possible orientation of the polypeptide molecule, either static or undergoing axial diffusion. The regions of large second moment correspond to the helix orientation for which the vector of an IS pair in close proximity ($\text{N}^i \rightarrow \text{H}_N^i$ for gA and $\text{C}'^i \rightarrow \text{H}_\alpha^i$ and $\text{C}'^i \rightarrow \text{H}_N^{i+1}$ for L16) is aligned with the magnetic field. These maps are useful as they represent the second moment space “sampled” by the molecule as it reorients in 3D due to whole body motions. It also allows a comparison of the extent of averaging leading to residual second moment due to axial diffusion. These values may be used as guidelines for predicting the correlation times from the $T_{1\rho}$ experiments.

6.3 Materials and Methods

6.3.1 Lipids

L- α -dimyristoylphosphatidylcholine (DMPC), non-deuterated ($M_r = 635$ Da) or chain- and head-group deuterated ($M_r = 702$ Da), were purchased from Avanti Polar Lipids (Alabama, USA) and used without further purification. Chain deuterated DMPC- d_{54} was synthesized as described in [59].

6.3.2 Polypeptides

$^{13}\text{C}'_{16}$ -polyleucine peptide (L16): A polypeptide with the amino acid sequence acetyl-K₂GL₁₆K₂A-amide, ^{13}C -labelled on all leucine-carbonyl groups C' , was produced by solid-phase synthesis using Boc chemistry on benzhydrylamine resin, as reported elsewhere [147].

^{15}N -gA: The 16-residue gA polypeptide, with alternating L- and D- amino acids, formyl-VGALAV₃(WL)₃W-ethanolamine, was biosynthesized with uniform 100% ^{15}N -labelling, according to the protocol described in Section 3.1 (p. 32).

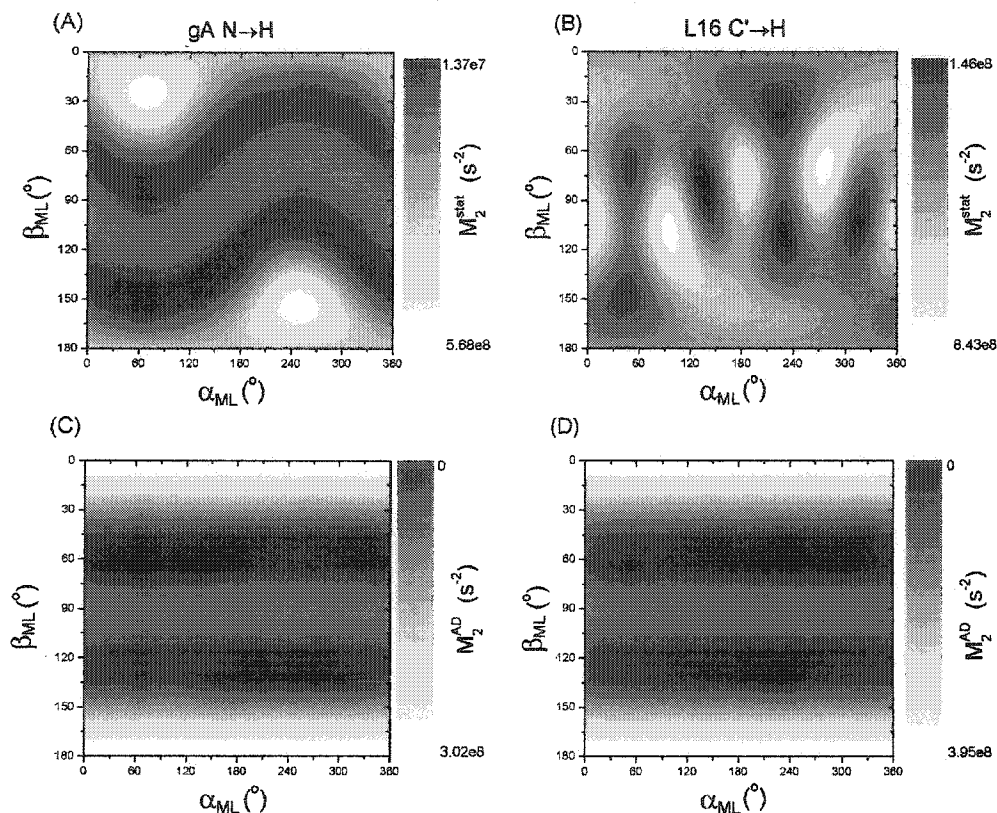


Figure 6.2: Second moment contour maps for the heteronuclear dipolar interaction (A,C) for the $^1\text{H}_x$ - ^{15}N of residue Val-8 of gA in the PDB:1mag conformation and (B,D) for the $^1\text{H}_x$ - $^{13}\text{C}'$ of residue Leu-8 of L16 in the ideal α -helix conformation, where $^1\text{H}_x$ are all the surrounding hydrogens. The maps in show (A,B) the asymmetric distribution of the static case and (C,D) the symmetric distribution of the freely diffusing helix around its long axis. The two axes represent the tilt (β_{ML}) and azimuthal (α_{ML}) angles of the helix moment of inertia principal axis (long axis) with the magnetic field. The light areas represent large second moment (indicating the direction of a neighboring ^1H) and the darker areas represent small second moment. The limits on the linear intensity scale indicate the maximum and minimum dipolar second moment for each case.

ALGA polypeptide: A 21-residue polypeptide chain with the amino acid sequence, acetyl-KKPVALIFAL¹⁰-GALAFILAGK²⁰-R-amine (called ALGA for the middle four residues), was produced by solid-phase synthesis using Fmoc chemistry. No further purification was necessary, since the majority of the resin-cleaved product showed no contaminating peaks by high-resolution ¹H NMR of ALGA in TFE (see Figure 6.7(B)). This sequence was designed to artificially mimic the hydrophobic transmembrane segment of a protein while promoting NMR spectral dispersion by avoiding the repetition of any succession of three residues along the primary sequence.

Neu-36: The 36-residue polypeptide chain encompassing the putative transmembrane region of the Neu/ErbB-2 receptor protein (sequence: QRASPVTFFI¹⁰-ATVVGVLFLI²⁰-LVVVVGILI³⁰-KRRRQK) was prepared by solid-phase synthesis using Fmoc chemistry, and purified by reversed-phase chromatography [131].

6.3.3 Sample Preparation:

Two types of samples were prepared for the work presented in this chapter: uniformly-oriented bilayers stacked between glass plates, and multilamellar “powder” samples rotated in the magic angle spinning condition.

Disordered multilamellar dispersion: For gA, ALGA, Neu-36 and Leucine-16 multilamellar dispersion samples, protein to lipid molar ratios of were prepared by co-dissolving the lipid and protein species in CHCl₃/MeOH (1:1 v/v) or trifluoroethanol and retrieved by evaporating the solvent under reduced pressure for several hours. The samples were rehydrated with potassium phosphate buffer (50 mM, pH 6.5; volume equal to 75 % of the dry sample mass), and then rigorously homogenized mechanically with a stainless steel rod. The viscous samples were then transferred to a 4-mm MAS rotor by centrifugation.

Oriented lamellar samples: For each sample, 8 mg of ¹³C-L16 and 80 mg of DMPC (1:33 mol/mol) were dissolved in 3 mL of MeOH/H₂O (9:1 v/v) and applied evenly onto 16 dust-free glass plates and allowed to dry at 40 °C under vacuum for several hours. The surface of the plates were then lightly hydrated with a few μ L of H₂O and stacked. The stacked sample was carefully placed in a 60 °C high-humidity

incubator overnight, after which the sample was annealed by alternately hydrating (at 57 °C for 21 h) and vacuum drying (at 25 °C for 3 h), until it oriented. Oriented samples, assessed by their transparency, were obtained on average after 3 d and were sealed in a cylindrical glass tube.

6.3.4 NMR experiments:

The ^1H $T_{1\rho}$ measurements on (^{15}N)-gA, ALGA and Neu-36 polypeptide chains in multilamellar dispersion were obtained on a Bruker Avance spectrometer (11.7 T), implemented with a 2-channel HR-MAS tuned at 500.13 MHz for ^1H . The spectra were acquired by applying a simple SL experiment ($[90_{\phi_1}]-[\text{SL}(\tau)_{\phi_2}]-[\text{acquisition}_{\phi_3}]$), where the SL pulse has a field amplitude of $\hbar\omega_1/\gamma_H$ and with frequency ω_{rf} offset by ω_{off} from the carrier frequency ω_0 tuned to the resonant frequency of the water peak at the centre of the 20-ppm spectrum (see Section 6.2.2 for description of these frequencies). The 90° -pulse was typically 2.43 μs and the recycling delay 2 s. The SL was applied for incremental values of τ between 0 and 20 ms, for each of which the signal from 128 scans was summed. A simple $\phi_1=[x,-x], \phi_2=[y,y], \phi_3=[x,-x]$ phase-cycling scheme was used.

The ^{15}N and ^{13}C $T_{1\rho}$ measurements on gA and L16 were achieved by means of the general pulse scheme ($[90_{\phi_1}^H]-[\text{CP}_{\phi_2}^H/\text{CP}_{\phi_3}^X]-[\text{SL}(\tau)_{\phi_4}^X]-[\text{H-decoupling/acquisition}_{\phi_5}]$).

For MAS ^{15}N -gA, the experiment was carried out on an Bruker Avance system, implemented with a 3-channel Doty probe tuned at 600.13 MHz for hydrogen and 60.82 MHz for nitrogen. Typical 90° pulse lengths were 5.2 μs and 17.2 μs . CP was optimized with two matched 0.2-ms rf pulses ($\omega_1 = 14.5$ kHz) on both channels. A typical experiment required 256 scans with a 2 second repetition time. ^1H -decoupling was accomplished using the XiX scheme [81], with a t_p/τ_R ratio of 1.85. The simple phase-cycling included phases: $\phi_1=[y,-y], \phi_2=[x], \phi_3=[x], \phi_4=[x]$ and $\phi_5=[x,-x]$.

The oriented experiments on ^{13}C -L16 were performed on a home-built H/X 2-channel static probe tuned at 360.010 MHz for hydrogen and 90.535 MHz for carbon. The 90° pulses were 5.63 μs and 8.0 μs . A 2-ms CP contact was matched with rf of about 8 kHz. A typical experiment required 600 scans with a repetition delay of

4.2 s. Straightforward CYCLOPS [148] phase-cycling was performed. ^1H decoupling was achieved using a continuous wave rf during acquisition.

6.4 Results and Discussion

6.4.1 $T_{1\rho}$ of ^1H of polypeptides in phospholipid bilayers under MAS

A series of $T_{1\rho}$ measurements was performed using a simple $(90)_x\text{-(SL)}_y$ -acquisition type experiment (see Section 3.4.3.5, p. 58). Figure 6.3 illustrates typical signal loss after prolonged SL pulses. Both (A) and (B) show ^1H MAS spectra ($\nu_R = 14$ kHz) of gA in DMPC- d_{67} (1/20 mol/mol) in 43% (v/w) deuterated P_i buffer (50 mM, pD 6.5) at 55°C , with the lock pulse applied on-resonance at an intensity equivalent to 40 kHz. The bottom spectrum (A) displays the ^1H NMR signal obtained after only 0.2 ms of SL, with resolvable ^1H resonances associated with the aromatic side chains and formyl group (6-8 ppm), the backbone α -hydrogens (5-6 ppm) and other aliphatic hydrogens (0-4 ppm). The larger peaks represent residual lipid and water ^1H resonances. The labile amide and indole hydrogens were exchanged with deuterium and are absent from this spectrum. The top spectrum (Figure 6.3 (B)) represents the residual signal after a 20 ms SL pulse. It is clearly seen that most of the polypeptide signal has relaxed away, whereas the majority of the phospholipid ^1H signal persists. The eradication of the protein signal demonstrates an important difference in the geometry and rates of motions between the flexible and mobile lipids and the compact hydrogen-bonded protein structures.

As a function of SL contact time, τ_{SL} , the signal relaxes initially close to a typical exponential decay profile from which a relaxation time can be extracted. Figure 6.4 shows the normalized area under the aromatic hydrogen peak from gA as a function of SL duration. The fitted exponential function indicates that the $T_{1\rho}$ fits to a 5.5 ± 0.4 ms relaxation time.

Making use of the resolution attainable by MAS, Table 6.1 compiles the relaxation rates fitted for ^1H species in gA dispersed in a multilamellar membrane sample with

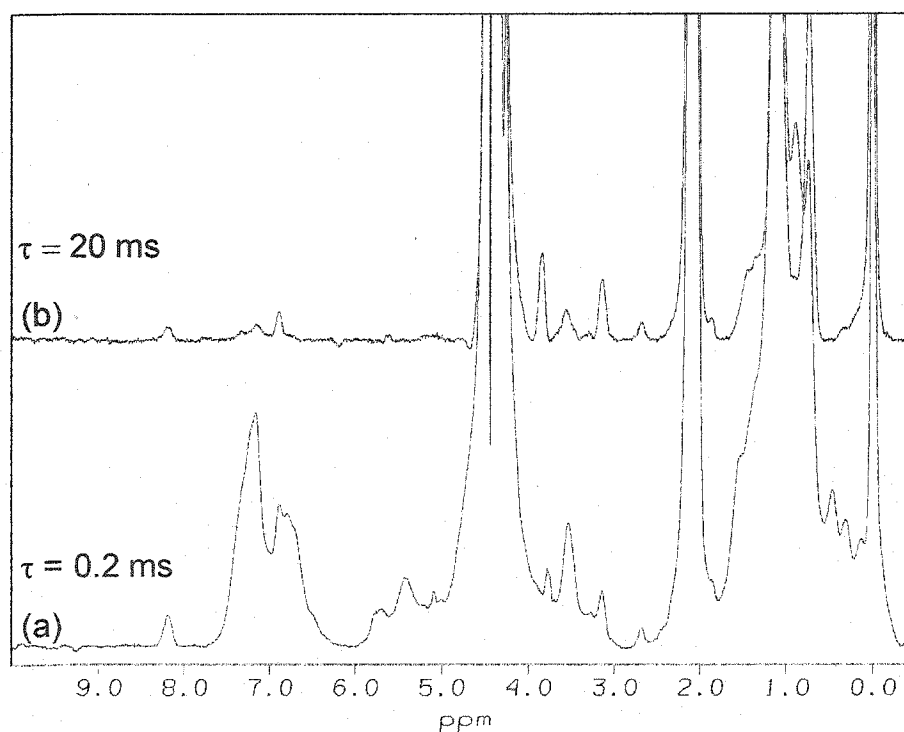


Figure 6.3: ^1H MAS NMR 1D spectra of gA/DMPC- d_{67} (1/20 mol/mol) with 43% (v/w) of deuterated phosphate buffer with pD 6.5 and $[\text{P}_i] = 50$ mM and with $\nu_R = 14$ kHz and $T = 55^\circ\text{C}$. The spectra were recorded following an on-resonance rf SL pulse with frequency, $\omega_e = 2\pi \times 40$ kHz and duration, $\tau = 0.2$ ms in (A) and 20 ms in (B).

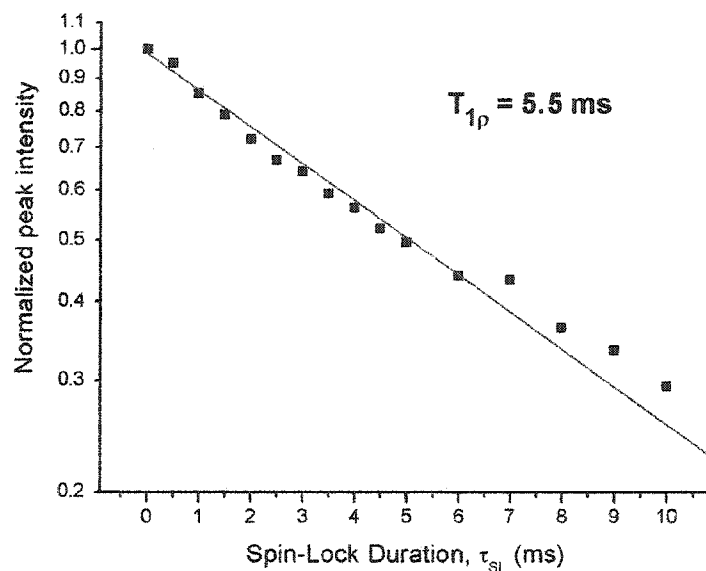


Figure 6.4: Exponential decay fit for the normalized area under the group of peaks corresponding to the aromatic hydrogens versus on-resonance rf ($\omega_e = 2\pi \times 40$ kHz) SL pulse duration. The sample was rotated at 14 kHz and the temperature maintained at 55°C.

Table 6.1: $T_{1\rho}$ of different ^1H species of gA in DMPC-d₆₇ (1/20 mol/mol) with 43% (v/w) buffer (pH or pD 6.5), in a multilamellar dispersion undergoing MAS at 8 and 14 kHz. The sample temperature was set at 55°C. The rf field, ω_e , of the on-resonance SL pulse was $2\pi \times 40$ kHz.

Species	position	$T_{1\rho}$ (ms)	
		$\nu_R = 8$ kHz	$\nu_R = 14$ kHz
$^1\text{H}_{ind}$	(11-9 ppm)	–	4.5 ± 0.4^a
$^1\text{H}_{form}$	(8.21 ppm)	2.2 ± 0.2	6.0 ± 0.7
$^1\text{H}_N$	(7.5-9 ppm)	–	1.8 ± 0.2^a
$^1\text{H}_{aro}$	(7.5-6 ppm)	4.0 ± 0.4	5.5 ± 0.4
$^1\text{H}_\alpha$	(4-6 ppm)	2.8 ± 0.2	2.9 ± 0.2
$^1\text{H}_{aliph}$	(0-4 ppm)	2.5 ± 0.2	3.2 ± 0.2
$^1\text{H}_{chol}$	(3.81 ppm)	≤ 100	≤ 100

^a using ^{15}N -gA and H_2O

conditions nearing those used in Farès *et al.* [94]. The relaxation rates in these samples are relatively rapid (in the ms time range) and are sensitive to the type of ^1H , as can be noted by the variability of rates among ^1H species. Hydrogen probes located near the extremities of the side chains, such as the indole, aromatic and aliphatic groups, which are more likely to rapidly reorient through *trans-gauche* isomerization of the side chain χ torsion angles, show longer relaxation times by at least a factor of two compared to the hydrogens close to the more rigid backbone (amide- and α -hydrogens). The relatively longer relaxation time for the formyl hydrogen, located at the N-terminal end of the protein backbone, but residing at the dimer interface deeply embedded in the hydrophobic interior, implies that this group reorients more readily than the rest of the backbone.

To find conditions which lengthens $T_{1\rho}$, a temperature dependence study was performed. Figure 6.5 shows the variation with temperature of $T_{1\rho}$, performed at $\omega_e = 2\pi \times 95$ kHz and $\nu_R = 14$ kHz, for four different hydrogen species. Over the temperature range from 30 to 55°C where the bilayers remain in the fluid phase, there is a very slight increase of $T_{1\rho}$ with temperature, of approximately 10-20%. It is difficult to interpret this behavior without a thorough understanding of the types of motions present, as temperature may affect both the correlation times and the

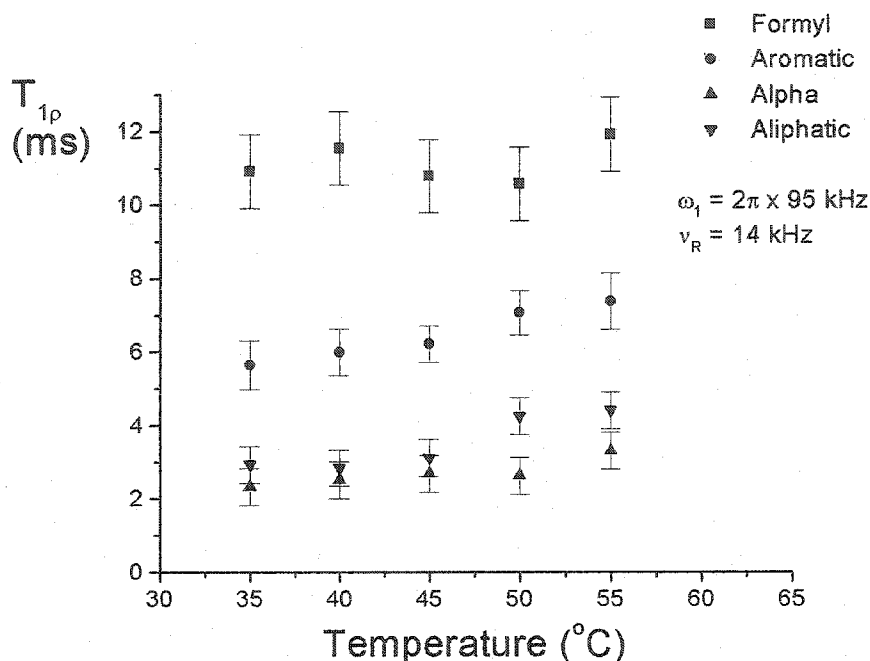


Figure 6.5: ^1H $T_{1\rho}$ data for gA under MAS (14 kHz and $\omega_1 = 2\pi \times 95$ kHz) plotted against sample temperature.

amplitudes of different motional modes simultaneously. It is clear, however, that the increase in temperature does not sufficiently reduce the low-frequency fluctuations which can inhibit the feasibility of scalar coupling based correlation experiments.

Another means of lengthening $T_{1\rho}$ would be to apply stronger SL pulses, thus transferring the peak sensitivity of $T_{1\rho}$ towards higher frequency motions. Figure 6.6 illustrates the growth of $T_{1\rho}$ with the square of the applied rf frequency, ω_1 , as expected from the general expression, Equation 6.13, for the spectral densities. The experiments were performed at a temperature of 55°C and with a MAS rate, $\nu_R = 14$ kHz. There is definitely an improvement in the duration of the signal with increasing SL field, but the improvement is such that 95% of the signal would still relax away after only 15 to 30 ms for side chain hydrogens, and within 10 ms for the backbone α -hydrogens. Attempts to further increase the applied rf field would add the complications of overheating, sample degradation and water evaporation.

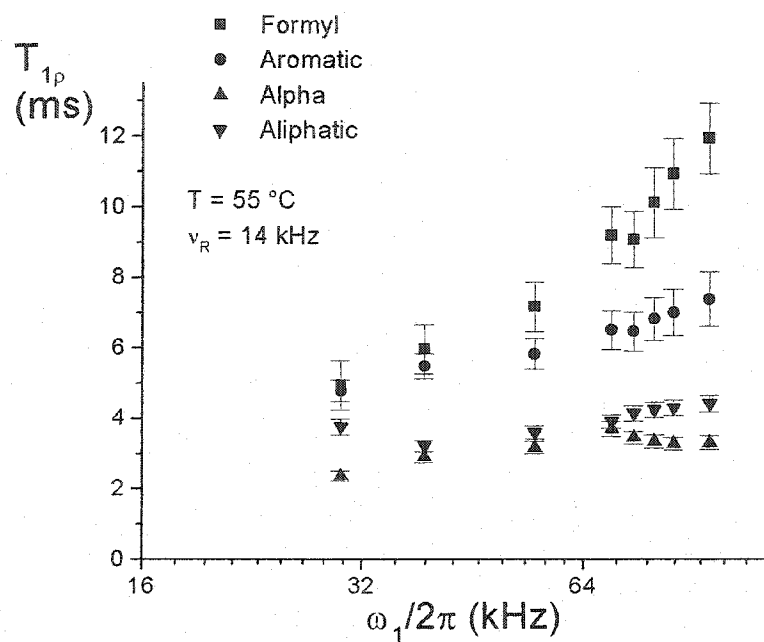


Figure 6.6: ^1H $T_{1\rho}$ data for gA under MAS (14 kHz and $T = 55\text{ }^{\circ}\text{C}$) plotted against on-resonance rf field for four different ^1H groups. N.B.: the frequency scale is not linear.

6.4.2 $T_{1\rho}$ of ^1H of other transmembrane polypeptides under MAS

Although the gA helical dimer is similar in molecular mass to single α -helices in a membrane-spanning configuration, their structures differ significantly. First, the diameter of the cylinder formed by the gA backbone is about 7 Å, about twice that of a typical α -helix. The internal structural details differ significantly in terms of ϕ and ψ dihedral angles and H-bonding network pattern. Also, the gA polypeptide chain does not extend as far into the aqueous region as model α -helices with the usual flanking charge residues. Finally, it is well known that gA can form a membrane ionic pore modeled to contain 9 water molecules [149]. It is reasonable, then, to assume that the slow motion dynamics, notably axial diffusion and off-axis reorientation, may be strongly affected by the shape of the transmembrane polypeptide. For comparison, the $T_{1\rho}$ values of the resolvable ^1H resonances are measured for two hydrophobic polypeptides, presumed to form transmembrane α -helices, under similar MAS and temperature conditions as described in the previous section.

The first model transmembrane polypeptide, ALGA, is a 22-residue chain with 16 consecutive hydrophobic amino acid side chains specifically designed to minimize the chances of ^1H signal overlap, especially for repeating residues. The ^1H MAS NMR spectrum at 14 kHz of this peptide dispersed with DMPC- d_{67} (1/15 mol/mol) and hydrated (43% v/w) with P_i buffer (50 mM, pH 6.5) is shown in Figure 6.7, overlaid with the high-resolution ^1H spectrum of the same polypeptide in a TFE- d_2 solution. As for gA, the ^1H resonance lines have different widths depending on the nature of their local dynamics. Dynamics will also strongly influence the values of $T_{1\rho}$ measured for each resolvable peak of Figure 6.7(A). The assignments of these peaks are as of yet only tentative and are based on their chemical shift correspondence with the peaks assigned in the solution spectrum. Figure 6.8 displays the $T_{1\rho}$ variation with the SL radio-frequency for a selection of five ^1H peaks labelled in Figure 6.7(A), and illustrates an even larger site-specific variability of the relaxation times for ^1H within the same polypeptide molecule. It is believed that the narrow and slow-relaxing peaks located near 7 ppm (peaks 6 and 9) belong mostly to the side chain

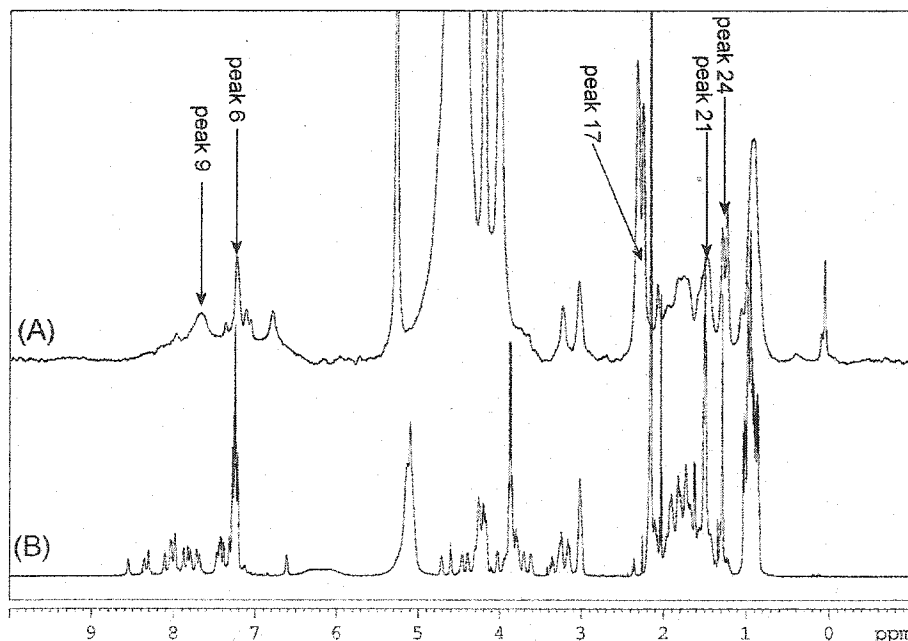


Figure 6.7: ^1H NMR of ALGA polypeptide (A) using MAS ($\nu_R=14$ kHz) of ALGA/DMPC- d_{67} (1/15, mol/mol) with 43% (v/w) potassium phosphate buffer with pH 6.5, $[\text{P}_i] = 50$ mM and $T = 55^\circ\text{C}$, (B) in solution with a polypeptide concentration of 1.5 mM in TFE- d_2 at 22°C . The labelled peaks in (A) are those for which $T_{1\rho}$ values were measured in Figure 6.8.

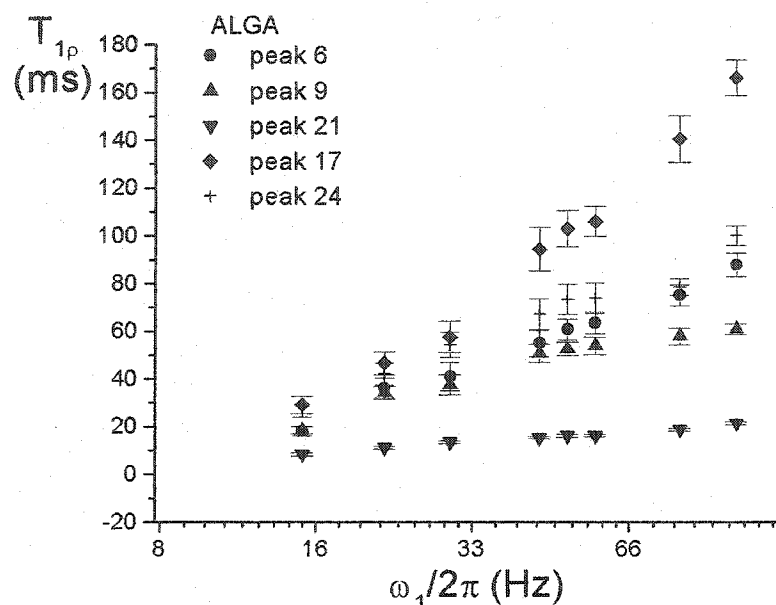


Figure 6.8: $T_{1\rho}$ results of five different non-assigned ^1H of the ALGA polypeptide as a function of SL amplitude ω_1 . N.B. The frequency scale is not linear.

amino groups of the lysine and arginine residues flanking the transmembrane region. These species can rapidly and freely reorient, thus strongly weakening the magnitude of the second moment involving these ^1H and, by extension, reducing the effect of slow whole-body motions on their $T_{1\rho}$. A similar interpretation can be made for peaks 17 and 24 whose chemical shifts correspond to those assigned for methylene and methyl groups in the high-resolution spectrum. Conversely, α -, β - and amide-hydrogens, which are structurally located near the α -helical backbone and within the hydrophobic interior of the membrane where the dynamics are strongly dictated by the whole-body motions, have typically shorter $T_{1\rho}$. Peak 21, for instance, may correspond to the H_β of Val in ALGA has a relaxation time of less than 20 ms in the rotating frame.

These experiments were repeated for the ^1H spins of the transmembrane region of the Neu polypeptide. Figure 6.9 shows the spectra for this polypeptide in multilayer dispersion (A), in SDS-micelles (B) and in TFE (C). Similar $T_{1\rho}$ values were obtained

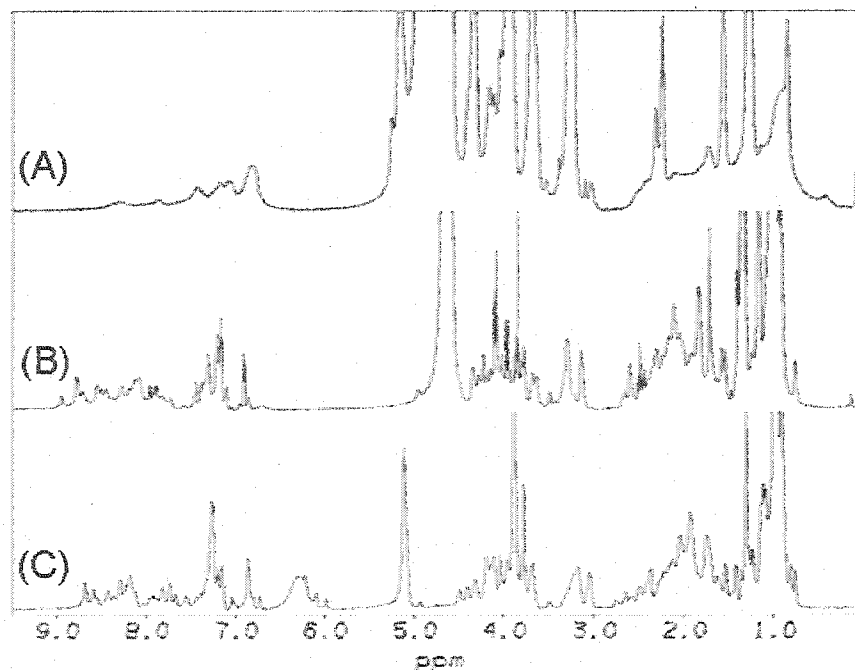


Figure 6.9: ^1H NMR of the Neu polypeptide (A) using MAS ($\nu_R = 10$ kHz) of Neu/DMPC- d_{67} (1/9, mol/mol) with 43% (v/w) aqueous phosphate buffer with pH 6.5, $[\text{P}_i] = 50$ mM and $T = 55$ °C (B) 1.0 mM dispersed in SDS- d_{23} micelles (100 mM) and sodium phosphate buffer (50 mM, pH 4, 10% D_2O) at $T = 40$ °C (C) 1.5 mM in 0.5 mL TFE- d_2 at $T = 30$ °C

for similar ^1H moieties (Data can be found in the upcoming Ph. D. thesis by R.S. Houliston).

It has become evident that low-frequency dynamics have a strong limiting effect on ^1H NMR mainly through broadening and relaxing effects, especially for the crucial ^1H spins located on or near the protein backbone. Indeed, the high abundance of hydrogens in proteins is responsible for the large homonuclear dipolar coupling compared to the relatively small chemical shift dispersion, which leads to crowded, imperfectly resolved 1D spectra. Despite its good sensitivity, this nucleus may ultimately not be ideally suited for unraveling dynamic and structural details because it will be difficult to resolve and identify the ^1H resonances without multidimensional correlation experiments with other nuclei (such as ^{15}N and ^{13}C).

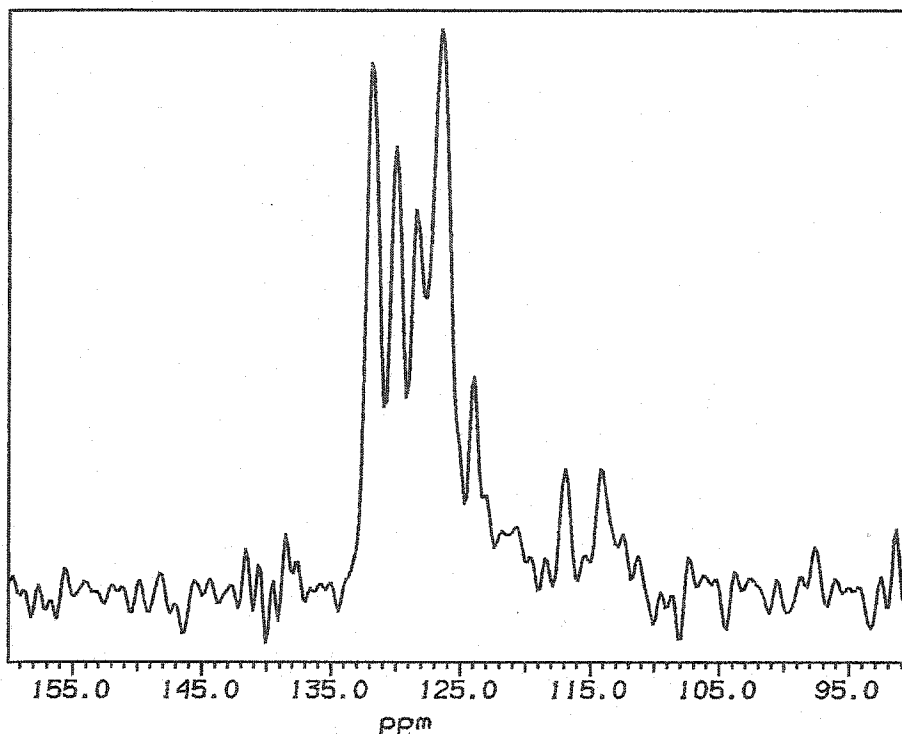


Figure 6.10: ^{15}N $\nu_R = 14$ kHz MAS spectrum of $^{15}\text{N}_{20}$ -labelled gA dispersed DMPC- d_{67} with 43% (v/w) phosphate buffer (50 mM, pH 6.5) at $T = 55^\circ\text{C}$. The spectrum was recorded following a CP sequence (see Section 3.4.3.3, p. 56). The sequence also used XiX decoupling during acquisition with a t_p/τ_R ratio of 1.85 [81].

6.4.3 $T_{1\rho}$ of ^{15}N of gA in phospholipid bilayers under MAS

The other useful nuclei of proteins, ^{15}N and ^{13}C , should provide more usable resolution for structural studies, owing principally to the small size of their nuclear dipole moment, but also to their simplified spectra with more favorable chemical shift spread. In this and following sections, a survey of $T_{1\rho}$ for these nuclei is conducted and their advantageous spectral features are used for understanding the low-frequency motions which animate small membrane proteins.

First, the ^{15}N nuclei in ^{15}N -labelled gA are employed under MAS conditions. Here, the backbone amides and indole groups at the ϵ_1 position of the aromatic side chain of Trp show some level of resolution in the 1D spectrum over a range of 40 ppm as shown in Figure 6.10. The tentative amide assignments are available from Table 7.3 (p. 168).

To describe the relaxation of the amide ^{15}N in the rotating frame, an estimate of its second moment is necessary. The amide ^{15}N CSA tensor has principal values σ_{11} , σ_{22} , σ_{33} of approximately 31.3, 55.2 and 201.8 ppm according to Davis and Auger [121] (this leads to $\delta = 105.7$ ppm and $\eta = 0.226$). The maximum full CSA second moment of a powder, $(\delta^2/15)(3 + \eta^2)$ according to Maricq and Waugh [150], is thus calculated to be $3.5 \times 10^8 \text{ s}^{-2}$ at 14.1 T. The tensor is oriented such that σ_{11} is perpendicular to the peptide plane and σ_{33} is in the plane and oriented 18° from the N-H bond and 104° from the N-C' bond (the Euler angles from the PAS frame (Frame P) to the frame defined by the N-H bond (z) and the normal to the plane (x) (Frame p) are $\alpha_{Pp} = 0^\circ$ and $\beta_{Pp} = 18^\circ$). By combining Wigner rotation transformations, the average angles of $\alpha_{PM} = 104.4 \pm 12.9^\circ$ and $\beta_{PM} = 22.4 \pm 7.0^\circ$ are obtained for every residue along the regular helical conformation of gA.

The amide ^{15}N experiences dipolar interactions mainly with its covalently bound $^1\text{H}_N$ but also interacts with other surrounding ^1H . The ^{15}N spin thus shows an important dipolar second moment regardless of the orientation of the molecule. Mapping all possible orientations of gA in the PDB:1mag [24] conformation reveals that the dipolar second moment always ranges within the approximate limits of 1.4×10^7 to $5.7 \times 10^8 \text{ s}^{-2}$ (see Figure 6.2(A)).

Upon the introduction of axial diffusion around the principal axis of the moment of inertia tensor for the PDB:1mag configuration, there is a small effect on the second moment for both these interaction tensors because both have principal axes nearly parallel to the axis of diffusion ($\beta_{PM}^{CSA} = 22.4 \pm 9.4^\circ$, $\beta_{PM}^D = 18.2 \pm 7.8^\circ$). Thus, the maximum residual CSA second moment is about $1.9 \times 10^8 \text{ s}^{-2}$ at 14.1 T (a reduction by a factor of 1.8), whereas the maximum residual dipolar second moment is on close to $3.02 \times 10^8 \text{ s}^{-2}$, as shown for residue Val-8 in Figure 6.2(C).

Figure 6.11 shows the dependence of the relaxation time $T_{1\rho}$ on the applied rf field. The ^{15}N -gA/DMPC- d_{67} sample was spinning at 14 kHz and the temperature was 55°C for these measurements. Because of power limitations of the spectrometer, rf fields above 15.5 kHz were obtained by moving off-resonance by an amount corresponding to the tilted frame angle, $\beta_{L\rho}$, indicated below the data point. A resonance minimum

at $\omega_e = 14$ kHz is seen. This is predicted by Equations 6.25 and 6.27. Other minima should appear at $\omega_e = 7$ and 28 kHz but would require too low or too high power to be made clear. This effect is important to show the agreement of measurements with the theory. This effect has been clearly observed in ω_1 studies of ^1H $T_{1\rho}$ of phospholipids [151].

The solid line in Figure 6.11 shows a nonlinear least-square fit obtained in a combination of Equations 6.35 through 6.38. Contribution from both the chemical shift and dipolar interaction are included, because as discussed above, it is expected that both interactions are important. It was also likely that both type of whole-body motion will participate in the relaxation. Hence, to a good approximation, the expression of the predicted $1/T_{1\rho}$ is given by the sum of all contributions [141]:

$$1/T_{1\rho} = \sum_{\lambda} \sum_i 1/T_{1\rho}^{(\lambda,i)} \quad (6.41)$$

where λ represents the type of interaction and i , the nature of the motions.

The parameters used for fitting included $\Delta M_2|_{AD}$ values of $1.39 \times 10^8 \text{ s}^{-2}$ and $5.56 \times 10^8 \text{ s}^{-2}$ for axial diffusion of the CSA and IS dipolar interactions and $M_2'|_{AD}$ values of $1.92 \times 10^8 \text{ s}^{-2}$ and $6.03 \times 10^8 \text{ s}^{-2}$ for both residual interactions undergoing off-axis reorientation. The best fit was obtained with correlation time values of $\tau_c^{AD} = 1.1 \times 10^{-8} \text{ s}$ for axial diffusion and $\tau_c^{DC} = 4.0 \times 10^{-5} \text{ s}$ for diffusion-in-a-cone with an amplitude corresponding to a narrow cone with semi-angle of about 10-20° ($\sum \mathcal{A}_{|m|} = 0.01$)).

Although the fit is satisfactory, it relies on a number of assumptions about the motional geometries and residual strengths of the existing interaction. A simplified study should be conducted, say for a single ^{15}N -label in a deuterium exchanged polypeptide to isolate the contribution of its CSA on the relaxation. Another useful backbone nucleus is the carbonyl ^{13}C , as discussed in the next section.

6.4.4 $T_{1\rho}$ of carbonyl ^{13}C of polypeptide L16 in phospholipid bilayers under MAS

In this section, the spin-lattice relaxation in the rotating frame is investigated for ^{13}C in the model polypeptide L16 [152]. More specifically, the ^{13}C spin on the peptide

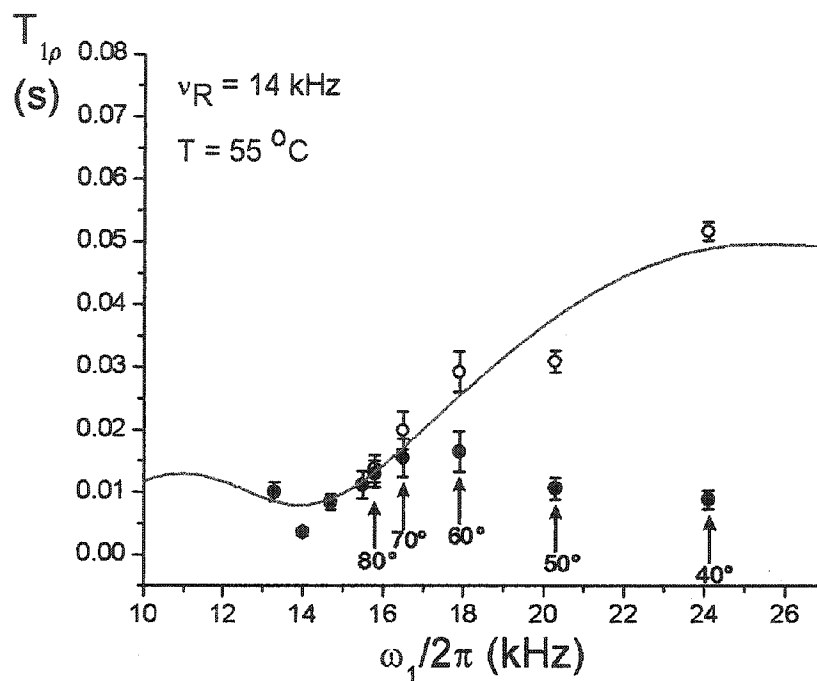


Figure 6.11: Changes in ^{15}N $T_{1\rho}$ of the sample described in Figure 6.10. The results for the total area under all peaks are shown as dark circles with error bars. Due to spectrometer limitations, the effective field was applied on-resonance except for the points labelled with the frame tilt, $\beta_{L\rho}$, indicated below the point. The open circles represent the same points corrected for the fact that they were obtained off-resonance, by multiplying the values by $\sin^2(\beta_{L\rho})$ according to Equations 6.25 and 6.27. The line represents the theoretical least square fit function for on-resonance rf fields. This line combines the contributions of axial diffusion of the CSA ($\Delta M_2|_{AD} = 1.39 \times 10^8 \text{ s}^{-2}$) and of the dipolar coupling ($\Delta M_2|_{AD} = 5.56 \times 10^8 \text{ s}^{-2} \text{ s}^{-2}$) as well as off-axis reorientation (with $M_2|_{AD}^{CSA} = 1.9 \times 10^8 \text{ s}^{-2}$ and $M_2|_{AD}^{IS} = 6.0 \times 10^8 \text{ s}^{-2}$). The best-fit curve yielded correlation times of $\tau_c^{AD} = 1.1 \times 10^{-8} \text{ s}$ for axial diffusion and $\tau_c^{DC} = 4.0 \times 10^{-5} \text{ s}$ for diffusion-in-a-cone with semi-angle of 10-20°.

bond carbonyl group of the 16 Leu residues is used to probe the slow molecular dynamics of the polypeptide backbone in a model membrane through measurements of spin-lattice relaxation rates in the rotating frame under MAS. This nucleus is located directly within the secondary structural scaffold of the polypeptide α -helix, and so its relaxation will be primarily affected by whole-body motions. Assuming near regular secondary structure throughout the polypeptide, one can expect the signal from all 16 leucine carbonyl groups to relax at very similar rates.

As for ^{15}N , the ^{13}C CSA and the heteronuclear dipolar coupling with surrounding ^1H can both contribute to the relaxation. This can be predicted from the relative magnitudes of the dominant interactions. For the CSA, the PAS tensor components have been measured in a single crystal of L-Ala by Naito *et al.* [153], namely $\sigma_{11} = -115.6$ ppm, $\sigma_{22} = -48.6$ ppm, and $\sigma_{33} = 40.6$ ppm relative to benzene (giving $\delta = 81.8$ ppm and $\eta = 0.82$) with Euler angles $\alpha_{Pp} = 204^\circ$ and $\beta_{Pp} = 90^\circ$ relative to a frame defined by the $\text{C}'\text{-C}_\alpha$ bond (z) and the peptide plane normal (x)². Thus, in an ideal α -helix, the σ_{33} component is nearly perpendicular to the helix moment of inertia principal axis ($\beta_{PM} = 78.4 \pm 3.1^\circ$ and $\alpha_{PM} = 25.3 \pm 3.1^\circ$). In the static limit, the chemical shift anisotropy has a maximum second moment, $M_2^{\text{stat,CSA}} = (\delta^2/15)(3 + \eta^2)$ [150] of $5.4 \times 10^8 \text{ s}^{-2}$ at 8.5 T in a polycrystalline sample. When introducing the assumed fast axial diffusion about the moment of inertia principal axis, the maximum residual chemical shift anisotropy second moment is reduced to only $1.5 \times 10^7 \text{ s}^{-2}$. The fluctuating part of the second moment due to the CSA in an axially diffusing ideal α -helix is $\Delta M_2|_{AD}^{\text{CSA}}$ is $5.2 \times 10^8 \text{ s}^{-2}$.

How does this compare to the reduction of the dipolar coupling second moment by the same motion? In the ideal α -helix, there are six backbone ^1H within 3.0 Å from the carbonyl C^i , of which the H_N^{i+1} and H_α^i are located about 2.06 and 2.15 Å away. Each of these would individually translate into a dominant dipolar splitting of about 3 kHz (when the internuclear vector, \vec{r} , is perpendicular to the field) and a maximum

² For convenience, this definition of the peptide plane frame (Frame p) is different from that of Chapter 2, p. 19 because the carbonyl ^{13}C nucleus is not adjacent to the N-H bond defining the z-axis. The two definitions can be unified knowing that the $\text{C}'\text{-C}_\alpha$ bond forms an angle of about 56° with the N-H bond. In the present case, the Euler angles would become $\alpha_{Pp} = 148^\circ$ and $\beta_{Pp} = 90^\circ$.

splitting of 6 kHz (with \vec{r} parallel to the field) on a powder spectrum or into static second moments ranging between $0 - 3.7 \times 10^8 \text{ s}^{-2}$. However, because the carbonyl ^{13}C interact with a number of surrounding ^1H , the total second moment is summed for all possible pairs. Since the H-C internuclear vectors have different directions, there is no orientation for which this second moment is zero (see Figure 6.2(B)). In fact, when searching the total dipolar second moment (due to all hydrogens in the peptide) for a given carbonyl ^{13}C over all possible orientations of the molecule, it is found that the mean squared strength of this interaction can fluctuate within the narrow range from $1.5 \times 10^8 \text{ s}^{-2}$ to $8.4 \times 10^8 \text{ s}^{-2}$. The average static second moment in a polycrystalline sample is $4.4 \times 10^8 \text{ s}^{-2}$. After introducing the assumed fast axial diffusion on an ideal α -helix, the maximum residual mean squared strength of the dipolar interaction along the diffusion (or helix) axis is on the order of $3.95 \times 10^8 \text{ s}^{-2}$ (see Figure 6.2(D)) which results in an average residual second moment of $7.9 \times 10^7 \text{ s}^{-2}$ in a powder distribution. Thus, the change in the second moment due to axial diffusion is $\Delta M_2|_{AD}^D = 3.6 \times 10^8 \text{ s}^{-2}$. These values are comparable to the CSA second moments. The contribution to the $T_{1\rho}$ due to axial diffusion and reorientation thus comes from the both interactions and so Equation 6.41 is used.

Under conditions where the orientation-dependent interactions are removed from the spectrum through MAS, the high-resolution signal from ^{13}C -labels on the carbonyl groups of the polyleucine peptide backbone was observed. Figure 6.12 demonstrates the resolution achievable for the ^{13}C NMR spectrum of $^{13}\text{C}'_{16}$ -L16 in DMPC in a non-oriented dispersion. Although the linewidths at half-height are of the order of tens of Hz, the resolution is insufficient to resolve individual carbonyl groups along the polypeptide chain. The following $T_{1\rho}$ measurements are thus measured for the ensemble of labelled residues in the protein.

The $T_{1\rho}$ time constants for this polyleucine are strongly influenced by the correlation times of the intermediate scale motions. The results of the dependence of the relaxation rate with MAS spinning rate are demonstrated in Figure 6.13 for an rf field of 4.4 kHz at three different temperatures. In every case, a continuous decrease in $1/T_{1\rho}$ is observed as the MAS rate is increased from 4 kHz to 10 kHz with the maxi-

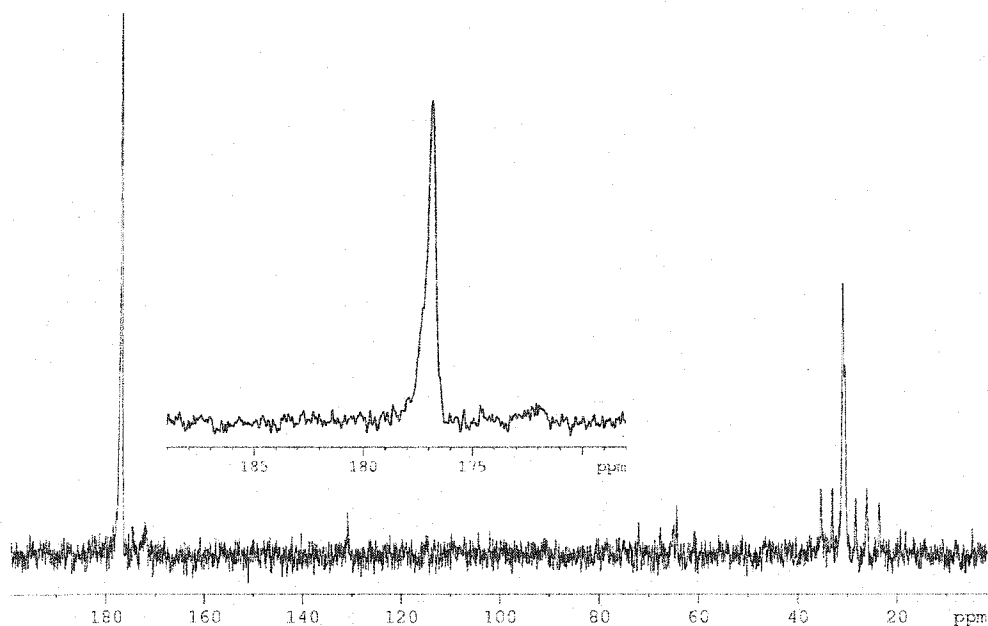


Figure 6.12: The ^{13}C MAS spectrum of the C_{16} -labelled transmembrane polypeptide L16 dispersed in hydrated POPC. Unshielded resonances on the right-hand side of the spectrum belong to the natural abundance ^{13}C spins of the lipid aliphatic hydrocarbon chains. The peak at 177 ppm correspond to the overlapping resonances of all 16 $^{13}\text{C}'$ -labels of the polyleucine stretch in L16. The spectrum was obtained at 55° with MAS speed of 8 kHz.

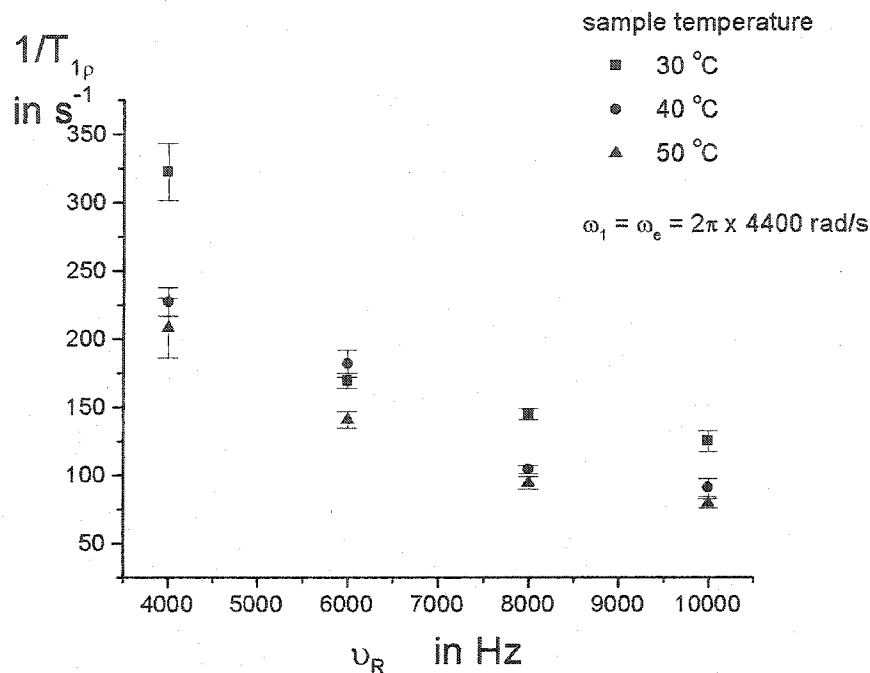


Figure 6.13: Changes in $1/T_{1\rho}$ of polypeptide L16 carbonyl ^{13}C as a function of MAS rate, ν_R , with an rf field applied on-resonance and with amplitude, $\omega_1 = 2\pi \times 4400$ kHz. The results were obtained at three different temperatures: 30° (squares), 40° (circles) and 50° (triangles). L16 was dispersed in DMPC (1:30 mol/mol) and hydrated with 43% (v/w) with H_2O .

mum near 4 kHz. Also, the increase in temperature improves the persistence of the signal, for example at 4 kHz, as $T_{1\rho}$ increases from 3.1 ms to 4.8 ms (see Figure 6.13).

Figure 6.14 illustrates the variation of the rotating frame relaxation rate with respect to the offset frequency, ω_{off} of the applied rf field (ω_1) of $2\pi \times 5.5$ kHz with $\nu_R = 2.5$ kHz. A significant improvement of $T_{1\rho}$ is seen as the offset frequency is increased from 0 to 12 kHz ($\beta_{L\rho} = 90^\circ$ to 11°). At 40 °C, $T_{1\rho}$ increases from 3 to 74 ms, a factor larger than 20. Here again, temperature slightly improves the persistence of the signal from 40 °C to 60 °C.

The continuous line on Figure 6.14 shows a nonlinear least square fit based on Equations 6.35 to 6.38 assuming that the CSA and the dipolar coupling between ^{13}C and surrounding ^1H are the main contributor to the relaxation in this regime through axial diffusion and off-axis reorientation. The line was obtained with the ΔM_2 and

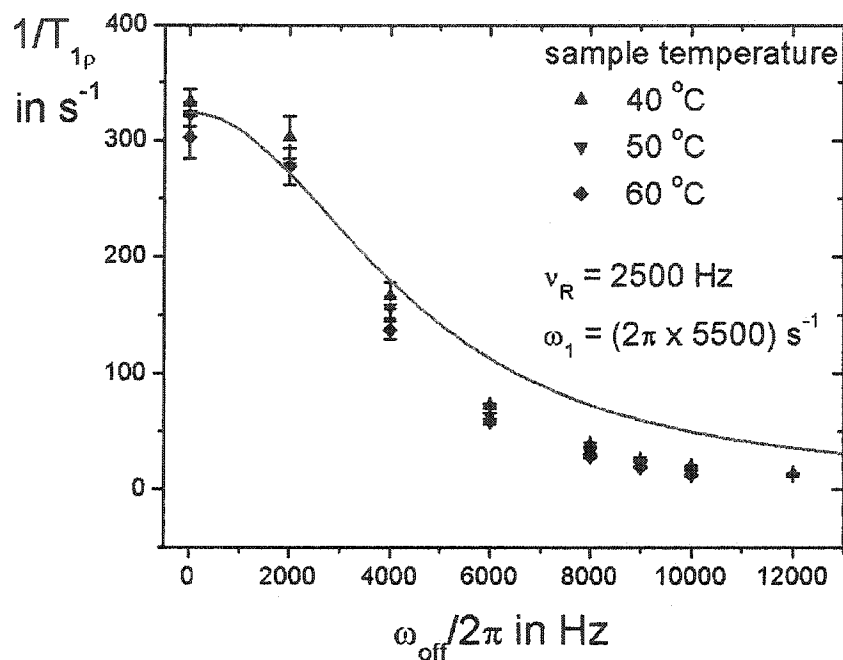


Figure 6.14: Changes in $1/T_{1\rho}$ of polypeptide L16 carbonyl ^{13}C with offset frequency, $\omega_{off}/2\pi$, with $\omega_1 = 2\pi \times 5500$ Hz and $\nu_R = 2500$ Hz. Results were obtained at three different temperatures: 40° (triangles), 50° (inverted triangles) and 60° (diamonds). The fitted line was obtained by adding the effects of axial diffusion and off-axis reorientation on $T_{1\rho}$ through the modulation of the ^{13}C CSA and 1H - ^{13}C dipolar coupling interactions. The fluctuating part of the second moment due to axial diffusion were $\Delta M_2|_{AD}^{CS} = 5.1 \times 10^8 s^{-2}$ and $\Delta M_2|_{AD}^{IS} = 3.6 \times 10^8 s^{-2}$ and the residual second moments modulated by the diffusion-in-a-cone model were $M_2'|_{AD}^{CS} = 1.5 \times 10^7 s^{-2}$ and $M_2'|_{AD}^{IS} = 7.9 \times 10^7 s^{-2}$. The correlation times for each type of motion were $\tau_c^{AD} = 1.2 \times 10^{-8} s$ and $\tau_c^{DC} = 1.3 \times 10^{-5} s$ and the amplitude of off-axis fluctuation corresponded to diffusion-in-a-cone with semi angle 10-20°.

M'_2 parameters stated above for the ^{13}C CSA and the ^1H - ^{13}C dipolar coupling. The best fit was obtained for correlation times of $\tau_c^{AD} = 2.7 \times 10^{-7}$ s and $\tau_c^{DC} = 4 \times 10^{-5}$ s, but was mostly sensitive to τ_c^{AD} . The off-axis reorientation amplitude corresponded to diffusion-in-a-cone with semi-angle of 10-20°. The poor agreement for larger values of offset, corresponding to DRTF frame tilted at angles smaller than $\sim 45^\circ$, could be explained by the increasing contribution of T_1 to the relaxation.

6.4.5 $T_{1\rho}$ of $^{13}\text{C}'$ of L16 in oriented phospholipid bilayers

In membrane samples with macroscopic orientation, the $T_{1\rho}$ of nuclear spins within the membrane protein are no longer summed over all possible orientations and will have a marked dependence on sample orientation. As seen from Equations 6.19 and 6.22, for NMR spectra dominated by CSA or dipolar interactions, the orientation dependence of $T_{1\rho}$ will depend strongly on the type of motions present. To illustrate this statement, Figure 6.15 displays the theoretical profile of $1/T_{1\rho}$ due solely to fluctuations in ^{13}C CSA and ^1H - ^{13}C dipolar coupling versus the macroscopic orientation of the sample. These curves were calculated by including the expression of the varying transformation $\langle \Delta \mathcal{D}_{MN} \rangle$ (Equation 6.28 or 6.29) for the two types of motion model into the expression for $T_{1\rho}$ (Equation 6.8). These profiles demonstrate that the values of $1/T_{1\rho}$ have a markedly different orientation-dependence according to the dominant motion. For axial diffusion, a correlation time of 10^{-7} s $^{-1}$ was chosen. For diffusion in a cone, a correlation time of 10^{-5} s $^{-1}$, a cone tilt angle of 20° and a cone semi-angle of 20° were chosen. Assuming that these model fluctuations are uncorrelated, the sum of their contributions to $1/T_{1\rho}$ are plotted in the third curve of Figure 6.15. To verify these trends, a set of relaxation measurements was performed on L16 dispersed in oriented DMPC bilayers at different ω_e [152].

Figure 6.16 shows the ^1H -decoupled ^{13}C NMR spectra of the oriented sample (at $\beta_{NL} = 0^\circ$ (A) and 90° (B)) of polypeptide L16 in fully hydrated DMPC bilayers at 90 MHz (8.5 T). The high-field peak (right) corresponds to the natural abundance ^{13}C mainly from the DMPC acyl chains, while the low-field peak (left) represents the signal from the polypeptide backbone leucine carbonyl groups. The position of the

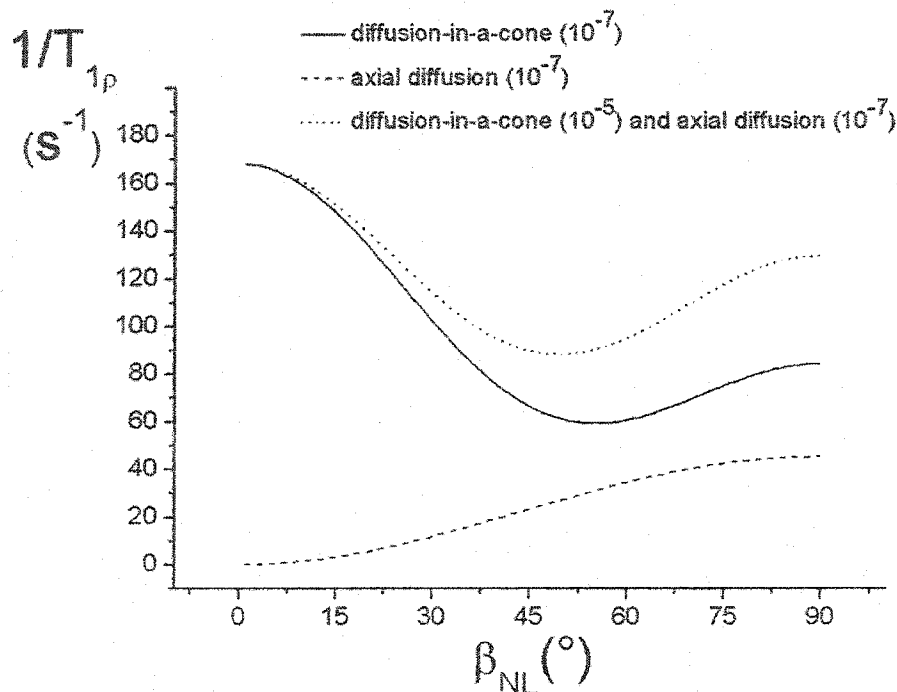


Figure 6.15: Predicted rotating-frame spin-lattice relaxation rates of $^{13}\text{C}'$ in an ideal α -helix ($\phi = -65^\circ$ and $\psi = -40^\circ$) as a function of the orientation, β_{NL} , of the membrane normal relative to the magnetic field. The solid curve represents the $1/T_{1\rho}$ profile due to off-axis reorientation which leads to fluctuations with correlation time $\tau_c = 1 \times 10^{-5}$ s of the dominant interactions for which the residual maximum strength after fast axial diffusion were estimated to be $(\gamma B_0 \delta)^2 = 7.6 \times 10^7 \text{ s}^{-2}$ (CSA) and $(\mu_0/4\pi)^2 (\gamma_I \gamma_s \hbar / r^3)^2 = 4.0 \times 10^{-8} \text{ s}^{-2}$ (dipolar coupling). The diffusion-in-a-cone model was used for which the helix axis can reorient within a hollow cone volume of average tilt 30° and of tilt range of $\pm 20^\circ$ was used (the resulting coefficients were $A_0 = 0.058$, $A_1 = 0.011$, $A_2 = 0.010$). The dashed curve depicts the orientation dependence profile of $1/T_{1\rho}$ for axial diffusion about the helical moment of inertia principal axis which causes fluctuations of the CSA and dipolar interactions with correlation time $\tau_c = 1 \times 10^{-7}$ s. The static limit values were used for the strength of these interactions ($(\gamma B_0 \delta)^2 = 2.2 \times 10^9 \text{ s}^{-2}$ and $(\mu_0/4\pi)^2 (\gamma_I \gamma_s \hbar / r^3)^2 = 8.4 \times 10^{-8} \text{ s}^{-2}$). For the freely diffusing non-tilted α -helix, the coefficients were $A_0 = B_0 = 0$, $A_1 = 0.058$, $A_2 = 0.345$, $B_1 = 0.499$, $B_2 = 0.156$ ($\beta_{MN} = 30^\circ$). The dotted curve shows the combined influence of the two motions, described above, obtained simply by adding the two previous curves. For every case, the effective rf field strength, ω_e , was $2\pi \times 8$ kHz and the magnetic field, B_0 , was 8.5 T.

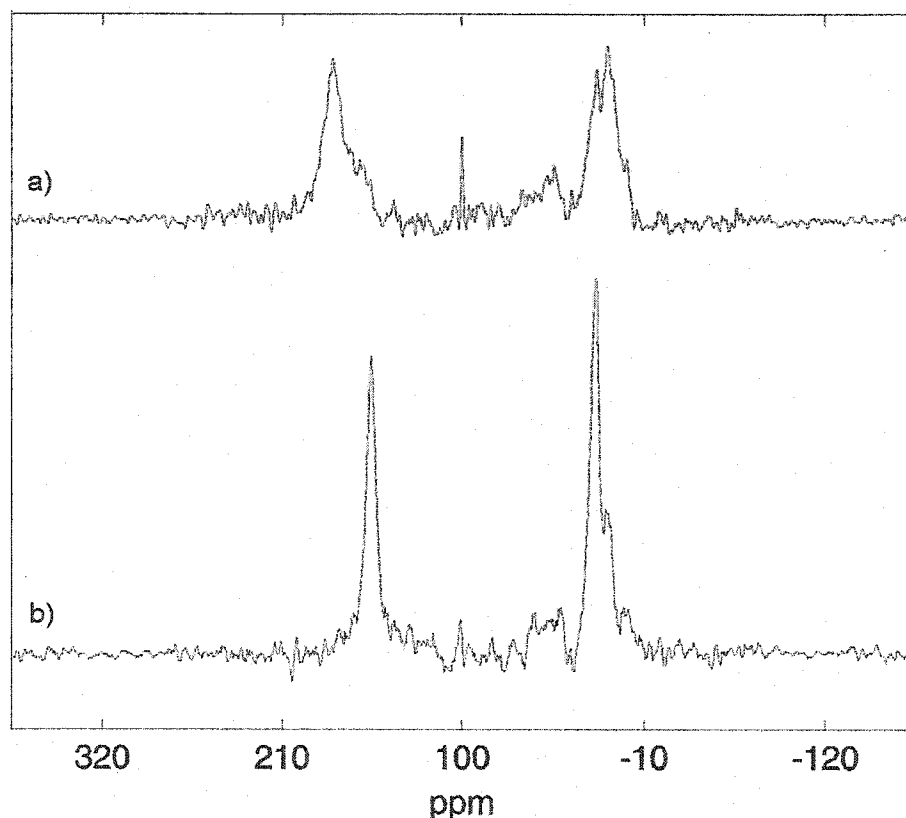


Figure 6.16: ^{13}C static NMR spectra of a hydrated, glass-plate supported $^{13}\text{C}'_{16}$ -L16/DMPC (1/30 mol/mol) sample at 40 °C with orientations a) $\beta_{NL} = 0^\circ$ and b) $\beta_{NL} = 90^\circ$. The right hand peak is assigned to natural abundance aliphatic DMPC ^{13}C signal whereas the left hand peak represents the polypeptide backbone carbonyl ^{13}C labels.

peptide peak shifts by 24 ppm (155 to 179 ppm) upon tilting the sample from 0° to 90° relative to the magnetic field. In contrast, the full CSA linewidth of polypeptide L16 in dry powder form spans about 200 ppm (data not shown). It can be concluded that the protein is undergoing relatively fast axial diffusion in the fluid DMPC bilayer which reduces the CSA significantly. Using Naito's chemical shift measurements [153], it can be shown that an ideal α -helix with ϕ and ψ angles of -65° and -40° , undergoing fast axial diffusion along its helix axis will have a spread of 16 ppm between σ_{\parallel} and σ_{\perp} . The difference in line widths between the two spectra can be accounted for by the residual ^1H - ^{13}C dipolar coupling scaled by $P_2(\cos\beta_{NL})$.

Figure 6.17 shows the dependence of the relaxation rate in the rotating frame (with

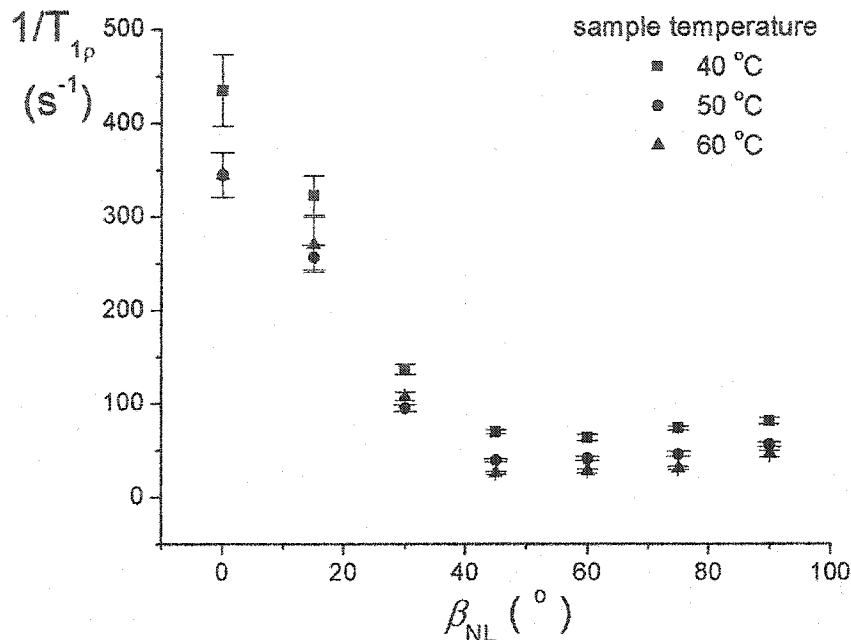


Figure 6.17: The dependence of membrane polypeptide L16 $^{13}\text{C}'$ $1/T_{1\rho}$ on sample orientation β_{NL} , with rf field, $\omega_e = 2\pi \times 8.07$ kHz at different temperatures. The sample temperature was set at 40 °C (squares), at 50 °C (circles) and at 60 °C (triangles).

$\omega_e = 8$ kHz $\beta_{L\rho} = 0$) on the orientation of the normal to the glass plates relative to the magnetic field, for three different temperatures (40, 50 and 60 °C). There is a noticeable increase in $T_{1\rho}$ with increasing temperature for all orientations. This suggests that the motional rates are increasing with sample temperature. Furthermore, the orientation profiles of the relaxation rates also exhibit a $|P_2(\cos \beta_{NL})|^2$ behavior, apparent from the maximum at 0° and a minimum at the magic angle (54.7°). This trend indicates that the motion predominantly modulates terms of $(\frac{1}{2}(3 \cos^2 \beta_{NL} - 1))^2$, indicating a dominant off-axis reorientational motion as described in Figure 6.1.

In Figure 6.18, the dependence of the rotating-frame relaxation rate is graphed for three on-resonance SL rf fields of 8 kHz, 17.8 kHz and 33 kHz, all taken at a temperature of 40 °C. With increasing rf field, the sensitivity of $T_{1\rho}$ is shifted towards faster motional rates and thus may allow to differentiate motions with different correlation times. Here, the increase in the applied field results in the relaxation

profiles adopting a largely different geometrical dependency. At 8 kHz, the relaxation rate profile resembles a $[P_2(\cos \beta_{NL})]^2$ function with a maximum at 0° , and at 33 kHz, the profile assumes a $(\sin \beta_{NL})^2$ function with a minimum at 0° .

The solid lines in Figure 6.18 represent a set of three curves obtained by substituting Equation 6.28 for axial diffusion and Equation 6.29 for diffusion-in-a-cone into Equation 6.19 and Equation 6.22 to describe the effect of motional modulations of the CSA and dipolar interactions involving ^{13}C . The lines were simultaneously fitted to the results of $1/T_{1\rho}$ for the three different values of applied rf field (ω_1), using the same set of parameters. The parameters used are listed in the figure caption. The correlation times obtained, namely $1 \times 10^{-8}\text{s}$ for axial diffusion and $1 \times 10^{-5}\text{s}$ for off-axis reorientation, concur with those obtained by MAS in the previous sections for gA and L16. The results suggest that the orientation profiles with increasing rf field strength clearly distinguish the motions investigated. The discrepancy between the fitted curve and the data showing large relaxation rates near 0° at 8 kHz could be accounted for by the presence of other types of motions, namely translation of the peptide through sample imperfections. This effect is not accurately described by diffusion-in-a-cone model and would have a maximum impact on relaxation for samples oriented at 0° .

6.5 Conclusions

This study demonstrates that $T_{1\rho}$ values for backbone ^1H , ^{13}C and ^{15}N of small membrane proteins in model membranes in liquid-crystalline phase are in the range of a few ms. In practice, they are too short to observe J-coupling (1-100 Hz) and may strongly reduce the signal when observing dipolar couplings (100-10000 kHz) through the use of SL or continuous wave type elements in pulse programs (TOCSY, PISEMA, etc.). Slow motions existing in the fluid membrane bilayer are responsible for the modulations of the residual orientation-dependent interactions, causing rapid relaxation. Nuclei on the side-chain and terminal ends experience larger scale fast-averaging motions, due to the larger degrees of freedom and thus have slightly longer values of $T_{1\rho}$ (tens of ms). Based on the contrast in $T_{1\rho}$'s between gA and typical

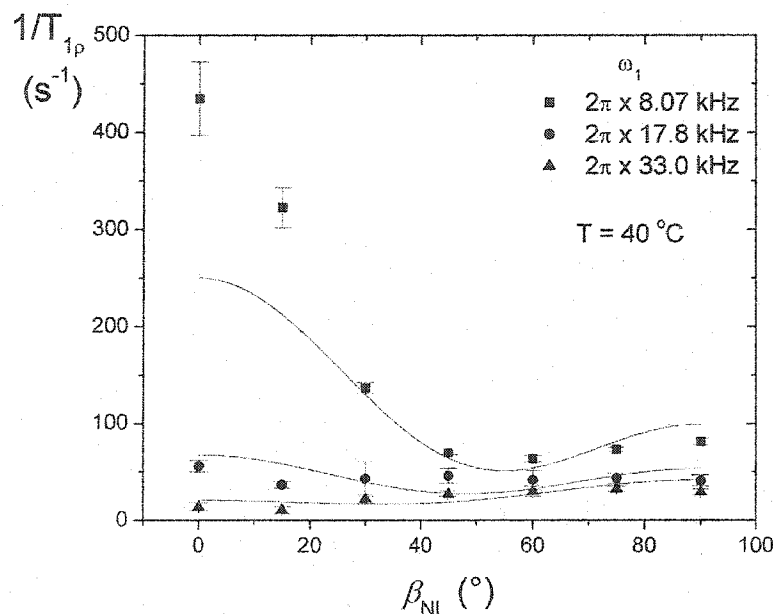


Figure 6.18: The dependence of $^{13}\text{C}'$ $1/T_{1\rho}$ for the membrane polypeptide L16 on sample orientation β_{NL} , at 40 °C at three values of ω_e . The rf field was set at $2\pi \times 8.07$ kHz (squares), at $2\pi \times 17.8$ kHz (circles) and at $2\pi \times 33$ kHz (triangles). The three lines represent simultaneous best fit lines for the three sets of data using the same set of parameters except for ω_e . The fit included the effect of the fluctuation of the mean square CSA and dipolar interactions by axial diffusion (with $(\gamma B_0 \delta)^2 = 2.2 \times 10^9 \text{ s}^{-2}$ and $(\mu_0/4\pi)^2 (\gamma_I \gamma_s \hbar / r^3)^2 = 8.4 \times 10^{-8} \text{ s}^{-2}$, $\eta = 0.82$, $A_0 = B_0 = 0$, $A_1 = 0$, $A_2 = 0.345$, $B_1 = 0.499$ and $B_2 = 0.156$) and by off-axis reorientation described by the diffusion-in-a-cone model (with $(\gamma B_0 \delta)^2 = 7.6 \times 10^7 \text{ s}^{-2}$, $(\mu_0/4\pi)^2 (\gamma_I \gamma_s \hbar / r^3)^2 = 4.0 \times 10^8 \text{ s}^{-2}$, $A_0 = 0.058$, $A_1 = 0.011$ and $A_2 = 0.01$). The correlation times for each type of motion were $\tau_c^{AD} = 2 \times 10^{-8} \text{ s}$ and $\tau_c^{DC} = 1.5 \times 10^{-5} \text{ s}$.

transmembrane α -helices, the size and shape of the protein are believed to have an important effect on its dynamical properties. Temperature can also reduce the relaxation rates by 10-20%, although by decreasing the correlation times.

Backbone ^{15}N and ^{13}C atoms are useful probes to investigate the details of the slow-scale motions. Complementary information may be obtained from the favorable resolution and simplified spectra obtainable in MAS and non-rotating oriented samples. In particular, a useful property of ^{13}C in oriented samples was used to clearly highlight the nature of these motions. Based on simple motional models (axial diffusion and diffusion-in-a-cone), the orientation dependence profiles of the relaxation clearly show a 2-mode dynamical model for an α -helical transmembrane polypeptide, with fast axial-diffusion (10^{-8} s) and off-axis reorientation (10^{-5}). These results agree with results by Prosser *et al.* [130].

These motions have an important impact on the feasibility of commonly used NMR experiments, and must be taken into consideration in the ongoing research to develop methods for the study membrane proteins. Many laboratories circumvent the problem by reducing the sample temperature, causing the bilayer to enter the more ordered and less dynamic gel phase. Another strategy would be to reduce the extent of the motion in the fluid phase by incorporating cholesterol and detergent into the bilayers. Perhaps a less invasive strategy would be to reduce the mean square dipolar interaction with the surrounding ^1H . Sacrificing hydrogen signal, by uniformly replacing 80% of the ^1H with ^2H , would theoretically reduce the dipolar second moment by a factor of 4.5 while reducing the ^1H signal by a factor of 5.



*- Problems worthy of attack prove
their worth by hitting back.*

- Piet Hein

^1H , ^{15}N -Cross-polarization spectroscopy of gramicidin A

7.1 Introduction

NMR is a powerful technique for unraveling the structure of biopolymers, as long as they are in solution where the rapid tumbling of molecules averages out the anisotropies such as chemical shift and dipole-dipole interactions. As a result of the achieved fine resolution, the resonances can be easily assigned and correlated. Membrane-associated proteins represent a unique class of biopolymers whose structure and function are dependent on their location within the hydrophobic interior of a lipid bilayer where total isotropic averaging can never take place. Micellar dispersions of small membrane polypeptides have been used to mimic the amphipathic nature of lipid membranes while allowing orientational averaging to give high-resolution spectra. However, because of their high curvature, micelles are criticized for not accurately representing the membrane bilayer. They also contribute to the overall size of the complex which effectively reduces the maximum size of the protein that can be used.

Because of the need for methods to study membrane protein structure, there have been many advances in the application of solid-state NMR to the study of membrane-associated proteins in recent years [121]. In some cases, the orientational distribution of the peptides in the membrane is narrowed by stacking the bilayers between glass plates; the anisotropic interactions are then used to deduce the orientation of the amide bonds in polypeptides relative to the bilayer normal, as described by Opella

and co-workers [35]. In other cases, the anisotropies are simply removed by MAS and by rf decoupling schemes, yielding liquid-like high-resolution spectra. Selected anisotropic interactions are then reintroduced by a wide variety of methods and are used to obtain structural constraints [121]. In either case, it is clear that the ability to achieve well-resolved signals is indispensable for using NMR as a technique to study membrane protein structure.

The dominant interaction for nuclei in polypeptides dispersed in multilamellar lipid phases is the strong dipolar coupling among the hydrogens. However, it has been shown that in the context of rapid axial reorientation within the membrane, the dipolar broadening becomes inhomogeneous and the protein exhibits sharp ^1H signals if it is submitted to MAS at a rate faster than the intermediate time scale motions [33]. Within the limits of the MAS speeds available today, this approach can provide proton signals for small membrane proteins with resolution approaching those of solution protein samples. Even so, the residual interactions are sufficiently strong to severely restrict the ability to perform J-coupling-based high-resolution experiments which often require delays of the order of several tens of milliseconds.

In the present chapter, a heteronuclear correlation experiment based on cross-polarization is proposed which demonstrates the dispersion and resolution of NMR signals from the amide groups in membrane polypeptides. For this, gA - a model membrane polypeptide dimer with a conformation that is highly sensitive to the environment - was incorporated into the fluid lamellar phase of chain and headgroup deuterated dimyristoylphosphatidylcholine (DMPC- d_{67}).

7.2 ^1H broadening in fluid membranes

In the Section 2.2.3 (p. 19), MAS was introduced simply as a sample configuration with periodic time dependence. In this section, a justification for its use to resolve ^1H signals is presented in the context of a fluid membrane. First, the general theory for the average Hamiltonian in rotating solids is explained, followed by the demonstration of its application to small membrane proteins undergoing fast axial reorientation. A more thorough treatment was presented by Maricq and Waugh [150].

7.2.1 Magic angle spinning and the average Hamiltonian

When MAS is applied for the purposes of resolution improvement, its mode of action is easy to explain. Fast rotation of the sample causes the projection of the complex interactions responsible for line broadening in a static powder sample onto the rotation axis. The residual interaction will have a $(3 \cos^2 \beta_{RL} - 1)$ dependence (where β_{RL} is the tilt angle between the rotation axis and the laboratory static magnetic field; see Figure 2.2) and will vanish when the rotation axis is carefully set at the magic angle ($\beta_{RL}=54.7^\circ$). The only requirement is that the sample be spun sufficiently fast. The effect of an explicit periodic time dependence on whole sample rotation was described using average Hamiltonian theory as early as 1967 by Haeberlen and Waugh [154, 155]. If the average interaction over any integer number of complete rotations of the sample is needed, without any concern for the details of the evolution of the spin system during a rotation, the corresponding average Hamiltonian is computed as an infinite sum of ordered terms:

$$\bar{\mathcal{H}} = \sum_{\mu=0}^{\infty} \bar{\mathcal{H}}_{\mu} \quad (7.1)$$

where the successive terms are

$$\begin{aligned} \bar{\mathcal{H}}_0 &= \frac{1}{\tau_R} \int_0^{\tau_R} \mathcal{H}(t) dt \\ \bar{\mathcal{H}}_1 &= \frac{-i}{2\tau_R} \int_0^{\tau_R} dt \int_0^t dt' [\mathcal{H}(t), \mathcal{H}(t')] \\ \bar{\mathcal{H}}_2 &= \frac{-1}{6\tau_R} \int_0^{\tau_R} dt \int_0^t dt' \int_0^{t'} dt'' \{ [\mathcal{H}(t), [\mathcal{H}(t'), \mathcal{H}(t'')]] + [\mathcal{H}(t''), [\mathcal{H}(t'), \mathcal{H}(t)]] \} \end{aligned} \quad (7.2)$$

...

To estimate the MAS speed necessary to rid the spectrum of any broadening due to orientation-dependent interactions, an investigation of the convergence of this series is needed for a given rotation period τ_R . Here, the commutators, $[\mathcal{H}(t), \mathcal{H}(t')] = \mathcal{H}(t)\mathcal{H}(t') - \mathcal{H}(t')\mathcal{H}(t)$ in all terms with $\mu > 0$, involve the Hamiltonian at a time t with itself at a different time t' . The series is greatly simplified for simple interactions such as the chemical shift anisotropy, the quadrupolar interaction, any heteronuclear

dipole-dipole interaction and even for homonuclear dipole-dipole interaction involving any number of spins in a 1D array, since their Hamiltonians commute at any time within a rotation period. This is the so-called “inhomogeneous” broadening case, where the only surviving term in the expansion is $\bar{\mathcal{H}}_0$. In this case, the sample undergoing MAS will result in a spectrum broken up into side bands with a sharply resolved centre band.

7.2.2 ^1H homogenous broadening and MAS

To show that the commutators of Equation 7.2 are non-zero for the dipole-dipole interaction between many like spins, the Hamiltonian presented in Equation 2.28 is generalized here for a system composed of n spins where a single spin labelled i is coupled to the other $(n-1)$ spins labelled j :

$$\mathcal{H}_d^i = -\gamma_H^2 \hbar \sum_{j \neq i} [3I_{iz}I_{jz} - \vec{I}_i \cdot \vec{I}_j] \zeta^{i,j}(t). \quad (7.3)$$

The term $\zeta^{i,j}(t)$ is the periodically time-varying geometrical factor which, in the simplest case of a static solid undergoing MAS, can be represented by:

$$\zeta^{i,j}(t) = \frac{1}{r_{ij}^3} \sum_{m'} \mathcal{D}_{0m'}^{(2)}(0) \beta_{PR}^{i,j} \gamma_{PR}^{i,j} \mathcal{D}_{m'0}^{(2)}(\alpha_{RL}(t)) \beta_{RL} 0 \quad (7.4)$$

where, as before, the Wigner transformations start from the PAS frame (P) to the laboratory frame (L) via the MAS rotor frame (R) (see Figure 2.2) and where the periodic rotation of the rotor is seen through the time dependence of the azimuthal angle, $\alpha_{RL}(t) = \omega_R t$. To predict the result of the average Hamiltonian higher-order terms, the commutator of the Hamiltonian at time t with the Hamiltonian at a later time t' is calculated:

$$[\mathcal{H}_d^i(t), \mathcal{H}_d^i(t')] = -\gamma_H^4 \hbar^2 \sum_{j \neq i} \sum_{k \neq i} \zeta^{i,j}(t) \zeta^{i,k}(t') \mathcal{C}_{jk}^i, \quad (7.5)$$

where

$$\mathcal{C}_{jk}^i = [3I_{iz}I_{jz}, \vec{I}_i \cdot \vec{I}_k] - [3I_{iz}I_{kz}, \vec{I}_i \cdot \vec{I}_j] - [\vec{I}_i \cdot \vec{I}_j, \vec{I}_i \cdot \vec{I}_k]. \quad (7.6)$$

Using $[\mathcal{H}_d^i(t), \mathcal{H}_d^i(t')] - [\mathcal{H}_d^i(t'), \mathcal{H}_d^i(t)] = 0$, as a condition for commutation, the following expression is obtained:

$$[\mathcal{H}_d^i(t), \mathcal{H}_d^i(t')] = -\frac{1}{2}\gamma_H^A \hbar^2 \sum_{j \neq i} \sum_{k \neq i} C_{j,k}^i \{ \zeta^{i,j}(t) \zeta^{i,k}(t') - \zeta^{i,k}(t) \zeta^{i,j}(t') \} \quad (7.7)$$

where, the relation $C_{j,k}^i = -C_{k,j}^i$ is imposed. Thus, the Hamiltonian for dipole-dipole interactions among many like spins, for a rotating sample, will commute with itself at all times if and only if

$$\zeta^{i,j}(t) \zeta^{i,k}(t') = \zeta^{i,k}(t) \zeta^{i,j}(t') \quad (7.8)$$

for all t and t' . It is easy to see from Equation 7.4 that in the absence of molecular motion the condition in Equation 7.8 is not fulfilled unless there are only two spins in the system (i.e. $j = k$) or unless all the spins lie in the same straight line (i.e. $\beta_{RL}^{ij} = \beta_{RL}^{ik}$).

Nevertheless, even if the higher order terms, $\bar{\mathcal{H}}_1, \bar{\mathcal{H}}_2, \dots$ do not vanish under MAS, they certainly become less important with increasing spinning rate as seen by their inverse relation to the period, τ_R . In the limit where MAS speed is infinite, only $\bar{\mathcal{H}}_0$ needs to be considered. Again, based on the work by Haeberlen and Waugh [154, 155], one can estimate the contribution to the linewidth due to the μ^{th} order term in the average Hamiltonian series to be:

$$k_\mu = \frac{1}{(\mu + 1)! \cdot T_2^{st}} \times \left(\frac{\tau_R}{T_2^{st}} \right)^\mu. \quad (7.9)$$

This equation is easily seen to be the result of the integration of each term in Equation 7.2 if one estimates the strength of the Hamiltonian to be approximately proportional to the relaxation rate $1/T_2^{st}$ of the static (non-spinning) sample. The residual linewidth is obtained by summing over all k_μ for $\mu > 0$. The second moment due to dipolar-coupled ^1H 's in a rigid protein sample is of the order of $1.7 \times 10^{10} \text{ s}^{-2}$; this translates to a spectral linewidth due to the ^1H - ^1H dipolar coupling of 21 kHz. The fastest currently achievable MAS rate of about 50 kHz would translate to only a 25% reduction of this linewidth according to Equation 7.9. In order to reduce the linewidths to a level where, say, one-bond ^1H - ^{15}N J-couplings can be measured (*ca.*

90 Hz), the sample would have to be rotated at an unrealistic rate of 2500 kHz! It is clear from these results that MAS accomplishes very little resolution improvement in the case of homogeneous broadening due to ^1H - ^1H dipolar coupling in perfectly rigid samples. In reality, this situation is slightly less dramatic because of the existence of fast, albeit low amplitude, motions near ambient temperatures which effectively reduce the mean square strength of the interaction. A particularly relevant question is: How does the axial reorientation diffusion of small membrane proteins embedded in fluid membranes affect the case of homogeneous broadening?

7.2.3 The effect of axially symmetric molecular reorientation

Before discussing the effect of fast axial diffusion, the expression of $\zeta^{i,j}(t)$ needs to be expanded to include a fourth reference frame, M, for the molecular moment of inertia system which, in principle, lies along or at a small angle from the axially symmetric frame defined by the membrane normal. Using the transformations $\text{P} \rightarrow \text{M} \rightarrow \text{R} \rightarrow \text{L}$ already mentioned in Section 2.2.3 and in Figure 2.2, the expression for the geometric term becomes:

$$\zeta^{i,j}(t, \tau) = \frac{1}{r_{ij}^3} \sum_{m'} \sum_{m''} \mathcal{D}_{0m''}^{(2)}(0, \beta_{PM}^{i,j}, \gamma_{PM}^{i,j}(t)) \mathcal{D}_{m''m'}^{(2)}(\alpha_{MR}, \beta_{MR}, 0) \mathcal{D}_{m'0}^{(2)}(\alpha_{RL}(\tau), \beta_{RL}, 0). \quad (7.10)$$

Whereas the angle $\beta_{PM}^{i,j}$ represents the tilt angle of the internuclear distance relative to the molecular moment of inertia long axis, the time dependence in the azimuthal angle $\gamma_{PM}^{i,j}(t)$, is modulated by the axial diffusion undergone by the molecule around the z-axis of its moment of inertia. Neglecting any other kind of molecular motion, the transformation $\mathcal{D}_{m''m'}^{(2)}(\alpha_{MR}, \beta_{MR}, 0)$ is considered time-independent and can be used to describe any sample configuration (powder, oriented, etc.). The sample rotation, as before, is described by the periodic time dependence $\alpha_{RL}(\tau) = \omega_R \tau$. The variable τ is used here to distinguish it from the much faster time variation due to axial diffusion described by t .

In the regime where the axial reorientation is considered fast and symmetric, the

Wigner transformation is simplified by replacing,

$$\mathcal{D}_{0m''}^{(2)}(0, \beta_{PM}^{i,j}, \gamma_{PM}^{i,j}(t)) = d_{0m''}^{(2)}(\beta_{PN}^{i,j}) e^{-m'' \gamma_{PM}^{i,j}(t)},$$

by its time average, where $\langle e^{-m'' \gamma_{PM}^{i,j}(t)} \rangle_t = 0$. The only surviving term will be those for which $m'' = 0$. Then, keeping only the secular part, the dipolar Hamiltonian for spin 'i' becomes

$$\mathcal{H}_d^i(\tau) = -\gamma_H^2 \hbar \sum_{j \neq i} [3I_{iz}I_{jz} - \vec{I}_i \cdot \vec{I}_j] \tilde{\zeta}^{i,j}(\tau) \quad (7.11)$$

where $\tilde{\zeta}^{i,j}(\tau)$ is the motionally-averaged periodically varying geometric term. It can be written as:

$$\tilde{\zeta}^{i,j}(\tau) = \mathcal{P}_{i,j} \mathcal{Q}(\tau) \quad (7.12)$$

for which \mathcal{P} depends on the spin pair (i,j) and \mathcal{Q} depends on τ :

$$\mathcal{P}_{i,j} = \frac{1}{r_{ij}^3} d_{00}^{(2)}(\beta_{PM}^{i,j}) \quad (7.13)$$

$$\mathcal{Q}(\tau) = \sum_{m'} d_{0m'}^{(2)}(\beta_{MR}) d_{m'0}^{(2)}(\beta_{RL}) e^{-im' \omega_R \tau} \quad (7.14)$$

Thus, taking the commutators to evaluate the higher-order terms in the expansion of the average Hamiltonian, one sees immediately that the products of the orientation-dependent factors are equal:

$$\begin{aligned} \tilde{\zeta}^{i,j}(\tau) \tilde{\zeta}^{i,k}(\tau') &= (\mathcal{P}_{i,j} \mathcal{Q}(\tau)) \times (\mathcal{P}_{i,k} \mathcal{Q}(\tau')) \\ &= \tilde{\zeta}^{i,j}(\tau') \tilde{\zeta}^{i,k}(\tau). \end{aligned} \quad (7.15)$$

Thus, the Hamiltonian $\mathcal{H}_d^i(\tau)$ commutes with itself at all times even for any distribution of two or more pairs of spins. The higher-order terms can therefore be ignored in the average Hamiltonian. In principle, a high-resolution ^1H NMR spectrum is achievable when applying MAS. The primary requirement is simply that the molecules within the membrane undergo axially symmetric reorientation with a correlation time $\tau_c \ll 8 \times 10^{-6}$ s.

Although the theory shows that the internal axial reorientation can open the way to high-resolution ^1H NMR on small membrane polypeptides, other internal motions can also strongly limit it. Indeed, the slower-scale off-axis reorientation, as seen in

Section 6.2.1 of Chapter 6, can cause important spin-lattice relaxation in the rotating frame. This same motion will also be responsible for strong spin-spin relaxation, T_2 , manifested directly on the spectrum by broader lines. A description of a high-resolution ^1H MAS NMR experiment on gA is described in the remainder of this chapter, as well as Chapter 8.

7.3 Methods

^{15}N -labelled gA was obtained as described in Section 3.1 while the DMPC- d_{67} was purchased from Avanti Polar Lipids (Alabaster, Alabama).

The peptide and deuterated phospholipids were weighed and combined in a molar ratio of 1:20, then co-dissolved in an MeOH-CHCl_3 mixture (1/1 v/v), which was then removed by rotary-evaporation followed by overnight vacuum-evaporation. The sample was hydrated by adding one "dry weight" equivalent of 50 mM potassium phosphate buffer ($\text{pH} = 6.0$) containing 10% by volume of D_2O for NMR lock purposes. The paste was homogenized manually using a stainless steel rod and introduced by centrifugation into a Doty 4-mm Si_3N_4 rotor with long Aurum caps, and allowed to stabilize for a prolonged period under experimental conditions until an equilibrium state was reached.

The entire set of NMR experiments was carried out on a Bruker 54-mm Avance Ultrashield-600 spectrometer (Karlsruhe, Germany) equipped with a Doty Scientific $^1\text{H/X/Y}$, XC4-NB, 4-mm MAS probe (Columbia, South Carolina) tuned at 600.13 MHz for ^1H and 60.82 MHz for ^{15}N . Typical ^1H and ^{15}N 90° pulse lengths were 5.8 s and 7.5 s, respectively. Cross-polarization was achieved with spin-lock fields of about 33 kHz. Figure 7.1 shows the profile of the cross-polarization spectroscopy (CROPSY) [156] pulse sequence reminiscent of the WISE experiment [157] but geared here towards high resolution. The MAS rate was 12 kHz, and the sample was maintained at a temperature of 55 $^\circ\text{C}$.

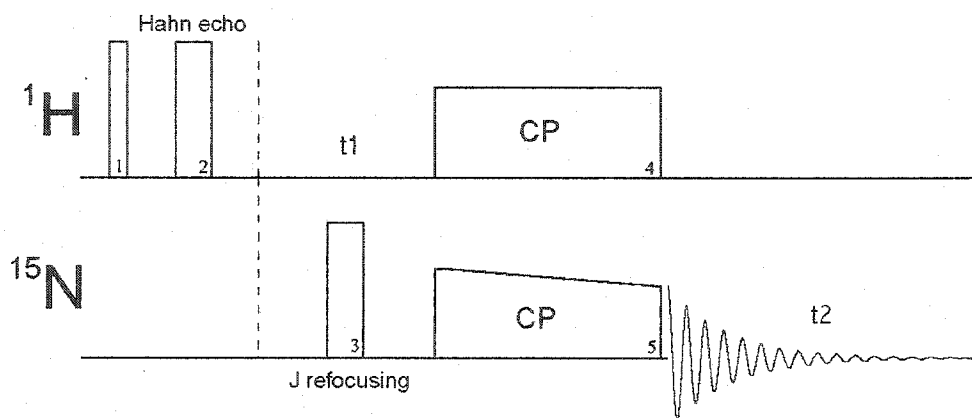


Figure 7.1: Pulses 1 and 2 form a short ^1H Hahn echo synchronized with a rotor period to simultaneously refocus the time-dependent local field and the spin-spin interactions at the start of the indirect evolution period t_1 . Pulse 3 refocuses the evolution of heteronuclear J_{HN} -coupling during t_1 . The ^1H coherence is transferred to ^{15}N via the straight and 100%-90% ramped cross-polarization pulses 4 and 5, respectively. The phase-cycling included $\phi_1=[(x)_2(-x)_2(y)_2(-y)_2]_2$, $\phi_2=(y,-y)_2(-x,x)_4(-y,y)_2$, $\phi_3=(x)_{16}$, $\phi_4=[(-x)_4(x)_4]_2$, $\phi_5=(x)_4(-x)_4(y)_4(-y)_4$, $\text{rcvr}=[(x)_2(-x)_2]_2[(-y)_2(y)_2]_2$

7.4 Results

The non-decoupled 2D CROPSY spectrum is shown in Figure 7.2. There is sufficient dispersion to identify a set of 19 peaks corresponding to the 20 H-N pairs for gA, with only two strongly overlapping peaks (Trp-11/Trp-15). Yet, eight peaks present no overlap at all. The full widths at half-height were 41 Hz and 164 Hz in the ^{15}N and ^1H dimensions on average over the resolved peaks. The intensity of the peaks shows important variations, which may be partially due to the dependence of the CP transfer on the N-H bond order parameter and on its orientation relative to the local membrane normal.

Although a definitive assignment of the resonances cannot be achieved from this experiment alone, it is nonetheless of interest to compare the chemical shifts to those obtained by high-resolution NMR experiments, such as HSQC on ^{15}N -gA in soluble form. The conformationally polymorphic gA was previously shown to form a stable right-handed $\beta^{6.3}$ -helix in sodium-dodecylsulfate (SDS) dispersion [115] and

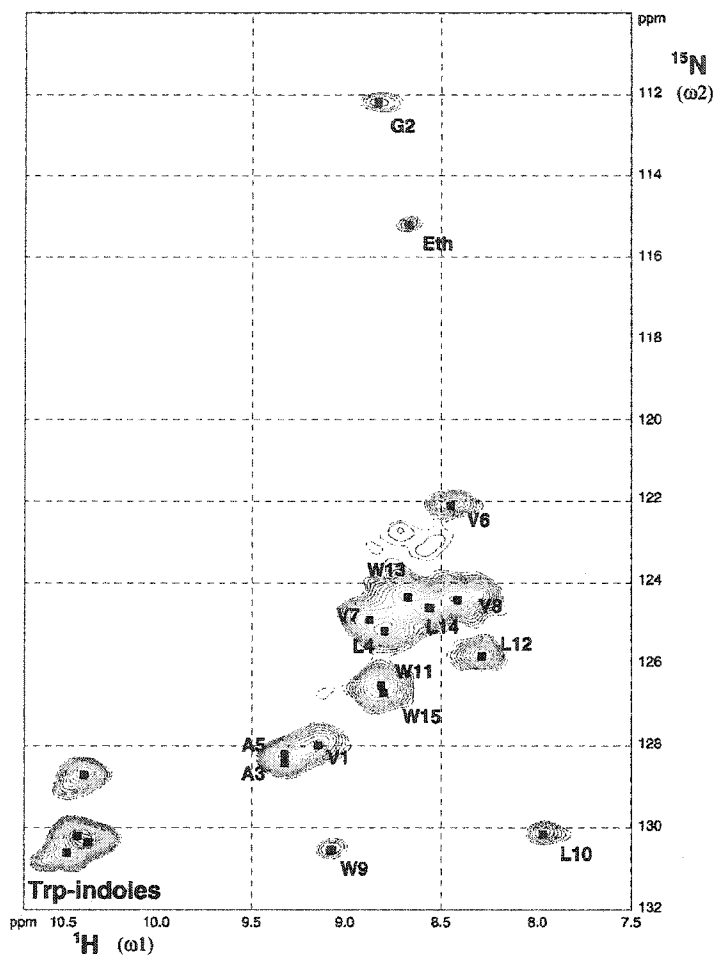


Figure 7.2: The experiment required 256 t_1 -increments, with 256 scans per increment and 2k points in t_2 . The recycling delay was 0.9 s. The sample was maintained spinning at the magic angle at 12 kHz with the temperature set at 55 °C. The spectrum was processed with a Gaussian apodization function (line broadening = -15 Hz, gaussian factor = 0.08) in 2, and with linear prediction and a squared sinebell apodization function in 1. The base contour level is at 70% of the peak intensity of the glycine peak. Labels represent tentative residue assignments based on similarity with the HSQC spectrum of gA in SDS.

Table 7.1: Summary of ^{15}N and ^1H assignments obtained by HSQC for gA in different soluble forms. These values were used in the computer-assisted peak association search with the smallest rms difference. The values for gA in DMSO were obtained from Hawks *et al.* [158].

	Residue	SDS (1/50)		TFE		DMSO		MeOH/ CHCl_3	
		^1H	^{15}N	^1H	^{15}N	^1H	^{15}N	^1H	^{15}N
1	Val	8.99	130.1	8.56	129.8	8.71	129.0	8.41	120.9
2	Gly	8.83	114.2	8.83	114.2	8.83	114.2	8.83	114.2
3	Ala	9.29	129.9	8.76	126.8	8.52	125.8	8.84	128.5
4	Leu	8.78	126.7	8.63	124.3	8.63	123.0	9.31	123.3
5	Ala	9.30	129.1	8.84	128.7	8.47	125.3	9.40	130.7
6	Val	8.42	124.2	8.59	128.9	8.31	117.6	8.36	132.1
7	Val	8.83	126.7	8.67	125.2	8.51	122.2	8.73	122.8
8	Val	8.22	126.4	8.69	125.5	8.42	122.2	9.12	125.2
9	Trp	9.02	131.8	8.82	127.5	8.66	127.7	9.18	132.0
10	Leu	7.97	132.0	8.59	120.7	8.52	126.8	9.02	128.4
11	Trp	8.70	128.6	9.00	126.7	8.73	125.7	9.47	129.5
12	Leu	8.14	127.5	8.73	129.1	8.52	126.9	9.25	127.9
13	Trp	8.61	126.3	8.95	126.1	8.73	126.1	9.85	131.4
14	Leu	8.35	126.2	8.41	129.6	8.61	127.7	7.71	130.8
15	Trp	8.83	127.8	8.53	125.7	8.78	126.5	8.77	132.4
16	Eth	8.33	116.9	8.58	118.6	8.36	115.4	8.62	123.3
	indole	9.87	130.3	10.24	129.4			10.47	132.6
	indole	9.96	129.9	10.28	129.4			10.76	133.5
	indole	9.73	130.0	10.26	129.4			10.60	132.7
	indole	9.85	130.5	10.26	129.4			10.40	131.9

a right-handed antiparallel $\beta^{7,2}$ -double-helical dimer in a MeOH/ CHCl_3 mixture in the presence of cesium thiocyanate [53]. Furthermore, it partly adopts the left- and right-handed $\beta^{4,4}$ -helix in trifluoroethanol (TFE) [88] and the left-handed $\beta^{6,3}$ -helix conformation in dimethylsulfoxide (DMSO) [158]. Only the latter reports ^{15}N assignments, and the assignments for the other three solvent media (SDS, TFE and MeOH/ CHCl_3) were completed using analogously prepared samples (see Section 4.4, p. 75).

To compare the amide chemical shifts (^1H and ^{15}N) from the CROPSY experiment with those reported in HSQC for gA in different forms (reported in Table 7.1), a computer-assisted peak association search was carried out until the smallest rms difference between chemical shifts in both dimensions was obtained. The minimized rms difference for each form of gA is summarized on Table 7.4. These results indicate that the relative shifts and range of dispersion of the resonances in both dimensions closely match those observed in the HSQC spectrum of gA dispersed in SDS, but agree only poorly with similar results in TFE, DMSO and MeOH/ CHCl_3 . The tenta-

Table 7.2: Minimum rms difference, summed over all backbone amide sites, for the ^1H and ^{15}N chemical shifts of gA in DMPC (obtained by CROPSY) relative to those observed for different soluble conformations by HSQC.

structure	reference	environment	^1H	^{15}N
right-handed N-to-N single-stranded helical dimer ($\beta^{6.3}$)	[115]	SDS	0.136	0.34 ^a
right-handed antiparallel double-helical dimer ($\beta^{7.2}$)	[53]	MeOH/ CHCl_3	0.301	2.06 ^a
left- and right-handed $\beta^{4.4}$ -helix	[88]	TFE	0.235	2.21 ^a
left-handed $\beta^{6.3}$ -helix	[158]	DMSO	0.331	3.32

^a The ^{15}N chemical shifts for these systems were obtained from HSQC experiments on ^{15}N -gA samples prepared as described in the references.

Table 7.3: Tentative ^{15}N and ^1H assignments for the CROPSY experiment on gA in DMPC. These values are obtained according to the peak association with the HSQC spectrum of gA in SDS micelles with the smallest rms difference in both dimension.

Residue	^1H	^{15}N
1 Val	9.15	130.0
2 Gly	8.83	114.2
3 Ala	9.34	130.3
4 Leu	8.82	127.1
5 Ala	9.34	130.2
6 Val	8.45	124.1
7 Val	8.90	126.9
8 Val	8.43	126.4
9 Trp	9.08	132.5
10 Leu	7.96	132.1
11 Trp	8.80	128.6
12 Leu	8.29	127.8
13 Trp	8.70	126.8
14 Leu	8.58	126.6
15 Trp	8.83	128.5
Eth	8.67	117.2
Trp-Indoles	10.38	128.7
	10.49	132.7
	10.35	132.4
	10.41	132.2

tive assignments shown in Table 7.3 are based on the closeness of fit of the chemical shifts to those obtained in SDS.

7.5 Conclusions

These results strongly support the premise that micellar dispersions can adequately mimic the amphipathic nature of a membrane bilayer even for a conformationally sensitive peptide like gA. Moreover, they are suggestive of the N-to-N right-handed $\beta^{6.3}$ -helix conformation of gA-dispersed in DMPC in a non-oriented sample under MAS, as reported previously in oriented systems [24]. More importantly, it was shown that this CROPSY experiment, when applied to small peptides associated with a non-oriented fluid membrane, offers sufficient peak resolution to simultaneously distinguish resonances from most residues. Accordingly, this experiment could be used in combination with protocols based on cross-relaxation or dipolar recoupling to collect distance and orientational restraints involving N-H groups.



*- Aucune armée ne peut résister à
la force d'une idée dont l'heure est
venue.*

- Victor Hugo

8

The nuclear Overhauser effect as a structural tool in ^1H MAS NMR of small membrane polypeptides

8.1 Introduction

The dipole-dipole coupling between any pair of spins permits relaxation through an internuclear route. This phenomenon of “cross-relaxation” has been predicted, described, and studied for homo- and heteronuclear spin systems in all sorts of samples from freely-tumbling molecules in gases and liquids to motionally-restricted species in condensed matter.

In solid-state NMR, the widely-used cross-polarization technique, discussed in the previous chapter, is a striking example of the use of cross-relaxation in a heteronuclear spin system. It makes use of the rather efficient cross-relaxation between a strong abundant spin and a weak rare spin for signal enhancement of the latter. However, by far the most successful application of cross-relaxation in NMR is the exquisitely selective nuclear Overhauser enhancement or effect (NOE) driven by the strong dipolar coupling between hydrogens in close proximity. The measurement of NOEs is extensively used today to evaluate ^1H - ^1H distance restraints for structure elucidation in high-resolution NMR in solution samples. This effect was first reported for a 2-spin system by Solomon as early as 1955 [159] and described as being the nuclear-spin equivalent of the enhancement effect of saturation of electron spins on

the nuclear spins of metals described by Overhauser [160, 161]. Although the same tightly-coupled nuclear spins also exist in solids, this homonuclear effect becomes useless with increasing sample viscosity, to some extent because the resolution typically no longer permits spin pairs to be distinguished on a chemical shift basis, but most importantly because spin-spin transitions are favored so efficiently that the system attains a common spin temperature. As this spin-diffusion limit is approached, it becomes impossible to relate the cross-relaxation rates to spin-spin distance.

How does inter-proton cross-relaxation behave in fluid membrane bilayers? The relevance of the question stems from the fact that membrane components possess important dynamic characteristics of both liquids and solids. With high-frequency internal motions and axial diffusion, fluctuations in the homonuclear dipolar interaction may be important enough to promote the nuclear Overhauser effect in a regime that is still useful for distance restraint evaluation. And with the use of MAS to narrow the ^1H linewidths, these NOEs between resolved ^1H resonance pairs can be directly observed. A series of recent papers by Gawrisch *et al.* have described the use of ^1H NOESY on phospholipid bilayers undergoing MAS [162–166]. A number of interesting conclusions have been put forward. Importantly, magnetization exchange between all possible pairs has been observed even between the most distant ones (such as between the methyl groups of the choline headgroups and the methyl groups at the end of the lipid hydrocarbon chains). These results were initially interpreted as the manifestation of spin-diffusion. However, using specifically-deuterated lipids to break up a possible spin-to-spin relaying network, it was demonstrated that any magnetization relaying mechanism is insignificant up to mixing times of 300 ms. It was therefore concluded that the wealth of NOE cross-peaks was the result of a high degree of lipid disorder. The existence of long-range NOE exchanges is mainly conducted through inter-molecular contacts between neighboring lipids, especially for hydrogens with similar spatial distributions along the bilayer normal. This was further supported by the fact that the magnetization transfer fits a single exponential relaxation mechanism corresponding to the correlation time and activation energy for lateral diffusion. Faster internal motions influence the efficiency of exchange by downscaling the mag-

nitude of the residual second moment modulated by the slower motions. These results were confirmed using molecular dynamics simulation trajectories to predict the pathway of cross-relaxation. In conclusion, the results of ^1H NOESY experiments on bilayer systems relate more to the overall phase behaviour and lipid distribution than strictly to the 3D structure of individual lipid molecules.

Turning to small membrane polypeptides, should similar results be expected in a NOESY experiment? It could be presumed that the pathway of NOE exchanges would not reflect those seen in lipids. First, the peptides are mainly in contact with lipids, which, when fully deuterated, cannot provide NOE exchange partners. Second, unlike fluid lipids which undergo large chain tilts, kinks or even upturns, polypeptide backbones are firmly held into their secondary structure by hydrogen bonding networks; in addition, their longitudinal position within the membrane bilayer is usually well delimited. Thus, individual hydrogens, especially those covalently bound to the protein backbone, are not as broadly distributed along the bilayer normal as in the case of lipids. It can thus be expected that if NOEs can be measured in polypeptide chains, they will reflect close-range intramolecular contacts. Preliminary results of ^1H NOE spectroscopy applied to small surface membrane polypeptide were presented in the past [167, 168] In this chapter, results and tentative assignments of ^1H NOE interactions are reported for the first time on a transmembrane protein, gA, in a lipid bilayer. These are preceded by some important considerations regarding the geometry and correlation times of the anisotropic dynamics leading to this potential source of membrane protein structural restraints.

8.2 Methods

8.2.1 The 1D-NOE experiment

The 1D-NOE experiments were performed on unlabelled gA undergoing MAS at 9 kHz (a home-made MAS probe implemented with a Doty high speed 5-mm MAS stator) in a field of 8.46 T (360 MHz spectrometer). It was important to carry out this experiment in completely deuterated lipids to suppress lateral NOE transfer from

peptide to lipids, such as those previously observed between lipids [165]. At that time, before deuterated phospholipids were available, it was decided to use the multilamellar phase (or “neat” phase) formed from laurate- d_{25} salts. Cesium laurate (CsL), was chosen to extend the existence of this phase up to 55 °C [169]. It was prepared by simple titration of lauric acid- d_{25} (CDN Isotopes, Pierrefonds, Québec) with cesium hydroxide (Sigma). The peptide/lipid mixture was retrieved by evaporation from TFE. The multilamellar sample thus contained gA/cesium laurate- d_{25} / D_2O (1:18:118 mol/mol/mol) for a total sample mass of 60 mg, which was introduced in a 5-mm Si_3N_4 Doty rotor with aurum end caps and equilibrated for at least 24 h under experimental condition before collecting data. The 1D-NOE experiment was described in Section 3.4.3.4 (p. 57). A presaturation pulse preceded the pulse sequence to suppress the water peak at 4.8 ppm.

8.2.2 The 2D-NOESY experiment

The NOESY experiment was performed on unlabelled gA (Sigma) dispersed in chain-deuterated (95%) DMPC- d_{54} synthesized by the method described by Gupta *et al.* [59]. The peptide/lipid mixture (1:9 molar ratio), extracted by evaporation from TFE, was hydrated with a 50 mM potassium phosphate buffer (D_2O) adjusted to pD = 6.0. A total sample mass of 68.3 mg was transferred to a 4-mm zirconia Bruker rotor with a Kel-F turbine cap. The experiment was carried out on a 500-MHz Bruker spectrometer using a 4-mm CP/MAS-VT probe tuned to the 1H resonance frequency (500.13 MHz). The sample was allowed to equilibrate extensively (over 24 h) under experimental conditions, i.e. at a temperature of 55 °C and MAS spinning rate of 14 kHz. The experimental pulse sequence was modified from the standard Bruker “noesytp” program (See Section 3.4.3.4, p. 57) to which a Hahn echo (with 500 μs delays) was implemented after the third 90° pulse. The typical 90° pulse length was 3.75 μs and the recycling delay was 1.2 s. A total of 80 FID scans of 4096 points were collected for each of the 256 increments in t_1 . The spectral sweep width was 12 ppm or 6000 Hz in both dimension. A 125-ms NOE mixing time was used. The experimental result was processed into a 2D spectral matrix (ω_2 : Gaussian

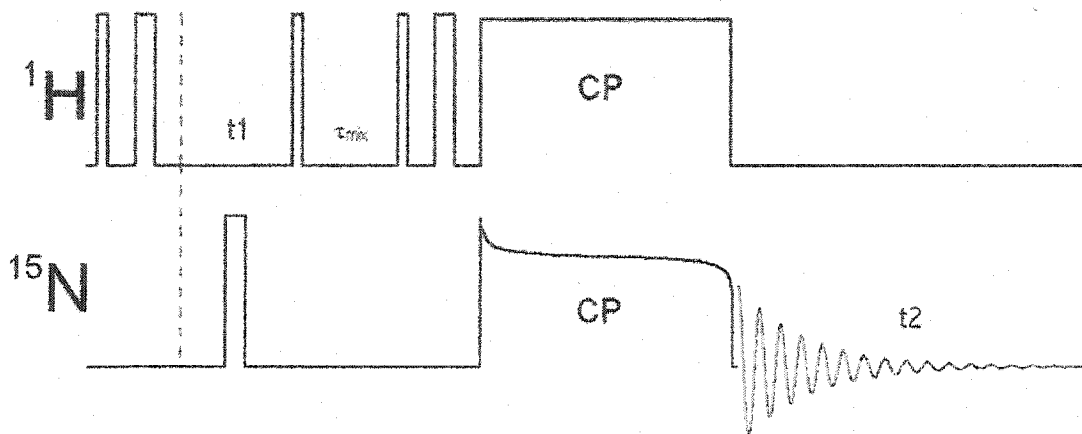


Figure 8.1: 2D-NOE-CROPSY pulse sequence.

apodization (line broadening: -5 Hz, coefficient: 0.3) + Fourier transform; ω_1 : linear prediction (256 points, 64 coefficients) + Gaussian apodization (line broadening: -5 Hz, coefficient: 0.1) + Fourier transform).

8.2.3 The 2D-NOE-CROPSY experiment

The sample composition and conditions used in this experiment were the same as described in Section 7.3 (p. 164). Figure 8.1 illustrates the pulse program designed to accomplish the required correlations. As for the CROPSY pulse sequence, a transverse ^1H magnetization is prepared and allowed to evolve during t_1 . It is then transferred onto the longitudinal axis for a duration τ_{mix} during which NOE exchanges are allowed to take place. Any exchanged magnetization onto $^1\text{H}_N$ is then transferred to the adjacent ^{15}N spin via a cross-polarization scheme at the end of which the FID is recorded. A ^1H - ^{15}N decoupling scheme (XiX [81]) is applied during the FID on the ^1H channel. This experiment was performed only once with an NOE mixing time, τ_{mix} , of 25 ms and a CP contact time of 200 μs (using a shaped pulse, following a downward tangential function with a midpoint level of 85%, on the ^{15}N side to efficiently match resonances [157]). The experiment used 128 increments in t_1 and a sweep width window of 12136 Hz (200 ppm) and with 2048 points in t_2 using a sweep width size

of 12000 kHz (20 ppm). The repetition time was 1 s which resulted in an overall experimental time of 36 hours. The program used two short Hahn echoes, before t_1 and after the NOE mixing time. These allowed small delays for power switching. The 90° -pulses were 6.8 and 9 μ s on the ^{15}N and ^1H channels respectively. The CP was achieved under a field of 28 kHz. The spectrum was processed with a squared sine (90° shift) and a 10-coefficient linear prediction of 128 additional points along the t_1 dimension and a Gaussian apodization (line broadening: -20 Hz, coefficient: 0.045) window functions in the t_2 dimension.

8.2.4 Simulations

In this chapter, simulated spectra of 2D-NOE-CROPSY are presented for gA. These were obtained using two fortran F77 programs called “anisoNOE.f” and “id-hsqc-noesy-ga.f”. From an initial PDB structure, the first program predicts the intensity of any ^1H -pair within 6 Å of each other based on their internuclear distance, their orientation relative to the molecular moment of inertia principal axis, as well as the motional correlation times and the order parameters for internal motions, axial diffusion around the moment of inertia principal axis and off-axis reorientation. This program was applied to the PDB:1mag model structure of gA [24]. The second program calculates the FID of each increments of a simulated 2D-NOE-CROPSY based on the output of the first program and the known assignments for gA. These were readable by the NMR processing program Felix 97 (Accelrys) in which the 2D spectrum was processed. Copies of the program codes can be found in the appendix (p. 241) of this thesis.

8.3 Theoretical considerations

The quantum energy states of a homonuclear 2-spin-1/2 system can be depicted as in Figure 8.2, with all possible transition rate constants denoted by W_{I_i} , W_{I_j} , W_0 and W_2 . While W_{I_i} and W_{I_j} represent the single quantum jumps of spins I_i and I_j the rate constants W_0 and W_2 , for zero- and double-quantum state transitions, respectively, are the only possible avenues for cross-relaxation. The Solomon equations predict

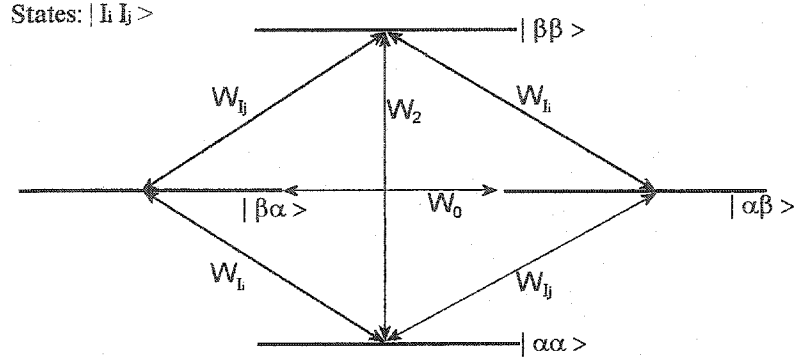


Figure 8.2: Quantum energy state diagram for a homonuclear coupled spin system. Transitions between $I_i I_j$ mixed states $|\alpha\alpha\rangle$, $|\alpha\beta\rangle$, $|\beta\alpha\rangle$, $|\beta\beta\rangle$, are represented by arrows and correspond to the transition rates, W_I , W_S , W_0 and W_2 , used in the Solomon equations.

that the evolution of the angular momentum I_{iz} towards its equilibrium I_{iz}^0 value (or using $\Delta I_{iz} = I_{iz} - I_{iz}^0$) is described by:

$$\frac{d\Delta I_{iz}(t)}{dt} = -\rho_{ii}\Delta I_{iz}(t) - \sigma_{ij}\Delta I_{2z}(t), \quad (8.1)$$

where ρ_i is the autorelaxation rate and σ_{ij} is the cross-relaxation rate for $i \neq j$. These are defined in terms of transition rates as:

$$\rho_{ii} = W_0 + 2W_{I_i} + W_2 \text{ and} \quad (8.2)$$

$$\sigma_{ij} = \sigma_{ji} = W_2 - W_0. \quad (8.3)$$

These definitions show that ρ 's are always positive, whereas σ can take a negative value when the "flip-flop" transitions dominate over the "flip-flip", giving a possible enhancement effect.

These equations can be extended into a matrix notation for an N-spin system (such as for complex proteins) with the result:

$$\Delta \mathbf{M}_z(t) = -e^{\vec{\mathbf{R}}t} \Delta \mathbf{M}_z(0) \quad (8.4)$$

where the relaxation matrix, $\vec{\mathbf{R}}$, is composed exclusively of the rate constants ρ_{ii} and σ_{ij} :

$$\vec{\mathbf{R}} = \begin{pmatrix} \rho_{11} & \sigma_{12} & \sigma_{13} & \cdots & \sigma_{1N} \\ \sigma_{21} & \rho_{22} & \sigma_{23} & \cdots & \sigma_{2N} \\ \sigma_{31} & \sigma_{32} & \rho_{33} & \cdots & \sigma_{3N} \\ \vdots & \vdots & \vdots & \ddots & \vdots \\ \sigma_{N1} & \sigma_{N2} & \sigma_{N3} & \cdots & \rho_{NN} \end{pmatrix} \quad (8.5)$$

In the simplest case scenario of an isolated 2-spin system, where $\sigma_{12} = \sigma_{21} = \sigma$ and $\rho_{11} = \rho_{22} = \rho$, the magnetization will evolve according to:

$$\begin{pmatrix} \Delta I_1(t) \\ \Delta I_2(t) \end{pmatrix} = \begin{pmatrix} a_{11}(t) & a_{12}(t) \\ a_{21}(t) & a_{22}(t) \end{pmatrix} \begin{pmatrix} \Delta I_1(0) \\ \Delta I_2(0) \end{pmatrix}, \quad (8.6)$$

where

$$a_{11}(t) = a_{22}(t) = \frac{1}{2}e^{-(\rho-\sigma)t}(1 + e^{-2\sigma t}), \quad (8.7)$$

$$a_{12}(t) = a_{21}(t) = -\frac{1}{2}e^{-(\rho-\sigma)t}(1 - e^{-2\sigma t}). \quad (8.8)$$

These equations show that the magnetization will follow a bi-exponential function, with the autorelaxation decaying to zero and the cross-relaxation following a bimodal function with an early rise and a late decay. Generally, the NOE cross-peak evolution is collected over the initial part of Equation 8.8, and fitted to a linear function with slope $-\sigma$.

How are the individual relaxation rates in the matrix evaluated as a function of motional fluctuations and correlation times? According to [40], the cross-relaxation terms σ_{ij} evolve as a difference of spectral density functions at twice the Larmor frequency and near zero frequency (corresponding to the frequency difference for the W_2 and W_0 transition rates, respectively):

$$\sigma_{ij} = \zeta[3J_{ij}(2\omega_0) - \frac{1}{2}J_{ij}(0)], \quad (8.9)$$

in which the proportionality constant ζ contains all the non-fluctuating dipole-dipole interaction constants ($\zeta = (2\pi/5)(\mu_0/4\pi)^2\gamma^4\hbar^2$), where γ is the gyromagnetic ratio for hydrogens. The spectral density function in Equation 8.9 is defined as the Fourier

transform of the normalized correlation function, $g_{20}(\tau)$, used similarly as in Chapter 2 (p. 13):

$$g_{20}(\tau) = \langle r_{ij}^{-6} \rangle^{-1} \left\langle \frac{\mathcal{D}_{00}^{(2)}(\Omega_{PL}(0))}{r_{ij}^3(0)} \frac{\mathcal{D}_{00}^{(2)}(\Omega_{PL}(\tau))}{r_{ij}^3(\tau)} \right\rangle. \quad (8.10)$$

The notation used here maintains consistency with the previous discussion on rotating-frame relaxation (Chapter 6). Other sources typically use the symbols $C(\tau)$ and $Y(t)$ for the correlation function and the fluctuating Wigner function [170]. For an isotropically tumbling rigid molecule, the spectral density obtained from 8.10 is simply:

$$J(\omega) = \frac{2}{5} \left(\frac{\tau_c}{1 + \omega^2 \tau_c^2} \right). \quad (8.11)$$

In the case of an anisotropic motion with label k , the contribution to the spectral density at frequency ω is described by this expression scaled by the amount $(1 - S_k^2)$, where S_k is the residual order parameter characteristic of that motion. The remaining interaction strength (or the residual second moment) can be further modulated by a slower anisotropic motions with resulting order parameter S_{k+1} , and so a second term like 8.11 is introduced with coefficient $(1 - S_{k+1}^2)S_k^2$, giving the general expression:

$$J(\omega) = \frac{2}{5} \sum_{k=1}^n \left(\left(\prod_{l=0}^{k-1} S_l^2 \right) (1 - S_k^2) \frac{\tau_k}{1 + \omega^2 \tau_k^2} \right). \quad (8.12)$$

for a system undergoing n types of uncorrelated motions, with correlation times, τ_k and following the rule $\tau_1 < \tau_2 < \tau_3 \cdots < \tau_n$. It is also assumed that $S_0^2 = 1$, representing the order parameter for an infinitely small correlation time. This expression has been used by Lipari and Szabo [171, 172] for systems with fast internal motions (such as methyl group reorientation) combined with the isotropic reorientation of the whole body for soluble proteins:

$$J(\omega) = \frac{2}{5} \left(\frac{(1 - S^2)\tau_e}{1 + \omega^2 \tau_e^2} + \frac{S^2 \tau_c}{1 + \omega^2 \tau_c^2} \right). \quad (8.13)$$

in which τ_e is the fast effective correlation time corresponding to internal motions and S_e^2 is the square of the order parameter after these internal motions. The correlation time, τ_c , is that of the isotropic tumbling of the molecule for which the resulting order parameter is $S_C^2 = 0$.

In general, the square order parameter leftover by any motional model can be expressed as:

$$S^2 = [\langle r_{ij}^{-6} \rangle]^{-1} \sum_{q=-2}^2 \left| \frac{\mathcal{D}_q^{(2)}(\Omega)}{r_{ij}^3} \right|^2. \quad (8.14)$$

In the following sections, the behaviour of ^1H - ^1H cross-relaxation in systems in the absence of any isotropic reorientation but undergoing model motional modes such as axial diffusion and small amplitude off-axis reorientation will be investigated. Later, the issue of whether a spin system undergoing cross-relaxation approaches the spin-diffusion limit with typical correlation times such as those evaluated for membrane polypeptides in Chapter 6 will be assessed.

8.4 Anisotropic motions and NOE

Before performing NOE-type experiments on a transmembrane polypeptide, it is important to have a full grasp of the effects of the anisotropic motions existing in a membrane bilayers. A convenient way to illustrate these effects relative to a conventional isotropically reorienting soluble protein, is to consider again the simplified model motions discussed in Chapter 6, and to use the channel structure coordinates (PDB:1mag) of gA in the calculation of the spectral density functions dictating the cross-relaxation rates. First the effect of the axial diffusion of the protein about its moment of inertia principal axis will be studied. Other known motions will then be introduced such as the slower whole-body off-axis reorientation originating from wobble or membrane undulation modes. Finally, the effect of fast internal motions will be considered by applying the models of Lipari and Szabo [171, 172]. In all cases, it will be assumed that: (1) all diffusive motions have a correlation function that decays exponentially with time constant τ_c^k , where k denotes the label of the type of motion, (2) all motions represented by τ_c^k are uncorrelated, (3) any residual static dipole-dipole interaction left over after the slowest of these motions is eliminated by the coherent averaging of the MAS, and (4) that MAS does not contribute to the cross-relaxation.

8.4.1 Axial diffusion alone

Introducing rigid-body axial diffusion (AD) as the sole source of dipole-dipole interaction fluctuation (neglecting any internal motions), it is straightforward to evaluate the S_{AD}^2 coefficient for any two neighboring pairs of ^1H ($< 6 \text{ \AA}$) in gA starting from the PDB:1mag coordinate file. Since r_{ij} is constant, the expression in Equation 8.14, reduces to:

$$S_{AD}^2 = \frac{1}{4} (3 \cos(\beta_{PM})^2 - 1)^2, \quad (8.15)$$

where β_{PM} is the angle between the internuclear vector and the axis of reorientation. To evaluate the cross-relaxation rate, only the term with $J(0)$ of Equation 8.9 is considered ($J(2\omega_0)$ is ignored) since the axial diffusion correlation time, τ_c^{AD} ($10^{-7} - 10^{-8} \text{ s}$), is typically much larger than $1/2\omega_0$ (10^{-10} s). The expression of the spectral density function in Equation 8.12, with this single dynamic mode, is simplified to:

$$J(0) = \frac{2}{5} (1 - S_{AD}^2) \tau_c^{AD}. \quad (8.16)$$

This relation implies that the cross-relaxation rate will be reduced by a factor of $1 - S_{AD}^2$, which can take any value between 0 and 1, depending on the orientation of the internuclear vector relative to the axis of diffusion. This scaling of the cross-peaks in a NOESY experiment will thus dramatically modify the interpretation of internuclear distance restraints from the cross-peak volumes. The distances will only be predictable with prior knowledge of the molecular structure and axis of reorientation.

However, it may still be possible to interpret the restraints in the conventional way. A statistical survey of all theoretical $^1\text{H}_N$ - ^1H contacts measured in the gA coordinate file show that very few cross-peaks are heavily reduced. Indeed, according to Figure 8.3(A) about 90% of all the peaks would be reduced by 30% or less in volume. The average reduction would be 18% ($1 - S_{AD}^2 = 0.82$). The solid-line overlay in this figure shows the theoretical probability curve of the $(1 - S_{AD}^2)$ parameter predicted for a powder-like distribution of ^1H - ^1H vectors. Consequently, when comparing the correlation between $^1\text{H}_N$ - ^1H cross-peak volumes (with a mixing time of 300 ms) and r^{-6} for an isotropically- and an axially-diffusing gA molecule as shown in Figure 8.3 (B) and (C), one can see a moderate deterioration in the r^{-6} /peak volume correlation

for the axial diffusion case. In a sample of 292 cross-peaks, fewer than 30 of these are far from the linear fit, with the majority corresponding to very small peak volumes. With this type of correlation, it is believed that a set of scaled restraints with wider limits could be applied in the simulated annealing protocol with satisfactory structural results, given that enough NOESY cross-peaks were measured.

It is also conceivable that more complex refining algorithms could be applied for simulated annealing, taking *both* orientation and distance into consideration in the restraining function for a single cross-relaxation measurement. Algorithms of this type already exist to fit anisotropic motions for large protein complexes in most simulated annealing packages, and the adaptation of these to membrane protein will constitute a future challenge. Unfortunately, slower motions can severely complicate the cross-relaxation picture of polypeptides in common fluid bilayers.

8.4.2 The effect of off-axis reorientation

As before, the slower off-axis reorientation motions in bilayer membranes are modeled following the diffusion-in-a-cone (*DC*) picture described earlier (Section 6.2.4, p. 121). Although the order parameter for this off-axis reorientation motion, estimated as

$$S_{DC}^2 = 1 - \sum_{m=-2}^2 \mathcal{A}_{|m|}, \quad (8.17)$$

(see Figure 6.1 for definitions of $\mathcal{A}_{|m|}$), is large (*ca.* 0.9-0.95), the correlation times for this motion on the order of 10^{-5} s. Hence, it is expected that this motion will influence the cross-relaxation rate due to terms in $J(0)$ much more than the motion of axial diffusion.

The expression of Equation 8.12 for a spin pair undergoing both motions is:

$$J(\omega) = \frac{2}{5} \left(\frac{(1 - S_{AD}^2)\tau_c^{AD}}{1 + \omega^2(\tau_c^{AD})^2} + \frac{S_{AD}^2(1 - S_{DC}^2)\tau_c^{DC}}{1 + \omega^2(\tau_c^{DC})^2} \right), \quad (8.18)$$

where τ_c^{AD} and τ_c^{DC} are the correlation times for axial diffusion and diffusion-in-a-cone.

This equation was used with typical parameter values of $\tau_c^{DC} = 1.5 \times 10^{-5}$ s, $S_{DC}^2 = 0.9$ (corresponding to diffusion of the molecular moment of inertia in a cone

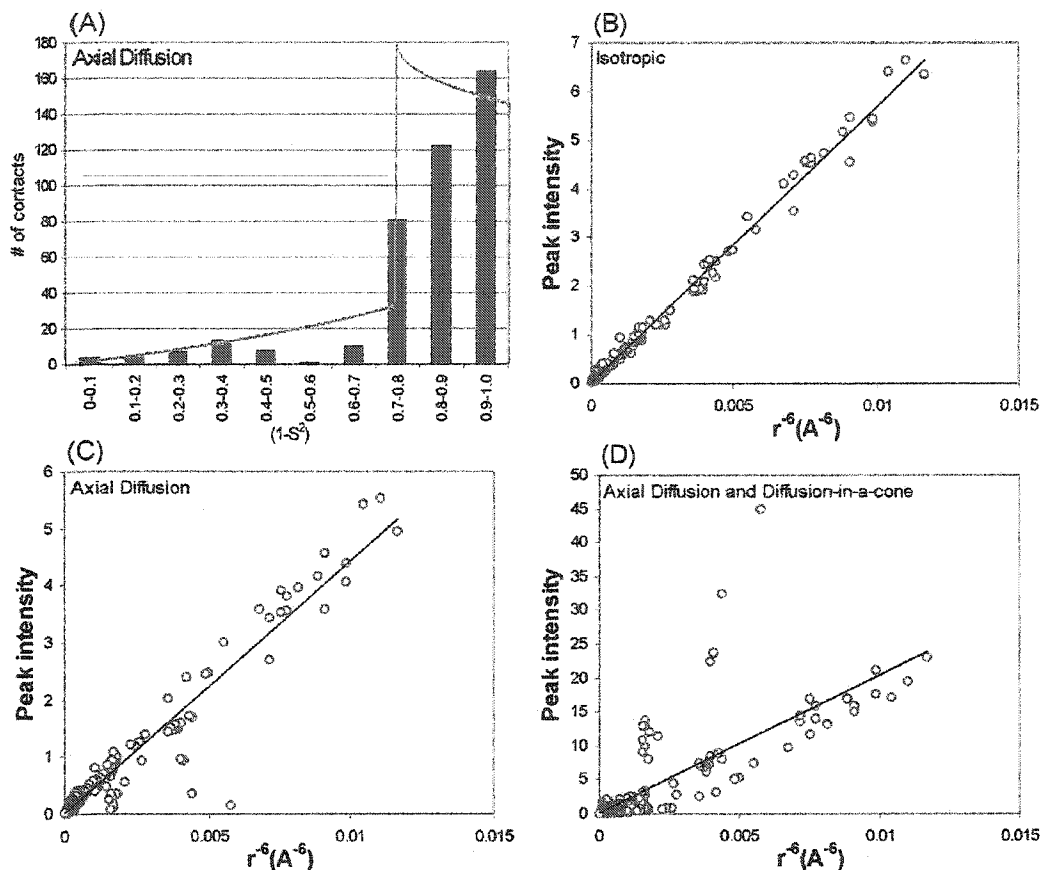


Figure 8.3: (A) The histogram bars represent the number of ^1H - ^1H contacts in the gA model structure PDB:1mag separated by less than 6\AA as a function of the disorder coefficient $1 - S_{AD}^2$. The sample (histograms) and “powder” theoretical (solid line) distribution show that the majority of contacts have a coefficient of 0.75 or larger. Values below 0.75 correspond to internuclear vectors with an orientation β_{PM} between 0 and 35.3° . (B, C, D) The relative NOE cross-peak intensity for all the ^1H - ^1H contacts in PDB:1mag is plotted as a function inverse internuclear distance to the sixth power for the model structure undergoing (B) isotropic reorientation, (C) axial diffusion alone ($\tau_c^{AD} = 1 \times 10^{-7}$ s) and (D) axial diffusion and off-axis reorientation ($\tau_c^{DC} = 1.5 \times 10^{-5}$ s, $S_{DC}^2 = 0.9$).

with a 30° semi-angle) and $\tau_c^{AC} = 1 \times 10^{-7}$ s to predict the relative NOE cross-peak volumes in a NOESY experiment. S_{AD}^2 was evaluated as before according to the angle β_{PM} between the internuclear vector and the moment of inertia principal axis. Again, observing the correlation between cross-peak intensity and internuclear distance in Figure 8.3 (D), a generally good distribution around a linear function for the majority of the peaks is observed. However, a small number of aberrant cross-peaks, corresponding to those with a near parallel orientation with the axis of diffusion (small β_{PM}), now have very large cross-peak volumes. These could be erroneously interpreted as very close internuclear contacts which would create severe energy penalties in a simulated annealing run. The following discussion on spectral density profiles can explain these exceptional cases.

Figure 8.4 (A) and (B) shows the spectral density functions for two pairs of ^1H with similar distance separations but different orientations, namely $^1\text{H}_N^{\text{Ala-3}} \rightarrow ^1\text{H}_\alpha^{\text{Ala-3}}$ ($r = 2.87$ Å, $\beta_{PM} = 19.6^\circ$, $S_{AD}^2 = 0.690$) and $^1\text{H}_N^{\text{Leu-14}} \rightarrow ^1\text{H}_\alpha^{\text{Leu-14}}$ ($r = 2.88$ Å, $\beta_{PM} = 51.0^\circ$, $S_{AD}^2 = 0.009$), as extracted from the PDB:1mag structure. The predicted functions were calculated for the gA dimer and were restricted to the contribution(s) from the isotropic reorientation ($\tau_c^{iso} = 2 \times 10^{-8}$ s, $S_{iso}^2 = 0$), from axial diffusion alone ($\tau_c^{AD} = 1 \times 10^{-7}$ s) or from axial diffusion plus diffusion-in-a-cone ($\tau_c^{DC} = 1.5 \times 10^{-5}$ s, $S_{DC}^2 = 0.9$). They do not include the contribution from the coherent motion of MAS. These functions help predict the spectral density values $J(0)$ and $J(2\omega_0)$, important for the cross-relaxation rate. For the Ala-3 spin pair, the residual interaction strength after the axial diffusion is relatively large and thus the slower motion causes a significant increase in the spectral density at zero frequency. The Leu-14 spin pair lies at an angle close to the magic angle relative to the diffusion axis, so that the axial diffusion projects out most of the interaction as in an isotropically reorienting sample. There is thus little residual interaction strength being modulated by the slower off-axis reorientation, causing only a small increase in $J(0)$.

These curves show that in solution, these NOE correlations would have similar intensities, but in a bilayer with both anisotropic motions, the Ala-3 cross-peak volume

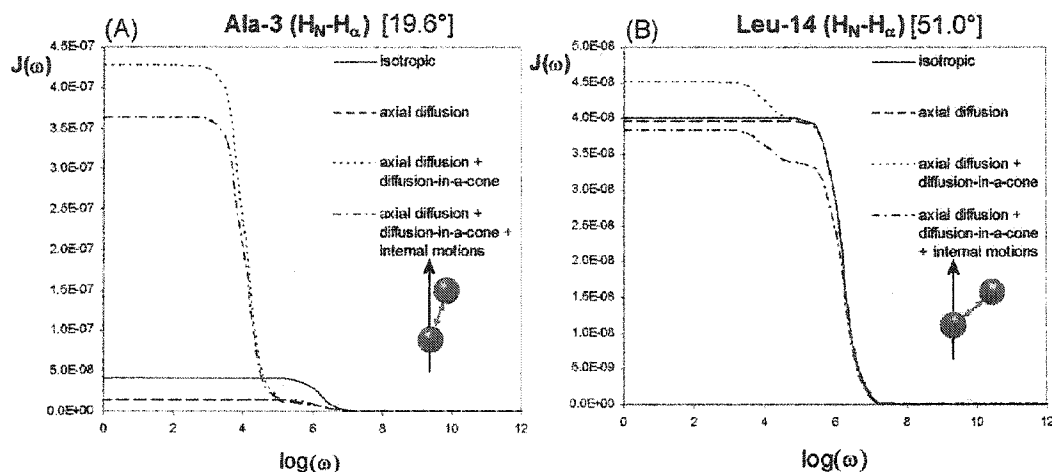


Figure 8.4: The spectral density distribution function for ω from 0 to 10^{12} s $^{-1}$ for two spin pairs separated by 2.87 Å but with different orientations (A) 19.6° and (B) 51.0° relative to the moment of inertia principal axis. These functions help understand the value of $J(0)$, relevant for the cross-relaxation rate, for four different motional models. The isotropic motion (with $\tau_c^{iso} = 2 \times 10^{-8}$ s) give the same $J(\omega)$ in both cases. With axial diffusion ($\tau_c^{AD} = 10^{-7}$ s), the Ala-3 spin pair results in a lower $J(0)$. Since the residual interaction is larger in Ala-3, the addition of off-axis diffusion through the diffusion-in-a-cone model ($\tau_c^{DC} = 1.5 \times 10^{-5}$ s and $S_{DC}^2 = 0.9$) increases $J(0)$ more than in Leu-14 for which most of the dipolar interaction is eliminated by axial diffusion. The implementation of fast internal motions ($\tau_c^{int} = 0.75 \times 10^{-9}$ s and $S_{int}^2 = 0.85$) simply reduces both $J(0)$ by 85%. In all cases, it is assumed that the residual interaction after the slowest motion is eliminated by the coherent rotation at the MA, which does not contribute to $J(0)$.

will be about 10 times larger than the corresponding Leu-14 cross-peak. This effect makes NOE experiments difficult to interpret since the NOE intensities contains not only distance but orientation information. It is conceivable that in this particular case, one could infer the orientation of each internuclear vector relative to the axis of reorientation knowing that both NOEs correspond to the same internuclear separation. It will be imperative, however, when interpreting data in this way, to have an accurate motional model, since the $J(0)$ value is extremely sensitive to the τ_c^{AD}/τ_c^{DC} ratio as well as to S_{DC}^2 . Indeed, Figure 8.3 shows that the introduction of slow off-axis motions changed the NOE volume ratio (Ala-3/Leu-14) from 0.31 to 9.5, but increasing τ_c^{AD} by a factor of 10 further increases this ratio to 52!

8.4.3 The effect of fast internal motion

Internal motions such as side-chain ring flips and methyl group reorientation, as well as vibrational modes which cause bond stretching and reorientations, have the opposite effect on the slower whole-body off-axis motions. Because they are rapid, they will not only reduce the mean-squared dipole-dipole interaction, but also contribute to the “flip-flip” transition expressed as the positive term in $J(2\omega_0)$ of the Equation 8.9. The full expression for $J(\omega)$, according to Equation 8.12 for this triple-motion system is:

$$J(\omega) = \frac{2}{5} \left(\frac{(1 - S_{int}^2)\tau_c^{int}}{1 + \omega^2(\tau_c^{int})^2} + \frac{S_{int}^2(1 - S_{AD}^2)\tau_c^{AD}}{1 + \omega^2(\tau_c^{AD})^2} + \frac{S_{int}^2 S_{AD}^2 (1 - S_{DC}^2)\tau_c^{DC}}{1 + \omega^2(\tau_c^{DC})^2} \right), \quad (8.19)$$

where τ_c^{int} corresponds to the correlation time of the internal motions resulting in the residual order parameter S_{int}^2 .

Unfortunately, with typical values for the order parameter and correlation times of the internal motions used for soluble proteins ($0.65 < S_{int}^2 < 0.85$ and $\tau_c^{int} = 0.75 \times 10^{-9}$ s), there is an overall reduction of the overall relaxation rate proportional to S_{int}^2 mainly due to the $J(0)$ in Equation 8.9. Unless they involve much larger amplitudes (smaller S_{int}^2), these internal molecular motions will not cause any significant reduction in the slow motion cross-relaxation enhancement of near parallel internuclear vectors. This is demonstrated in Figure 8.4 as the spectral density curves for

the three-motion model. In both the Ala-3 and Leu-14 cases, the $J(0)$ is reduced by a factor of $S_{int}^2 = 0.85$ relative to the two-motion model.

8.5 The spin-diffusion limit

So far, NOE cross-peaks have been treated as being the result of the isolated neighboring spin pairs. In reality, the simultaneous cross-relaxation of a nuclear spin with numerous neighbors can promote magnetization relaying. As a consequence, distant spins can exchange magnetization via one or more intermediate spins. This spin-diffusion effect becomes more important with increasing magnitude of the cross-relaxation rate and with increasing mixing time. It will be important to avoid this effect when choosing mixing times in NOE-type experimentation on membrane polypeptides in a bilayer dispersion.

To predict the onset of third-party relaying, a three-spin system (I_1 , I_2 and I_3) is established in a configuration such that the coupled pairs are $I_1 \leftrightarrow I_2$ and $I_2 \leftrightarrow I_3$, but I_1 and I_3 are too distant to show any significant dipolar coupling. The relaxation matrix, $\vec{\mathbf{R}}$, from Equation 8.5 is written as:

$$\vec{\mathbf{R}} = \begin{pmatrix} \rho_{11} & \sigma_{12} & 0 \\ \sigma_{21} & \rho_{22} & \sigma_{23} \\ 0 & \sigma_{32} & \rho_{33} \end{pmatrix}. \quad (8.20)$$

In this system, the evolution of the NOESY cross-peak at the 2D frequencies coordinates $(\omega_{I_1}, \omega_{I_k})$ corresponding to the signal from spin I_1 , due to spin I_k , (where k is 1, 2, or 3), will be dictated by the equation:

$$\Delta I_{1z}(t)|_{I_{kz}} = [e^{(-\vec{\mathbf{R}}\tau_{mix})}]_{1k} \Delta I_{kz}(0) \quad (8.21)$$

$$= [\vec{\mathbf{1}}_{1k} - \vec{\mathbf{R}}_{1k}\tau_{mix} + \frac{1}{2}\vec{\mathbf{R}}_{1k}^2\tau_m^2 + \cdots] \Delta I_{kz}(0), \quad (8.22)$$

where τ_{mix} is the mixing time. Since NOE volumes are typically measured in the initial part of the buildup, one can ignore the higher order terms beyond third-order in Equation 8.22. The importance of magnetization relaying can be addressed by comparing the evolution of NOE cross-peaks between the directly coupled pair versus

the cross-peaks between the indirectly coupled pair. As a function of mixing time, the evolution of the NOESY cross-peaks for I_1 with I_2 and with I_3 are described by [44, p. 387]:

$$\begin{aligned} \Delta I_{1z}(\tau_{mix})|_{I_{2z}} &= (-\sigma_{12}\tau_{mix} + \frac{1}{2}(\rho_{11} + \rho_{22})\sigma_{12}\tau_{mix}^2 \\ &\quad - \frac{1}{6}[(\rho_{11}^2 + \sigma_{12}^2)\sigma_{12} + (\rho_{11} + \rho_{22})\rho_{22}\sigma_{12} + \sigma_{12}\sigma_{23}^2]\tau_{mix}^3)\Delta I_{2z}(0), \end{aligned} \quad (8.23)$$

$$\Delta I_{1z}(\tau_{mix})|_{I_{3z}} = (\frac{1}{2}\sigma_{12}\sigma_{23}\tau_{mix}^2 - \frac{1}{6}(\rho_{11} + \rho_{22} + \rho_{33})\sigma_{12}\sigma_{23}\tau_{mix})\Delta I_{3z}(0). \quad (8.24)$$

In Figure 8.5, the evolution of the ratio between Equations 8.24 and 8.23 is plotted for three close-range NOE contacts (with a typical separation of the $H_N^i-H_\alpha^i$ of 2.88 Å) but with three different orientation β_{PM} , corresponding to those already mentioned above for the examples of Ala-3 ($S_{AD}^2 = 0.69$) and Leu-14 ($S_{AD}^2 = 0.009$) of gA (PDB:1mag) as well as a third orientation with the intermediate value $S_{AD}^2 = 0.39$. The cross-relaxation rates σ_{12} and σ_{23} are calculated with the spectral densities predicted (from Equation 8.19) with three types of motions: internal geometrical fluctuations ($\tau_c^{int} = 0.75 \times 10^{-9}$ s, $S_{int}^2 = 0.85$), axial diffusion ($\tau_c^{AD} = 1 \times 10^{-7}$ s, $S_{AD}^2(\beta_{PM})$) and diffusion-in-a-cone ($\tau_c^{DC} = 1.5 \times 10^{-5}$ s, $S_{DC}^2 = 0.90$). The cross-relaxation rates were -211 s $^{-1}$, -52 s $^{-1}$ and -13 s $^{-1}$, for the S_{AD}^2 values of 0.69, 0.39 and 0.009. According to this three-spin model, the maximum ratio of intensities between the indirect $I_1 \rightarrow I_3$ and direct $I_1 \rightarrow I_2$ cross-peaks is $1/\sqrt{2}$.

Figure 8.5 shows that the importance of spin-diffusion strongly depends on the orientation of interacting spins and that the maximum is reached faster for fast cross-relaxation. Fortunately, the large- S_{AD}^2 spin-pairs (such as for Ala-3) are scarce ($<10\%$) and the probability of having a nucleus with two partners with large S_{AD}^2 is even smaller ($<1\%$). The intermediate curve (for $S_{AD}^2 = 0.39$) represents the most probable situation in our model systems. According to this curve, mixing times should be kept under 25 ms to maintain the spin-diffusion contribution below 50% of the direct cross-relaxation contribution. This range is smaller than that recommended for solutions work, where mixing times between 75 ms and 250 ms are typically used. Fortunately, the cross-relaxation rates are on the order of 10-100 times those seen in solution for protein of similar size, so that sufficient signal should be detectable with

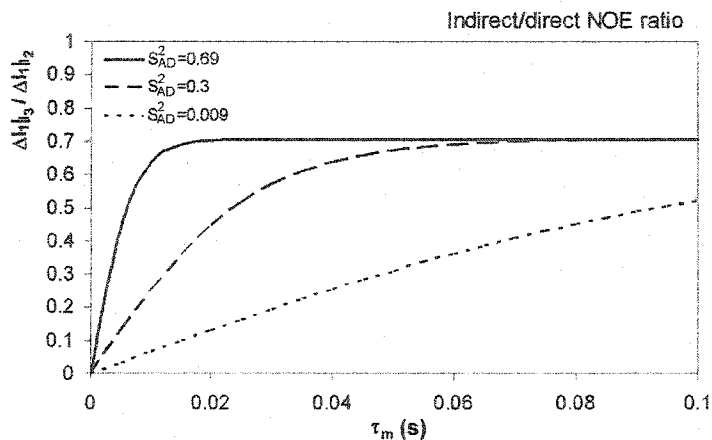


Figure 8.5: Evolution of the ratio between indirect and direct NOE cross-peak intensity as a function of mixing time for three prototypical three-spin configurations. Spins I_1 , I_2 and I_3 are colinear and separated by 2.88 Å in all cases. The internuclear vector directions relative to the axis of diffusion are 19.6°, 39.7° and 51.0° for S_{AD}^2 values of 0.69, 0.15 and 0.009. The cross-relaxation rates were evaluated as described in the text.

mixing time of 25 ms.

8.6 1D-NOE measurements

To support the theory of direct NOE in fluid liquid crystals and their structural relevance for membrane polypeptides, it is important to show evidence of the feasibility of the experiment and the observation of the cross-relaxation exchange. The most straightforward way to measure NOE interactions between hydrogen spins is to perform the 1D-NOE experiment described in Section 3.4.3.4 (p. 57). This experiment is performed simply as a series of 1D spectra whereby a selective irradiation of variable length set at the resonance of the spin of interest is applied prior to the observation of all spin resonances; any interacting spins will show a reduced peak intensity compared to the spectrum obtained after a simple 90° pulse.

The 1D spectrum of gA in CsL-d₂₅ at 16 kHz is shown in Figure 8.6. Five regions of interest are well defined, namely those attributed to (from left to right) the formyl group, the Trp aromatic groups, the backbone α -groups, the β -groups primarily from

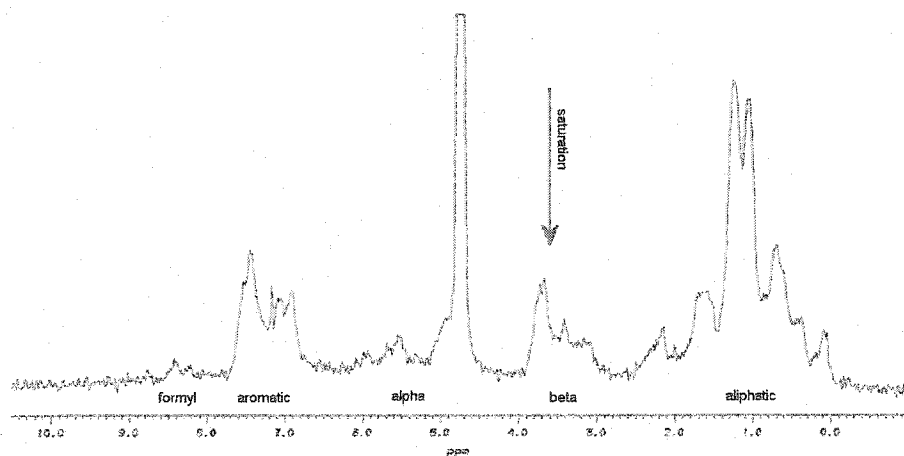


Figure 8.6: 1D NMR spectrum of multilamellar gA/CsL-d₂₅ with MAS ($\nu_R = 16$ kHz). The labels are the assignments to the ^1H resonances. The arrow shows at what frequency the selective irradiation pulse was applied.

the Trp residues, and all the other aliphatic groups either from the hydrophobic residue side chains or from the lipid aliphatic chains (residual protonation). The amide and indole hydrogen resonances are not visible on this spectrum because of deuteration, and because of the relaxation effect discussed in Chapter 9. The arrow points to the area where the selective saturation was applied for the 1D-NOE measurements.

Figure 8.7 shows the evolution of the peak intensities (measured as the area under the peak) of four regions as a function of saturation duration (or NOE mixing time). These were recorded as the difference between the spectra recorded with the saturation set on resonance with the Trp- $^1\text{H}_\beta$ peaks (3.6 ppm), and far off resonance. The buildup rates take on different values depending on which peak is examined, and were fitted to a double exponential function described in Equation 8.8. The peaks belonging to the Trp H_{aro} spins displayed the most rapid buildup rate, with a cross-relaxation rate of -5.6 s^{-1} . The intermediate buildup rate was observed for the Leu methyl groups, with resonances between 0 and 1 ppm. The curve was fitted to a cross-relaxation rate of -1.7 s^{-1} . Finally the slowest exchange occurred with the residual undeuterated lipid methylene peaks (1.4 ppm), with an exchange rate of -0.33 s^{-1} . The figure also displays the constant intensity of the selectively irradiated

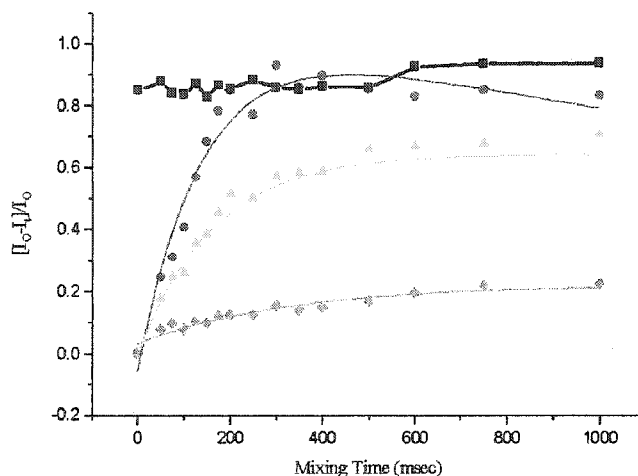


Figure 8.7: The selective saturation pulse was applied on the resonance frequency of Trp H_β (residue 9-11-13-15 at 3.6 ppm). The cross-relaxation rates were categorized as “strong” [red circles] (Trp- $H_{aromatic}$, $\sigma = -11 \text{ s}^{-1}$), “medium” [yellow triangles] (Leu- H_{methyl} , $\sigma = -3.3 \text{ s}^{-1}$) and “weak” [green diamonds] (lipid $H_{methylene}$, $\sigma = -0.66 \text{ s}^{-1}$). Black squares show the normalised intensity of the saturated peak.

peak.

The results of this simple experiment demonstrate some important characteristics of NOE measurements in membrane polypeptides. First, cross-relaxation rates are negative, and are in a regime where an experimentalist can differentiate between rapidly and slowly exchanging species. Despite the lack of resolution in a 1D spectrum, which restricts the identification of exchange rates between two isolated and assigned hydrogen peaks, it is possible to speculate that the exchange rates are mainly related to the inter-hydrogen distance. Indeed, the Trp- H_β and the Trp- H_{aro} are part of the same sidechains and are therefore expected to exchange efficiently. The four Trp residues are also intercalated with three Leu groups between residues 9 and 15. It is therefore not surprising to observe smaller NOE interactions between Trp- H_β and methyl hydrogen groups located at the end of the Leu residues. Finally, much slower exchange exists between the Trp side chains which extend out into the hydrophobic interface of the bilayers. These are intermolecular NOE transfers such as

those reported between lipids. They are expected to be slower because of the scarcity of these hydrogens (the lipids are deuterated to 98%) and because of the finite lateral diffusion rate at which a lipid moves to and from a site adjacent to the polypeptide. It is important to mention as well that NOE transfer to all types of hydrogens may also denote the proximity to the onset of the spin-diffusion limit. According to these curves, it will be important to keep the mixing times short (≤ 100 ms) to ensure that exchange occurs in the linear part of the build-up.

8.7 The 2D-NOESY and 2D-NOE-CROPSY experiments

The experiments described above demonstrate the behaviour of NOEs in membrane polypeptides, but offer poorly specific structural information because of the low resolution potential of a 1D experiment. To measure specific NOE contacts, it will be necessary to advance to multidimensional NOESY experimental techniques where the improved resolution potential can be used to identify individual hydrogen resonances. However, it must be remembered that the samples typically offer very little signal and thus a 2D experiment must be conducted over a period of several days, during which the stability of the protein and lipids as well as the stability of the fast MAS rate must be assured. In this section, preliminary attempts to measure ^1H - ^1H NOE contacts with multidimensional experiments are presented and discussed.

8.7.1 2D-NOESY correlations

An initial attempt of a 2D-NOESY experiment was performed on an unlabelled gA sample mixed with chain-deuterated DMPC- d_{54} (*ca.* 95% deuteration). The spectrum displayed three groups of cross-peaks. The first type were the most intense, and involved hydrogen pairs from the headgroup, backbone and hydrocarbon chains of the DMPC- d_{54} lipid molecules. Although the chains are only partly protonated, their cross-peak intensities benefit from the good resolution arising from the rapid internal motions of lipids. These lipid peaks show a full cross-relaxing pattern as described by Huster *et al.* [162, 163] and dominate the polypeptide ^1H peaks. A second family

of peaks of lesser intensity involved ^1H spins from the same lipids and those from the gA polypeptide, mainly from the sidechain groups (aromatic or aliphatic regions). Again, because of the highly dynamic nature of the membrane bilayer, these cross-peaks represent intermolecular contacts.

It is only the third type of cross-peaks that may contain relevant polypeptide structural information. These cross-peaks occur between pairs of hydrogen spins from within the polypeptide chain. A strip from the 2D-NOESY spectrum centered around the Trp aromatic ^1H frequency region in ω_2 is shown in Figure 8.8. The peptide-lipid peaks have been digitally filtered out to simplify the spectrum. This region displays cross-relaxation pathways to the Trp sidechains. The most intense cross-peaks are found at the ω_1 frequencies of the aromatic and aliphatic ^1H resonances. Smaller cross-peaks are also observed at the frequency of the Trp $^1\text{H}_\beta$ (3-3.5 ppm). These cross-peaks are all relevant as intra- and inter-residue connectivities in the C-terminal half of the gA channel dimer structure. These results agree with those seen in the 1D-NOE experiment described above, in which the intra-residue Trp NOE interactions were the most important. It should be reminded that in the 1D transient experiment, the evolution of the *normalized peak area* is fitted to an exponential growth curve. However, in the NOESY experiment, a snapshot of the cross-relaxation is taken at the end of a single mixing time. A 2D contour map highlights the *absolute maximum peak intensity*, which, in this case, depends not only on the cross-relaxation rate but also on the peak resolution, number of overlapping ^1H resonances and ^1H multiplicity.

Without adequate resolution and assignments, it is clear that this NOESY experiment provides very incomplete structural information. However, it is still informative in terms of recommendations for more advanced experimentation. The cross-relaxation rates in membrane dispersed polypeptides are large and can vary for ^1H within the same peptide. Thus, it is important here to repeat this experiment with a series of mixing times, unlike experiments on soluble proteins where all cross-peak intensities are directly proportional to the cross-relaxation rate over the same range of mixing times. An accurately fitted evolution may also reveal the existence of more than one exchange rate for a given cross-peak, due to poorly-resolved overlapping

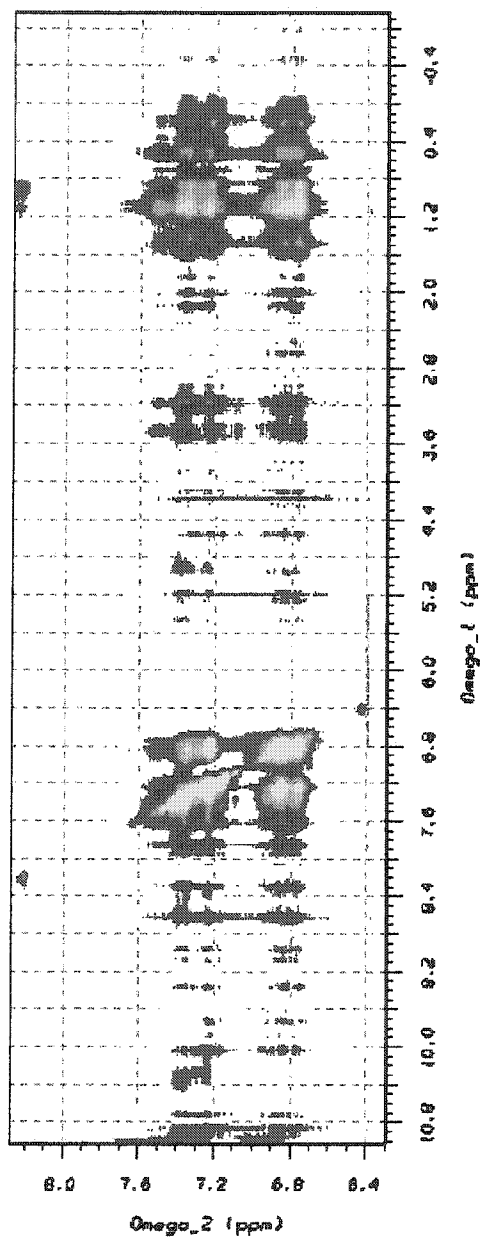


Figure 8.8: 2D-NOESY strip plot of gA/DMPC- d_{52} centered around the Trp aromatic region.

peaks. Also, as revealed from this experiment and from the predicted cross-relaxation rates, mixing times should be chosen on the order of tens of ms rather than hundreds of ms, which is the range commonly used for soluble proteins. Before it will be possible to perform such a series of experiments, the sample signal-to-noise ratio needs to be improved. This can be achieved with larger samples, higher peptide/lipid ratio and higher magnetic field. The perdeuteration of the lipids to a higher percentage, will simplify the spectra and allow to use a more favorable receiver dynamic range. Finally, resolution, especially for the backbone ^1H , is still the most important limiting factor. In the next subsection, a novel experiment is proposed which reduces the likelihood of cross-peak overlap by editing the NOESY connectivities through the ^{15}N spin.

8.7.1.1 The 2D-NOE-CROPSY correlations

Certainly, the best way to further improve the resolution of a NOESY experiment without modifying the sample composition or conditions would be to further increase the dimensionality of the experiment. A straightforward way to do this is to use the frequency of the ^{15}N nucleus as an extra dimension. There are many advantages associated with this nucleus. First, ^{15}N occurs at every position along the polypeptide backbone but not in most of the sidechains, making it an ideal “filtering” nucleus to lighten the cross-peak population, limiting the spectrum to NOE contacts near the backbone. It was demonstrated in Section 4.6 (p. 79) that a crude peptide structure can be retrieved with a reduced population of NOE contacts involving at least one H_N . In addition, ^{15}N is less abundant than ^1H and has a smaller magnetic moment. Thus both heteronuclear and homonuclear dipolar broadening is small and so ^{15}N offers more favorable resolution than ^1H . This was seen in the 2D-CROPSY experiment on gA (Section 7.4, p. 165). The CROPSY experiment already allowed the proposal of a complete tentative ^{15}N assignment for gA. These will be useful to identify at least one member of the NOE interacting ^1H partners. Finally, it will be demonstrated in Section 9.3 (p. 202) that ^{15}N -labelling is absolutely required in membrane polypeptides if one wishes to abolish the strong relaxation pathway through the quadrupolar

^{14}N spin and observe the $^1\text{H}_\text{N}$ resonances.

Unfortunately, the sample size and spectrometer sensitivity do not permit the realization of an experiment that combines 2D-NOESY presented above and 2D-CROPSY into 3D-NOE-CROPSY. It is estimated that the minimal requirement of $64\ t_1\text{-increments} \times 64\ t_2\text{-increments} \times 256\ \text{scans} \times 2\ \text{s}$ repetition time would result in a 290-hour or 12-day experiment. Despite, the robust nature of gA, the integrity of the sample at 55 °C, and the stability of the MAS spinning, will be difficult to guarantee over such an extended period of time. This experiment will have to await conditions permitting at least twice the signal-to-noise ratio, which will reduce the experimental time by a factor of four.

Instead, the 2D version of the NOE-CROPSY experiment was attempted on the ^{15}N -gA sample with fully deuterated DMPC at 55 °C undergoing MAS at a rate of 14 kHz.

The processed result of this experiment is shown on Figure 8.9(A). On this spectrum, the cross-peaks represent the NOE contact from any $^1\text{H}_x$ to any $^1\text{H}_\text{N}$. They occur on the spectrum at the chemical shift frequency of the $^1\text{H}_x$ in ω_1 and at the chemical shift frequency of the ^{15}N covalently-bonded to $^1\text{H}_\text{N}$ in ω_2 . It is observed that there are cross-peaks at every ^{15}N chemical shift assigned in Table 7.3 (p. 168). The cross-peaks appear in all major ^1H chemical shift regions, namely in the indole (10.5-11 ppm), amide (8.25-10 ppm), aromatic (7.25-8.25 ppm), α - (4.75-6.25 ppm), β - (3.25-4.25 ppm) and aliphatic (0-2.75 ppm) regions. Even with a short mixing time of 25 ms, there are large clusters of cross-peaks for these regions. Even so, the spectrum does not indicate an overall onset of spin-diffusion since clearly there are regions with no intensity where one might have expected signal if spin diffusion was important. The large clustered regions are highly overlapped due to the width of the cross-peaks, which seriously limit their assignment. These ambiguities could potentially be resolved in the 3D version of this experiment.

Nevertheless, a survey of all cross-peak maxima and their tentative assignment was carried out, as before (Section 7.4, p. 165), by matching simultaneously the ^{15}N and ^1H chemical shifts of the cross-peak maxima with those from a simulated spec-

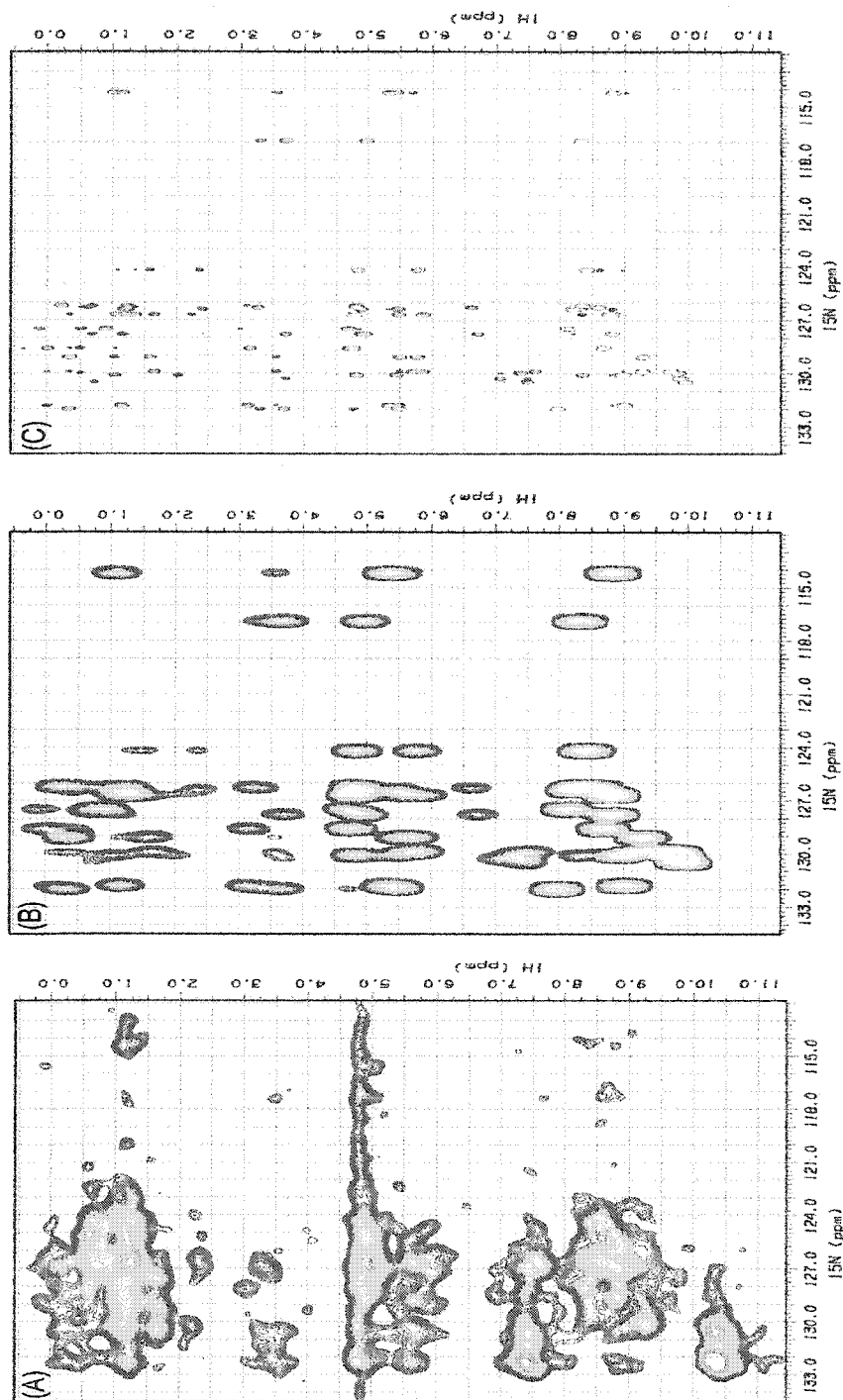


Figure 8.9: 2D-NOE-CROPSY of ^{15}NgA . (A) Experimental results obtained on ^{15}NgA in DMPC- d_{67} (1/20 mol/mol) and 43% (v/w) of P_i buffer (pH 6.5) with MAS ($\nu_R = 14 \text{ kHz}$) at 55°C . (B,C) Simulated spectra for the model gA structure PDB:1mag with (B) and without (C) heavy broadening.

trum based on the published ^1H chemical shifts [53], and the ^{15}N chemical shifts of Table 7.3. The predicted existence of a cross-peak was based on the structure coordinate file, PDB:1mag [24]. The simulated spectra, shown in Figure 8.9(B) and (C), include only the $^1\text{H}_x\text{-}^1\text{H}_N$ or $^1\text{H}_x\text{-}^1\text{H}_{N\epsilon 1}$ contacts of 6 Å or less and assumes no indirect coupling (magnetization relaying). The intensities are a function of the proximity (r^{-6}), ^1H multiplicity (e.g. methyl groups) and orientation (β_{PM}) of the internuclear vector relative to the the moment of inertia axis of the folded gA (1mag). The simulation used three simultaneous motional models according to Equation 8.19, namely the internal rapid fluctuations ($S_{int}^2 = 0.85$, $\tau_c^{int} = 0.75 \times 10^{-9}$ s), axial diffusion ($S_{AD}^2(\beta_{PM})$, $\tau_c^{AD} = 1 \times 10^{-7}$ s) and off-axis reorientation ($S_{DC}^2 = 0.9$, $\tau_c^{DC} = 1.5 \times 10^{-5}$ s). Whereas the spectrum in (C) displays finite high-resolution, the one in (B) was processed with a squared sine window function over the first 36 ms and 9 ms of the FID in t_2 and t_1 before the Fourier transform to create the illusion of the broader spectrum similar to that observed in the experimental NOE-CROPSY. It should be noted that the simulation does not include the effect of the HN vector orientation on the efficiency of CP.

Table 8.1 lists the frequency coordinates in ω_2 and ω_1 of all the peak maxima (above a threshold corresponding to 5% of the highest peak) with an ω_2 ^{15}N CS near those assigned in Table 7.3 (p. 168). The table is divided into 7 groups of cross-peaks according to 7 resolved regions of ^{15}N chemical shifts. Within each group, each cross-peak is assigned a ^1H -partner based on the simulated spectrum of the known gA structure (PDB:1mag). The assignment follows the rules that (1) the ω_2 chemical shift provided the assignment of $^1\text{H}_N$ (with some ambiguity) based on Table 7.3, (2) the ω_1 chemical shift is within 0.5 ppm of the ^1H chemical shift assignment of Arseniev *et al.* [53], (3) the simulation predicts from the PDB:1mag internuclear distances that a cross-peak should be present. Evidently, these rules allow for many ambiguous assignments as shown in Table 7.3. Only 6 of the 77 cross-peak maxima were not matched with a theoretical assignment. The presence of these cross-peaks can be interpreted as resulting from small structural differences with the theoretical PDB:1mag structure, from inconsistencies with the motional models, or with the

choice of order parameters and correlation times, or from magnetization relaying (or spin-diffusion) having been neglected in the simulation.

8.8 Concluding remarks

In this chapter, the mechanism of ^1H - ^1H cross-relaxation through the dipole-dipole coupling was derived for several motional model scenarios of small membrane polypeptides. The possibility of using ^1H - ^1H NOE measurements as a structural tool for membrane polypeptide structural elucidation was evaluated.

The theory reveals that cross-relaxation rates in membranes have an important orientation dependence, in addition to the usual internuclear distance (r^{-6}) dependence. This orientation effect stems from the nature of the anisotropic motion, such as the fast axial diffusion and slower off-axis reorientation. This complicates the interpretation of NOE measurements, which nonetheless could still be used as internuclear distance restraints, albeit with much looser restraining limits. On the other hand, they could serve as a source of orientation constraints if the internuclear distance can be interpreted by other means.

Another concern is that of the magnetization relaying mechanism leading to spin-diffusion. The cross-relaxation rates in small membrane polypeptides can be quite large based on the motional models. It was estimated that the mixing times must be kept shorter than 25 ms to avoid spin-diffusion. In the 2D-NOE-CROPSY experiment, it is not clear how important the magnetization relaying really is. However, because most peaks observed can be accounted for based on a simple direct cross-relaxation for the model structure used, it seems that spin-diffusion does not play a major role. It will be important to carry out this experiment over a series of mixing times to observe the evolution profile of the cross-peaks and to assess the importance of this indirect mechanism.

The most important limitation is that associated with resolution. The resolution improvement by MAS is substantial, yet slower motions in the membrane make it difficult to resolve NOE cross-peaks even in a typical 2D-NOESY of a small membrane polypeptide. The proposed ^{15}N -edited 3D-NOE-CROPSY experiment, which pro-

Table 8.1: The tentative assignment for the 2D-NOE-CROPSY experiment ($\tau_{mix} = 25$ ms) based on the tentative ^{15}N CROPSY assignments (p. 168) in ω_2 and on the Arseniev assignments [53] of ^1H in ω_1 . This table also lists the $^1\text{H}_N \leftrightarrow ^1\text{H}_x$ distance and orientation relative to the moment of inertia principal axis in the PDB:1mag structure. The scaling factor represents the ratio between the cross-peak volume of a molecule undergoing axial diffusion ($S_{AD}^2(\beta_{PM})$, $\tau_c^{AD} = 1 \times 10^{-7}$ s), small amplitude off-axis reorientation ($S_{DC}^2 = 0.9$, $\tau_c^{DC} = 1.5 \times 10^{-5}$ s) and rapid internal motions ($S_{int}^2 = 0.85$, $\tau_c^{int} = 0.75 \times 10^{-9}$ s) versus that of an isotropically reorienting molecule.

^{15}N CS	^1H CS	residue 1	residue 2	^{15}N CS	^1H CS	scaling	$\text{H}_N\text{-H}$ dist.	$\text{H}_N\text{-H}$ β_{PM}
114.2	1.13	2 N	1 $\text{H}_{\gamma 1}$	114.2	1.01	4.47	3.79	77.9
114.2	1.30	2 N	8 $\text{H}_{\gamma 2}$	114.2	1.15	3.24	4.24	139.2
114.2	4.82	2 N	8 H_{α}	114.2	5.33	92.28	2.47	167.2
114.2	8.35	2 N	2 H_N	114.2	8.83	1.00	0.00	—
		2 N	7 H_N	114.2	8.83	4.60	4.31	101.6
116.9	1.17	16 N	16 H_{γ}	116.9	0	2.31	4.58	67.7
116.9	3.47	16 N	15 $\text{H}_{\beta 1}$	116.9	3.71	1.70	4.27	46.5
		16 N	16 $\text{H}_{\alpha 1}$	116.9	3.32	5.52	2.94	83.6
116.9	4.82	16 N	15 H_{α}	116.9	4.97	3.77	2.14	74.6
116.9	4.95	16 N	15 H_{α}	116.9	4.97	3.77	2.14	74.6
116.9	8.35	16 N	16 H_N	116.9	8.33	1.00	0.00	—
124.2	0.66	6 N	12 $\text{H}_{\delta 1}$	124.2	0.63	1.26	5.06	119.7
124.2	1.21	6 N	6 $\text{H}_{\gamma 2}$	124.2	1.35	2.74	4.89	69.9
124.2	2.22	6 N	6 H_{β}	124.2	2.35	5.90	3.10	87.1
124.2	4.86	6 N	12 H_{α}	124.2	4.85	23.72	2.51	157.3
		6 N	6 H_{α}	124.2	4.83	3.49	2.93	40.1
124.2	5.29	6 N	7 H_{α}	124.2	5.48	3.86	4.22	104.9
124.2	8.41	6 N	6 H_N	124.2	8.42	1.00	0.00	—
124.2	8.59	6 N	13 H_N	124.2	8.61	6.23	3.33	145.1
127.0	0.13	13 N	12 $\text{H}_{\beta 2}$	126.3	-0.12	5.44	4.69	97.0
126.8	0.75	13 N	12 $\text{H}_{\delta 1}$	126.3	0.63	5.95	4.41	88.0
126.8	1.24	14 N	7 $\text{H}_{\gamma 1}$	126.2	1.23	9.31	5.10	31.2
		8 N	7 $\text{H}_{\gamma 1}$	126.4	1.23	6.00	3.65	89.3
127.7	1.63	4 N	3 H_{β}	126.7	1.65	1.36	3.41	61.2
126.6	2.30	13 N	6 H_{β}	126.3	2.35	4.84	3.63	37.2
		7 N	6 H_{β}	126.7	2.35	2.39	4.43	111.9
		7 N	7 H_{β}	126.7	2.22	2.78	2.97	110.0
		8 N	8 H_{β}	126.4	2.41	5.44	2.92	97.0
127.0	3.35	13 N	13 $\text{H}_{\beta 1}$	126.3	3.28	5.15	2.54	98.7
		8 N	13 $\text{H}_{\beta 1}$	126.4	3.28	3.22	4.54	107.9
126.8	4.93	4 N	10 H_{α}	126.7	4.78	315.38	2.36	172.9
126.7	5.66	7 N	7 H_{α}	126.7	5.48	152.22	2.94	169.9
		4 N	4 H_{α}	126.7	5.51	3.59	3.07	39.9
126.3	5.93	4 N	5 H_{α}	126.7	5.78	5.10	4.75	99.0
127.3	5.97	4 N	3 H_{α}	126.7	5.86	4.30	2.25	77.0
127.2	6.89	13 N	13 $\text{H}_{\zeta 3}$	126.3	6.92	1.75	4.52	64.3
		13 N	13 $\text{H}_{\epsilon 3}$	126.3	6.62	2.69	2.43	69.6
127.0	7.41	14 N	13 $\text{H}_{\delta 1}$	126.2	7.40	5.15	4.13	98.7
126.5	7.59	12 N	11 $\text{H}_{\delta 1}$	127.5	7.62	4.00	3.98	104.3
126.9	7.67	12 N	11 $\text{H}_{\delta 1}$	127.5	7.62	4.00	3.98	104.3
		4 N	10 H_N	126.7	7.97	29.50	4.92	159.1
126.7	8.62	13 N	13 H_N	126.3	8.61	1.00	0.00	—
127.0	8.84	14 N	13 H_N	126.2	8.61	2.83	4.52	41.9
		7 N	7 H_N	126.7	8.83	1.00	0.00	—
		4 N	4 H_N	126.7	8.78	1.00	0.00	—
		8 N	15 H_N	126.4	8.83	4.72	3.68	142.6
		8 N	2 H_N	126.4	8.83	27.95	4.72	21.3
127.1	10.36	—	—	—	—	—	—	—

continued on next page

^{15}N CS	^1H CS	residue 1		residue 2		^{15}N CS	^1H CS	scaling	H_N -H dist.	H_N -H β_{PM}
129.0	-0.08	11	N	10	H $_{\beta 1}$	128.6	-0.38	6.00	4.21	89.4
128.4	0.27	15	N	14	H $_{\beta 1}$	127.8	0.22	1.44	4.56	118.1
		11	N $_{\epsilon 1}$	10	H $_{\delta 1}$	129.9	0.33	3.26	4.47	72.3
129.2	0.56	11	N	10	H $_{\beta 2}$	128.6	0.49		3.12	98.3
128.2	0.60	15	N	14	H $_{\delta 1}$	127.8	0.66	5.93	4.84	92.4
128.5	1.17	15	N	8	H $_{\gamma 1}$	127.8	1.15	6.63	5.87	34.4
		15	N	8	H $_{\gamma 2}$	127.8	1.15	6.35	4.72	34.7
129.1	1.63	11	N	4	H $_{\gamma}$	128.6	1.70	4.52	3.72	37.8
128.3	4.88	15	N	14	H $_{\alpha}$	127.8	4.90	5.06	2.25	80.8
		11	N	10	H $_{\alpha}$	128.6	4.78	5.80	2.16	85.9
128.8	5.66	15	N	9	H $_{\alpha}$	127.8	5.48	1.04	3.41	56.9
		11	N	5	H $_{\alpha}$	128.6	5.78	1.16	3.40	59.0
128.5	6.91	11	N	11	H $_{C3}$	128.6	6.92	4.44	4.79	77.7
128.3	7.42	11	N $_{\epsilon 1}$	11	H $_{C2}$	129.9	7.35	1.06	2.76	57.3
128.7	7.78	15	N	10	H $_N$	127.8	7.97	3.31	4.53	72.5
128.1	8.37	15	N	14	H $_N$	127.8	8.35	2.84	4.32	109.6
		11	N	6	H $_N$	128.6	8.42	3.93	4.71	75.4
128.7	8.84	15	N	15	H $_N$	127.8	8.83	1.00	0.00	-
		11	N	4	H $_N$	128.6	8.78	3.31	3.29	40.6
128.9	9.23	-	-	-	-	-	-	-	-	-
128.9	9.60	-	-	-	-	-	-	-	-	-
128.1	10.30	11	N $_{\epsilon 1}$	11	H $_{\epsilon 1}$	129.9	9.73	1.00	0.00	-
130.3	0.21	3	N	19	H $_{\beta}$	129.9	0.00	2.32	4.40	43.7
		1	N	21	H $_{\beta}$	130.1	0.00	1.12	5.14	58.4
130.5	0.44	5	N	4	H $_{\delta 2}$	129.1	0.34	5.75	3.10	85.4
		5	N	4	H $_{\delta 1}$	129.1	0.34	2.87	5.55	109.5
130.2	1.13	5	N	6	H $_{\gamma 1}$	129.1	1.07	4.87	5.39	100.2
		5	N	4	H $_{\beta 1}$	129.1	1.05	2.17	4.43	113.1
		1	N	22	H $_{\gamma 1}$	130.1	1.07	1.00	3.54	55.4
130.5	1.67	3	N	3	H $_{\beta}$	129.9	1.65	1.20	3.02	120.5
		5	N	5	H $_{\beta}$	129.1	1.58	1.17	3.02	120.9
130.3	2.20	1	N	22	H $_{\beta}$	130.1	2.35	9.95	5.11	30.6
		1	N	1	H $_{\beta}$	130.1	2.02	4.14	2.91	103.7
		5	N	17	H $_{\beta}$	129.1	2.02	1.22	3.70	59.8
130.5	3.31	5	N	18	H $_{\alpha 1}$	129.1	3.56	40.21	3.96	18.4
		3	N	2	H $_{\alpha 1}$	129.9	3.56	3.58	3.17	106.2
130.5	3.68	5	N	18	H $_{\alpha 1}$	129.1	3.56	40.21	3.96	18.4
		3	N	2	H $_{\alpha 1}$	129.9	3.56	3.58	3.17	106.2
130.3	4.80	1	N	22	H $_{\alpha}$	130.1	4.83	26.12	2.50	21.9
130.3	5.60	5	N	4	H $_{\alpha}$	129.1	5.51	5.41	2.26	82.8
130.6	5.70	3	N	2	H $_{\alpha 2}$	129.9	5.71	5.05	2.19	80.7
		5	N	18	H $_{\alpha 2}$	129.1	5.71	5.03	3.15	36.9
		3	N	19	H $_{\alpha}$	129.9	5.86	23.75	4.82	22.7
130.7	7.45	-	-	-	-	-	-	-	-	-
130.0	8.45	1	N	22	H $_N$	130.1	8.42	107.84	4.66	11.9
130.5	8.90	5	N	6	H $_N$	129.1	8.42	4.16	4.33	141.4
		1	N	2	H $_N$	130.1	8.83	8.03	4.19	147.4
		1	N	1	H $_N$	130.1	8.99	1.00	0.00	-
130.2	9.29	3	N	3	H $_N$	129.9	9.29	1.00	0.00	-
		5	N	5	H $_N$	129.1	9.30	1.00	0.00	-
130.5	10.34	-	-	-	-	-	-	-	-	-

continued on next page

^{15}N CS	^1H CS	residue 1		residue 2		^{15}N CS	^1H CS	scaling	H_N -H dist.	H_N -H β_PM
132.3	0.27	10	N	10	$\text{H}_{\delta 1}$	132.0	0.33	4.73	4.53	100.9
		10	N	10	$\text{H}_{\delta 2}$	132.0	0.33	4.66	3.54	101.3
132.6	0.42	10	N	10	$\text{H}_{\beta 2}$	132.0	0.49	2.12	4.15	66.6
132.1	0.80	15	$\text{N}_{\epsilon 1}$	14	$\text{H}_{\delta 2}$	130.5	0.72	3.04	4.07	71.3
132.5	1.22	9	N	8	$\text{H}_{\gamma 1}$	131.8	1.15	5.95	5.04	88.0
		9	N	8	$\text{H}_{\gamma 2}$	131.8	1.15	4.79	3.45	100.6
		9	$\text{N}_{\epsilon 1}$	8	$\text{H}_{\gamma 2}$	130.3	1.15	2.26	5.48	43.9
132.1	3.45	10	N	16	$\text{H}_{\alpha 1}$	132.0	3.32	19.63	4.75	155.6
		10	N	9	$\text{H}_{\beta 2}$	132.0	3.32	1.68	3.38	63.8
		9	N	9	$\text{H}_{\beta 2}$	131.8	3.32	1.36	3.68	118.7
132.4	3.59	9	N	2	$\text{H}_{\alpha 1}$	131.8	3.56	18.57	4.03	24.9
		10	N	16	$\text{H}_{\beta 2}$	132.0	3.71	57.54	4.60	164.2
		10	N	16	$\text{H}_{\beta 1}$	132.0	3.68	22.81	2.88	156.9
132.3	4.78	9	N	10	H_{α}	131.8	4.78	4.44	4.74	102.3
		10	N	11	H_{α}	132.0	4.69	5.33	4.72	97.6
132.2	5.09	-	-	-	-	-	-	-	-	-
132.4	5.63	9	N	9	H_{α}	131.8	5.48	34.01	2.92	160.3
		10	N	9	H_{α}	132.0	5.48	4.11	2.12	76.2
132.4	7.43	9	$\text{N}_{\epsilon 1}$	9	H_{α}	130.3	5.48	2.09	4.85	66.4
		13	$\text{N}_{\epsilon 1}$	13	$\text{H}_{\delta 1}$	130.0	7.40	5.83	2.48	93.8
		9	$\text{N}_{\epsilon 1}$	15	$\text{H}_{\delta 1}$	130.3	7.49	9.51	4.65	149.0
		9	$\text{N}_{\epsilon 1}$	9	$\text{H}_{\zeta 2}$	130.3	7.49	1.58	2.89	63.1
132.3	7.90	10	N	10	H_N	132.0	7.97	1.00	0.00	-
132.5	8.92	9	N	9	H_N	131.8	9.02	1.00	0.00	-
		10	N	9	H_N	132.0	9.02	3.27	4.30	40.7
		10	N	15	H_N	132.0	8.83	3.31	4.53	107.5
132.2	10.36	13	$\text{N}_{\epsilon 1}$	13	$\text{H}_{\epsilon 1}$	130.0	9.85	1.00	0.00	-
		9	$\text{N}_{\epsilon 1}$	9	$\text{H}_{\epsilon 1}$	130.3	9.87	1.00	0.00	-
		15	$\text{N}_{\epsilon 1}$	15	$\text{H}_{\epsilon 1}$	130.5	9.96	1.00	0.00	-

vides one additional dimension, as well as a reduced cross-peak population, promises to diminish the chances of overlap. The use of NOEs in this type of sample will also greatly benefit from technical improvements leading to an enhanced signal-to-noise ratio.



- *No, no, you're not thinking,
you're just being logical.*

- Niels Bohr

The residual quadrupolar effect of ^{14}N on the resolution of ^1H

9.1 Introduction

The achievement of high-resolution ^1H NMR signals from a small polypeptide embedded in a lipid membrane using MAS was an early objective of the present work. By analogy with liquid samples, once this condition was met, one could naively project the application of the family of standard multidimensional experiments for assignment and structural purposes. A closer investigation of the complex anisotropic dynamic nature of membrane bilayers suggests that the analogy with liquid samples is not straightforward. The effects of slow motions on the linewidths of ^1H signals have already been examined and discussed in Chapter 6. The results of another unique effect in membrane-bound protein systems are presented in this chapter. The discussion is restricted to some likely interpretations without carrying out a full investigation.

Early experimentation on unlabelled gA dispersed in membrane bilayers showed an unexpected result. Whereas MAS improved the resolution of the ^1H covalently bound to any carbon, the amide ^1H nuclei, with frequencies normally shifted in the range from 7.5 to 9 ppm, remained broad and featureless, perhaps due to an abnormally strong relaxation mechanism. This could not be due to residual homogeneous broadening along the backbone since the C_α -bound $^1\text{H}_\alpha$ were detectable. It was also noticed that the Trp indole ring $^1\text{H}_{\text{Ne}}$ resonances (at 10.5 ppm) were also uncharacteristically broad compared to their neighboring carbon-bound aromatic ^1H (from

6.5-7.5 ppm). Despite attempts to improve the resolution of these $^1\text{H}_\text{N}$ by increasing the MAS rate or the sample temperature, these resonances showed no signs of narrowing, and remained hidden.

9.2 Lability of H_N as a possible source of line broadening

Exchange processes, especially when occurring in the intermediate time scale regions (10^{-5} - 10^{-2} s) are known to yield broad NMR lineshapes. It seemed possible that under the current sample conditions, the labile $^1\text{H}_\text{N}$ may exchange with bulk water at a rate on the order of several kHz. An easy approach for studying the role of ^1H exchange with bulk water in the broadening of $^1\text{H}_\text{N}$ in a membrane bilayer is to follow the effect of pH on the lineshape of a single amide group ^1H in the context of lipid bilayers. Sphingomyelin (SM) was chosen as a test molecule. SM is a derivative of ceramide ($\text{CH}_3-(\text{CH}_2)_{11}-\text{CH}=\text{CH}-\text{CH}(\text{OH})-\text{CH}(\text{NH}_3)-\text{CH}_2\text{OH}$) to which a phosphocholine group is covalently linked via a phosphodiester bond to the terminal alcohol group (CH_2OH), and to which an acyl chain is bonded to the sphingoid base ($\text{CH}(\text{NH}_3)$) via an amide bond. These are able to form fluid bilayer phases with DMPC at a relatively high molar ratio at ambient temperature. In a simple SM/DMPC binary mixture, the ^1H signal from the amide group can be easily studied since no other ^1H spin resonates in the amide range. Although SM is structurally very different from proteins, the amide bond of SM is similar to the protein peptide bonds. It is located at the interface between the hydrophobic and hydrophilic regions of the membrane bilayer, where there is limited access to the bulk water for possible exchange. In the N-to-N gA channel conformation, H_2O molecules must also overcome a significant energy barrier in order to access the backbone amide groups from the pore interior. The phospholipid also shows a higher structural order in the backbone compared to the headgroup or acyl chains, as does the protein backbone relative to the side chains.

A series of ^1H spectra were obtained using a simple Hahn-echo sequence from

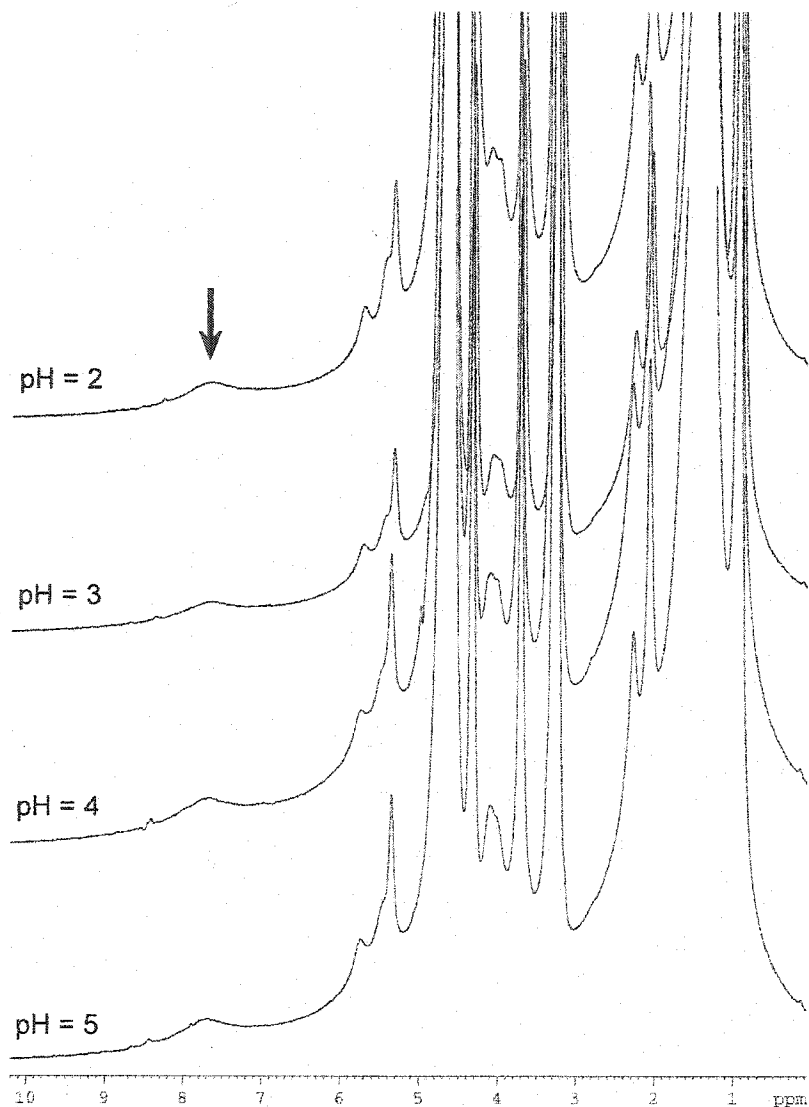


Figure 9.1: ^1H NMR spectrum of SM/DMPC mixtures (molar ratio 1:1) with 43% by weight of P_i buffer (50 mM) with MAS rates of $\nu_R = 7$ kHz and temperature $T = 55^\circ\text{C}$ as a function of pH. The wide peak (0.5 ppm at half-height) at 7.7 ppm is assigned to the SM amide $^1\text{H}_N$ group and does not vary with pH. The width of this peak compared to all other ^1H resonances (<0.2 ppm at half-height) can be explained by the large quadrupolar moment of the covalently-bound ^{14}N (see Section 9.3).

non-deuterated SM(14:0)/DMPC samples (1:1 mol/mol), hydrated with a volume of buffer equivalent to 3/4 of the sample dry weight (43% of total sample weight). The samples were maintained under similar temperature and spinning rate conditions as the membrane polypeptide sample studied by MAS in the previous results chapters. The pH of each sample was carefully controlled with potassium phosphate buffers (50 mM) adjusted to 4 different values, to establish a large range of hydrogen exchange potentials. In principle, if the exchange rate is the dominant broadening mechanism, a varying $^1\text{H}_\text{N}$ linewidth should be observed as a function of pH.

The results of Figure 9.1 show a much different picture. Although the H^+ concentrations of the four samples cover four orders of magnitude, there is no significant change in the width of the unique signal at 7.7 ppm. The resolution remains in all cases around 0.5 ppm (300 Hz) measured at half-height. This is significantly broader than all other peaks, including the ^1H nuclei from the phospholipid headgroup, acyl chains or backbone. These results suggest that ^1H exchange is too slow to have any effect on the ^1H NMR spectrum and is not the principal source of broadening of the $^1\text{H}_\text{N}$ lines.

9.3 The effect of the quadrupole moment of spin S on the dipolar-coupled spin I

Because the contrast between the $^1\text{H}_\text{N}$ and the $^1\text{H}_\text{C}$ lineshapes cannot be explained from the difference in the lability of the chemical bond, an explanation may come from the difference in the physical nature of the covalently-bonded nitrogen and carbon. Whereas the naturally abundant ^{12}C nucleus has no spin, the naturally abundant ^{14}N has a nuclear spin $S = 1$ with a relatively small gyromagnetic ratio of $1.933 \times 10^7 \text{ rad}\cdot\text{s}^{-1}\cdot\text{T}^{-1}$. The magnitude of the quadrupolar interaction for the ^{14}N spin involved in a peptide bond in a static sample is on the order of 3-4 MHz [173]. This is comparable to the magnitude of 43.3 MHz for the Zeeman interaction for this nucleus in a static field of 14.1 T. In this situation, it is not justified to use the *small perturbation approximation*, discussed in Section 2.3.1 (p. 23), to describe the

quadrupolar interaction of ^{14}N . Instead, the axis of quantization of the quadrupolar interaction lies along the direction defined by the vectorial sum of the static field and the principal axis of the electric field gradient fixed within the molecular frame. This effect is manifested by frequency-shifted lineshapes in the powder ^{14}N NMR spectrum.

How can this quadrupolar effect affect the resonance of neighboring ^1H spins? ^{14}N is dipolar-coupled to the directly-bonded $^1\text{H}_N$, with a maximum splitting of about 16 kHz in a static sample. In isotropically reorienting samples or with conventional sample rotation at the magic angle of 54.7° , an inhomogeneous dipolar coupling of this magnitude is easily eliminated. However, in this particular case where the small perturbation approximation does not apply, the quantized states of the ^{14}N - ^1H coupled spin system must also be defined in a new reference frame. Thus, the averaging effect of conventional MAS will not be able to completely eliminate the powder frequency distribution in a ^1H NMR spectrum of a ^{14}N - ^1H coupled spin system.

The effect of a quadrupolar moment of spin $S > 1/2$ on the spectral second moment of a dipolar-coupled spin $I = 1/2$ was first reported by Vanderhart *et al.* [174] for metal-hydrogen pairs in static samples of $\text{HMn}(\text{CO})_5$ and $\text{HCo}(\text{CO})_4$. This effect has since been reported for the NMR spectra of ^{13}C coupled to ^{14}N of organic solids including amino acids and dipeptides [173, 175–177]. In the past, ^1H has not been a commonly observed nucleus in organic molecules by solid-state NMR, mainly because of the severely broadened spectra due to the strong homogeneous ^1H - ^1H coupling; thus, to the best of the author's knowledge, no report of the quadrupolar moment effect on ^1H has been published for the common ^{14}N - ^1H spin system of proteins. To obtain an appreciation of the magnitude of this effect in small membrane proteins dispersed in a fluid membrane, the simulation of the spectrum is presented in the following.

The theory of this interaction in the presence of MAS was first described by Lippmaa *et al.* in cyano groups [178]. The complex theoretical treatment of the ^{14}N - ^{13}C coupled system in the presence of MAS has been presented with a number of different approximations by Hexem *et al.* [173], Naito *et al.* [176], Zumbulyadis *et al.* [175] and more recently Gan and Grant [177]. Since the theoretical treatment can be found

elsewhere, the method proposed by Gan and Grant was followed for the simulations presented here. They used the average Hamiltonian theory (Equation 7.2, p. 159) [154], limited to the zeroth- and first-order terms to describe the frequency spectrum of a spin $I = 1/2$ coupled to a spin $S \geq 1$. The zeroth-order term, $\bar{\mathcal{H}}_0$, contains the secular terms of the chemical shift of I and the dipolar interaction between I and S . Used by itself, this term represents the small perturbation approximation. The $\bar{\mathcal{H}}_1$ term describes the effect of the combined quadrupolar and dipolar interactions to first order. Gan and Grant showed that this first-order approximation is sufficient to simulate the frequency spectrum of I as long as $|\mathcal{H}_Q|/|\mathcal{H}_Z|$ is less than 0.4 for spin S . For the present case of the ^1H - ^{14}N spin system, this ratio is less than 0.1. In addition, this approximation is sufficient for the present case where only the scale of the effect is of interest.

The Wigner rotation matrices used by Gan and Grant are equivalent to the following transformations defined in this thesis in Figure 2.2 (p. 22):

$$P_Q \overrightarrow{(\alpha_{Pp}, \beta_{Pp}, \gamma_{Pp})} P_D \overrightarrow{(\alpha_{pR}, \beta_{pR}, 0)} R \overrightarrow{(\alpha_{RL}(t), \beta_{RL}, 0)} L, \quad (9.1)$$

where P_Q represents the PAS frame for the electric field gradient of spin S . The second frame, p_D , is both the HN dipolar frame and the molecular-fixed frame (or peptide frame). Thus, α_{Pp} , β_{Pp} , and γ_{Pp} are the angles between the two interaction PAS. With these transformations, Gan and Grant arrived at the general expression for the spectral frequency (in rad/s) of spin I as a function of isotropic chemical shift, dipolar coupling and first-order quadrupolar effect [177], simplified here for the MAS of the sample at 54.7° :

$$\omega_m^I = 2\pi \times (S(S+1) - 3m^2) \left[A_{00} + P_4(\cos(54.7^\circ)) \times \sum_{n=-4}^4 \mathcal{D}_{n0}^{(4)}(\alpha_{PR}, \beta_{PR}, 0) A_{4n} \right], \quad (9.2)$$

where S is the quadrupolar spin number with spin states $m = -1, 0$ and 1 . The IS J-coupling is assumed to be small and is neglected in this expression, while the isotropic chemical shift of spin I was set to the center of the spectrum at 0 ppm. The fourth-order Legendre polynomial (P_4) from the $\bar{\mathcal{H}}_1$ term demonstrates why

conventional MAS at 54.7° does not eliminate this effect. The only non-zero A_{ln} terms of Equation 9.2 are:

$$A_{00} = -\frac{2\pi}{5\omega_0^S} \mathcal{F}_{20,D}^p \mathcal{F}_{20,Q}^p \quad (9.3)$$

$$A_{40} = -\frac{24\pi}{35\omega_0^S} \mathcal{F}_{20,D}^p \mathcal{F}_{20,Q}^p \quad (9.4)$$

$$A_{4\pm1} = -\frac{4\pi\sqrt{30}}{35\omega_0^S} \mathcal{F}_{20,D}^p \mathcal{F}_{2\pm1,Q}^p \quad (9.5)$$

$$A_{4\pm2} = -\frac{2\pi\sqrt{15}}{70\omega_0^S} \mathcal{F}_{20,D}^p \mathcal{F}_{2\pm2,Q}^p. \quad (9.6)$$

The variable ω_0^S is the Larmor frequency of spin S (in rad/s), and the factors \mathcal{F}_Q^p and \mathcal{F}_D^p are the spherical tensor components of the spin part of the quadrupolar and dipolar interactions, given by:

$$\mathcal{F}_{20,D}^p = -\sqrt{6}D \quad (9.7)$$

$$\mathcal{F}_{20,Q}^p = \frac{\sqrt{6}\chi}{8S(2S-1)} (3\cos^2\beta_{Pp} - 1 - \eta_Q \sin^2\beta_{Pp} \cos 2\alpha_{Pp}) \quad (9.8)$$

$$\begin{aligned} \mathcal{F}_{2\pm1,Q}^p = & -\frac{\chi}{8S(2S-1)} (\pm 3\sin 2\beta_{Pp} \pm \eta_Q \sin 2\beta_{Pp} \sin 2\alpha_{Pp} \\ & + 2i\eta_Q \sin \beta_{Pp} \sin 2\alpha_{Pp}) \end{aligned} \quad (9.9)$$

$$\begin{aligned} \mathcal{F}_{2\pm2,Q}^p = & -\frac{\chi}{8S(2S-1)} (-3\sin^2\beta_{Pp} + \eta_Q(1 + \cos^2\beta_{Pp}) \cos 2\alpha_{Pp} \\ & \pm 2i\eta_Q \cos \beta_{Pp} \sin 2\alpha_{Pp}). \end{aligned} \quad (9.10)$$

In these expressions, the dipole-dipole and quadrupolar interaction constants, D and χ , given in units of Hz:

$$D = \frac{\mu_0 \gamma_I \gamma_S \hbar}{4\pi r^3}, \quad (9.11)$$

$$\chi = \frac{e^2 Q q}{h}. \quad (9.12)$$

Finally, the quadrupolar asymmetry parameter, η_Q , follows the same convention as for CSA, but with the principal electric field gradient tensor components:

$$\eta_Q = \frac{q_{22} - q_{11}}{q_{33}}. \quad (9.13)$$

9.4 Spectral simulation for the ^{14}N - ^1H coupled pairs in axially diffusing gA

To calculate the spectrum of an unoriented static sample, the summation of an oscillating function with a frequency defined by Equation 9.2 must be carried out over the solid angle ($\int_{\alpha_{pR}=0}^{2\pi} \int_{\beta_{pR}=-\pi}^{\pi} \sin(\beta_{pR}) d\beta_{pR} d\alpha_{pR}$). The static dipolar coupling constant for the ^{14}N - ^1H pair with the standard N-H internuclear distance of 1.02 Å is 16.4 kHz with the alignment along the internuclear vector (using Equation 2.33). The strength of the ^{14}N quadrupolar moment, χ , is -3.2 MHz [173]. The principal components of this interaction are fixed within the peptide plane frame with the components q_{zz} normal to the plane and q_{xx} along the N-H bond [173]. The asymmetry parameter η_Q is 0.31 [173]. Therefore, using the internuclear vector as the z-direction of the dipolar interaction frame, the angles α_{Pp} and β_{Pp} are both 90° and $\gamma_{Pp} = 0^\circ$.

It is also possible to estimate the resulting spectrum of the axially diffusing gA about its long axis. Assuming that the rotational diffusion correlation time is fast compared to the quadrupolar (10^{-7} - 10^{-6} s) and the dipolar (10^{-5} - 10^{-4} s) interactions, a simple projection of both these interactions spatial tensors are applied to the moment of inertia principal axis. With the peptide plane normal being nearly perpendicular and the N-H bond nearly parallel to this axis, the reduced interaction magnitudes are estimated to be $\chi' = 2.1$ MHz and $D' = 13.8$ kHz. As a result of axial diffusion, the residual interactions are both axially symmetric ($\eta'_Q = 0$) and co-linear ($\alpha'_{Pp} = \beta'_{Pp} = 0^\circ$).

The bottom traces in Figure 9.2(A) and (B) show the resulting ^1H MAS (54.7°) NMR spectra for a static and axially diffusing single ^1H - ^{14}N spin system from gA. The spectra are composed of an asymmetrically split doublet, with the right band (corresponding to the $m = 0$ state) being characteristically half the intensity but twice the width of the left band (the coinciding peaks for the $m = -1$ and $m = +1$ states). Since the size of the splitting depends not only on the magnitude of the interactions but also on the relative orientation between them, axial diffusion has the effect of *increasing* the average splitting by a factor of about 1.5 (=

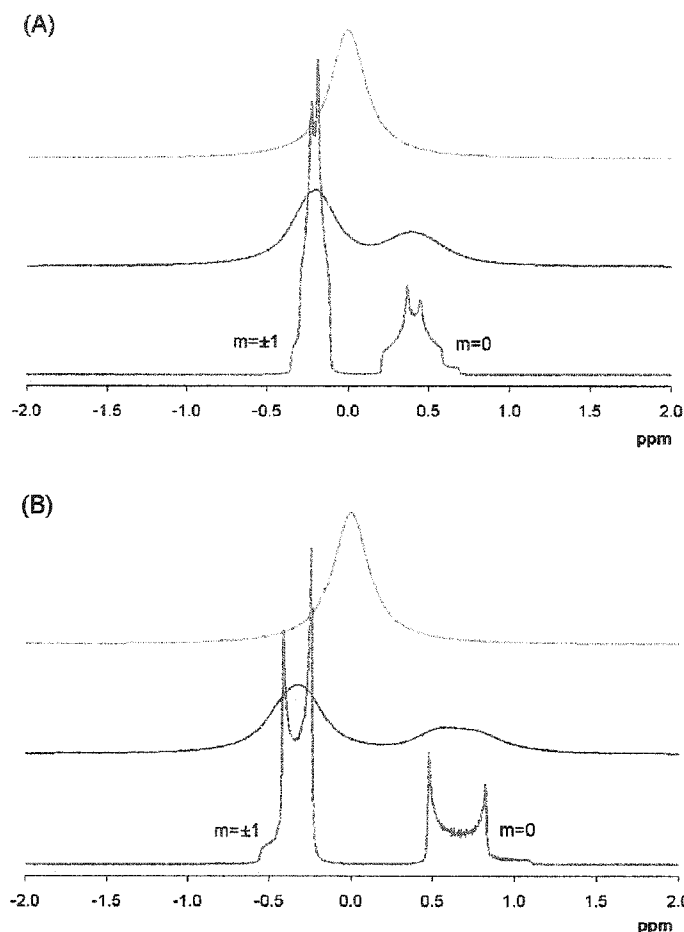


Figure 9.2: Simulated powder ^1H NMR spectra of a peptide ^1H - ^{14}N spin system undergoing MAS. The spin configuration was based on a typical peptide bond in gA (PDB:1mag) when the molecule is (A) static ($D = 16.4$ kHz, $\chi = -3.2$ MHz, $\eta_Q = 0.31$, $\beta_{Pp} = 90^\circ$, $\alpha_{Pp} = 90^\circ$), or (B) undergoing rapid axial diffusion around the moment of inertia principal axis ($D' = 13.8$ kHz, $\chi' = 2.9$ MHz, $\eta'_Q = 0$, $\beta'_{Pp} = 0^\circ$, $\alpha'_{Pp} = 0^\circ$). The spectra were obtained by applying a solid angle summation of an exponentially decaying oscillating function of frequency ω_m^I given in Equation 9.2, followed by a fast Fourier transformation. The bottom spectra used an exponential factor of 20 s^{-1} while the middle spectra used a factor of 500 s^{-1} . To obtain the solid angle distribution, 100 incremental values of β_{pR} between 0 and $\pi/2$, 200 values of α_{pR} between 0 and π were used. The static field, B_0 , was 14.1 T for the relative frequency scale and the evaluation of the Larmor frequency of ^{14}N . For comparison, the top spectra in both (A) and (B) show the broadened resonance line for a ^1H spin without the ^{14}N quadrupolar effect. The simulations were computed using a visual C++ program and a Maple (v.7) worksheet, both available in the appendix of this thesis.

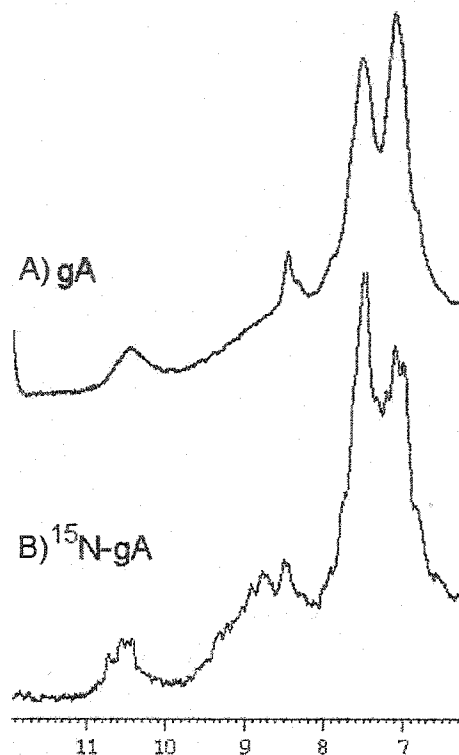


Figure 9.3: Amide region of the ^1H MAS NMR of unlabelled (A) and ^{15}N -labelled (B) gA in DMPC- d_{67} ($\nu_R = 15$ kHz, $T = 55$ °C, $B_0 = 14.1$ T). The amide ^1H resonances are too broad to be resolved and appear to be absent in the region between 8-9.5 ppm in the unlabelled gA spectrum due to the quadrupole moment effect of ^{14}N . The same effect is also responsible for the broadening of the $^1\text{N}_{\text{Ne}}$ peaks around 10.5 ppm.

$(\chi'/\chi)(D'/D)(P_2(\cos \beta'_{Pp})/P_2(\cos \beta_{Pp}))$). To obtain the middle trace in Figure 9.2(A) and (B), these spectra were broadened by multiplying the FID by an exponentially decaying function with a factor of 500 s^{-1} before the Fourier transformation. This allowed comparison of the lineshape resulting from the quadrupolar effect with that of an unperturbed ^1H MAS NMR resonance line with an estimated width of *ca.* 160 Hz, such as the backbone $^1\text{H}_\alpha$ in gA undergoing slow off-axis reorientation (top spectra). The combined broadening effect of slow motions and the ^{14}N quadrupolar effect could explain the featureless wide signal in the 8-9.5 ppm region for the 16 backbone ^1H - ^{14}N groups of gA.

In the experimental ^1H spectrum of unlabelled gA dispersed in a membrane bilayer

shown in Figure 9.3(A), the amide region displays no resolvable signal except for the formyl hydrogen at 8.21 ppm. When the sample is substituted with ^{15}N -gA, where all 20 ^{14}N are replaced with ^{15}N spins ($S = 1/2$), this effect is lost and the spectrum retrieves near-resolvable $^1\text{H}_\text{N}$ resonances (Figure 9.3(B)). The $^1\text{H}_\text{N}$ on the indole rings are visible in both spectra, but the peaks are better resolved in the ^{15}N -gA spectrum. This can be explained by the internal geometrical fluctuations such as the aromatic ring flips of the four Trp residues. The lower order parameter of the side chain signals, which is responsible for the sharper lines, also causes a greater reduction in the quadrupolar moment of ^{14}N ; this reduces the effect of this interaction on the additional broadening of these spins. It should be noted as well that this effect can potentially affect not only directly-bonded ^1H but also all neighboring ^1H spins. Its mean squared strength, however, is inversely proportional to the internuclear distance to the sixth power. The backbone $^1\text{H}_\alpha$ spins, for example, are about 2 Å from the ^{14}N nucleus and should therefore experience a ^{14}N quadrupolar effect 1/64 smaller than $^1\text{H}_\text{N}$.

9.5 Conclusion

It is clear from the simulations that the large electric field gradient of the spin $S = 1$ of ^{14}N , can cause a large perturbation on the ^1H spectrum of membrane polypeptides dispersed in bilayers even under MAS conditions. This effect causes important broadening on the resonances of all neighboring ^1H , particularly to the covalently-bonded $^1\text{H}_\text{N}$, fundamental for structural studies of any protein (high-resolution fingerprint region in NOESY, PISEMA). Because of the importance of the quadrupolar moment, mechanical (MAS)¹ or decoupling strategies cannot eliminate its effect on ^1H . Although this effect becomes less important with increasing magnetic field, it is clear that with current available superconducting magnets, any NMR experiment on this type of sample, requires the complete isotopic labelling of ^{15}N in the vicinity of the

¹ The first-order approximation of the average Hamiltonian theory suggests that with rotation at an angle of 70.1° or 35.6°, the $P_4(\cos \beta_{RL})$ terms vanish. Thus, with double MAS, this effect could in principle be completely eliminated [177]

¹H of interest.



- *No te esfuerces tanto, las mejores cosas suceden cuando menos te las esperas.*

- Gabriel García Márquez

10

Summary and future considerations

This thesis makes a small contribution to the establishment of NMR as a tool for high-resolution structure and dynamics elucidation of membrane proteins. The research project, aimed mainly at making innovative use of ^1H spins as a structural and dynamic probe for small transmembrane polypeptides, entailed a large body of interdisciplinary work. In the initial sample preparation stage, the biosynthesis of an isotopically-labelled atypical polypeptide and the synthesis of perdeuterated phospholipids have been revised and adapted for the needs of this project. The second stage consisted of the application of both well-established and novel heteronuclear multi-dimensional NMR experiments, employing advanced pulse sequences and requiring modern spectrometers implemented with some home-built equipment. Finally, using computer-assisted calculations and simulations, the data were carefully analysed to retrieve some structural information and to characterize the role of the dynamic nature of fluid membranes in the appearance of NMR spectra of ^1H , ^{13}C and ^{15}N specifically in small membrane polypeptides.

10.1 Summary of the results

Of interest to some readers are the reviewed protocols for the biosynthetic preparation of ^{15}N -labelled gA and the chemical synthesis of perdeuterated DMPC- d_{72} presented in Chapter 3 (“Materials and Methods”, p 32). These were inspired from older protocols by Nicholson *et al.* [46, 47] and by Bersch *et al.* [64], and adapted to be

both cost- and time-efficient.

The first half of Chapter 4 (p 65), entitled **“Heteronuclear high-resolution NMR on gramicidin A”** presents some common high-resolution heteronuclear solution NMR work to make the assignments of a majority of the ^{13}C and ^{15}N spins for gA in several different solvents. Although much NMR data have been published on gA in soluble form, the literature lacks information on these isotope labels, essential for structure and dynamics elucidation in the context of a membrane bilayer. In the second half of this chapter, a structure for ^{15}N -gA in SDS-micelles is obtained solely based on $^1\text{H}_\text{N}$ - ^1H NOE connectivities using the reduced cross-peak population of an ^{15}N -filtered HSQC-NOESY experiment. Novel solid-state NMR on the same molecule will initially heavily rely on the type of data presented in this chapter.

The objective of Chapter 5 (p 91), **“The effects of structural variations on NMR spectra of membrane proteins in oriented bilayers”**, is to investigate the effects of the natural variabilities existing in “regular” secondary structural patterns (α -helix, β -strands) and of the membrane polypeptide motional fluctuations on the appearance of SLF NMR spectroscopy on non-rotating oriented samples. Solely based on theoretical prediction of the shift and splitting in HN/N spectra of different model peptides, it is clear that these variations have important consequences. For one, they make the assignment strategies based solely on the regularity of the secondary structure impractical. Peak assignments will have to rely on correlation strategies reminiscent of those used in high-resolution NMR. Secondly, unless motions can be completely eliminated, the interpretation of structural data from the constraints of such experiments will have to include the effect of motions such as internal geometrical fluctuations, whole-body axial diffusion and off-axis reorientation.

Using the favorable resolution attainable for ^1H in small membrane peptides with MAS, the spin-lattice relaxation times in the rotating frame were measured in Chapter 6 (p 110), **“Rotating frame spin-lattice relaxation time of small membrane polypeptides”**, to evaluate the duration of the ^1H signal under applied rf field conditions. The dependence of this effect on temperature, spinning rate and polypeptide size and shape were also investigated. Under typical conditions, the

magnetization decays beyond practical detection within a few tens of Hz. This makes it difficult to perform correlation transfers in multidimensional experiment based on scalar coupling. The investigation was pursued on different nuclei along the peptide backbone, namely ^{13}C and ^{15}N . On one hand, these results revealed that these nuclei offered slightly better signal persistence. They also allowed the suggestion of the plausible nature of the motions leading to the short relaxation time. Particularly the $T_{1\rho}$ of the $^{13}\text{C}'$ nucleus in an α -helical transmembrane segment, when studied as a function of sample orientation in non-rotating oriented samples, can quite readily reveal the correlation times of the axial diffusion and off-axis reorientation through two interactions (CSA and H-C dipolar coupling).

Over nine years ago, Davis *et al.* predicted that the ^1H resonances could be used as a resolvable and assignable signal in small axially-diffusing membrane polypeptides [33]. Chapter 7 (p 157), entitled “ ^1H , ^{15}N -Cross-polarization spectroscopy of gramicidin A”, introduces a novel experiment for which the 2D ^1H - ^{15}N correlation spectrum allows for the resolution of a majority of the 20 $^1\text{H}_\text{N}$ peaks of gA in a membrane bilayer. Since the scalar coupling between the two nuclei is too small, the residual direct dipolar coupling was employed instead as the interaction mechanism to transfer the correlation from the ^1H to the ^{15}N via a CP transfer of 200 μs . The resulting chemical shifts in both dimensions closely match those observed for gA in its N-to-N right-handed single-helix channel form by high-resolution NMR in a micellar dispersion and led to a tentative assignment of the ^1H and ^{15}N .

As a follow-up to Chapter 7, Chapter 8 (p 170), called “The nuclear Overhauser effect as a structural tool in ^1H MAS NMR of small membrane polypeptides”, discusses the use of 1D and 2D cross-relaxation experiments to obtain distance constraints between ^1H spins with resolvable signal, in order to retrieve membrane polypeptide structural information. Some concerns, particularly regarding the efficiency of cross-relaxation due to the dynamic properties of the embedded polypeptides, are discussed. It was shown that the efficiency of the cross-relaxation rates, and by extension the size of the corresponding NOE peaks, are strongly influenced by the orientation of the internuclear vector and by the motional rates and

modes of the polypeptide. Theoretical simulations show that for a majority of peaks, there is good correlation between the cross-relaxation efficiency and the internuclear distance. However, for a small number of close contacts (those nearly parallel to the axis of diffusion corresponding to < 25% of the cross-peaks), the off-axis reorientation causes anomalously fast cross-relaxation. It is also predicted that, with typical correlation times of membrane polypeptides, the cross-relaxation is so efficient that mixing times should be kept well under 100 ms to observe mainly direct transfers over indirect ones. The best experimental results were obtained in a novel 2D combination experiment whereby the CROPSY sequence is preceded by a longitudinal cross-relaxation period to elicit cross-peaks corresponding to only $^1\text{H}_\text{N}$ - ^1H NOEs. In this ^{15}N -filtered experiment, the peak correspondence between the experimental and theoretical 2D-NOE-CROPSY suggested a number of assignments representing 70 potential $^1\text{H}_\text{N}$ - ^1H NOE distance restraints.

One last consequence of the anisotropy and correlation times of motions in the membrane is briefly reviewed in Chapter 9 (p 202), called “**The residual quadrupolar effect of ^{14}N on the resolution of ^1H** ”. The experiments suggest that in unlabelled gA, additional broadening of the amide ^1H is caused by the dipolar coupling to the ^{14}N , characterized by its very large electric quadrupole moment. Simulations using first order approximation of the average Hamiltonian theory show that this residual quadrupolar effect results in fine structure broadening in the ^1H spectrum even under conventional MAS conditions. The best way to eliminate this ^{14}N -driven relaxation of the amide ^1H is to use ^{15}N -labelled membrane polypeptides.

10.2 Prospective experiments

Despite these advances, the use of ^1H as a structural probe in membrane polypeptides is still severely limited by sensitivity, resolution and relaxation mechanisms. These affect all aspects of structural studies by NMR, namely peak dispersion, assignment strategies and structural restraint measurements. The pursuit of solving these problems is made most impractical by the limits in sensitivity. Besides using larger or more concentrated samples, the best improvement can be achieved by making use of

of state-of-the-art spectrometers. The highest field available today reaches 21.2 T which would not only represent an improvement of 75% in signal-to-noise ratio, but also 50% in peak resolution in 1D. A more subtle amelioration is expected at higher fields, for which the chemical shift difference between some neighbouring ^1H 's exceeds the strength of their dipolar coupling; in this case, the "flip-flop" transition no longer conserves energy and the commutation terms of the higher order term of the average Hamiltonian 7.2 become less important. As a consequence, it is expected that the backbone $^1\text{H}_\alpha$ and $^1\text{H}_N$ will be even more easily resolved by MAS at higher fields.

The use of pulsed field gradients within the CROPSY pulse sequence would also provide an important improvement in signal-to-noise. Currently, this sequence relies on the detection of the signal from the insensitive nuclei (^{15}N , ^{13}C). After the selective gradient-driven elimination of the ^1H coherence following the first CP, it will be possible to transfer the ^{15}N or ^{13}C signal back to the ^1H for sensitive indirect detection.

A more favourable signal-to-noise ratio will open the way to numerous new avenues. A straightforward implementation would be to upgrade the 2D-NOE-CROPSY experiment to the corresponding 3D experiment. With the extra $^1\text{H}_N$ dimension, it should be possible to further resolve the NOE cross-peaks already listed in Table 8.1.

Perhaps an even more important benefit of improved signal would be to allow for partial deuteration of the polypeptides. Site-specific or random deuteration methods exist whereby an expression system is grown on minimal media using deuterated nutrients (acetate, glucose) or water [179, 180]. A random deuteration level of, say 80%, would result in loss of ^1H signal by a factor of 5 but should also provide a reduction of the dipolar second moments of ^{13}C , ^{15}N and ^1H with ^1H by a factor of 4.5 according to the Van Vleck equation (p. 125). The immediate advantage of a reduced second moment is that the ^1H $T_{1\rho}$ and T_2 relaxation times are expected to be several fold longer. This will not only considerably reduce their linewidths helping resolution and peak dispersion, but also favour signal persistence perhaps up to several hundred ms.

More reliable assignment strategies need to be developed. Initially, with solid-phase synthesis of transmembrane polypeptides, single labels may be inserted at

several positions to confirm the tentative assignment attainable with CROPSY. Alternatively, with uniform ^{13}C - ^{15}N -labelled polypeptides, it may be possible to design assignment strategies based on CROPSY-type experiments with additional sequence-specific transfers from ^1H to ^{15}N to ^{13}C reminiscent of the solution NMR triple-channel 3D-HNCA and HNCOCA experiments. With additional partial deuteration of these already labelled peptides, these experiments will benefit from higher resolution and may use the more selective J-coupling route (rather than CP transfer) for the same assignment strategies.

Despite initial success with NOEs, problems of resolution, number of constraints, spin-diffusion, orientation-dependence and NOE calibration must be overcome. As previously mentioned, with additional signal or larger sample size, it will be necessary to upgrade to 3D experiments. With ^{13}C labels, a 2D- or 3D-NOE-CROPSY will highlight additional NOE contacts closer to the side chains, which may naturally show better resolution because of larger internal motional amplitudes along the side chains. Partial deuteration can also improve the quality of cross-relaxation experiments. For example, 80% random deuteration will reduce the efficiency of cross-relaxation by a factor of 5 and the efficiency of 3-spin relaying spin-diffusion by a factor of 25. The orientation-dependence of cross-relaxation could in principle be used not only as a distance but also as an orientation restraint. Another option is to complement the loose NOE restraints measured by these methods with orientation restraints obtained from oriented samples. Algorithms will have to be developed to allow for the combination of both types of constraints within the same simulated annealing protocol.



- The reasonable man adapts himself to the world; the unreasonable one persists in trying to adapt the world to himself. Therefore all progress depends on the unreasonable man.

- George Bernard Shaw

References

- [1] D. Voet and J. G. Voet, **Biochemistry**, J. Wiley, New York, Toronto (1995).
- [2] S. A. Aaronson, **Growth factors and cancer**, *Science* **254**: 1146–1153 (1991).
- [3] T. Gudermann, B. Nurnberg, and G. Schultz, **Receptors and G proteins as primary components of transmembrane signal transduction**, *J. Mol. Med.* **73**: 51–63 (1995).
- [4] L. R. Berg, **Introductory Botany - Plants, People and the Environment**, McMillan Publishing Co., New York (1997).
- [5] T. J. Stevens and I. T. Arkin, **Do more complex organisms have a greater proportion of membrane proteins in their genomes?**, *Proteins* **39**: 417–420 (2000).
- [6] Protein Data Bank/Research Collaboratory for Structural Bioinformatics, <http://www.rcsb.org/pdb/>.
- [7] S. Singer and G. L. Nicolson, **The fluid mosaic model of the structure of cell membranes**, *Science* **175**: 720–731 (1972).
- [8] D. A. Brown and E. London, **Functions of lipid rafts in biological membranes**, *Annu. Rev. Cell Dev. Biol.* **14**: 111–136 (1998).
- [9] N. A. Campbell and J. B. Reece, **Biology**, 6th edition, Benjamin Cummings, Boston (2002).

- [10] N. Kamiya and J.-R. Shen, **Crystal structure of oxygen-evolving photosystem II from *Thermosynechococcus vulcanus* at 3.7-Å Resolution**, *Proc. Natl. Acad. Sci. USA* **100**: 98–103 (2003).
- [11] M. H. Bracey, M. A. Hanson, K. R. Masuda, R. C. Stevens, and B. F. Cravatt, **Structural adaptations in a membrane enzyme that terminates endocannabinoid signaling**, *Science* **298**: 1793–1796 (2002).
- [12] S. Murakami, R. Nakashima, E. Yamashita, and A. Yamaguchi, **Crystal Structure of Bacterial Multidrug Efflux Transporter Acrb**, *Nature* **419**: 587–593 (2002).
- [13] V. Gordeliy, J. Labahn, R. Moukhametzianov, R. Efremov, J. Granzin, R. Schlesinger, G. Buldt, T. Savopol, A. J. Scheidig, J. P. Klare, and M. Engelhard, **Molecular basis of transmembrane signalling by sensory rhodopsin II-transducer complex**, *Nature* **419**: 484–487 (2002).
- [14] C. Toyoshima and H. Nomura, **Structural changes in the calcium pump accompanying the dissociation of calcium**, *Nature* **418**: 605–611 (2002).
- [15] K. R. Mackenzie, J. H. Prestegard, and D. M. Engelman, **A transmembrane helix dimer: structure and implications**, *Science* **276**: 131–133 (1997).
- [16] F. C. Almeida and S. J. Opella, **Fd coat protein structure in membrane environments: structural dynamics of the loop between the hydrophobic trans-membrane helix and the amphipathic in-plane helix**, *J. Mol. Biol.* **270**: 481–495 (1997).
- [17] C. Fernandez, C. Hilty, S. Bonjour, K. Adeishvili, K. Pervushin, and K. Wuthrich, **Solution NMR studies of the integral membrane proteins OmpX and OmpA from *Escherichia coli***, *FEBS Lett.* **504**: 173–178 (2001).
- [18] R. Prosser, V. B. Volkov, and I. V. Shiyanovskaya, **Solid-state NMR studies**

- of magnetically aligned phospholipid membranes: taming lanthanides for membrane protein studies, *Biochem. Cell Biol.* **76**: 443–451 (1998).
- [19] J. A. Losonczi and J. H. Prestegard, Improved dilute bicelle solutions for high-resolution NMR in biological macromolecules, *J. Biomol. NMR* **12**: 447–451 (1998).
- [20] J. A. Whiles, R. R. Vold, and E. A. Dennis, Bicelles in structure-function studies of membrane-associated proteins, *Bioorganic Chem.* **30**: 431–442 (2002).
- [21] Q. Teng and T. A. Cross, The *in situ* determination of the ^{15}N chemical shift tensor orientation in a polypeptide, *J. Mag. Res.* **85**: 439–447 (1989).
- [22] Q. Teng, L. K. Nicholson, and T. A. Cross, Experimental determination of torsion angles in the polypeptide backbone of the gramicidin A channel by solid state nuclear magnetic resonance, *J. Mol. Biol.* **218**: 607–619 (1991).
- [23] W. Mai, W. Hu, C. Wang, and T. Cross, Orientational constraints as three-dimensional structural constraints from chemical shift anisotropy: the polypeptide backbone of gramicidin A in a lipid bilayer, *Prot. Sci.* **2**: 532–542 (1993).
- [24] R. R. Ketchum, K. C. Lee, S. Huo, and T. A. Cross, Macromolecular structural elucidation with solid-state NMR-derived orientational constraints, *J. Biomol. NMR* **8**: 1–14 (1996).
- [25] L. K. Thompson, A. E. McDermott, J. Raap, C. M. van der Wielen, and J. Lugtenburg, Rotational resonance NMR study of the active site structure in bacteriorhodopsin: conformation of the Schiff base linkage, *Biochemistry* **31**: 7931–7938 (1992).
- [26] K. V. Lakshmi, M. Auger, J. Raap, J. Lugtenburg, R. G. Griffin, and J. Herzfeld, Internuclear distance measurement in a reaction interme-

- diate: solid-state carbon-13 NMR rotational resonance determination of the Schiff base configuration in the M photointermediate of bacteriorhodopsin, *J. Am. Chem. Soc.* **115**: 8515–8516 (1993).
- [27] A. T. Petkova, M. Hatanaka, C. P. Jaroniec, J. G. Hu, M. Belenky, M. Verhoeven, J. Lugtenburg, R. G. Griffin, and J. Herzfeld, **Tryptophan interactions in bacteriorhodopsin: a heteronuclear solid-state NMR study**, *Biochemistry* **41**: 2429–2437 (2002).
- [28] M. A. Lemmon, J. M. Flanagan, H. R. Treutlein, J. Zhang, and D. M. Engelman, **Sequence specificity in the dimerization of transmembrane α -helices**, *Biochemistry* **31**: 12719–12725 (1992).
- [29] A. McDermott, T. Polenova, A. Bockmann, K. W. Zilm, E. K. Paulsen, R. W. Martin, and G. Montelione, **Partial NMR assignments for uniformly (^{13}C , ^{15}N)-enriched BPTI in the solid state**, *J. Biomol. NMR* **16**: 209–219 (2000).
- [30] J. Pauli, M. Baldus, B. van Rossum, H. J. M. de Groot, and H. Oshkinat, **Backbone and side-chain ^{13}C and ^{15}N signal assignments of the α -spectrin SH3 domain by magic angle spinning solid-state NMR at 17.6 Tesla**, *ChemBioChem* **2**: 272–281 (2001).
- [31] V. Ladizhansky, C. P. Jaroniec, A. Diehl, H. Oshkinat, and R. Griffin, **Measurement of multiple psi torsion angles in uniformly ^{13}C , ^{15}N -labeled alpha-spectrin SH3 domain using 3D ^{15}N - ^{13}C - ^{13}C - ^{15}N MAS dipolar-chemical shift correlation spectroscopy**, *J. Am. Chem. Soc.* **125**: 6827–6833 (2003).
- [32] F. Castellani, B. van Rossum, A. Diehl, M. Schubert, K. Rehbein, and H. Oshkinat, **Structure of a protein determined by solid-state magic-angle-spinning NMR spectroscopy**, *Nature* **420**: 98–102 (2002).

- [33] J. H. Davis, M. Auger, and R. S. Hodges, **High resolution ^1H nuclear magnetic resonance of a transmembrane peptide**, *Biophys. J.* **69**: 1917–1932 (1995).
- [34] H. Schwalbe and A. Bielecki, **Recent advances in high-resolution solid-state NMR spectroscopy**, *Angew. Chem. (Int. Ed.)* **40**: 2045–2050 (2001).
- [35] S. J. Opella, C. Ma, and F. M. Marassi, **Nuclear magnetic resonance of membrane-associated peptides and proteins**, *Meth. Enz.* **339**: 285–313 (2001).
- [36] J. K. Denny, J. Wang, T. A. Cross, and J. R. Quine, **PISEMA powder patterns and PISA wheels**, *J. Mag. Res.* **152**: 217–226 (2001).
- [37] F. M. Marassi, **A simple approach to membrane protein secondary structure and topology based on NMR spectroscopy**, *Biophys. J.* **80**: 994–1003 (2001).
- [38] H. J. M. de Groot, **Solid-state NMR spectroscopy applied to membrane proteins**, *Curr. Op. Str. Biol.* **10**: 593–600 (2000).
- [39] B. Bechinger, **The structure, dynamics and orientation of antimicrobial peptides in membranes by multidimensional solid-state NMR spectroscopy**, *Biochim. Biophys. Acta* **1462**: 157–183 (1999).
- [40] A. Abragam, **The principles of nuclear magnetism**, Oxford University Press, London (1961).
- [41] M. Mehring, **Principles of high resolution NMR in solids**, Springer-Verlag, Heidelberg - Berlin - New York (1983).
- [42] C. P. Slichter, **Principles of magnetic resonance 3rd ed.**, Springer-Verlag, Heidelberg - Berlin - New York (1990).
- [43] A. Steigel and W. Spiess, **Dynamic NMR spectroscopy**, Springer-Verlag, Berlin, Heidelberg, New York (1978).

- [44] J. Cavanagh, W. J. Fairbrother, A. G. P. III, and N. J. Skelton, **Protein NMR spectroscopy. Principles and practice**, Academic Press, New York (1996).
- [45] R. N. Zare, **Angular momentum**, Wiley, New York (1988).
- [46] L. K. Nicholson, F. Moll, T. E. Mixon, P. V. LoGrasso, J. C. Lay, and T. A. Cross, **Solid-state ^{15}N NMR of oriented lipid bilayer bound gramicidin A'**, *Biochemistry* **26**: 6621–6626 (1987).
- [47] L. K. Nicholson, **The structural motif and backbone dynamics of membrane-bound gramicidin-A using solid-state ^{15}N nuclear magnetic resonance spectroscopy**, Ph.D. thesis, Florida State University, Tallahassee (1990).
- [48] T. C. B. Vogt, S. Schinzel, and B. Bechinger, **Biosynthesis of isotopically labeled gramicidins and tyrocidins by *Bacillus brevis***, *J. Biomol. NMR* **26**: 1–11 (2003).
- [49] R. D. Hotchkiss and R. J. Dubos, **Bactericidal fractions from an aerobic sporulating bacillus**, *J. Biol. Chem.* **136**: 803–804 (1940).
- [50] O. S. Andersen, **Gramicidin channels**, *Annu. Rev. Physiol.* **46**: 531–548 (1984).
- [51] B. Mach, E. Reich, and E. L. Tatum, **Separation of the biosynthesis of the antibiotic polypeptide tyrocidine from protein biosynthesis**, *Biochemistry* **50**: 175–181 (1963).
- [52] D. Salom and C. Abad, **Chromatographic purification and characterization of synthetic tryptophan-substituted gramicidin A analogues**, *J. Chromat. A* **725**: 315–322 (1996).
- [53] A. S. Arseniev, I. L. Barsukov, and V. F. Bystrov, **NMR solution structure of Gramicidin A Complex with Caesium Cation**, *FEBS Lett.* **180**: 33–39 (1985).

- [54] Y. Lapidot, I. Barzilay, and J. Hajdu, The synthesis of diacyl-*dl*-(and-*L*-) α -glycerol phosphate, *Chem. Phys. Lip.* 3: 125-134 (1969).
- [55] R. Aneja, J. S. Chadha, and A. P. Davies, A general synthesis of glycerophospholipids, *Biochim. Biophys. Acta* 218: 102-111 (1970).
- [56] R. Aneja and J. S. Chadha, A total synthesis of phosphatidylcholines, *Biochim. Biophys. Acta* 248: 455-457 (1971).
- [57] K. M. Patel, J. D. Morrisett, and J. T. Sparrow, A convenient synthesis of phosphatidylcholines: acylation of *sn*-glycero-3-phosphocholine with fatty acid anhydride and 4-pyrrolidinopyridine, *J. Lipid Res.* 20: 674-677 (1979).
- [58] P. Comfurius and R. F. Zwaal, The enzymatic synthesis of phosphatidylserine and purification by CM-cellulose column chromatography, *Biochim. Biophys. Acta* 488: 36-42 (1977).
- [59] C. M. Gupta, R. Radhakrishnan, and H. G. Khorana, Glycerophospholipid synthesis: improved general method and new analogs containing photoactivable groups, *Proc. Natl. Acad. Sci. USA* 74: 4315-4319 (1977).
- [60] P. B. Kingsley and G. W. Feigenson, The synthesis of perdeuterated phospholipid: 1,2-dimyristoyl-*sn*-glycero-3-phosphocholine- d_{72} , *Chem. Phys. Lip.* 24: 135-147 (1979).
- [61] H. Eibl, Synthesis of glycerophospholipids, *Chem. Phys. Lip.* 26: 405-429 (1980).
- [62] J. T. Mason, A. V. Broccoli, and C. Huang, A method for the synthesis of isomerically pure saturated mixed-chain phosphatidylcholines, *Anal. Biochem.* 113: 96-101 (1981).
- [63] G. S. Harbison and R. G. Griffin, Improved method for the synthesis of phosphatidylcholines, *J. Lipid Res.* 25: 1140-1142 (1984).

- [64] B. Bersch, J. P. Starck, A. Milon, Y. Nakatani, and G. Ourisson, **Interaction of a synthetic amphiphilic polypeptide and lipids in a bilayer structure**, *B. Soc. Chim. Fr.* **130**: 575–583 (1993).
- [65] P. Desnuelle, **The Enzymes of Lipid Metabolism; Proceedings [65a]** (p. 465), Pergamon Press, Oxford, New York (1961).
- [66] Z. Selinger and Y. Lapidot, **Synthesis of fatty acid anhydrides by reaction with dicyclohexylcarbodiimide**, *J. Lipid Res.* **7**: 174–175 (1966).
- [67] M. Kates, **Techniques of lipidology: isolation, analysis and identification of lipids**, Elsevier, New York (1972).
- [68] J. A. Killian, K. U. Prasad, D. Hains, and D. W. Urry, **The membrane as an environment of minimal interconversion. A circular dichroism study on the solvent dependence of the conformational behavior in gramicidin in diacylphosphatidylcholine model membranes**, *Biochemistry* **27**: 4848–4855 (1988).
- [69] J. S. Frye and G. E. Maciel, **Setting the magic angle using a quadrupolar nuclide**, *J. Mag. Res.* **48**: 125–131 (1982).
- [70] R. R. Ernst, G. Bodenhausen, and A. Wokaun, **Principles of nuclear magnetic resonance in one and two dimensions**, Clarendon Press, Oxford (1986).
- [71] G. Bodenhausen and D. J. Ruben, **Natural abundance nitrogen-15 NMR by enhanced heteronuclear spectroscopy**, *Chem. Phys. Lett.* **69**: 185–188 (1980).
- [72] A. Pines, G. Gibby, and J. S. Waugh, **Proton-enhanced NMR of dilute spins in solids**, *J. Chem. Phys.* **59**: 569–590 (1973).
- [73] J. S. and E. O. Stejskal, **Carbon-13 nuclear magnetic resonance of polymers spinning at the magic angle**, *J. Am. Chem. Soc.* **98**: 1031–1032 (1976).

- [74] S. R. Hartmann and E. L. Hahn, **Nuclear double resonance in the rotating frame**, *Phys. Rev. II* **128**: 2042–2063 (1962).
- [75] K. Wüthrich, **NMR in biological research : peptides and proteins**, Elsevier, Amsterdam, Holland (1976).
- [76] R. L. Vold, J. S. Waugh, M. P. Klein, and D. E. Phelps, **Measurement of spin relaxation in complex systems**, *J. Chem. Phys.* **48**: 3831–3832 (1968).
- [77] A. J. Shaka, J. Keeler, and R. Freeman, **Evaluation of a new broadband decoupling sequence: WALTZ-16**, *J. Mag. Res.* **53**: 313–340 (1983).
- [78] A. Bax and D. G. Davis, **MLEV-17-Based two-dimensional homonuclear magnetization transfer spectroscopy**, *J. Mag. Res.* **65**: 355–360 (1985).
- [79] A. J. Shaka, C. J. Lee, and A. Pines, **Iterative schemes for bilinear operators: Applications to spin decoupling**, *J. Mag. Res.* **77**: 274–293 (1988).
- [80] A. E. Bennett, C. M. Rienstra, M. Auger, K. V. Lakshmi, and R. G. Griffin, **Heteronuclear decoupling in rotating solids**, *J. Chem. Phys.* **103**: 6951–6958 (1995).
- [81] A. Detken, E. H. Hardy, M. Ernst, and B. H. Meier, **Simple and efficient decoupling in magic-angle spinning solid-state NMR: the XiX scheme**, *Chem. Phys. Lett.* **356**: 298–304 (2002).
- [82] K. Wüthrich, **NMR studies of structure and function of biological macromolecules (Nobel Lecture)**, *J. Biomol. NMR* **27**: 13–39 (2003).
- [83] B. A. Wallace, **Recent advances in high resolution structures of bacterial channels: gramicidin A**, *J. Struct. Biol.* **121**: 123–141 (1998).
- [84] N. Foundation, **Gramicidin and related ion channel-forming peptides**, Wiley, New York, USA (1999).

- [85] S. M. Pascal and T. A. Cross, **Structure of an isolated gramicidin A double helical species by high-resolution nuclear magnetic resonance**, *J. Mol. Biol.* **226**: 1101–1109 (1992).
- [86] I. L. Barsukov, A. S. Arseniev, and V. F. Bystrov, **Spatial structures of gramicidin A in organic solvents. ^1H -NMR analysis of four species in ethanol**, *Bioorg. Khim. (Russian)* **13**: 1501– (1987).
- [87] V. F. Bystrov and A. S. Arseniev, **Diversity of the gramicidin A spatial structure: Two-dimensional ^1H NMR study in solution**, *Tetrahedron* **44**: 925–940 (1988).
- [88] N. Abdul-Manan and J. F. Hinton, **Conformation states of gramicidin A along the pathway to the formation of channels in model membranes determined by 2D NMR and circular dichroism spectroscopy**, *Biochemistry* **33**: 6773–6783 (1994).
- [89] S. M. Pascal and T. A. Cross, **High-resolution structure and dynamic implications for a double-helical gramicidin A conformer**, *J. Biomol. NMR* **3**: 495–513 (1993).
- [90] Y. Chen, A. Tucker, and B. A. Wallace, **Solution structure of a parallel left-handed double-helical gramicidin A determined by ^1H NMR**, *J. Mol. Biol.* **264**: 757–769 (1996).
- [91] A. L. Lomize, V. Y. Orekhov, and A. S. Arseniev, **Refinement of the spatial structure of the gramicidin A transmembrane ion channel**, *Bioorg. Khim. (Russian)* **18**: 182–200 (1992).
- [92] L. E. Townsley and J. F. Hinton, **The structure of gramicidin A in DPC micelles: The effects of lipid and Na^+ on the gramicidin ion channel**, unpublished.

- [93] D. W. Urry, M. C. Goodall, J. D. Glickson, and D. F. Mayers, **The gramicidin A transmembrane channel: characteristics of the head-to-head dimerized $\pi_{L,D}$ helices**, *Proc. Natl. Acad. Sci. USA* **68**: 1907–1911 (1971).
- [94] C. Farès, F. J. Sharom, and J. H. Davis, **^{15}N , ^1H Heteronuclear Correlation NMR of Gramicidin A in DMPC- d_{67}** , *J. Am. Chem. Soc.* **128**: 11232–11233 (2002).
- [95] U. Piantini, W. Sørensen, and R. R. Ernst, **Multiple quantum filters for elucidating NMR coupling networks**, *J. Am. Chem. Soc.* **104**: 6800–6801 (1982).
- [96] M. Rance, W. Sørensen, G. Bodenhausen, G. Wagner, R. R. Ernst, and K. Wüthrich, **Improved spectral resolution in COSY ^1H NMR. Spectra of proteins via double quantum filtering for preparative separation with moderate resolution**, *Biochem. Biophys. Res. Commun.* **117**: 479–485 (1983).
- [97] L. Braunschweiler and R. R. Ernst, **Coherence transfer by isotropic mixing – Application to proton correlation spectroscopy**, *J. Mag. Res.* **53**: 521–528 (1983).
- [98] J. Jeener, B. H. Meier, P. Bachmann, and R. R. Ernst, **Investigation of exchange processes by two-dimensional NMR spectroscopy**, *J. Chem. Phys.* **71**: 4546–4563 (1979).
- [99] D. J. States, R. A. Haberkorn, and D. J. Ruben, **A Two-Dimensional Nuclear Overhauser Experiment with Pure Absorption Phase in Four Quadrants**, *J. Mag. Res.* **48**: 286–292 (1982).
- [100] H. J. Dyson and P. E. Wright, **Defining solution conformations of small linear peptides**, *Annu. Rev. Biophys. Chem.* **20**: 519–538 (1991).
- [101] A. A. Bothner-By, R. L. Stephens, J.-M. Lee, C. Warren, and R. W. Jeanloz, **Structure determination of a tetrasaccharide: transient nuclear**

- Overhauser effects in the rotating frame, *J. Am. Chem. Soc.* **106**: 811–813 (1985).
- [102] T.-L. Hwang and A. J. Shaka, Cross relaxation without TOCSY: transverse rotating-frame Overhauser effect spectroscopy, *J. Am. Chem. Soc.* **114**: 3157–3159 (1992).
- [103] M. P. Williamson, T. Asakura, , E. Nakamura, and M. Demura, A method for the calculation of protein α -CH chemical shifts, *J. Biomolecular NMR*, *J. Biomol. NMR* **2**: 83–89 (1992).
- [104] M. Karplus, Contact Electron-Spin Coupling of Nuclear Magnetic Moments, *J. Chem. Phys.* **30**: 11–15 (1959).
- [105] A. Pardi, M. Billeter, and K. Wüthrich, Calibration of the angular dependence of the amide proton-C- α proton coupling constants, $^3J_{HN\alpha}$, in a globular protein, *J. Mol. Biol.* **180**: 741–751 (1984).
- [106] M. Bendall, D. M. Doddrell, and D. T. Pegg, Editing of carbon-13 NMR spectra. A pulse sequence for the generation of subspectra, *J. Am. Chem. Soc.* **103**: 4603–4605 (1981).
- [107] G. A. Morris and R. Freeman, Enhancement of nuclear magnetic resonance signals by polarization transfer, *J. Am. Chem. Soc.* **101**: 760–762 (1979).
- [108] A. Bax and M. F. Summers, Proton and carbon-13 assignments from sensitivity-enhanced detection of heteronuclear multiple-bond connectivity by 2D multiple quantum NMR, *J. Am. Chem. Soc.* **108**: 2093–2094 (1986).
- [109] D. Marion, P. C. Driscoll, L. E. Kay, P. T. Wingfield, A. Bax, A. M. Gronenborn, and G. M. Clore, Overcoming the overlap problem in the assignment of proton NMR spectra of larger proteins by use of three-dimensional

- heteronuclear proton-nitrogen-15 Hartmann-Hahn-multiple quantum coherence and nuclear Overhauser-multiple quantum coherence spectroscopy: application to interleukin 1 β , *Biochemistry* **28**: 6150–6156 (1989).
- [110] A. T. Brünger, A. T. Clore, G. M. Gronenborn, and M. Karplus, **Three-dimensional structure of proteins determined by molecular dynamics with interproton distance restraints: application to crambin**, *Proc. Natl. Acad. Sci. USA* **83**: 3801–3805 (1986).
- [111] M. Nilges, G. M. Clore, and A. M. Gronenborn, **Determination of three-dimensional structures of proteins from interproton distance data by hybrid distance geometry-dynamical simulated annealing calculations**, *FEBS Lett.* **229**: 317–324 (1988).
- [112] M. Nilges, G. M. Clore, and A. M. Gronenborn, **Determination of three-dimensional structures of proteins from interproton distance data by dynamical simulated annealing from a random array of atoms. Circumventing problems associated with folding**, *FEBS Lett.* **239**: 129–136 (1988).
- [113] C. D. Schwieters, J. J. Kuszewski, N. Tjandra, and G. M. Clore, **The Xplor-NIH NMR Molecular Structure Determination Package**, *J. Mag. Res.* **160**: 66–74 (2003).
- [114] A. T. Brünger, **X-PLOR Version 3.1, User's Manual**, Yale University Press, Yale (1992).
- [115] A. S. Arseniev, I. L. Barsukov, V. F. Bystrov, A. L. Lomize, and V. F. Bystrov, **¹H-NMR study of gramicidin A transmembrane ion channel. Head-to-head right-handed, single-stranded helices**, *FEBS Lett.* **186**: 168–174 (1985).

- [116] K. R. Mackenzie, **Structure determination of the dimeric membrane spanning domain of glycoporphin A in detergent micelles by triple resonance nuclear magnetic resonance**, Ph.D. thesis, Yale University, New Haven (1996).
- [117] M. Nilges, **A calculation strategy for the structure determination of symmetric dimers by ^1H NMR**, *Proteins* **17**: 297–309 (1993).
- [118] C. H. Wu, A. Ramamoorthy, and S. J. Opella, **High resolution heteronuclear dipolar solid-state NMR spectroscopy**, *J. Mag. Res. A* **109**: 270–272 (1994).
- [119] T. Vosegaard and N. C. Nielsen, **Towards high-resolution solid-state NMR on large uniformly ^{15}N - and $[^{13}\text{C}, ^{15}\text{N}]$ -labeled membrane proteins in oriented lipid bilayers**, *J. Biomol. NMR* **22**: 225–247 (2002).
- [120] M. Lee and W. I. Goldberg, **Nuclear-magnetic-resonance line narrowing by a rotating rf field**, *Phys. Rev. A* **140**: 1261–1271 (1965).
- [121] J. H. Davis and M. Auger, **Static and magic angle spinning NMR of membrane peptides and proteins**, *Prog. NMR Spect* **35**: 1–84 (1999).
- [122] F. M. Marassi and S. J. Opella, **A solid-state NMR index of helical membrane protein structure and topology**, *J. Mag. Res.* **144**: 150–155 (2000).
- [123] J. Wang, J. Denny, C. Tian, S. Kim, Y. Mo, F. Kovacs, Z. Song, K. Nishimura, Z. Gan, R. Fu, J. R. Quine, and T. A. Cross, **Imaging membrane protein helical wheels**, *J. Mag. Res.* **144**: 162–167 (2000).
- [124] R. Engh and R. Huber, **Accurate bond and angle parameters for X-ray protein structure refinement**, *Acta Cryst. A* **47**: 392–400 (1991).
- [125] M. W. MacArthur and J. M. Thornton, **Deviations from planarity of the peptide bond in peptides and proteins**, *J. Mol. Biol.* **264**: 1180–1195 (1996).

- [126] H. Luecke, B. Schobert, H. T. Richter, J. P. Cartailler, and J. K. Lanyi, **Structure of bacteriorhodopsin at 1.55 Å resolution**, *J. Mol. Biol.* **291**: 899–911 (1999).
- [127] N. D. Lazo, W. Hu, , and T. A. Cross, **Low-temperature solid-state ^{15}N NMR characterization of polypeptide backbone librations**, *J. Mag. Res. B* **107**: 43–50 (1995).
- [128] C. L. North and T. A. Cross, **Correlations between function and dynamics: time scale coincidence for ion translocation and molecular dynamics in the gramicidin channel backbone**, *Biochemistry* **34**: 5883–5895 (1995).
- [129] R. S. Prosser, J. H. Davis, F. W. Dahlquist, and M. A. Lindorfer, **^2H nuclear magnetic resonance of the gramicidin A backbone in a phospholipid bilayer**, *Biochemistry* **30**: 4687–4696 (1991).
- [130] R. S. Prosser and J. H. Davis, **Dynamics of an integral membrane peptide: a deuterium NMR relaxation study of gramicidin**, *Biophys. J.* **66**: 1429–1440 (1994).
- [131] R. S. Houliston, F. J. Sharom, R. S. Hodges, and J. H. Davis, **Comparison of proto-oncogenic and mutant forms of the transmembrane region of the Neu receptor in TFE**, *FEBS Letters* **535**: 39–43 (2003).
- [132] B. M. van der Ende, F. Sharom, and J. H. Davis, **Molecular dynamics simulations of wild-type and mutant Neu transmembrane domains**, *Biophys. J.* (submitted) (2003).
- [133] A. Arora and L. K. Tamm, **Biophysical approaches to membrane protein structure determination**, *Curr. Op. Str. Biol.* **11**: 540–547 (2001).
- [134] F. A. Kovacs, J. K. Denny, Z. Song, J. R. Quine, and T. A. Cross, **Helix Tilt of the M2 Transmembrane Peptide from Influenza A Virus: An Intrinsic Property**, *J. Mol. Biol.* **295**: 117–125 (2000).

- [135] C. Tian, K. Tobler, R. A. Lamb, L. H. Pinto, and T. A. Cross, **Expression and Initial Structural Insights from Solid-State NMR of the M2 Proton Channel from Influenza A Virus**, *Biochemistry* **41**: 11294–11300 (2002).
- [136] M. Goetz, C. Carlotti, F. Bontems, and E. J. Dufoure, **Evidence for a α -Helix \rightarrow π -Bulge Helicity Modulation for the Neu/ErbB-2 Membrane-Spanning Segment. A ^1H -NMR and Circular Dichroism Study**, *Biochemistry* **40**: 6534–40 (2001).
- [137] F. M. Marassi and S. J. Opella, **Simultaneous assignment and structure determination of a membrane protein from NMR orientational restraints**, *Prot. Sci.* **12**: 403–411 (2003).
- [138] J. Gesell, M. Zasloff, and S. J. Opella, **Two-dimensional ^1H NMR experiments show that the 23-residue magainin antibiotic peptide is an alpha-helix in dodecylphosphocholine micelles, sodium dodecylsulfate micelles, and trifluoroethanol/water solution**, *J. Biomol. NMR* **9**: 127–135 (1997).
- [139] Z. O. Shenkarev, T. A. Balasheva, R. G. Efremov, Z. A. Yakimenko, T. V. Ovchinnikova, J. Raap, and A. S. Arseniev, **Spatial Structure of Zervamicin Iib Bound to Dpc Micelles: Implications for Voltage-Gating**, *Biophys. J.* **82**: 762–771 (2002).
- [140] C. J. Franklin, J. F. Ellena, S. Jayasinghe, L. P. Kelsh, and D. S. Cafiso, **Structure of micelle-associated alamethicin from ^1H NMR. Evidence for conformational heterogeneity in a voltage-gated peptide**, *Biochemistry* **33**: 4036–4045 (1994).
- [141] Z.-Y. Peng, V. Simplaceanu, I. Lowe, and C. Ho, **Rotating-frame relaxation of slow motions in fluorinated phospholipid model membranes**, *Biophys. J.* **54**: 81–95 (1988).

- [142] J. S. Blicharski, Nuclear magnetic relaxation in rotating frame, *Act. Phys. Pol. A* **41**: 223–236 (1972).
- [143] B. Geil and G. Hinze, Influence of data treatment on the shape of ^2H NMR T_1 curves, *Chem. Phys. Lett.* **216**: 51–55 (1993).
- [144] R. J. Wittebort and A. Szabo, Theory of NMR relaxation in macromolecules: Restricted diffusion and jump models for multiple internal rotations in amino acid side chains, *J. Chem. Phys.* **69**: 1722–1736 (1978).
- [145] G. Lipari and A. Szabo, Padé approximants to correlation functions for restricted rotational diffusion, *J. Chem. Phys.* **75**: 2971–2976 (1981).
- [146] J. H. V. Vleck, The dipolar broadening of magnetic resonance lines in crystals, *Phys. Rev.* **74**: 1168 (1948).
- [147] J. H. Davis, M. D. Clare, R. S. Hodges, and M. Bloom, Interaction of a synthetic amphiphilic polypeptide and lipids in a bilayer structure, *Biochemistry* **22**: 5298–5305 (1983).
- [148] D. I. Hoult, The NMR receiver: A description and analysis of design, *Prog. NMR Spect* **12**: 41–77 (1978).
- [149] B. L. de Groot, D. P. Tieleman, P. Pohl, and H. Grubmuller, Water permeation through gramicidin A: desformylation and the double helix: a molecular dynamics study, *Biophys. J.* **82**: 2934–42 (2002).
- [150] M. M. Maricq and J. S. Waugh, NMR in rotating solids, *J. Chem. Phys.* **70**: 3300–3316 (1979).
- [151] J. Clair, S. Buchoux, and J. H. Davis, ^1H $T_{1\rho}$ of membrane phospholipids, Technical report, University of Guelph (2003).

- [152] J. Qian, **The dynamics of peptide-16 in DMPC bilayer membranes: An NMR relaxation study**, Ph.D. thesis, University of Guelph, Guelph, Canada (1997).
- [153] A. Naito, S. Ganapathy, K. Akasaka, and C. A. McDowell, **Chemical shielding tensor and ^{13}C - ^{15}N dipolar splitting in single crystals of L-alanine**, *J. Chem. Phys.* **74**: 3190–3197 (1981).
- [154] U. Haeberlen and J. S. Waugh, **Coherent averaging effects in magnetic resonance**, *Phys. Rev.* **175**: 453–467 (1968).
- [155] U. Haeberlen and J. S. Waugh, **Spin-lattice relaxation in periodically perturbed systems**, *Phys. Rev.* **185**: 420–429 (1969).
- [156] S. Everts and J. H. Davis, **^1H and ^{13}C NMR of multilamellar dispersions of polyunsaturated (22:6) phospholipids**, *Biophys. J.* **79**: 885–897 (2000).
- [157] K. Schmidt-Rohr, J. Clauss, and H. W. Spiess, **Correlation of structure, mobility, and morphological information in heterogeneous polymer materials by two-dimensional wideline-separation NMR spectroscopy**, *Macromol.* **25**: 3273–3277 (1992).
- [158] G. E. Hawkes, L.-Y. Lian, and E. W. Randall, **The conformation of gramicidin A in dimethylsulphoxide solution. A full analysis of the one- and two-dimensional ^1H , ^{13}C , and ^{15}N nuclear-magnetic-resonance spectra**, *Eur. J. Biochem.* **166**: 437–542 (1987).
- [159] I. Solomon, **Relaxation processes in a system of two spins**, *Phys. Rev.* **99**: 559–565 (1955).
- [160] A. W. Overhauser, **Paramagnetic relaxation in metals**, *Phys. Rev.* **89**: 689–700 (1953).
- [161] A. W. Overhauser, **Polarization of nuclei in metals**, *Phys. Rev.* **92**: 411–415 (1953).

- [162] D. Huster, K. Arnold, and K. Gawrisch, Investigation of lipid organization in biological membranes by two-dimensional nuclear Overhauser enhancement spectroscopy, *J. Phys. Chem.* **103**: 243–251 (1999).
- [163] D. Huster and K. Gawrisch, NOESY NMR crosspeaks between lipid headgroups and hydrocarbon chains: spin diffusion or molecular disorder?, *J. Am. Chem. Soc.* **121**: 1992–1993 (1999).
- [164] S. E. Feller, D. Huster, and K. Gawrisch, Interpretation of NOESY cross-relaxation rates from molecular dynamics simulation of a lipid bilayer, *J. Am. Chem. Soc.* **121**: 8963–8964 (1999).
- [165] W.-M. Yau and K. Gawrisch, Lateral lipid diffusion dominates NOESY cross-relaxation in membranes, *J. Am. Chem. Soc.* **122**: 3971–3972 (2000).
- [166] S. E. Feller, C. A. Brown, D. T. Nizza, and K. Gawrisch, Nuclear Overhauser enhancement spectroscopy cross-relaxation rates and ethanol distribution across membranes, *Biophys. J.* **82**: 1396–1404 (2002).
- [167] C. L. Guernevé and M. Seigneuret, High-resolution mono- and multidimensional magic angle spinning ^1H nuclear magnetic resonance of membrane peptides in non-deuterated lipid membranes and H_2O , *Biophys. J.* **71**: 2633–2644 (1996).
- [168] D. Huster, K. Kuhn, D. Kadereit, H. Waldmann, and K. Arnold, ^1H High resolution magic angle spinning NMR spectroscopy for the investigation of a Ras lipopeptide in a lipid membrane, *Angew. Chem. (Int. Ed.)* **40**: 1056–1058 (2001).
- [169] F. Husson, H. Mustacchi, and V. Luzzati, La structure des colloïdes d'association. II. Description des phases liquide-cristallines de plusieurs systèmes amphiphile-eau: amphiphiles anioniques, cationiques, non-ioniques, *Acta Cryst.* **13**: 668–677 (1960).

- [170] K. Gawrisch, N. V. Eldho, and I. V. Polozov, Novel NMR tools to study the structure and dynamics of biomembranes, *Chem. Phys. Lett.* **116**: 135–151 (2002).
- [171] G. Lipari and A. Szabo, Model-free approach to the interpretation of nuclear magnetic resonance in macromolecules. 1. Theory and range of validity, *J. Am. Chem. Soc.* **104**: 4546–4559 (1982).
- [172] G. Lipari and A. Szabo, Model-free approach to the interpretation of nuclear magnetic resonance in macromolecules. 2. Analysis of experimental results, *J. Am. Chem. Soc.* **104**: 4559–4570 (1982).
- [173] J. G. Hexem, M. H. Frey, and S. J. Opella, Molecular and structural information from ^{14}N - ^{13}C dipolar couplings manifested in high resolution ^{13}C NMR spectra of solids, *J. Chem. Phys.* **77**: 3847–3856 (1982).
- [174] D. L. Vanderhart, G. S. Gutowsky, and T. Farrar, Dipole-dipole interactions of a spin-1/2 nucleus with a quadrupole-coupled nucleus, *J. Am. Chem. Soc.* **89**: 5056–5057 (1967).
- [175] N. Zumbulyadis, P. M. Henrichs, and R. H. Young, Quadrupole effects in the magic-angle-spinning spectra of spin-1/2 nuclei, *J. Chem. Phys.* **75**: 1603–1611 (1981).
- [176] A. Naito, S. Ganapathy, and C. McDowell, ^{14}N quadrupole effect in CP-MAS ^{13}C NMR spectra of organic compounds in the solid state, *J. Mag. Res.* **48**: 367–381 (1982).
- [177] Z. Gan and D. M. Grant, Molecular and structural information from variable-angle spinning NMR dipolar spectra of ^{13}C - ^{14}N systems, *J. Mag. Res.* **90**: 522–534 (1990).
- [178] E. Kundla and M. Alla, Line splittings through dipole-dipole interaction with quadrupole nuclei in high resolution NMR powder spectra,

magnetic resonance and related phenomena, *Proc. Cong. AMPERE 20th.* **27**: 92 (1979).

- [179] K. H. Gardner and L. E. Kay, The use of ^2H , ^{13}C , ^{15}N multidimensional NMR to study the structure and dynamics of proteins, *Annu. Rev. Biophys. Biomol. Struct.* **27**: 357–406 (1998).
- [180] N. K. Goto and L. E. Kay, New developments in isotope labeling strategies for protein solution NMR spectroscopy, *Curr. Op. Str. Biol.* **10**: 585–592 (2000).

A

Appendix: Simulations and computer programs

All computer-based files, including Fortran 77 and C++ program code, Maple calculations, Xplor parameters and input can be accessed on the attached CD-ROM labelled "CF-THESIS-03". The following is an annotated inventory of the content of the CD-ROM.

A.1 Xplor parameter, input and results files

All parameter, input and resulting PDB files for the Xplor distance geometry / simulated annealing protocol can be found on the CD-ROM. These include the following stepwise input files:

0-xplor-spectrum.inp	Prediction of a spectrum from a 3D structure
1-make-psf-ga.inp	Generation of a structure file and internal coordinates
2-gen-templ-gasds.inp	Generation of a template coordinate set
3-xplor-dg.inp	DG sub-embedding of monomer sub-structures
4-xplor-dgsa.inp	SA regularization and DG refinement for monomer sub-structures
5-xplor-refine.inp	SA refinement on monomer structure
6-xplor-accept.inp	Analysis of a family of monomer structures
7-growinter.inp	Dimerization of 2 accepted monomer structures
8-xplor-refine.inp	SA refinement of dimer structure
9-xplor-accept.inp	Analysis of a family of dimer structures
10-xplor-average.inp	Calculate an average structure from the accepted dimer structures

A.2 Program code

A.2.1 "PDBMI"

The Fortran program "pdbmi.f" (author: J.H. Davis) reads in the coordinates of a structure file (PDB format), calculates its moment of inertia principal axis system, and outputs the values of the ^{15}N CS, ^{15}N - ^1H dipolar coupling, $^{13}\text{C}'$ CS, $^{13}\text{C}'$ - $^{13}\text{C}_\alpha$, and $^2\text{H}_\alpha$ quadrupolar splitting for each peptide plane (except for Pro) and for each orientation prescribed by the polar angles ρ and τ . The input file (*.cfg) has the following format:

y	;put molecule in MI frame?
n	;axial diffusion around MI principal axis?
6	;number of tau values
36	;number of rho values
imag.pdb	;name of *.pdb orr *.ent file
imagmi.pdb	;name of output coordinate file (in MI frame)
imag.res	;name of results file
imag.pis	;name of pisema file
600.000	;1H Larmor frequency
0.0	;15N offset in ppm
0.0	;initial tau value
0.0	;initial rho value

A.2.2 "SECONDMOMENT"

The Fortran program "secondmoment.f" (authors: J.H. Davis and C. Farès) is derived from the previous one, but calculates the total second moment due to the dipolar coupling of the backbone $^{13}\text{C}'$, ^{15}N , $^1\text{H}_\alpha$ and $^1\text{H}_\text{N}$ with all surrounding ^1H for each residue, for each orientation of the moment of inertia principal axis relative to the magnetic field and for a static and axially diffusing molecules. The input file for this program should follow the following example format:

0.0	;initial tau value
19	;number of tau values
5.0	;tau increments
40.0	;initial rho value
1	;number of rho values
imag.pdb	;name of *.pdb or *.ent input file
imagmi.pdb	;name of output coordinate file (in MI frame)
imag.sm	;name of second moment results file

A.2.3 "anisoNOE"

The Fortran program "anisoNOE.f" (author: C. Farès) back-calculates the cross-peak intensities for the PDB:Imag conformation of gA for every pair of ^1H within 6 Å

of each other within the peptide undergoing fast isotropic tumbling, axial diffusion alone, axial diffusion + diffusion-in-a-cone, or axial diffusion + diffusion-in-a-cone + Lipari-Szabo-type internal motions.

A.3 Maple files

A number of Maple files are also included on the CD-ROM. The ones found under the directory “T1rho” were used to develop the expressions of $T_{1\rho}$ for static and MAS samples, for the CSA and dipolar coupling and for motional models including axial reorientation and diffusion-in-a-cone. The files in the directory “14NdipH” were used to calculate the simulated spectra for $^1\text{H}_N$ strongly coupled to ^{14}N .

A.4 Bruker Pulse sequences

All the pulse sequences used in this work are compiled under the directory “pulse-prog”.



B

Appendix: Derivations

This appendix presents the details of the steps involved in the derivations of the expression of the spin-lattice relaxation rate ($1/T_{1\rho}$) for the different interactions and different sample configurations.

B.1 Chemical shift anisotropy in oriented membranes

The derivation starts with the expression of the Hamiltonian of the chemical shift interaction in the rotating frame, ρ , in terms of its spin- and spatial-dependent parts \mathcal{T}^L and \mathcal{F}^P :

$$\begin{aligned}
 \mathcal{H}_{CSA}^{\rho} &= \sum_k \sum_{m=-k}^k (-1)^m \mathcal{T}_{km}^{\rho} \mathcal{F}_{k-m}^L \\
 &= \sum_k \sum_{m=-k}^k (-1)^m \sum_{m'=-k}^k \left(\mathcal{T}_{km'}^L \mathcal{D}_{m'm}^{(k)}(\Omega_{L\rho}(t)) \right) \times \\
 &\quad \sum_{n=-k}^k \sum_{n'=-k}^k \left(\mathcal{F}_{kn}^P \mathcal{D}_{nn'}^{(k)}(\Omega_{PN}(t)) \mathcal{D}_{n'-m}^{(k)}(\Omega_{NL}) \right) \\
 &= \frac{1}{24} \gamma B_0 \delta \left(\sin(\beta_{L\rho}) (I_- e^{+i\omega_e t} + I_+ e^{-i\omega_e t}) \times \right. \\
 &\quad \sum_{m=-2}^2 \left((6\sqrt{3} \mathcal{D}_{0m}^{(2)}(\Omega_{PN}) \mathcal{D}_{m0}^{(2)}(\Omega_{NL}) \right. \\
 &\quad \left. - 3\sqrt{2} \eta (\mathcal{D}_{2m}^{(2)}(\Omega_{PN}) + \mathcal{D}_{-2m}^{(2)}(\Omega_{PN})) \mathcal{D}_{m0}^{(2)}(\Omega_{NL})) \right) \\
 &\quad \left. + \cos \beta_{L\rho} I_z \times \sum_{m=-2}^2 \left((24 \mathcal{D}_{0m}^{(2)}(\Omega_{PN}) \mathcal{D}_{m0}^{(2)}(\Omega_{NL}) \right. \right. \\
 &\quad \left. \left. - 4\sqrt{6} \eta (\mathcal{D}_{2m}^{(2)}(\Omega_{PN}) + \mathcal{D}_{-2m}^{(2)}(\Omega_{PN})) \mathcal{D}_{m0}^{(2)}(\Omega_{NL})) \right) \right) + \dots \quad (\text{B.1})
 \end{aligned}$$

The (\dots) symbol indicate that more terms exist, corresponding to those with $m' \neq 0$. Because $\omega_0 \ll \omega_e$, these terms do not significantly contribute to $T_{1\rho}$. The expression of the

spin-lattice relaxation rate is given by:

$$\begin{aligned}
\frac{1}{T_{1\rho}} &= \int_0^\infty \frac{[\Delta\mathcal{H}_{CSA}^\rho(t), [\mathcal{H}_{CSA}^{\rho*}(t+\tau), I_z]]d\tau}{\langle I_z \rangle} \\
&= \frac{1}{64} \frac{(\gamma B_0 \delta)^2}{\langle I_z \rangle} \sin^2 \beta_{L\rho} \sum_{m=-2}^2 \left(|\mathcal{D}_{m0}^{(2)}(\Omega_{NL})|^2 (12\langle \Delta\mathcal{D}_{0m}^{PN2} \rangle \right. \\
&\quad \left. + 2\eta^2 (\langle \Delta\mathcal{D}_{2m}^{PN2} \rangle + \langle \Delta\mathcal{D}_{-2m}^{PN2} \rangle)) \right) \times \\
&\quad \int_0^\infty [I_- e^{+i\omega_e t} + I_+ e^{-i\omega_e t}, [I_+ e^{-i\omega_e(t+\tau)} + I_- e^{+i\omega_e(t+\tau)}, I_z]] e^{-\tau/\tau_c} d\tau \quad (B.2)
\end{aligned}$$

where the short form $\langle \Delta\mathcal{D}_{pq}^2 \rangle$ represents the fluctuating portion of the transformation expressed fully by $\langle |\mathcal{D}_{pq}^{(2)}(\Omega)|^2 \rangle - |\langle \mathcal{D}_{pq}^{(2)}(\Omega) \rangle|^2$. The terms in with I_z were immediately dropped because they commute. Then, applying the following commutation property:

$$[aI_+ + bI_-, [a'I_- + b'I_+, I_z]] = 2I_z(aa' + bb')$$

where $I_z \sim \langle I_z \rangle$, the expression reduces to:

$$\begin{aligned}
\frac{1}{T_{1\rho}} &= \frac{1}{64} \frac{(\gamma B_0 \delta)^2}{\langle I_z \rangle} \sin^2(\beta_{L\rho}) \sum_{m=-2}^2 \left(|\mathcal{D}_{m0}^{(2)}(\Omega_{NL})|^2 (12\langle \Delta\mathcal{D}_{0m}^{PN2} \rangle \right. \\
&\quad \left. + 2\eta^2 (\langle \Delta\mathcal{D}_{2m}^{PN2} \rangle + \langle \Delta\mathcal{D}_{-2m}^{PN2} \rangle)) \right) \times \\
&\quad \int_0^\infty 4I_z \cos(\omega_e \tau) e^{-\tau/\tau_c} d\tau, \quad (B.3)
\end{aligned}$$

an using the definition of the spectral density:

$$\int_0^\infty \cos(\omega_e \tau) e^{-\tau/\tau_c} d\tau = \frac{\tau_c}{1 + \omega_e^2 \tau_c^2} = j(\omega_e)$$

The expression becomes:

$$\begin{aligned}
\frac{1}{T_{1\rho}} &= \frac{1}{16} (\gamma B_0 \delta)^2 \sin^2 \beta_{L\rho} \sum_{m=-2}^2 |\mathcal{D}_{m0}(\Omega_{NL})|^2 \\
&\quad (12\langle \Delta\mathcal{D}_{0m}^{PN2} \rangle + 2\eta^2 (\langle \Delta\mathcal{D}_{2m}^{PN2} \rangle + \langle \Delta\mathcal{D}_{-2m}^{PN2} \rangle)) \times j(\omega_e). \quad (B.4)
\end{aligned}$$

Now expanding the relevant Wigner transformation terms, and using the definitions given by Equation 6.20 (p. 118) for \mathcal{A}_m and \mathcal{B}_m , one obtains:

$$\begin{aligned}
\frac{1}{T_{1\rho}} &= \frac{1}{16} (\gamma B_0 \delta)^2 \sin^2 \beta_{L\rho} j(\omega_e) \left(|\mathcal{D}_{-20}^{(2)}(\Omega_{NL})|^2 \cdot (12\mathcal{A}_2 + 2\eta^2 \mathcal{B}_2) \right. \\
&\quad + |\mathcal{D}_{-10}^{(2)}(\Omega_{NL})|^2 \cdot (12\mathcal{A}_1 + 2\eta^2 \mathcal{B}_1) \\
&\quad + |\mathcal{D}_{00}^{(2)}(\Omega_{NL})|^2 \cdot (12\mathcal{A}_0 + 2\eta^2 \mathcal{B}_0) \\
&\quad + |\mathcal{D}_{10}^{(2)}(\Omega_{NL})|^2 \cdot (12\mathcal{A}_1 + 2\eta^2 \mathcal{B}_1) \\
&\quad \left. + |\mathcal{D}_{20}^{(2)}(\Omega_{NL})|^2 \cdot (12\mathcal{A}_2 + 2\eta^2 \mathcal{B}_2) \right) \quad (B.5)
\end{aligned}$$

in which the following identities:

$$|\mathcal{D}_{00}(\Omega_{NL})|^2 = \frac{1}{4}(3 \cos^2 \beta_{NL} - 1)^2$$

$$|\mathcal{D}_{\pm 10}(\Omega_{NL})|^2 = \frac{3}{8} \sin^2 2\beta_{NL}$$

$$|\mathcal{D}_{\pm 20}(\Omega_{NL})|^2 = \frac{3}{8} \sin^4 \beta_{NL}$$

can be grouped to give the final expression of for $1/T_{1\rho}$:

$$\begin{aligned} \frac{1}{T_{1\rho}} &= \frac{1}{16}(\gamma B_0 \delta)^2 \sin^2 \beta_{L\rho} j(\omega_e) \left[\frac{1}{2}(3 \cos^2 \beta_{NL} - 1)^2 \cdot (6\mathcal{A}_0 + \eta^2 \mathcal{B}_0) \right. \\ &\quad \left. + \frac{3}{2} \sin^2 2\beta_{NL} \cdot (6\mathcal{A}_1 + \eta^2 \mathcal{B}_1) \right. \\ &\quad \left. + \frac{3}{2} \sin^4 \beta_{NL} \cdot (6\mathcal{A}_2 + \eta^2 \mathcal{B}_2) \right] \end{aligned} \quad (\text{B.6})$$

B.2 The direct heteronuclear (*IS*) spin-spin dipolar interaction in oriented membranes.

The general expression of the Hamiltonian for the dipolar interaction between unlike spins *I* and *S*,

$$\begin{aligned} \mathcal{H}_{IS}^\rho &= \sum_k \sum_{m=-k}^k (-1)^m T_{km}^\rho \mathcal{F}_{k-m}^L \\ &= \sum_k \sum_{m=-k}^k (-1)^m \sum_{m'=-k}^k \left(T_{km'}^L \mathcal{D}_{m'm}^{(k)}(\Omega_{L\rho}(t)) \right) \times \\ &\quad \sum_{n=-k}^k \sum_{n'=-k}^k \left(\mathcal{F}_{kn}^P \mathcal{D}_{nn'}^{(k)}(\Omega_{PN}(t)) \mathcal{D}_{n'-m}^{(k)}(\Omega_{NL}) \right) \end{aligned} \quad (\text{B.7})$$

is expanded to:

$$\begin{aligned} \mathcal{H}_{IS}^\rho &= \frac{3}{4} \frac{\mu_0}{4\pi} \frac{\gamma_I \gamma_S \hbar^2}{r_{IS}^3} \sum_{m=-2}^2 \mathcal{D}_{0m}^{(2)}(\Omega_{PN}(t)) \mathcal{D}_{m0}^{(2)}(\Omega_{NL}) \times \\ &\quad \left(\sin^2(\beta_{L\rho}) \times (I_- S_- e^{-2i\omega_e t} - I_+ S_+ e^{2i\omega_e t}) \right. \\ &\quad \left. + \sin 2(\beta_{L\rho}) \times ((I_z S_+ + I_+ S_z) e^{-i\omega_e t} + (I_z S_- + I_- S_z) e^{+i\omega_e t}) \right. \\ &\quad \left. - (3 \cos^2(\beta_{L\rho}) - 1) \times 2I_z S_z \right) + \dots \end{aligned} \quad (\text{B.8})$$

Only the terms precessing at a rate near ω_e are laid out and are carried forward from here on. The expression of the spin-lattice relaxation rate is thus given by:

$$\begin{aligned}
\frac{1}{T_{1\rho}} &= \int_0^\infty \frac{[\Delta\mathcal{H}_{IS}^\rho(t), [\mathcal{H}_{IS}^{\rho*}(t+\tau), I_z]] d\tau}{\langle I_z \rangle} \\
&= \frac{9}{16\langle I_z \rangle} \left(\frac{\mu_0}{4\pi} \right)^2 \left(\frac{\gamma I \gamma_S \hbar^2}{r_{IS}^3} \right)^2 \sum_{m=-2}^2 |\mathcal{D}_{m0}(\Omega_{NL})|^2 \langle \Delta\mathcal{D}_{0m}^{PN2} \rangle \\
&\quad \int_0^\infty \left(\sin^4 \beta_{L\rho} ([I_+ S_+ + I_- S_-] e^{+2i\omega_e t}, [(I_- S_- + I_+ S_+) e^{-2i\omega_e(t+\tau)}, I_z]) \right. \\
&\quad + \sin^2 2\beta_{L\rho} ([I_z S_+ + I_+ S_z] e^{-i\omega_e t}, [(I_z S_- + I_- S_z) e^{i\omega_e(t+\tau)}, I_z]) \\
&\quad + [(I_z S_- + I_- S_z) e^{i\omega_e t}, [(I_z S_+ + I_+ S_z) e^{-i\omega_e(t+\tau)}, I_z]) \\
&\quad \left. + (3 \cos^2 \beta_{L\rho} - 1)^2 [2I_z S_z, [2I_z S_z, I_z]] \right) e^{-\tau/\tau_c} d\tau
\end{aligned} \tag{B.9}$$

Given the following commutation properties:

$$\begin{aligned}
[a(I_+ S_+ + I_- S_-), [a'(I_- S_- + I_+ S_+), I_z]] &= 4I_z S_z (aa'), \\
[a(I_z S_\pm + I_\pm S_z), [a'(I_z S_\mp + I_\mp S_z), I_z]] &= 0, \\
[aI_z S_z, [a'I_z S_z, I_z]] &= 0,
\end{aligned}$$

and that

$$8I_z S_z \cos(2\omega_e \tau) = 8/3 \langle I_z \rangle S(S+1) \cos(2\omega_e \tau).$$

the expression for $1/T_{1\rho}$ is reduced to:

$$\begin{aligned}
\frac{1}{T_{1\rho}} &= \frac{9}{16\langle I_z \rangle} \left(\frac{\mu_0}{4\pi} \right)^2 \left(\frac{\gamma I \gamma_S \hbar^2}{r_{IS}^3} \right)^2 \sin^4(\beta_{L\rho}) \sum_{m=-2}^2 |\mathcal{D}_{m0}^{(2)}(\Omega_{NL})|^2 \langle \Delta\mathcal{D}_{0m}^{PN2} \rangle \times \\
&\quad \int_0^\infty \frac{4}{3} S(S+1) \langle I_z \rangle 2 \cos(2\omega_e \tau) e^{\tau/\tau_c} d\tau \\
&= \frac{3}{2} \left(\frac{\mu_0}{4\pi} \right)^2 \left(\frac{\gamma I \gamma_S \hbar^2}{r_{IS}^3} \right)^2 S(S+1) \sin^4(\beta_{L\rho}) \sum_{m=-2}^2 |\mathcal{D}_{m0}^{(2)}(\Omega_{NL})|^2 \langle \Delta\mathcal{D}_{0m}^{PN2} \rangle j(2\omega_e) \\
&= \frac{3}{8} \left(\frac{\mu_0}{4\pi} \right)^2 \left(\frac{\gamma I \gamma_S \hbar^2}{r_{IS}^3} \right)^2 S(S+1) \sin^4(\beta_{L\rho}) j(2\omega_e) \times \\
&\quad \left(\mathcal{A}_0 (3 \cos^2 \beta_{NL} - 1)^2 + 3\mathcal{A}_1 \sin^2 2\beta_{NL} + 3\mathcal{A}_2 \sin^4 \beta_{NL} \right)
\end{aligned} \tag{B.10}$$

where, once again the definitions of Equation 6.20 (p. 118) were used.

B.3 The direct homonuclear (II) spin-spin dipolar interaction in oriented membranes.

The general expression of the Hamiltonian for the dipolar interaction between like spins I and I' ,

$$\begin{aligned}
 \mathcal{H}_{II}^{\rho} &= \sum_k \sum_{m=-k}^k (-1)^m T_{km}^{\rho} \mathcal{F}_{k-m}^L \\
 &= \sum_k \sum_{m=-k}^k (-1)^m \sum_{m'=-k}^k \left(T_{km'}^L \mathcal{D}_{m'm}^{(k)}(\Omega_{L\rho}(t)) \right) \times \\
 &\quad \sum_{n=-k}^k \sum_{n'=-k}^k \left(\mathcal{F}_{kn}^P \mathcal{D}_{nn'}^{(k)}(\Omega_{PN}(t)) \mathcal{D}_{n'-m}^{(k)}(\Omega_{NL}) \right)
 \end{aligned} \tag{B.11}$$

is expanded to:

$$\begin{aligned}
 \mathcal{H}_{II'} &= \frac{3}{4} \frac{\mu_0}{4\pi} \frac{\gamma_I^2 \hbar^2}{r_{II'}^3} \sum_{m=-2}^2 \mathcal{D}_{0m}^{(2)}(\Omega_{PN}(t)) \mathcal{D}_{m0}^{(2)}(\Omega_{NL}) \times \\
 &\quad \left(\sin^2(\beta_{L\rho}) \times (I_- I'_- e^{-2i\omega_e t} - I_+ I'_+ e^{2i\omega_e t}) \right. \\
 &\quad \left. + \sin(2\beta_{L\rho}) \times ((I_z I'_+ + I_+ I'_z) e^{-i\omega_e t} + (I_z I'_- + I_- I'_z) e^{+i\omega_e t}) \right. \\
 &\quad \left. - (3 \cos^2(\beta_{L\rho}) - 1) \frac{2}{3} (3 I_z I'_z - \vec{I} \cdot \vec{I}') \right) + \dots
 \end{aligned} \tag{B.12}$$

Once again, only those terms precessing at rates near ω_e are carried forward. The expression of the spin-lattice relaxation rate is thus given by:

$$\begin{aligned}
 \frac{1}{T_{1\rho}} &= \int_0^\infty \frac{[\Delta \mathcal{H}_{II}^{\rho}(t), [\mathcal{H}_{II}^{\rho*}(t+\tau), I_z]] d\tau}{\langle I_z + I'_z \rangle} \\
 &= \frac{9}{16 \langle I_z + I'_z \rangle} \left(\frac{\mu_0}{4\pi} \right)^2 \left(\frac{\gamma_I^2 \hbar^2}{r_{IS}^3} \right)^2 \left(\frac{16}{3} \right) I(I+1) \langle I_z + I'_z \rangle \sum_{m=-2}^2 |\mathcal{D}_{m0}(\Omega_{NL})|^2 \langle \Delta \mathcal{D}_{0m}^{PN2} \rangle \times \\
 &\quad \int_0^\infty \cos(2\omega_e \tau) e^{\tau/\tau_c} d\tau \\
 &= 3 \left(\frac{\mu_0}{4\pi} \right)^2 \left(\frac{\gamma_I^2 \hbar^2}{r_{IS}^3} \right)^2 I(I+1) \sum_{m=-2}^2 |\mathcal{D}_{m0}(\Omega_{NL})|^2 \langle \Delta \mathcal{D}_{0m}^{PN2} \rangle j(2\omega_e) \\
 &= \frac{3}{4} \left(\frac{\mu_0}{4\pi} \right)^2 \left(\frac{\gamma_I^2 \hbar^2}{r_{II'}^3} \right)^2 I(I+1) \sin^4(\beta_{L\rho}) j(2\omega_e) \times \\
 &\quad \left(\mathcal{A}_0 (3 \cos^2 \beta_{NL} - 1)^2 + 3 \mathcal{A}_1 \sin^2 2\beta_{NL} + 3 \mathcal{A}_2 \sin^4 \beta_{NL} \right)
 \end{aligned} \tag{B.13}$$

where the following simplifications were used:

$$\begin{aligned}
 [a(I_+ I'_+ + I_- I'_-), [a'(I_- I'_- + I_+ I'_+), I_z + I'_z]] &= 4 I_z I'_z (aa') \\
 [a(I_z I'_\pm + I_\pm I'_z), [a'(I_z I'_\mp + I_\mp I'_z), I_z + I'_z]] &= 0,
 \end{aligned}$$

$$[a(3I_z I'_z - \vec{I} \cdot \vec{I}'), [a'(3I_z I'_z - \vec{I} \cdot \vec{I}'), I_z + I'_z]] = 0$$

and

$$8I_z I'_z \cos(2\omega_e \tau) = 16/3 \langle I_z + I'_z \rangle I(I+1) \cos(2\omega_e \tau).$$

B.4 The chemical shift anisotropy in MAS membrane samples

As above, the derivation starts with the expression of the Hamiltonian. The chemical shift Hamiltonian for a MAS sample requires one more transformation involving the rotor frame R . Keeping only the relevant terms, the following expression is obtained:

$$\begin{aligned} \mathcal{H}_{CS}^\rho &= \sum_k \sum_{m=-k}^k (-1)^m T_{km}^\rho \mathcal{F}_{k-m}^L \\ &= \sum_k \sum_{m=-k}^k (-1)^m \sum_{m'=-k}^k \left(T_{km'}^L \mathcal{D}_{m'm}^{(k)}(\Omega_{L\rho}(t)) \right) \\ &\quad \sum_{n=-k}^k \sum_{n'=-k}^k \sum_{n''=-k}^k \left(\mathcal{F}_{kn}^P \mathcal{D}_{nn'}^{(k)}(\Omega_{PN}(t)) \mathcal{D}_{n'n''}^{(k)}(\Omega_{NR}) \mathcal{D}_{n''-m}^{(k)}(\Omega_{RL}(t)) \right) \\ &= \frac{\sqrt{3}}{48} \gamma \delta B_0 \sin(\beta_{L\rho}) \\ &\quad \times \sum_{m=-2}^2 \left(2\sqrt{3} \mathcal{D}_{0m}^{(2)}(\Omega_{PN}(t)) - \sqrt{2} \eta \left(\mathcal{D}_{2m}^{(2)}(\Omega_{PN}(t)) + \mathcal{D}_{-2m}^{(2)}(\Omega_{PN}(t)) \right) \right) \\ &\quad \times \left(\sqrt{2} \mathcal{D}_{m-2}^{(2)}(\Omega_{NR}) [I_+ e^{-it(\omega_e - 2\omega_R)} + I_- e^{it(\omega_e + 2\omega_R)}] \right. \\ &\quad - 2\mathcal{D}_{m-1}^{(2)}(\Omega_{NR}) [I_+ e^{-it(\omega_e - \omega_R)} + I_- e^{it(\omega_e + \omega_R)}] \\ &\quad + 2\mathcal{D}_{m+1}^{(2)}(\Omega_{NR}) [I_+ e^{-it(\omega_e + \omega_R)} + I_- e^{it(\omega_e - \omega_R)}] \\ &\quad \left. + \sqrt{2} \mathcal{D}_{m+2}^{(2)}(\Omega_{NR}) [I_+ e^{-it(\omega_e + 2\omega_R)} + I_- e^{it(\omega_e - 2\omega_R)}] \right) + \dots \end{aligned} \quad (\text{B.14})$$

From here on, terms with ω_0 , represented by (\dots) , are dropped. The short form $\omega_{\pm n} = \omega_e \pm n\omega_R$ is used for convenience. Other simplification, defined previously, are also implemented:

$$\begin{aligned} \frac{1}{T_{1\rho}} &= \frac{1}{192} (\gamma B_0 \delta)^2 \sin^2 \beta_{L\rho} \sum_{m=-2}^2 (12 \langle \Delta \mathcal{D}_{0m}^{PN2} \rangle + 2\eta^2 (\langle \Delta \mathcal{D}_{2m}^{PN2} \rangle + \langle \Delta \mathcal{D}_{-2m}^{PN2} \rangle)) \times \\ &\quad \int_0^\infty \left(|\mathcal{D}_{m-2}^{(2)}(\Omega_{NR})|^2 (e^{+i\omega_{-2}\tau} + e^{-i\omega_{+2}\tau}) \right. \\ &\quad + 2|\mathcal{D}_{m-1}^{(2)}(\Omega_{NR})|^2 (e^{+i\omega_{-1}\tau} + e^{-i\omega_{+1}\tau}) \\ &\quad + 2|\mathcal{D}_{m1}^{(2)}(\Omega_{NR})|^2 (e^{+i\omega_{+1}\tau} + e^{-i\omega_{-1}\tau}) \\ &\quad \left. + |\mathcal{D}_{m2}^{(2)}(\Omega_{NR})|^2 (e^{+i\omega_{+2}\tau} + e^{-i\omega_{-2}\tau}) \right) e^{-\tau/\tau_c} d\tau \end{aligned} \quad (\text{B.15})$$

Since the sample is not oriented, applying the solid angle summation on the transformation NR gives a common result for any term $|\mathcal{D}_{pq}^{(2)}(\Omega_{NR})|^2$:

$$(4\pi)^{-1} \int_0^{2\pi} \int_0^\pi |\mathcal{D}_{pq}^{(2)}(\Omega_{NR})|^2 \sin \beta_{NR} d\beta_{NR} d\alpha_{NR} = 1/5$$

and yields the expression for $1/T_{1\rho}$:

$$\begin{aligned} \left\langle \frac{1}{T_{1\rho}} \right\rangle_{\text{powder}} &= \frac{1}{192} (\gamma B_0 \delta)^2 \sin^2 \beta_{L\rho} \sum_{m=-2}^2 (12 \langle \Delta \mathcal{D}_{0m}^{PN2} \rangle + 2\eta^2 (\langle \Delta \mathcal{D}_{2m}^{PN2} \rangle + \langle \Delta \mathcal{D}_{-2m}^{PN2} \rangle)) \times \\ &\quad \frac{1}{5} \int_0^\infty \left((2 \cos(\omega_{-2}\tau) + 2 \cos(\omega_{+2}\tau) + 4 \cos(\omega_{-1}\tau) + 4 \cos(\omega_{+1}\tau)) d\tau e^{-\tau/\tau_e} \right) \\ &= \frac{1}{480} (\gamma B_0 \delta)^2 \sin^2 \beta_{L\rho} \sum_{m=-2}^2 (12 \langle \Delta \mathcal{D}_{0m}^{PN2} \rangle + 2\eta^2 (\langle \Delta \mathcal{D}_{2m}^{PN2} \rangle + \langle \Delta \mathcal{D}_{-2m}^{PN2} \rangle)) \times \\ &\quad (j(\omega_{-2}) + j(\omega_{+2}) + 2j(\omega_{-1}) + 2j(\omega_{+1})) \\ &= \frac{1}{240} (\gamma B_0 \delta)^2 \sin^2 \beta_{L\rho} \left(\sum_{m=-2}^2 6A_{|m|} + \eta^2 B_{|m|} \right) \times \\ &\quad (j(\omega_e - 2\omega_R) + j(\omega_e + 2\omega_R) + 2j(\omega_e - \omega_R) + 2j(\omega_e + \omega_R)) \end{aligned} \quad (\text{B.16})$$

B.5 The direct heteronuclear (IS) spin-spin dipolar interaction in MAS membrane samples

Starting with the full Hamiltonian expression of the dipolar interaction between unlike spins, including the rotor frame, R :

$$\begin{aligned} \mathcal{H}_{IS}^\rho &= \sum_k \sum_{m=-k}^k (-1)^m T_{km}^\rho \mathcal{F}_{k-m}^L \\ &= \sum_k \sum_{m=-k}^k (-1)^m \sum_{m'=-k}^k \left(T_{km'}^L \mathcal{D}_{m'm}^{(k)}(\Omega_{L\rho}(t)) \right) \times \\ &\quad \sum_{n=-k}^k \sum_{n'=-k}^k \sum_{n''=-k}^k \left(\mathcal{F}_{kn}^P \mathcal{D}_{nn'}^{(k)}(\Omega_{PN}(t)) \mathcal{D}_{n'n''}^{(k)}(\Omega_{NR}) \mathcal{D}_{n''-m}^{(k)}(\Omega_{RL}(t)) \right) \\ &= \frac{\sqrt{3}}{4} \frac{\mu_0}{4\pi} \frac{\gamma_I \gamma_S \hbar^2}{r_{IS}^3} \sin^2 \beta_{L\rho} \sum_{m=-2}^2 \mathcal{D}_{0m}^{(2)}(\Omega_{PN}(t)) \times \\ &\quad \times \left(1/\sqrt{2} \mathcal{D}_{m-2}^{(2)}(\Omega_{NR}) (I_+ S_+ e^{i\omega_{+2}t} - I_- S_- e^{i\omega_{-2}t}) \right. \\ &\quad - \mathcal{D}_{m-1}^{(2)}(\Omega_{NR}) (I_+ S_+ e^{i\omega_{+1}t} - I_- S_- e^{i\omega_{-1}t}) \\ &\quad + \mathcal{D}_{m+1}^{(2)}(\Omega_{NR}) (I_+ S_+ e^{i\omega_{-1}t} - I_- S_- e^{i\omega_{+1}t}) \\ &\quad \left. + 1/\sqrt{2} \mathcal{D}_{m+2}^{(2)}(\Omega_{NR}) (I_+ S_+ e^{i\omega_{-2}t} - I_- S_- e^{i\omega_{+2}t}) \right) + \dots \end{aligned} \quad (\text{B.17})$$

omitting all terms with $m' \neq 0$. For simplicity, the terms vanishing in the up-coming commutation were also dropped and the expression $2\omega_0 \pm n\omega_e$ is substituted by the short

form $\omega_{\pm n}$: Performing the relevant commutations already mentioned above, the expression for the relaxation rate of interest becomes:

$$\begin{aligned}
\frac{1}{T_{1\rho}} &= \int_0^\infty \frac{[\Delta\mathcal{H}_{IS}^\rho(t), [\mathcal{H}_{IS}^{\rho*}(t+\tau), I_z]]d\tau}{\langle I_z \rangle} \\
&= \frac{3}{16\langle I_z \rangle} \left(\frac{\mu_0}{4\pi}\right)^2 \left(\frac{\gamma_I \gamma_S \hbar^2}{r_{IS}^3}\right)^2 \sum_{m=-2}^2 \langle \Delta\mathcal{D}_{0m}^{PN2} \rangle \int_0^\infty \frac{4}{3} \langle I_z \rangle S(S+1) \times \\
&\quad \left(\frac{1}{2} |\mathcal{D}_{m-2}^{(2)}(\Omega_{NR})|^2 (e^{+i\omega_{-2}\tau} + e^{-i\omega_{+2}\tau}) \right. \\
&\quad + |\mathcal{D}_{m-1}^{(2)}(\Omega_{NR})|^2 (e^{+i\omega_{-1}\tau} + e^{-i\omega_{+1}\tau}) \\
&\quad + |\mathcal{D}_{m1}^{(2)}(\Omega_{NR})|^2 (e^{+i\omega_{+1}\tau} + e^{-i\omega_{-1}\tau}) \\
&\quad \left. + \frac{1}{2} |\mathcal{D}_{m2}^{(2)}(\Omega_{NR})|^2 (e^{+i\omega_{+2}\tau} + e^{-i\omega_{-2}\tau}) \right) e^{-\tau/\tau_c} d\tau \quad (\text{B.18})
\end{aligned}$$

Now applying the powder average followed by the transformation to spectral density terms, the expression of the initial relaxation rate constant can be obtained:

$$\begin{aligned}
\left\langle \frac{1}{T_{1\rho}} \right\rangle_{\text{powder}} &= \frac{1}{4} \left(\frac{\mu_0}{4\pi}\right)^2 \left(\frac{\gamma_I \gamma_S \hbar^2}{r_{IS}^3}\right)^2 S(S+1) \sum_{m=-2}^2 \langle \Delta\mathcal{D}_{0m}^{PN2} \rangle \times \\
&\quad \int_0^\infty \frac{1}{5} \left(\cos(\omega_{-2}\tau) + \cos(\omega_{+2}\tau) + 2\cos(\omega_{-1}\tau) + 2\cos(\omega_{+1}\tau) \right) e^{-\tau/\tau_c} d\tau \\
&= \frac{1}{20} \left(\frac{\mu_0}{4\pi}\right)^2 \left(\frac{\gamma_I \gamma_S \hbar^2}{r_{IS}^3}\right)^2 S(S+1) \sum_{m=-2}^2 (\mathcal{A}_{|m|}) \times \\
&\quad (j(2\omega_e - 2\omega_R) + j(2\omega_e + 2\omega_R) + 2j(2\omega_e - \omega_R) + 2j(2\omega_e + \omega_R)) \quad (\text{B.19})
\end{aligned}$$

B.6 The direct homonuclear (II') spin-spin dipolar interaction in MAS membrane samples

In a similar fashion to the derivation in the case of unlike spins, the dipolar interaction between like spin in a MAS sample requires the initial expression of the Hamiltonian including

the transformation to and from the rotor frame R :

$$\begin{aligned}
\mathcal{H}_{II}^\rho &= \sum_k \sum_{m=-k}^k (-1)^m T_{km}^\rho \mathcal{F}_{k-m}^L \\
&= \sum_k \sum_{m=-k}^k (-1)^m \sum_{m'=-k}^k \left(T_{km'}^L \mathcal{D}_{m'm}^{(k)}(\Omega_{L\rho}(t)) \right) \times \\
&\quad \sum_{n=-k}^k \sum_{n'=-k}^k \sum_{n''=-k}^k \left(\mathcal{F}_{kn}^P \mathcal{D}_{nn'}^{(k)}(\Omega_{PN}(t)) \mathcal{D}_{n'n''}^{(k)}(\Omega_{NR}) \mathcal{D}_{n''-m}^{(k)}(\Omega_{RL}(t)) \right) \\
&= \frac{\sqrt{3}}{4} \frac{\mu_0}{4\pi} \frac{\gamma_I^2 \hbar^2}{r_{II'}^3} \sin^2 \beta_{L\rho} \sum_{m=-2}^2 \mathcal{D}_{0m}^{(2)}(\Omega_{PN}(t)) \times \\
&\quad \left(1/\sqrt{2} \mathcal{D}_{m-2}^{(2)}(\Omega_{NR}) (I_+ I'_+ e^{i\omega+2t} - I_- I'_- e^{i\omega-2t}) \right. \\
&\quad - \mathcal{D}_{m-1}^{(2)}(\Omega_{NR}) (I_+ I'_+ e^{i\omega+1t} - I_- I'_- e^{i\omega-1t}) \\
&\quad + \mathcal{D}_{m+1}^{(2)}(\Omega_{NR}) (I_+ I'_+ e^{i\omega-1t} - I_- I'_- e^{i\omega+1t}) \\
&\quad \left. + 1/\sqrt{2} \mathcal{D}_{m+2}^{(2)}(\Omega_{NR}) (I_+ I'_+ e^{i\omega-2t} - I_- I'_- e^{i\omega+2t}) \right) + \dots
\end{aligned} \tag{B.20}$$

where only the relevant terms which contribute to the spin-lattice relaxation are shown. Thus, the expression for the spin-lattice relaxation is derived after applying the relevant commutation already defined above.

$$\begin{aligned}
\frac{1}{T_{1\rho}} &= \int_0^\infty \frac{[\Delta \mathcal{H}_{II}^\rho(t), [\mathcal{H}_{II}^{\rho*}(t+\tau), I_z + I'_z]] d\tau}{\langle I_z + I'_z \rangle} \\
&= \frac{3}{16 \langle I_z + I'_z \rangle} \left(\frac{\mu_0}{4\pi} \right)^2 \left(\frac{\gamma_I^2 \hbar^2}{r_{II'}^3} \right)^2 \sum_{m=-2}^2 \langle \Delta \mathcal{D}_{0m}^{PN2} \int_0^\infty \frac{8}{3} \langle I_z + I'_z \rangle I(I+1) \times \\
&\quad \left(1/2 |\mathcal{D}_{m-2}^{(2)}(\Omega_{NR})|^2 (e^{+i\omega-2\tau} + e^{-i\omega+2\tau}) \right. \\
&\quad + |\mathcal{D}_{m-1}^{(2)}(\Omega_{NR})|^2 (e^{+i\omega-1\tau} + e^{-i\omega+1\tau}) \\
&\quad + |\mathcal{D}_{m+1}^{(2)}(\Omega_{NR})|^2 (e^{+i\omega+1\tau} + e^{-i\omega-1\tau}) \\
&\quad \left. + 1/2 |\mathcal{D}_{m+2}^{(2)}(\Omega_{NR})|^2 (e^{+i\omega+2\tau} + e^{-i\omega-2\tau}) \right) e^{-\tau/\tau_c} d\tau
\end{aligned} \tag{B.21}$$

Finally, applying, as before, the powder average and the reduction to spectral density terms, an average expression is obtained corresponding to the initial time constant of the relaxation

function.

$$\begin{aligned}
\left\langle \frac{1}{T_{1\rho}} \right\rangle_{\text{powder}} &= \frac{1}{2} \left(\frac{\mu_0}{4\pi} \right)^2 \left(\frac{\gamma_I^2 \hbar^2}{r_{II'}^3} \right)^2 I(I+1) \sum_{m=-2}^2 \langle \Delta \mathcal{D}_{0m}^{PN2} \rangle \times \\
&\quad \int_0^\infty \frac{1}{5} \left(\cos(\omega_{-2}\tau) + \cos(\omega_{+2}\tau) + 2\cos(\omega_{-1}\tau) + 2\cos(\omega_{+1}\tau) \right) e^{-\tau/\tau_c} d\tau \\
&= \frac{1}{10} \left(\frac{\mu_0}{4\pi} \right)^2 \left(\frac{\gamma_I^2 \hbar^2}{r_{II'}^3} \right)^2 I(I+1) \sum_{m=-2}^2 (A_{|m|}) \times \\
&\quad (j(2\omega_e - 2\omega_R) + j(2\omega_e + 2\omega_R) + 2j(2\omega_e - \omega_R) + 2j(2\omega_e + \omega_R)) \quad (\text{B.22})
\end{aligned}$$

—◆—



Request for Permission to Use Prentice Hall Higher Education Content in Print Format

TO: PERMISSIONS DEPARTMENT FAX: 201-236-3290		FROM: <i>Christophe FARES</i>	
BOOK TITLE: <i>Biology, 6/E</i>		EDITION:	
AUTHOR: <i>Neil A. Campbell and Jane B. Reece</i>			
ISBN: <i>0-8053-6624-5</i>			
ANCILLARY:			
REQUESTED MATERIAL INCLUDING PAGES, ILLUSTRATION AND FIGURE NUMBERS; CHAPTERS, PAGES, CHARTS, PHOTOGRAPHS, AND THE PAGE NUMBERS ON WHICH THEY APPEAR: <i>Figure 8.6 Page 142, only.</i>			
HOW THE REQUESTER WISHES TO USE THE MATERIAL: i.e., CLASSROOM HANDOUT, COURSEPACK, REPUBLICATION: <i>As a support figure in a Ph.D. thesis.</i>			
FOR CLASSROOM USE:		FOR OTHER USES:	
PROFESSOR'S NAME:		REQUESTOR'S NAME: <i>Christophe FARES</i>	
FULL SCHOOL MAILING ADDRESS:		FULL MAILING ADDRESS:	
E-MAIL ADDRESS:		E-MAIL AND FAX:	
FAX NUMBER:		CLIENT'S NAME (if applicable):	
COURSE NAME:		USER'S NAME AND ADDRESS (if different than requestor's):	
SEMESTER:			
NUMBER OF STUDENTS:			
REQUESTOR'S NAME, ADDRESS, E-MAIL, AND FAX (if different than professor):		INTENDED USE, INCLUDING ANY PUBLICATION INFORMATION, SUCH AS: PUBLISHER, TERRITORY, PRINT RUNS, DATE OF INTENDED FIRST PUBLICATION OR USE: <i>Figure in a scientific Ph.D. thesis.</i>	
PERMISSION GRANTED Exclusive of material acknowledged to another source. One time use. CREDIT: Title, author(s) copyright notice. Reprinted by permission of Pearson Education, Inc. Fee: \$ Date: <i>8/16/03</i> <i>[Signature]</i> Beth Weller		NUMBER OF COPIES OR UNITS THAT WILL BE REPRODUCED: <i>4 copies</i>	
		USER TYPE: (e.g., enrolled students, on campus students, others?): <i>Colleagues</i>	
		WILL THE TEXTBOOK BE ADOPTED AND STUDENTS REQUIRED TO PURCHASE THE TEXT OR PRODUCT FOR THE COURSE? <i>NO</i>	

If permission is being requested for use in an electronic/digital format, please use the "Electronic/Digital Permission Request" form.

Global Rights Group

Servicing rights and permission for Brooks/Cole • Course Technology • Custom Publishing •
Delmar Learning • Heinle • Nelson Canada • Peterson's • South-Western • Wadsworth
Thomson Learning Global Rights Group 10 Davis Drive, Belmont, California 94002 USA
Phone: 800 730-2214 Fax: 800 730-2215 Email: thomsonrights@thomsonlearning.com
For fastest service, please visit our web site at www.thomsonrights.com

THOMSON

LEARNING

Response # 78342

08/29/2003

Christophe Fares

wing Brooks/Cole material

Title: Introductory Botany: Plants, People, and the Environment 1st edition
Author(s): Berg ISBN: 0030754534
Publisher: Brooks/Cole © Year: 1997
Specific material: Figure 3-4 only, no caption: Page 39
Total pages: 1

For use by:

Instructor: Fares

School / University / Company: University of Guelph

Course title / number: Ph.D. Thesis

Term of use: Fall Term 2003

Intended use:

For inclusion in a research paper, master's thesis, doctoral dissertation, or manuscript to be prepared and submitted for publication. If at a later date a publishing contract is achieved, additional permission will be required.

for Ph.D. thesis only.

The permission granted in this letter extends only to material that is original to the aforementioned text.

This credit line must appear on the first page of text selection and with each individual figure or photo:

From Introductory Botany: , Plants, People, and the Environment 1st edition by Berg. © 1997. Reprinted with permission of Brooks/Cole, a division of Thomson Learning: www.thomsonrights.com.

Sincerely,

Joohee Lee